**The Dissertation Committee for Julio Antonio Zambrano Ferreira certifies that this is the approved version of the following dissertation:**

# Evaluation of Soil-Geogrid Interaction at Different Load Levels Using Pullout Tests and Transparent Soil

**Committee:**

Jorge G. Zornberg, Supervisor

Kenneth H. Stokoe

Robert B. Gilbert

Jorge A. Prozzi

Eric M. Taleff

# Evaluation of Soil-Geogrid Interaction at Different Load Levels Using Pullout Tests and Transparent Soil

**by**

**Julio Antonio Zambrano Ferreira, M.Sc.**

**Dissertation**

Presented to the Faculty of the Graduate School of

The University of Texas at Austin

in Partial Fulfillment

of the Requirements

for the Degree of

**Doctor of Philosophy**

**The University of Texas at Austin**

**August 2013**

# Dedication

To my parents, José and Anita, and to Dr. Benedito Bueno.

# Acknowledgements

I would like to acknowledge CAPES (Brazilian Federal Agency for the Support and Evaluation of Graduate Education) for the scholarship provided to me for the first four years of my period in the Geotechnical Engineering Ph.D. Program at the University of Texas at Austin. I also want to acknowledge TxDOT (Texas Department of Transportation) for financial support in tuition costs given to me through project 5-4829, which I worked on for almost my entire stay at UT Austin. I would also like to acknowledge the partial funding provided to this project by Tensar Corporation– Atlanta office, for the development and implementation of the transparent pullout system.

I want to thank my supervisor during my Ph.D. Degree, Dr. Jorge Zornberg, and my supervisor during my Master's Degree, Dr. Benedito Bueno, for their support and work with CAPES for the scholarship that was awarded to me. I also appreciate the discussions, suggestions, and collaborations of the members of my committee to my research: Dr. Jorge Zornberg, Dr. Jorge Prozzi, Dr. Eric Taleff, Dr. Robert Gilbert, and Dr. Kenneth Stokoe. I want to thank my supervisor and Dr. Jorge Prozzi for guidance throughout my endeavor towards my Ph.D. degree and work on the TxDOT project 5-4829. I want to express my gratitude to Dr. Benedito Bueno, who introduced me to the world of geosynthetics and taught me most of my current knowledge on geosynthetics, laboratory testing, and scientific methodology throughout the years he supervised me during my undergraduate and Master's program research.

I could not have achieved a Ph.D. degree without the incredible support of my parents. Their support cannot be properly described with any words in any language in this world. I also want to thank my partner, Sam Serrano, who not only emotionally

supported me during my Ph.D. program, but also reviewed the writing of most of the chapters of my dissertation. She greatly improved the quality of this dissertation. I also appreciate the review and suggestions in the discussion of my results, provided by Jeff Kuhn. I want to thank Xin Peng for his help with the direct shear tests and the preparation of some of the transparent pullout tests. I want to thank Eddie and Esther for all of their great support in the most decisive moments of me getting my Ph.D. degree.

Special thanks to Onur and Yiorgos for their friendship for life, their support, and amazing time spent under the same roof that made my time in Austin so much better. I want to thank all of the friends that I made at the German House Co-op, where I spent my first years in Austin; especially Jack for being such a great roommate. I appreciate the help and laughs from my friend Alvaro.

I want to thank all of my lab mates throughout my years at UT-Austin, who helped me to adjust to American culture, shared their ideas with me, and helped with great suggestions and technical discussions. I want to thank all of the undergraduate students who worked with me on the laboratory testing portion of TxDOT project 5-4829. Finally, I appreciate the great help of the staff members of the Geotechnical Engineering Graduate Program and the Civil Engineering Department in completing my project and paperwork.

# Evaluation of Soil-Geogrid Interaction at Different Load Levels Using Pullout Tests and Transparent Soil

Julio Antonio Zambrano Ferreira, Ph.D.

The University of Texas at Austin, 2013

Supervisor: Jorge G. Zornberg

Geogrids have been used for decades as reinforcement for mechanically stabilized earth retaining walls and base layers of pavements. However, literature on these applications is contradictory regarding the displacement and strain levels at which the bearing mechanism of interaction between soil and geogrid is developed along the transverse ribs of geogrids. No data are available on the deflections and displacement profiles of transverse ribs during loading of geogrids. Field and laboratory data on strain distributions along geogrids are limited. Accordingly, the objective of this study is to better understand the mechanisms of soil-geogrid interaction that develop at different stages of pullout tests, especially at small displacements and strains. Moreover, the behavior of transverse ribs throughout pullout testing is evaluated. Pullout loads were obtained from a load cell synchronized with two 5 MP cameras. Images of the geogrid were analyzed using the Particle Image Velocimetry (PIV) technique to obtain displacement profiles along the entire geogrid specimen throughout the duration of the test. Five transparent pullout tests were conducted using a confining pressure of 35 kPa (5 psi) on polypropylene geogrids with different configurations. Displacements along the polypropylene geogrid used in this study are well represented by an exponential equation. The bearing mechanism along transverse ribs was observed to develop at small

displacements. The contribution of the bearing mechanism was first observed at 25 % of the maximum pullout force. Interference between transverse ribs was first observed at approximately 60 % of the maximum pullout force. High interference between transverse ribs was observed when the ratio of spacing between transverse ribs (S) over the thickness of the transverse ribs (B) was equal to 24. Negligible interference was observed when S/B was equal to 57. Displacements of soil particles were observed when the ratio distance from the soil-geogrid interface (d) over the $D_{50}$ of the soil was equal to 3, but they were orders of magnitude smaller than the displacements of the geogrid specimens. The observed boundary of the zone of influence of geogrids was for values of $3 < d/D_{50} < 7$ for the transparent soil used in this study.

# Table of Contents

# List of Tables

# List of Figures

# 1 INTRODUCTION

## 1.1 Motivation

Geosynthetics, especially geogrids, have been used for several years for reinforcement of the unbound aggregate in the base layer of flexible paved roads. However, design approaches for this application remain highly empirical. There is no established standard laboratory testing and design procedure despite numerous studies reported in the literature that involve field monitoring, laboratory tests, and numerical simulations (Al-Qadi et al. 2008, Brown et al., 2007, Chan et al. 1989, Gupta 2009, Konietzky et al. 2004, Perkins et al. 2004, Saad et al. 2006, Qian et al. 2011, Zornberg et al. 2012).

Geogrids have also been used for decades as reinforcement in earth retaining wall systems. This type of application is the target in most of the extensive literature on soil-geogrid interaction. Besides the large experience accumulated with decades of using geogrids as reinforcement in base layer of pavements and earth retaining walls, soil-geogrid interaction is not fully understood yet.

In fact, studies on soil-geogrid interaction related to base layer reinforcement of pavements are divergent to studies on soil-geogrid interaction related to earth retaining walls. In the literature on base layer reinforcement, the bearing mechanism is reported to be the responsible for soil-geogrid interaction at relatively small strains. In the literature on geogrid-reinforced earth retaining walls, the bearing mechanism is reported to be the main responsible for soil-geogrid interaction only at relatively large strains.

For the case of applications such as reinforced pavements, the relevant interaction mechanisms are those that occur at comparatively small strains. Studies have attributed

the reinforcement contribution of geogrids in pavement base layers to the interlocking mechanism created by soil particles located within the apertures of geogrids (Chan et al. 1989, Perkins and Ismek 1997, Perkins 1999). This geometry allows for interaction of the geosynthetic with the soil through the bearing mechanism. The bearing mechanism develops as loading from traffic is applied to the pavement, and particles in the base layer tend to move laterally towards the shoulder of the pavement, where the confinement is smaller (Perkins and Ismek 1997). This lateral movement is impeded through the bearing resistance developed against the ribs of the geogrid perpendicular to the movement of the soil particles.

For the case of applications such as earth retaining walls, the relevant interaction mechanisms are those that occur at relatively large strains. The most used laboratory test in studies focusing on earth retaining walls is the pullout test, because this is a relatively simple test to conduct. In a pullout test, a geogrid specimen is placed at mid-height of a box that is filled with compacted soil. The test consists of pulling the geogrid specimen out of the box at a constant displacement rate, and recording the generated pullout force and the displacements of different points along the length of the geogrid.

Farrag et al. (1993), Palmeira and Milligan (1989) and Teixeira et al. (2007) reported that most of the maximum pullout force generated in pullout tests relies on bearing resistance developed along the transverse ribs, but they are developed only at comparatively large strains. In the case of small strains, the main interaction mechanism has been reported to be the interface friction developed along the surface of the geogrid ribs (Farrag et al. 1993, Teixeira et al. 2007).

Accordingly, the different soil-geogrid interaction mechanisms that develop at different strain levels have not been fully addressed in the literature, which points at the need for a thorough understanding of the soil-geogrid interaction mechanisms at

relatively small strains. Limited information is available on strains developed in geogrids at low stress levels. Among the various applications involving soil reinforcement, the reinforcement of base pavements is the one that would probably benefit the most from a better understanding of soil-geogrid interaction mechanisms.

An effective approach to contribute to the understanding of the soil-geogrid interaction mechanisms at different stress levels would involve visualization of the deformations that develop in the various geogrid components under confined conditions. Recent improvements in transparent soil technology have made the visualization and measurement of small strains developed throughout the geogrid attainable. A transparent soil with geotechnical characteristics similar to sand developed by Ezzein and Bathurst (2011a) was used in this investigation. Figure 1.1 shows the view through 150 mm (5.9 in.) of transparent soil and 38.1 mm (1.5 in.) of polycarbonate plates that are part of the transparent box. The transparent soil is composed of particles of crushed fused quartz saturated with a mix of white mineral oil.

This research focuses on understanding the interaction mechanisms developed in stages of pullout tests. While the emphasis is on the strains developed in the geogrid at low and intermediate percentages of the pullout force, strains mobilized towards pullout failure will also be analyzed. A new transparent pullout apparatus was developed for tests that allow direct measurement of the displacements throughout the entire geogrid specimen with image analysis.

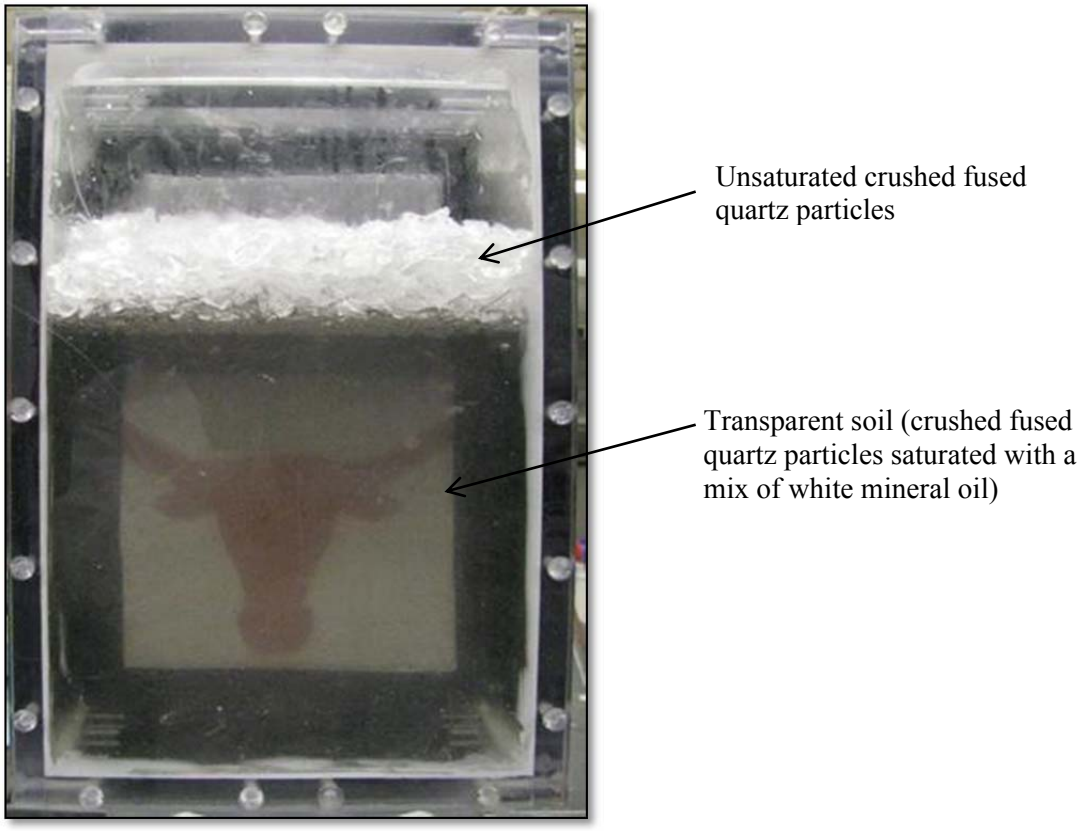


Figure 1.1: View of the transparent soil used in this study.

## 1.2 Overall Objective

The objective of this research is to identify and quantify the mechanisms of soil-geogrid interaction, at different stages of the pullout test, through digital image processing of displacements obtained from geogrid specimens tested under the confinement of transparent soil. While the primary focus of this research will be on the stresses mobilized at small strains, stresses and strains mobilized closer to pullout failure will also be evaluated and compared.

## 1.3 Specific Objectives

In order to reach the overall objective, this research will seek answering the following specific questions:

1. How is the distribution of strains throughout the geogrid specimen during a pullout test? Specifically:
    a. What is the strain distribution along the longitudinal ribs at different stages of the test?
    b. How is the distribution of strains along longitudinal ribs when no transverse ribs are present?
    c. How do these strains change with different configurations of the geogrid?
    d. Is the strain distribution along the longitudinal ribs affected by the magnitude of the spacing between transverse ribs?

2. How do the transverse ribs contribute to the soil-geogrid interaction during a pullout test? Specifically:
    a. What are the deflections in the transverse ribs for different geogrid configurations?
    b. What is the percentage of the maximum pullout force at which the deflections in the transverse ribs can be observed?

3. How do transverse ribs interfere with each other? Specifically:
    a. Are the deflections of a transverse rib affected by the presence of another transverse rib?
    b. At what stages of the pullout test this interference occur?

c. How does this interference change when the distance between transverse ribs changes?

4. What are the displacements of soil particles adjacent to the interface? Specifically:
   a. At what distance from the interface that displacement of the soil particles are observed?
   b. Do the soil particles near the interface move together with the geogrid? Or are there large relative displacements between the geogrid and soil particles adjacent to the interface?

## 1.4 Additional Objectives

The transparent soil used in this study is composed of artificial soil particles (crushed fused quartz) saturated with a mixture of white mineral oil that is more viscous than water. Thus, an assessment will be made of the effects of the materials used to implement the transparent soil technology on soil-geogrid interaction. Accordingly, the following additional questions will be addressed:

1. What is the effect on pullout test results of using crushed fused quartz instead of a conventional granular soil (Monterrey sand)?
2. What is the effect on pullout test results of saturating the crushed fused quartz with the mineral oil mix?

## 1.5 Dissertation Structure

This dissertation includes six chapters. The next chapter provides background information on the key elements involved in this research. This includes soil-geogrid interaction (laboratory and numerical studies, and soil-geogrid models), transparent soil, image acquisition systems and particle image velocimetry (PIV) calculations.

The third chapter presents the materials and methods used in this research, including a description of the soils, the geogrid product, the image acquisition system and software for the analyses. Also, the transparent pullout test device developed in this research is described along with the testing procedure.

The fourth chapter includes the results of the tests for characterization of the soils and the geogrid product used in this research. An evaluation is also presented of the effect of the materials used in the transparent soil (fused quartz and white mineral oil mix) on pullout tests. The results of the transparent pullout tests conducted are presented individually with curves of pullout force against displacements along the geogrid specimen, as traditionally shown in literature.

The fifth chapter provides a discussion of the pullout test results conducted using transparent soil. The sixth includes the conclusion of this dissertation and recommendations for improvement of the equipment, and possible future studies with the test developed in this research.

# 2 BACKGROUND INFORMATION

This chapter presents background information on the literature on soil-geogrid interaction that motivated this research. This includes a literature review of theoretical and numerical models developed to predict the performance of geogrids in confined loading. Experimental studies in laboratory aiming at understanding soil-geogrid interaction are also presented.

This chapter also presents background information on the tools used in this research: (i) transparent soil technology, (ii) image acquisition systems, and (iii) particle image velocimetry (PIV). The concept of transparent soil is explained and the research found in the literature using this technology is discussed. The concepts behind image acquisition systems are also discussed, and the advantages and limitations of these systems are presented. Finally, PIV calculations used to obtain the data from the tests performed in this study are explained and the limitations associated with them are discussed.

## 2.1 Soil-geogrid interaction

Studies involving soil-geogrid interaction can be divided into two major fields. First, there are studies using pullout tests focused on the application of geogrid reinforcement in earth retaining walls. Second, there are studies focused on the application of geogrid reinforcement in the base layer of pavements. Research in these two major fields investigates different aspects of the soil-geogrid interaction. Applications focused towards reinforcement of earth retaining walls aim at understanding the mechanisms of soil-geogrid interactions at failure of the interface between the soil

and the geogrid. Applications focused towards base layer reinforcement of pavements aim at understanding the mechanisms of soil-geogrid interactions at the initial stiffness of the interface between soil and geogrid.

Studies of reinforced flexible pavements have shown that geosynthetics placed within the base layer, or at the interface between the base and the subgrade, can significantly improve the performance of the pavement in relation to unreinforced ones (Chan et al. 1989, Collin et al. 1996, Perkins and Ismeik 1997). Flexible pavements are asphalt roads composed of 3 basic layers: the surface cover (asphalt concrete or asphalt coat), the base course (granular material, ideally gravel) and the subgrade (compacted on-site soil, including clays). Additional layers can be used such as a subbase layer which is an intermediate layer between the base course and the subgrade.

Geosynthetics used as reinforcement of pavements are sheets of polymeric materials in a textile or grid form referred as geotextiles and geogrids, respectively. Geotextiles can be woven or nonwoven, with the first being more commonly used as pavement reinforcement. Geogrids can be integrally formed, welded, or knitted. Integrally formed geogrids are made from extruded sheets that can be punched and stretched to the geogrid shape.

Welded geogrids have integrally formed ribs that are welded at the junctions. Knitted geogrids are composed of yarns that are knitted at the junctions and coated for extra protection of the yarns. Reinforced flexible pavements have inclusions of a layer or multiple of geosynthetic within the base course, or between the base course and the subgrade, or between the base course and subbase. The primary focus of this research is to understand the reinforcement mechanisms of geogrids embedded in granular soils that control the initial stiffness and the failure of the soil-geogrid interface.

In order for geosynthetics to be beneficial to asphalt paved roads, the reinforcing mechanisms are believed to develop at small strains. Lateral restraint is believed to be the interaction mechanism through which geosynthetics provide reinforcement to the unbound aggregate of base layers (Perkins 1999). Under traffic loading, the aggregate particles in the base layer tend to move laterally towards the shoulders of the pavement where the confinement is smaller. This gradual loss of material degrades the capacity of the paved structure to support loads. The interaction between soil and geosynthetic increases the confinement of the soil, thus restraining this lateral movement.

Moreover, studies have shown that geogrids outperform geotextiles (Chan et al. 1989, Perkins 1999). This advantage of geogrids is due to their geometry. The geometry of geogrids allow for an interlocking mechanism to be created by the particles located in the apertures of the geogrid, and the resultant interaction with the ribs transverse to the soil movement. Interface friction is another interaction mechanism available and occurs along the surface of the geogrid ribs and the adjacent soil. In geotextiles, interface friction is the only interaction mechanism with soils.

Although the interlocking mechanism is accepted in the literature to be the main mechanism of reinforcement provided by geogrids to base courses, there is no established standard laboratory test to provide parameters to be used in design directly or indirectly through correlations. This occurs mainly because the characteristics of geogrids and soils that affect their interaction are not well understood, neither the interference between the interaction mechanisms regardless of the rich literature in this area.

### 2.1.1 EXPERIMENTAL STUDIES

Numerous experimental studies focused on the soil-geogrid reinforcement in earth retaining walls were conducted with pullout tests. Pullout tests have also been used in studies focused on geogrid-reinforced base course.

#### 2.1.1.1 Laboratory Pullout Tests

In contrast to the reinforced pavement studies, literature on soil-geosynthetic interaction suggests that benefits of the interlocking mechanism created by the particles located in the geogrid apertures is only developed towards failure of the interface. Interface friction is believed to be the primary interaction mechanism at low strains (Farrag et al. 1993, Teixeira et al. 2007).This is due to the extensibility of geosynthetics that causes progressive mobilization of the reinforcement as the pullout force increases. Thus, larger displacements in the geogrid are observed at the junctions near the application of the force, while smaller displacements are observed at the far end of the geogrid.

This behavior is illustrated in the results of large pullout tests performed by Ochiai et al. (1996) presented in Figure 2.1. In this figure, junction No. 1 is the one closest to the front wall (i.e. the application of the pullout force), while junction No. 6 is the farthest one. As observed in Figure 2.1, the larger the confining pressure, the larger the difference of displacements along the geogrid specimen due to the extensibility of the material.

The complexity in understanding the interaction mechanism between soil and geogrid is due to the extensibility of the reinforcement, and the synergism between the friction and bearing components of the interaction mechanisms (Teixeira et al. 2007). As the transverse ribs move, a zone of disturbance is formed. This affects the friction forces

along the longitudinal members (Teixeira et al. 2007), and the bearing forces on the transverse ribs entering this disturbed zone created by the transverse ribs immediately before them (Palmeira 2004).

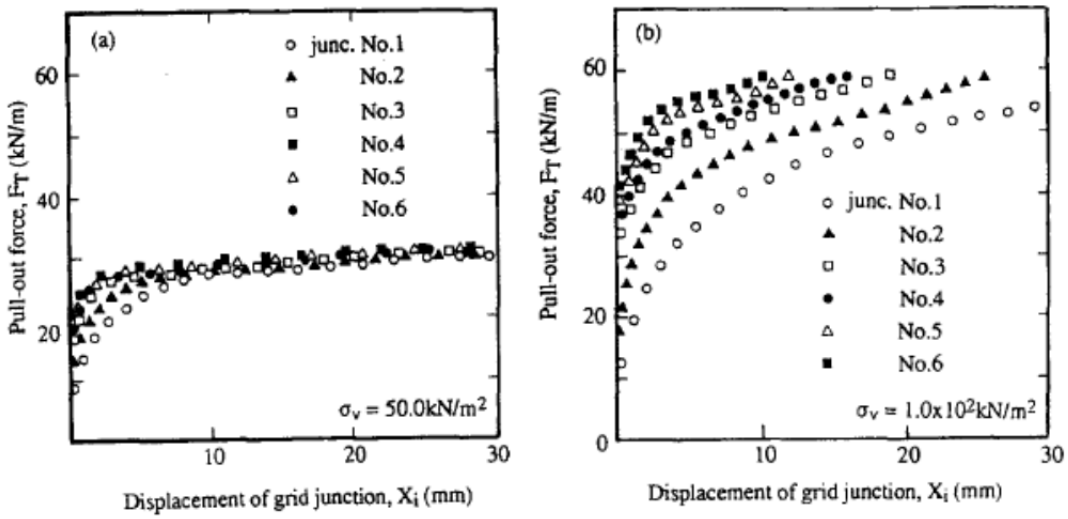


Figure 2.1: Typical large pullout test results. Junction No. 1 is the one closest to the front wall (i.e. the application of the pullout force) while junction No. 6 is the farthest one. (a) Confining pressure of 50 kPa (7.3 psi). (b) Confining pressure of 100 kPa (14.5 psi). (Source: Ochiai et al. 1996).

Teixeira et al. (2007) performed large pullout tests and measured normal pressures in the soil mass near the interface with an earth pressure cell located between longitudinal ribs, thus closely above the path of a transverse rib, and an earth pressure cell located directly over a longitudinal rib (Figure 2.2). The results in this figure show oscillations on the normal stresses in the soil mass adjacent to the geogrid due to the bearing stresses developed by the movement of a transverse rib (TSC1 in Figure 2.2). At the same time, the normal stresses on a longitudinal rib decrease (TSC2 in Figure 2.2), what leads to a reduction in the friction component of the interaction mechanism.

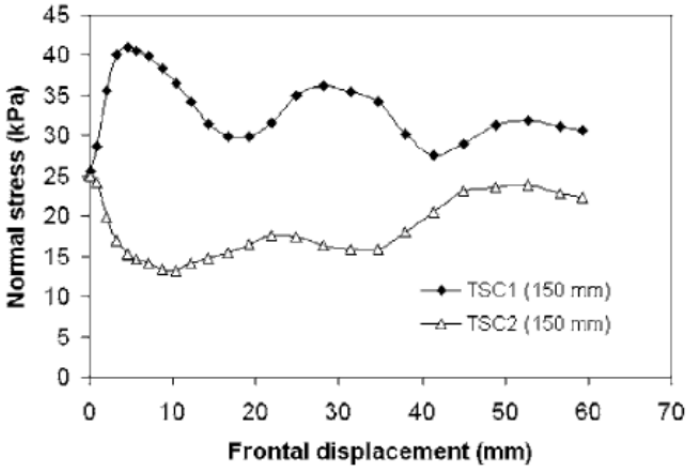


Figure 2.2: Normal stress variations during a large pullout test, 150 mm (5.9 in.) from the front wall in locations in the soil mass adjacent to the geogrid: between longitudinal members (TSC1) thus above the path of a transverse rib, and directly above a longitudinal rib (TSC2). (Source: Teixeira et al. 2007).

These disturbances also cause interferences between transverse ribs as one rib moves into the disturbed zone created by the other rib (Palmeira 2004). Accordingly, if the distance between transverse ribs is small enough, the bearing stresses are affected. Dyer (1985) showed with photo-elastic studies that the regions behind the transverse ribs have low stresses due to movement of the geogrid.

The main focus of the majority of the studies on soil-geogrid interaction found in the literature is not on the stiffness of the interface, but rather on the failure and the maximum force developed in pullout mechanisms. This is because pullout testing was developed to evaluate failure of the interface for limit equilibrium analyses of geosynthetic reinforced earth retaining walls. Thus, many of these studies tested uniaxial geogrids which are used in earth retaining walls, as opposed to the biaxial or triaxial geogrids used in pavements. The thickness and the distance between transverse ribs of uniaxial geogrids are significantly higher than the thickness and distance between

transverse ribs of biaxial geogrids. Uniaxial geogrids are also more extensible than biaxial geogrids.

Palmeira and Milligan (1989) conducted pullout tests in a 1 $m^3$ box using sand and steel grids with different configurations of the transverse ribs. Friction along the longitudinal ribs was minimized with the application of grease on these ribs, thus minimizing the development of the interaction mechanism of interface friction. The distance between transverse ribs was changed in this series of tests. The thickness of the transverse ribs was also changed in this series of tests. The authors concluded that interference between transverse ribs is negligible for ratios above 50 of the distance between transverse ribs over the thickness of the transverse ribs (Figure 2.3).

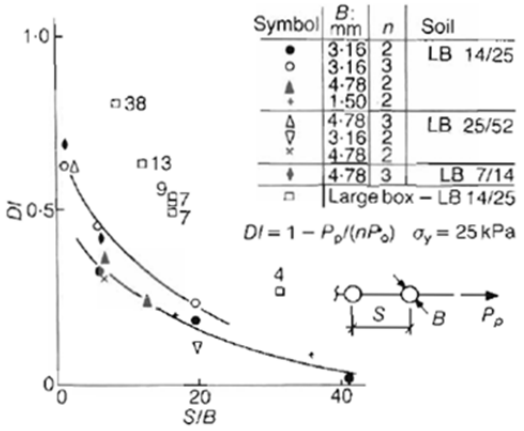


Figure 2.3: Degree of interference between transverse ribs with different combinations of distance between transverse ribs and thickness of the transverse ribs (Source: Palmeira and Milligan, 1989).

Palmeira (2009) simulated pullout tests from Palmeira and Milligan (1989) using the Finite Element Method (FEM). Palmeira (2009) compared the predicted strains along the geogrid specimen with FEM to strains calculated from the pullout test data reported

by Palmeira and Milligan (1989). A good agreement was found between the results (Figure 2.4).

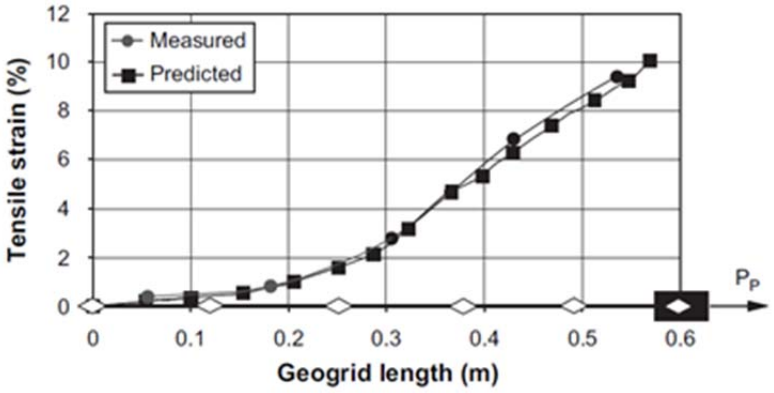


Figure 2.4: Comparison of predicted strains with FEM to measured strains along a geogrid specimen in a pullout test with dense sand reported by Palmeira (2009).

Chang et al. (1995) reported limited data of strains measured along the geogrid specimen in large pullout tests (Figure 2.5). The authors concluded that the distribution of strains along the geogrid specimen follow a triangular pattern.

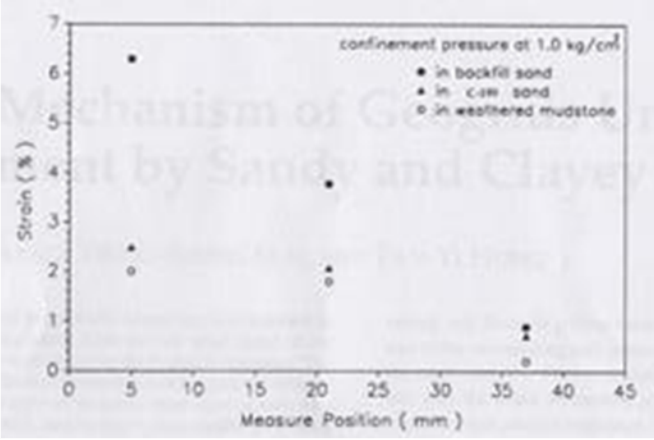


Figure 2.5: Strain data along the geogrid specimen in large pullout test reported by Chang at el. (1995).

#### 2.1.1.2 Laboratory evaluation of geogrid reinforced granular soils

Despite the understanding that base course reinforcement comes from the interaction between the geogrid and the surrounding soil, specifications for geogrids to be used in this application, such as from the Texas Department of Transportation (TxDOT DMS-6240), are still based solely on the unconfined properties of the geogrid (e.g. tensile strength and stiffness, junction efficiency, percent of open area, aperture size, and rib thickness). On the other hand, several researchers have proposed confined tests that have the potential to be adopted as standard tests for obtaining parameters to be used in design.

Moghaddas-Nejad and Small (2003) and Perkins et al. (2004) used cyclic large triaxial tests to study the benefits of geogrid reinforcement of granular materials. Both studies concluded that the geogrid has a negligible effect on the resilient modulus ($M_R$) of granular materials. The $M_R$ is the equivalent of the Modulus of Elasticity ($E$) for cyclic loading and it is used as an input parameter for designing pavements with the Mechanistic-Empirical design method developed by the National Cooperative Highway Research Program (NCHRP, 2004). This design method by the NCHRP is the most advanced design procedure available in the literature.

On the other hand, these studies observed significant improvement on the permanent axial deformations of the granular soil by restraining the radial strains. Perkins et al. (2004) identified a zone of influence of the geogrid in the granular material of 150 mm (5.9 in.) above and below the geosynthetic in the soil. However, the repeatability of these tests are relatively poor and, while there is a distinct difference between the reinforced and unreinforced case, there is no distinction of the benefits provided by different geogrid products (Perkins et al., 2004).

Cuelho and Perkins (2005) adapted a pullout test device to apply cyclic pullout loads on the geogrid specimen in a trial to determine an interface shear modulus that

mimics the resilient modulus obtained in cyclic triaxial tests. However, cyclic pullout tests also provided poor repeatability of the results.

Han et al. (2011) adapted an Asphalt Pavement Analyzer to test geosynthetic reinforced granular material for rutting. This test consists of a box with an open surface and dimensions of 480 x 380 x 100 mm (18.9 x 15 x 3.9 in.) corresponding to width, length and height, respectively. The box is filled with compacted granular soil and when utilized, the reinforcement is placed at the mid-depth. The surface of the soil is then loaded with miniature wheels passing back and forth on pressurized hoses, simulating traffic loading (Figure 2.6). The results of these tests are measurements of the rutting depth under the wheels with the number of passes.

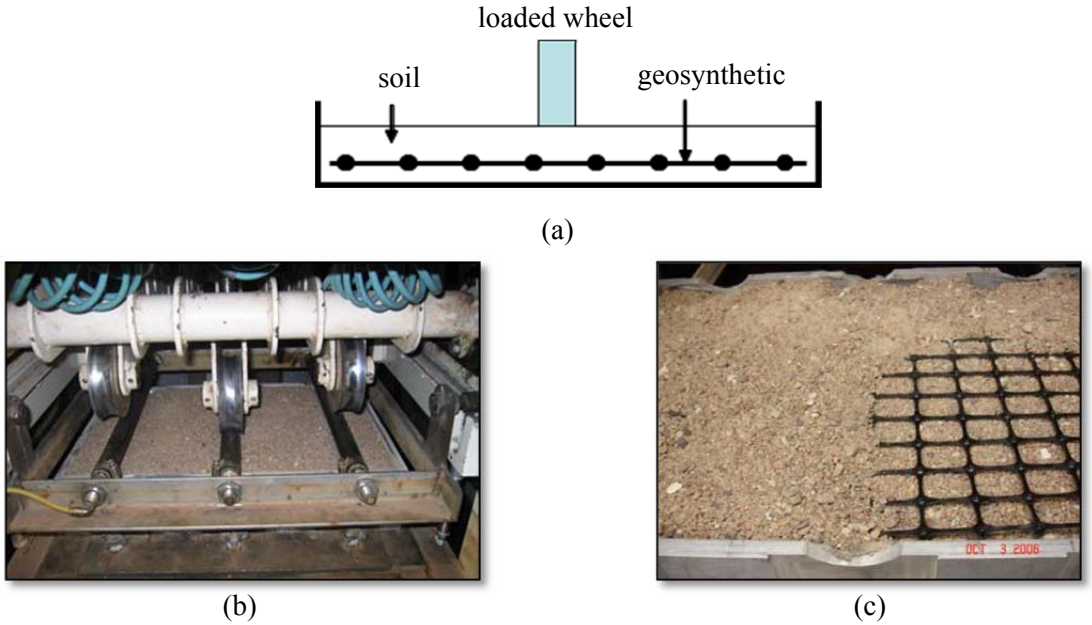


Figure 2.6: Modified Asphalt Pavement Analyzer for testing geosynthetic reinforced granular soil against rutting. (a) Schematic cross-section. (b) Loaded wheels. (c) Placement of the geogrid specimen. (Source: Han et al., 2011)

The authors reported good repeatability of the results and were able to differentiate the performance among different geogrid products. However, this type of tests does not provide any measurement of a fundamental mechanical property of the interface, such as stiffness, that could be used for design. This test can be incorporated into design procedures of reinforced pavements through solely empirical correlations.

### 2.1.2 SOIL-GEOGRID INTERACTION MODELS

Palmeira (2004) proposed a numerical model for soil-geogrid interfaces and compared the results to measurements from pullout tests. The main assumption of the model is the development of a disturbed zone formed behind a transverse member as the geogrid displaces. Another important assumption is the interference between transverse ribs due to the development of disturbed zones by the movement of transverse ribs. These concepts used in the mode,l developed by Palmeira (2004), are shown in Figure 2.7.

Gupta (2009) proposed the use of traditional monotonic large pullout tests combined with an interaction model that quantifies the stiffness of the interface using the test data. The proposed model is based on load and displacement data from 5 LVDTs that are connected to inextensible wires, which in turn, are attached at different locations along the geogrid specimen. The stiffness of the interface is evaluated with the coefficient of soil-geosynthetic interaction $K_{SGI}$, which is a parameter that accounts for the shear strength of the soil and the confined stiffness of the geosynthetic.

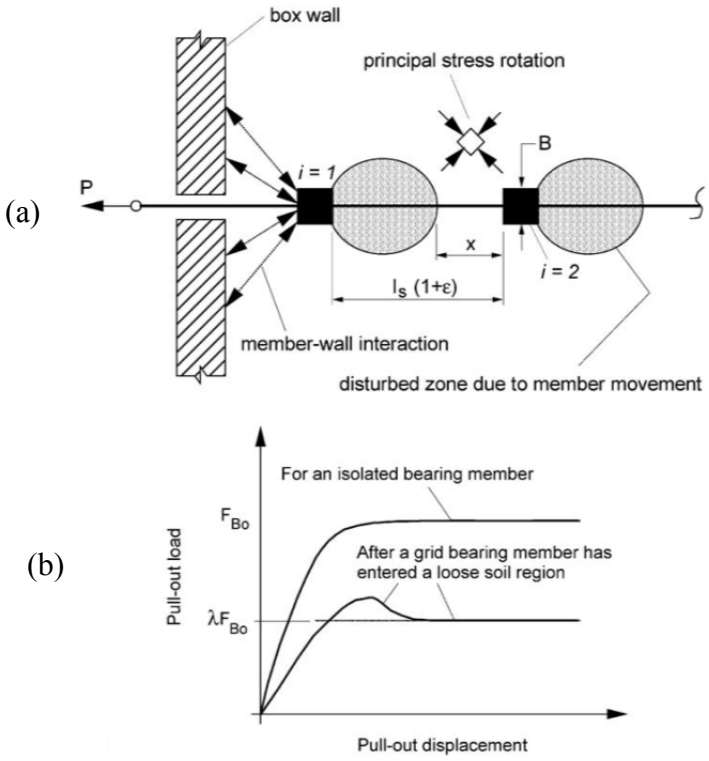


Figure 2.7: Interference between transverse ribs of a geogrid during pullout testing. (a) Illustration of the disturbed zone created by the movement of the transverse ribs. (b) Example of reduction of the bearing stresses due to this interference. (Source: Palmeira 2004).

The author reported good repeatability of the results and was able to distinguish performances among different geosynthetics. However, the units of the parameter $K_{SGI}$ are difficult to interpret since they are expressed in $(kN/m)^2/mm$ or $(kN/m)^2/m$. Moreover, the large pullout test is expensive and difficult to prepare since it is labor-intensive and needs dedicated equipment and room space.

## 2.2 Transparent soil

Traditional pullout tests only allow monitoring the displacement of a few points along the geogrid specimen. The measurements are made with wires attached at different junctions distributed throughout the geogrid specimen, which in turn are connected to displacement sensors. Consequently, the individual contributions of longitudinal and transverse ribs of the geogrid specimen, as well as the strain field developed, are not able to be evaluated with traditional methods. However, recent developments with the transparent soil technology have created possibilities for such evaluations. With transparent soil, strain measurements can be taken through pictures of a geosynthetic specimen, which is visible because it is embedded in transparent soil and loaded with a pullout test apparatus in a box with transparent walls.

### 2.2.1 CONCEPT OF TRANSPARENT SOIL

Transparent soils have been used in geotechnical engineering to evaluate a variety of foundation engineering problems (Wakabayashi 1950, Gill and Lehane 2001, Sadek et al. 2003, McKelvey et al. 2004, Song et al. 2009, Iskander and Liu 2010). The principle of transparent soils is based on submerging a translucent material into a liquid with the same refractive index. The equal refractive index of the liquid makes the translucent material become transparent when saturated in this liquid.

### 2.2.2 PHOTO-ELASTIC STUDIES

Wakabayashi (1950) applied this principle with crushed glass and a solution of carbon-disulphide and benzene to conduct photo-elastic studies of stress distribution generated by a loaded footing on the soil surface. Dyer (1985) produced a transparent soil

with crushed pyrex glass and a colorless liquid paraffin to conduct photo-elastic experiments with direct shear and pullout tests. However, transparent soils obtained from crushed glass do not have similar geotechnical properties to sands (Sadek et al. 2002).

### 2.2.3 TRANSPARENT SOIL WITH SILICA GEL BEADS

Sadek et al. (2002) used transparent soil obtained from silica gel beads saturated with a blend of white mineral oil and paraffinic solvent. The authors reported geotechnical properties of this transparent soil to be comparable with the properties of sands after extensive triaxial and direct shear testing. However, two layers of rubber membrane were necessary to perform the triaxial tests because the oil mix attacks the membrane. In standard triaxial tests only one membrane is used. The authors did not assess the effect of two membranes on the test results. This transparent soil also has other disadvantages.

The paraffinic solvent is volatile, thus classified as hazardous material. Also, the transparency of the soil degrades with time, probably caused by the volatility of the solvent and other chemical processes. The silica gel beads are porous, which leads to a long preparation time as vacuum needs to be used to eliminate air bubbles entrapped inside and between the submerged beads. Also, the silica gel beads are highly compressible (Sadek et al. 2002).

### 2.2.4 TRANSPARENT SOIL WITH CRUSHED FUSED QUARTZ

Ezzein and Bathurst (2011a) have developed a transparent soil to be used in a large transparent pullout test apparatus. The transparent soil has geotechnical behavior comparable to sands, and the matching refractive index fluid is composed of non-volatile,

non-hazardous, white mineral oils. Moreover, this transparent soil is composed of particles of crushed fused quartz, which are non-porous and incompressible. The transparency of the material does not degrade over time.

Ezzein and Bathurst (2011b) used the transparent soil with coarse fused quartz in large scale pullout tests. The bottom plate of the pullout box is transparent and composed of a 25 mm-thick (1 in.) Plexiglas plate. This pullout equipment is significantly larger than traditional, large pullout equipment that follows the minimum recommendations of the ASTM D 6706. The boundary conditions of the geogrid sample are also different than traditional pullout tests in which the geogrid is clamped on the edge near the rear wall of the box. In traditional tests, the edge of the geogrid near the rear wall of the box is free to move during the test.

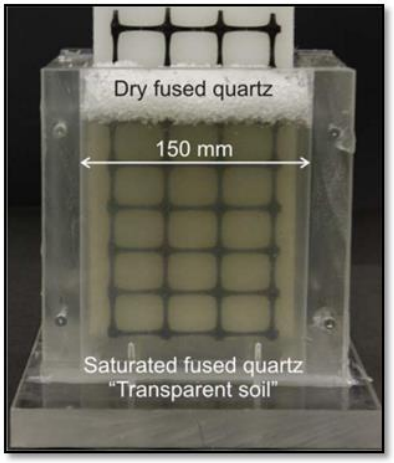


Figure 2.8: Transparent soil produced by Ezzein and Bathurst (2011a). Geogrid is seen through a wall of 25 mm (1 in.) thick Plexiglas and 120 mm (4.7 in.) of transparent soil. (Source: Ezzein and Bathurst 2011a).

## 2.3 Particle Image Velocimetry (PIV)

Particle image velocimetry (PIV) is a technique used to obtain velocity measurements through digital image correlations. It is traditionally used in studies of fluid mechanics. In these studies, seeding particles are added to the fluid and work as tracers since these seeding particles are chosen such as they create a significant contrast against the fluid. Images are obtained at a specific rate and the images are later processed and compared to determine the velocity vectors at each time step.

### 2.3.1 PIV CONCEPT

White et al. (2003) applied the principles of PIV to geotechnical engineering by using the texture of sands as the features that create a pattern to be recognized with the correlation function in replacement of the seeding particles in fluid. The texture of sands in the image is created by their grains of different colors and the shadows between adjacent grains created by illumination, creating a pattern of different grey shades, or light intensity values, in the image. These values are recorded by each pixel that forms a 2D array of thousands of points in the image of resolution $X$ x $Y$. For example, an image with a resolution of 5 Megapixels (MP) is generally composed by an array of 2,452 x 2,056 pixels ($X$ x $Y$). The location of a pixel in the image is defined by the coordinates ($x$,$y$).

The initial steps of the PIV calculations are illustrated in Figure 2.9. First, each image is divided into a grid of sub-regions named interrogation areas. The dimensions $U$ x $V$ of the interrogation areas determine the spatial resolution of the measurements (Jensen 2004). In the example shown in Figure 2.9, the size of the highlighted IA is 200 x 150 pixels. Then, two consecutive images are compared. The pattern of light intensity

values, *f(x,y)* for Image 1 and *g(x,y)* for Image 2 within each interrogation area (IA), is obtained in both images.

Next, a search window is defined for each IA. This search window can be, 2, 4 or 8 times larger than the IA. The initial interrogation areas are then evaluated by means of a cross-correlation function (Liu and Iskander 2004). Next, the initial IA in Image 2 is shifted by distances $\Delta x$ and $\Delta y$ in all directions defined by the size of the search window (Figure 2.9b). Each time the interrogation areas in Image 2 are shifted, the respective *g(x,y)* functions are obtained and evaluated against the original IA in Image 1 with the cross-correlation function.

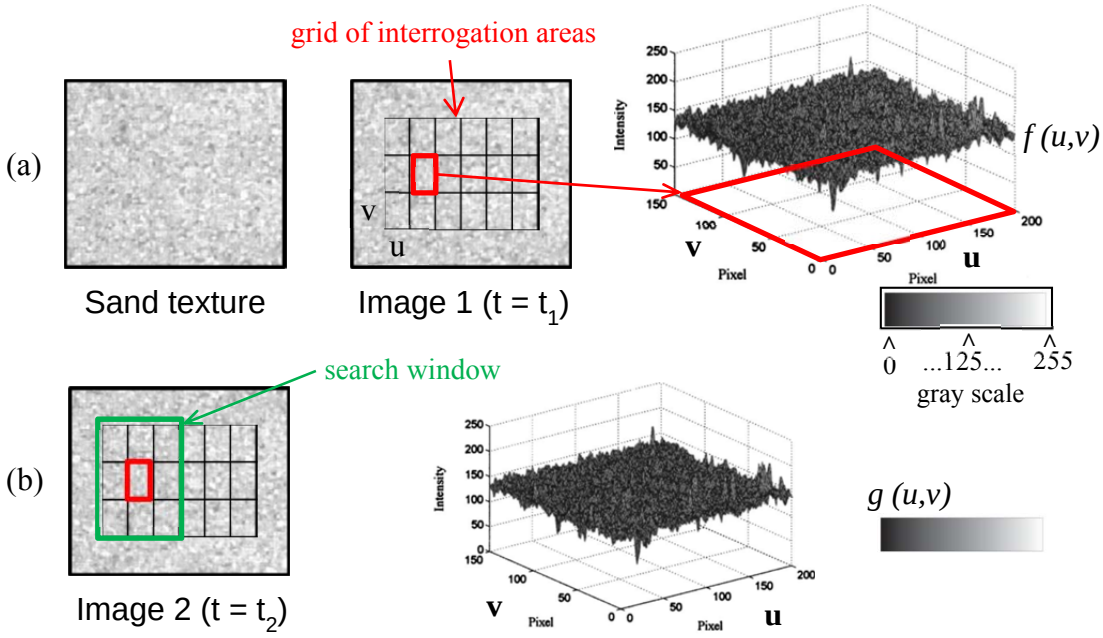


Figure 2.9: Illustration of the initial steps in the PIV analysis. (a) Division of Image 1 into several interrogation areas (IAs) with an example of the light intensity function f(u,v) of an interrogation area. (b) Division of Image 2 into IAs and the g(u,v) of an IA for initial comparison in the search window (Source: adapted from Liu and Iskander 2004; White et al. 2003).

The cross-correlation function is defined as follows (Liu and Iskander 2004):

$$C(\Delta x, \Delta y) = \frac{1}{UV} \sum_{u=0}^{U-1} \sum_{v=0}^{V-1} f(u,v) g(u + \Delta x, v + \Delta y) \quad (2.1)$$

In which:

*U, V* = dimensions of the interrogated areas (N$^o$ of pixels)

*f(u,v), g(u,v)* = light intensity functions of the 2 images being interrogated

$\Delta x$, $\Delta y$ = shifting distances of images for generation of the correlation function values

After the values of the cross-correlation functions are obtained from the shifts of the IA in Image 2 in all directions inside the search window, the location of the peak of the correlation function is obtained. The offset between the center of the IA in Image 1 and the location of the correlation peak in Image 2 is associated with a displacement vector (White et al. 2003) as shown in Figure 2.10. Accordingly, depending on the size of the image and of the interrogation areas, hundreds or thousands of displacement vectors are evaluated simultaneously for each image (Jensen 2004).

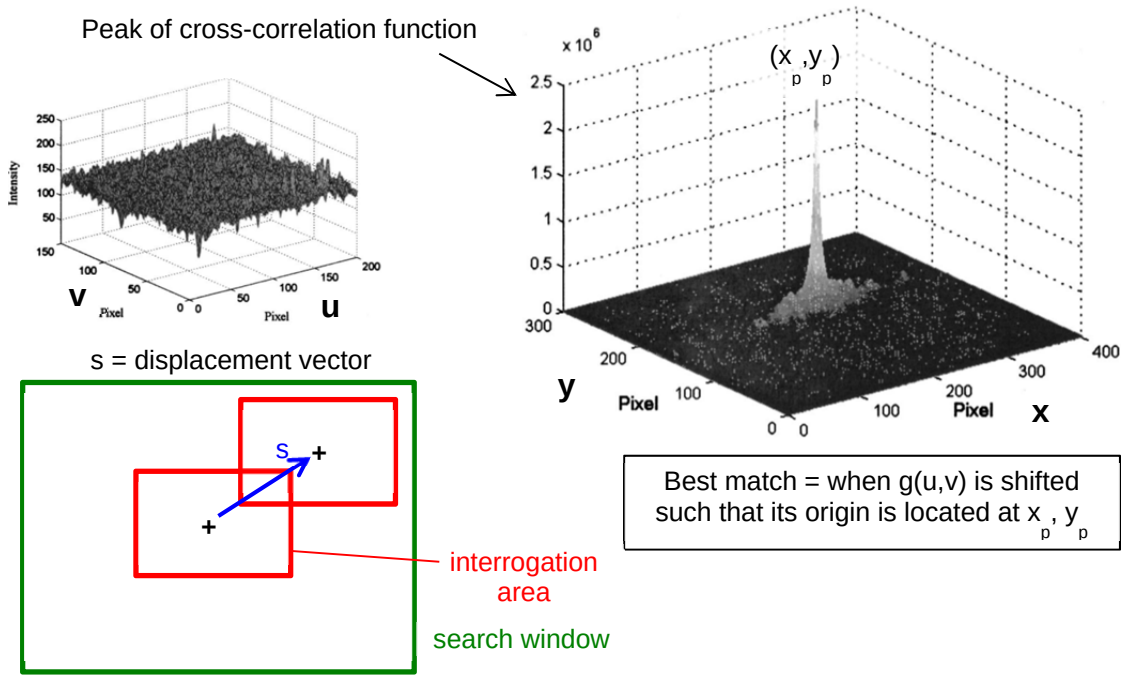


Figure 2.10: Search of the peak of the cross-correlation function and assignment of the displacement vector. (Source: adapted from Liu and Iskander 2004)

The light intensity functions *f(x,y)* and *g(x,y)* are discrete functions since they are limited to the numeric value stored in each pixel. Thus, the resolution of the magnitude of the displacement vector is limited to integer values (Figure 2.11a). However, the data of the discrete function can be fitted to a continuous function allowing for a sub-pixel resolution of the magnitude of the displacement vector (Figure 2.11b). This data treatment can lead to a resolution of 0.005 pixel (or 1/200$^{th}$ of a pixel) for the calculated displacement (White et al. 2003).

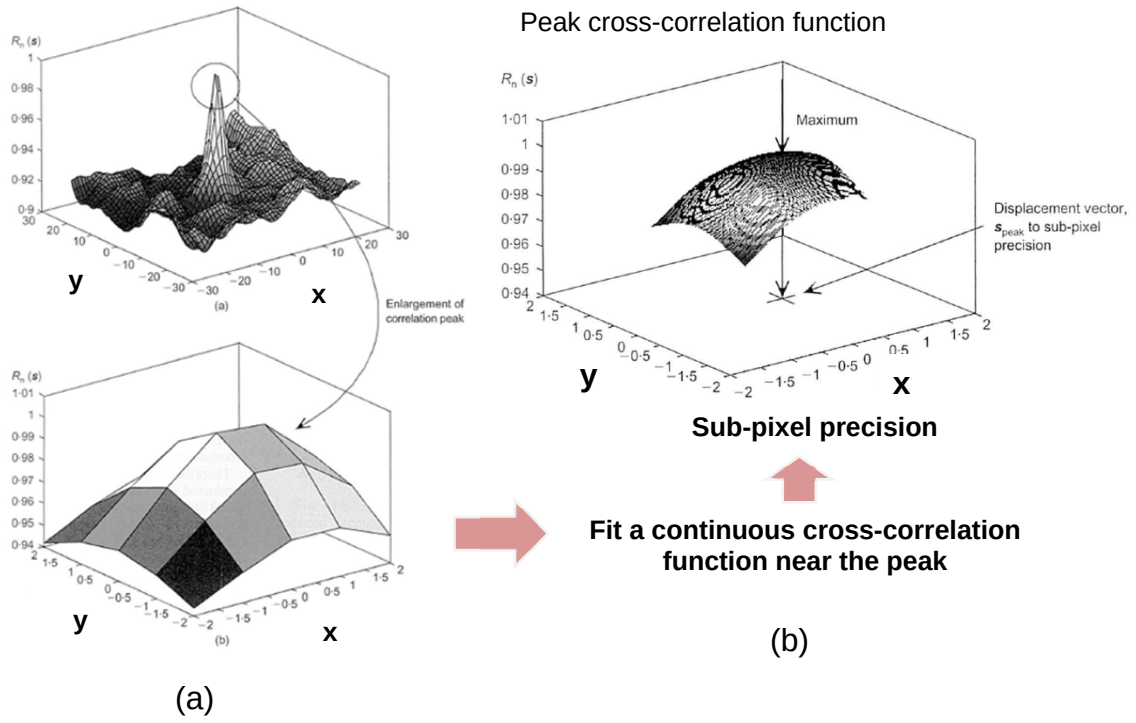


Figure 2.11: Results of the cross-correlation function. (a) Discrete results allowing for a resolution of integer values for the magnitude of the displacement vector. (b) Continuous function fitted to the data allowing for sub-pixel resolution for the magnitude of the displacement vector. (Source: adapted from White et al. 2003).

Once the displacement vectors are calculated, the final step is to convert the displacements in pixels from the image space to mm in the object space. This conversion can be done using a scale factor properly measured by obtaining images of an object of known dimensions with the same test setup used for the experiment. For example, the marks of known distance on a ruler can be used as a reference and this distance measured in pixels from the image. The ratio between the distance between the marks in number of pixels and in millimeters is the scale factor. More sophisticated models can also be used to make this conversion. These models take into account the errors due to the radial and

tangential distortion created by the curvature and the non-collinearity of the center of multiple lenses of a camera (White et al. 2003).

### 2.3.2 ADAPTIVE CROSS-CORRELATION

Other refinements in the PIV calculations can be made; such as using overlapped interrogation areas and refining the interrogation area in interactive steps. Each displacement vector is assigned to an interrogation area and corresponds to the average displacement of all pixels contained in the IA. Thus the spatial resolution of the displacement field is limited to one vector per IA. This spatial resolution can be refined without changing the size of the IA, by overlapping interrogation areas. The overlap can be in the horizontal and/or vertical directions from 25 to up to 75 % of the area. This procedure generates additional vectors and is an oversampling of the displacement field. It does not increase the accuracy of the calculations or the spatial resolution (Dantec Dynamics 2005).

The interrogation area can be refined such that a large interrogation area size is first used for general direction of movement. Then, smaller areas are used to better define local displacements.

### 2.3.3 ERRORS DUE TO OUT-OF-PLANE MOTION

Errors in the PIV calculations may arise due to displacement of particles that are perpendicular to the plane of 2D images. This is not an issue for displacements along the geogrid specimen in pullout tests. However, soil markers in the transparent soil may move perpendicular to the camera sensor. This situation is illustrated in Figure 2.12.

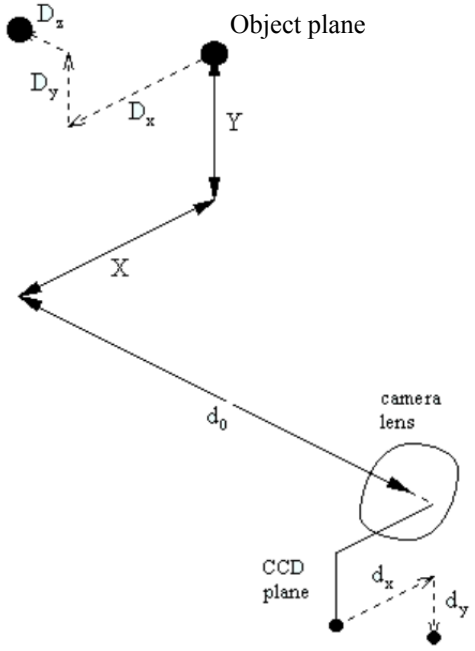


Figure 2.12: Error in displacement measurements due to out-of-plane motion (Source: Dantec Dynamics, 2005).

In Figure 2.12, the CCD plane is the plane of the camera sensor and is parallel to the plane of the object captured in the images. The plane of the camera sensor on which the images are generated is on the X and Y directions, as well as the object plane. As it can be observed in Figure 2.12, displacements in the Z direction are not captured in the images. To reduce the measurement errors related to out-of-plane motion, the camera needs to be positioned relatively far from the object plane (Dantec Dynamics, 2005). This minimizes the errors introduced by the decrease or increase in size of the particles moving away or towards the camera in the Z direction.

# 3 MATERIALS AND METHODS

A description of the soils used in this research is presented in this chapter. The characteristics of the transparent soil used in this study are introduced. Next, the image acquisition system and the PIV software used for analysis are described. Then the characteristics of the geogrid product used in this research are presented. Finally, a description of the new transparent pullout test device developed in this research is provided, followed by a description of the testing procedures.

## 3.1 Soils

Two different soils were used in this research: Monterey #30 Sand and crushed fused quartz (FQ). The particle size distribution curves of the soils are presented in Figure 3.1.

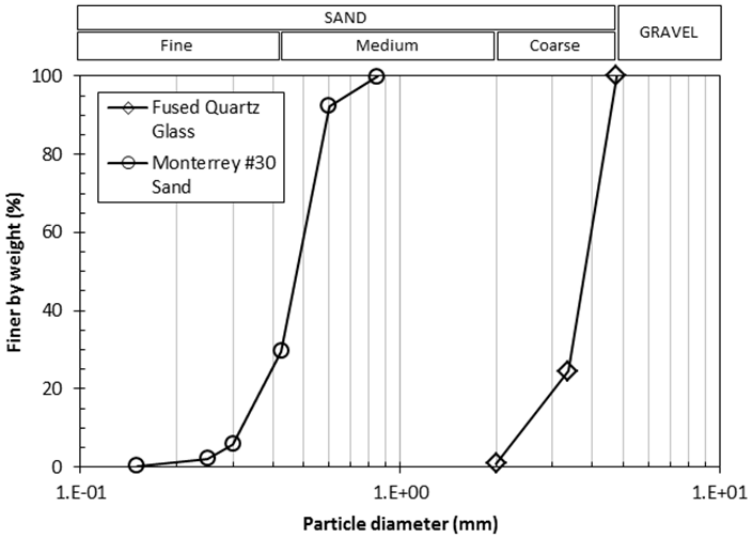


Figure 3.1: Particle size distribution curves of the soils used in this research.

The Monterey #30 sand is uniform grade, standard, medium sand classified as SP in the Unified Soil Classification System (USCS). This soil is constituted of quartz and smaller amounts of feldspars and other minerals. The particles are rounded to sub-rounded (Lee, 2005). The Monterey sand was used to evaluate the effect of different pullout test equipment and test boundary conditions on the results of pullout tests.

Initially, research with transparent soil had started as part of this study using silica gel beads, white mineral oil and the paraffinic solvent used by Sadek et al. (2002). However, manufacturing of the paraffinic solvent used by the authors had been stopped by the supplier in 2010. In the search to find a replacement for the solvent, the transparent soil developed by Ezzein and Bathurst (2011a) was identified. This soil is composed of crushed fused quartz particles and two white mineral oils. Due to the advantages of the transparent soil with fused quartz, this material was adopted in this study, replacing the silica gel beads.

The fused quartz is a non-porous material with high hardness and high chemical resistance. It is obtained by melting crystalline silica from quartz sand. Fused quartz is routinely used for manufacturing laboratory glassware, semiconductors, and optical components, among other industries. The crushed fused quartz used in this research has particle sizes in the range of coarse sand. This material was supplied by Mintec (Mineral Technology Corporation)[1]. The properties of the soils are shown in Table 3.1.

The fused quartz was sieved to minimize potential interaction of particles exiting the pullout box during tests with the sleeve at the front wall of the box. The maximum diameter of fused quartz particles used in this study is 4.75 mm (0.187 in.) as shown in

[1] Mintec, PO Box 872, Custer, SD 57730, USA.

Table 3.1. The original fused quartz supplied by Mintec had 13 % of the weight of the particles larger than 4.75 mm (0.187 in.).

| Property | Soil | |
|---|---|---|
| | Monterey sand | Crushed fused quartz |
| Specific Gravity, Gs (ASTM D854) | 2.655 | 2.203 |
| Minimum Void Ratio, $e_{min}$ (ASTM D4253) | 0.52 | 0.65 |
| Maximum Void Ratio, $e_{max}$ (ASTM D4254) | 0.79 | 0.83 |
| Uniformity coefficient, Cu | 1.5 | 1.6 |
| Coefficient of gradation, Cc | 1.1 | 1.2 |
| USCS Classification | SP | SP |

Table 3.1: Properties of the soils used.

Sieving of the fused quartz was necessary because as the geogrid is pulled out of box during pullout tests; the soil particles at the aperture of the sleeve move into the gap between the surfaces of the sleeve. Friction between the soil particles and the surfaces of the sleeve can develop as the pullout test progresses. This would add additional pullout forces on the geogrid that are not related to soil-geogrid interaction.

Sieving the fused quartz to a maximum particle size ($D_{max}$) of 4.75 mm (0.187 in.) proved to be sufficient to minimize interaction with the sleeve of the wall. This is explained in Chapter 4 “Presentation of the Results”. The ratio between the aperture of the sleeve of the box (12.7 mm) and the $D_{max}$ of the fused quartz (4.75 mm) is 2.7.

## 3.2 Mineral Oils and Transparent soil

The concept of transparent soil involves finding a fluid that matches the refractive index of the granular material so it becomes transparent. The material must be 100 % saturated by the fluid. The presence of air bubbles compromises the transparency of the material. In this research, the obtained crushed fused quartz has a refractive index (RI) of 1.4585. This RI was indirectly measured by observing the degree of transparency of the granular material saturated with mixtures of mineral oils of different proportions. The RI of the mineral oil mixtures were directly measured with a refractometer.

The fluid with matching RI is a mixture of two white mineral oils: Puretol 7 and Krystol 40 manufactured by Petro-Canada[2]. The RI of the oils was measured with a digital hand-held "Pocket" refractometer, model PAL-RI manufactured by Atago Co. The RI of Puretol 7 is equal to 1.4637 at 22 $^{o}$C and the RI of Krystol 40 is 1.4458 at 23 $^{o}$C. The resolution of the measurements by this device is 0.0001 for the RI and 0.1 $^{o}$C for the temperature. The accuracy is ± 0.0003 for the RI and ± 1 $^{o}$C.

The ratio used in this research for the oil mix to provide the RI of 1.4585 was 69 % of Puretol 7 and 31 % of Krystol 40 by volume at 22 $^{o}$C. This mix is slightly different from the one used by Ezzein and Bathurst (2011a) of 68 % of Puretol 7 and 32 % of Krystol 40 reported at 22$^{o}$C. The change is due to the difference in the RI of Krystol 40 reported by Ezzein and Bathurst (2011a) to be equal to 1.4505 at 22 $^{o}$C. The difference in the reported RI of Puretol 7 is within the range of accuracy of the refractometer. The authors reported that their mineral oil mix is 10 times more viscous than water.

The observed thickness of the transparent soil with no transparency degradation was 150 mm (5.9 in.) looking through a 12.7 mm (0.50 in.) thick polycarbonate plate.

[2] Petro-Canada, 2310 Lakeshore Road West, Mississauga, Ontario, L5J 1K2, Canada.

This polycarbonate plate is the same as the ones used in the design of the new transparent pullout box developed in this study.

An example of the clear view provided by the transparent soil used in this study is shown in Figure 3.2. In this figure, the calibration box used for the transparent pullout tests is presented. The box is filled with transparent soil compacted with the same procedure adopted for the pullout tests. A 305 mm (12 in.) long stainless steel ruler is embedded in the transparent soil in the calibration box.

The ruler is used as a reference for calibration of distances measured in the transparent soil. The thickness of transparent soil between the ruler and the plate of the calibration box is the same 75 mm (3.0 in.) of the transparent pullout tests between the geogrid and the plate of the pullout box. This is important because the refraction of the light into the transparent plate and the transparent soil creates a magnification effect of the objects embedded in the transparent soil.

The marks near the edges of the ruler are used as targets for calibration of the images of the transparent pullout tests in the PIV program. The distance between the marks on the ruler is used to convert displacement measurements from the PIV program from pixels to millimeters. This procedure minimizes the error in the measurements due to the magnification effect caused by refraction of light.

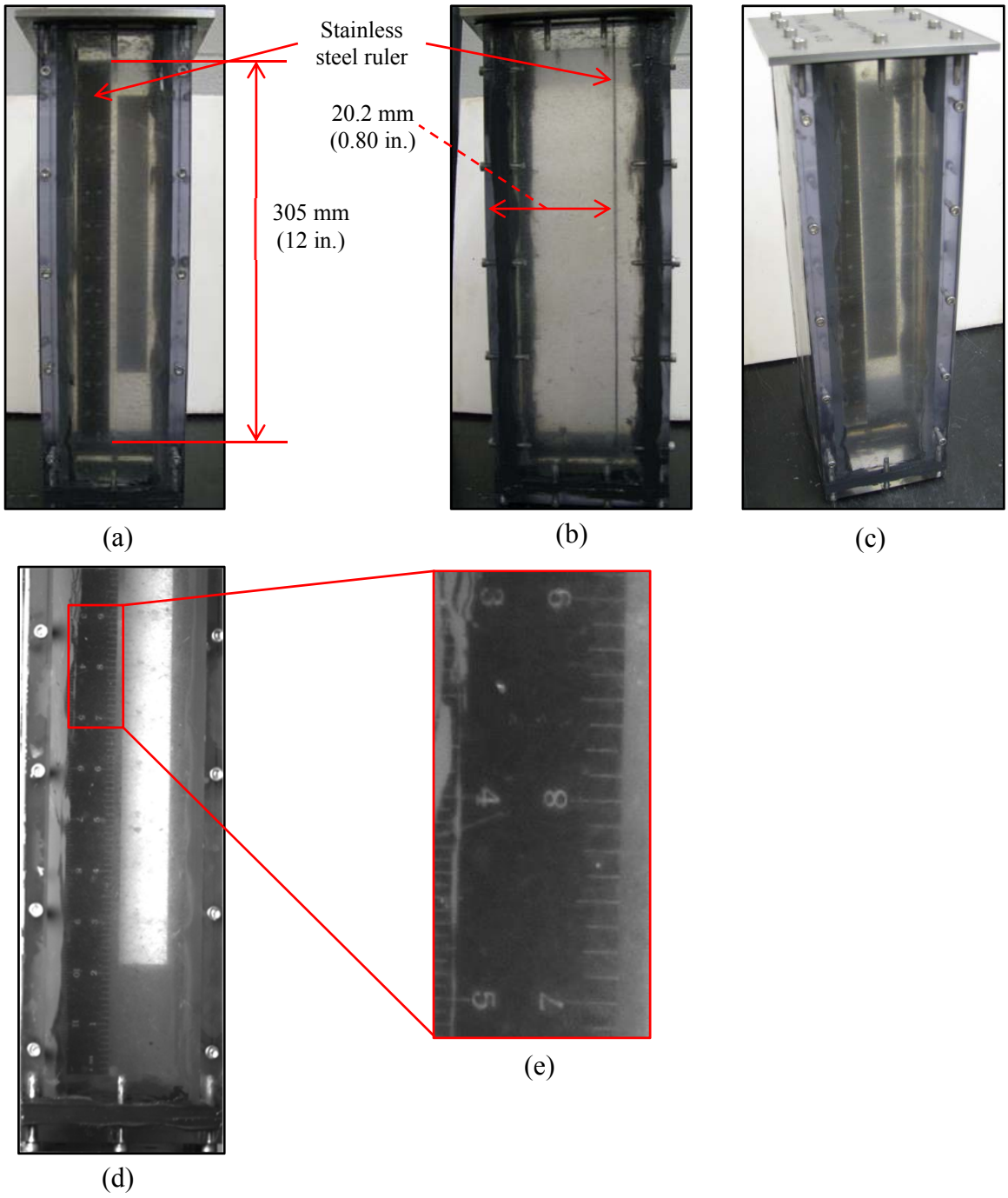


Figure 3.2: Calibration box: (a) Front view. (b) Side view. (c) View in perspective. (d) Front view, image from cam0 used for calibration. (e) Detail from (d).

## 3.3 Direct Shear Tests

Direct shear tests were conducted with Monterey sand and fused quartz following the recommendations of the ASTM D3080. All direct shear tests were performed at a constant rate of displacement of 0.05 mm/min. (0.02 in./min.).

Two series of tests with Monterey sand were conducted. The soil was tested with a water content of 1.5 % and saturated with water. For the tests saturated with water, the sand was compacted at a water content of 1.5 % and then the shear box apparatus was flooded with water. Three series of tests were conducted with the crushed fused quartz. The fused quartz was tested with a water content of 1.5 %, saturated with water and saturated with the mineral oil mix. The water content of 1.5 % was used to facilitate compaction of the soils.

### 3.3.1 DIRECT SHEAR TESTS WITH SAND

The Monterey sand was tested in a circular shear box with a diameter equal to 63.5 mm (2.5 in.) and a height of 31.75 mm (1.25 in.). The tests were performed with initial normal stresses of 21, 42 and 84 kPa (3, 6 and 12 psi) with a water content of 1.5 % and saturated with water. The average dry unit weight of the soil specimens for the series of test with a water content of 1.5 % was 16.3 kN/m$^3$ (dry density of 102 pcf). The correspondent average relative density (RD) was 70 %. The average dry density and RD were the same for the series of tests with sand saturated with water.

The failure envelopes for the two series of tests are presented in Figure 3.3. The friction angles for the sand with water content of 1.5 % and saturated with water are the same (39$^o$). The regression lines for the envelopes were forced to intercept at zero shear stress.

The shear stress curves for the tests with Monterey sand are shown in Figure 3.4. The peaks of shear stress of the tests with saturated water are similar to the tests with 1.5 % of water content for all normal stresses (Figure 3.4).

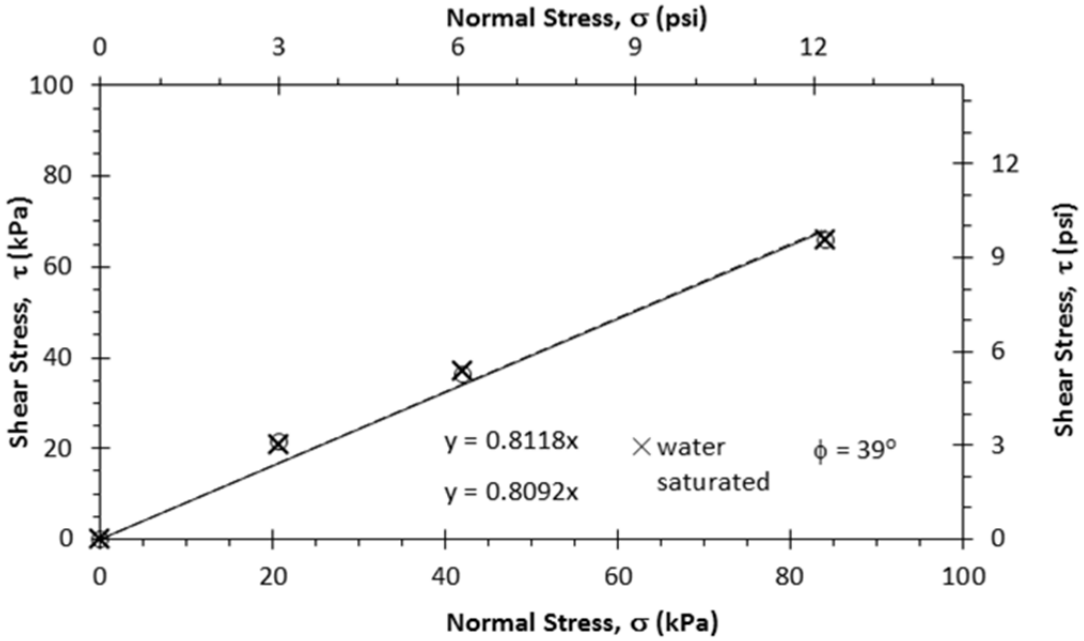


Figure 3.3: Failure envelopes from direct shear tests with Monterey sand with water content of 1.5 % and saturated with water.

The vertical strain data from the direct shear tests with Monterey sand are presented in Figure 3.5. The plots in this figure show that the soil dilates during shearing for all normal stresses tested. For both conditions, the vertical strain becomes constant after 4 mm (0.16 in.) of horizontal displacement. It can also be observed in Figure 3.5 that the higher the normal stress, the smaller the vertical strain, as expected.

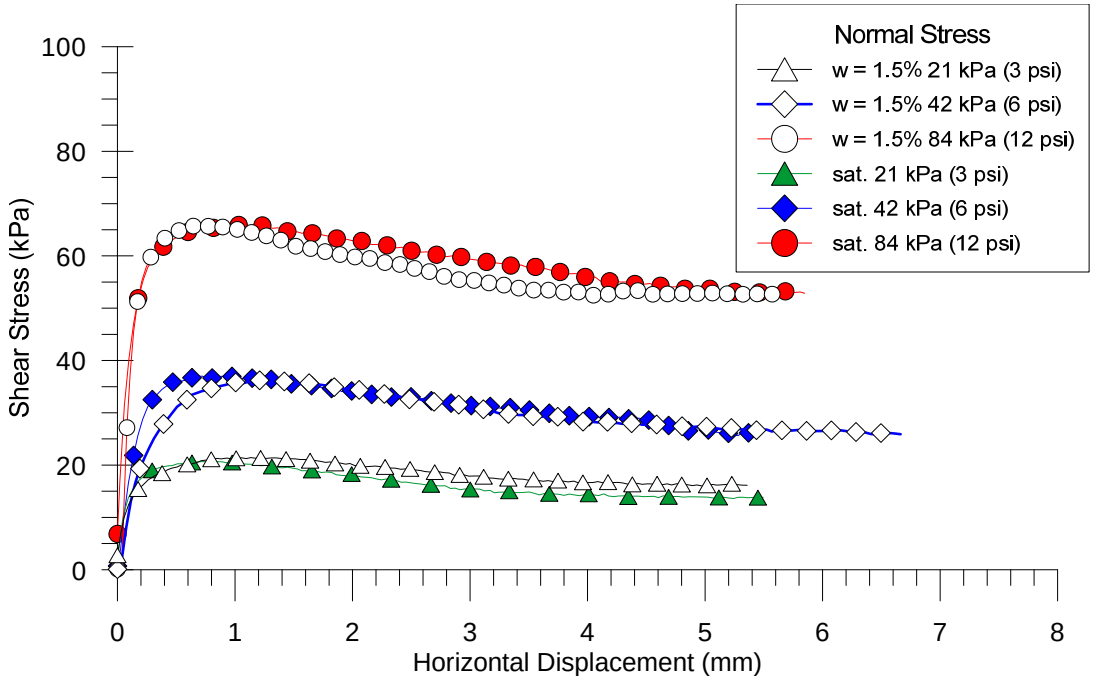


Figure 3.4: Data of direct shear tests with Monterey sand at a water content of 1.5 % and saturated with water.

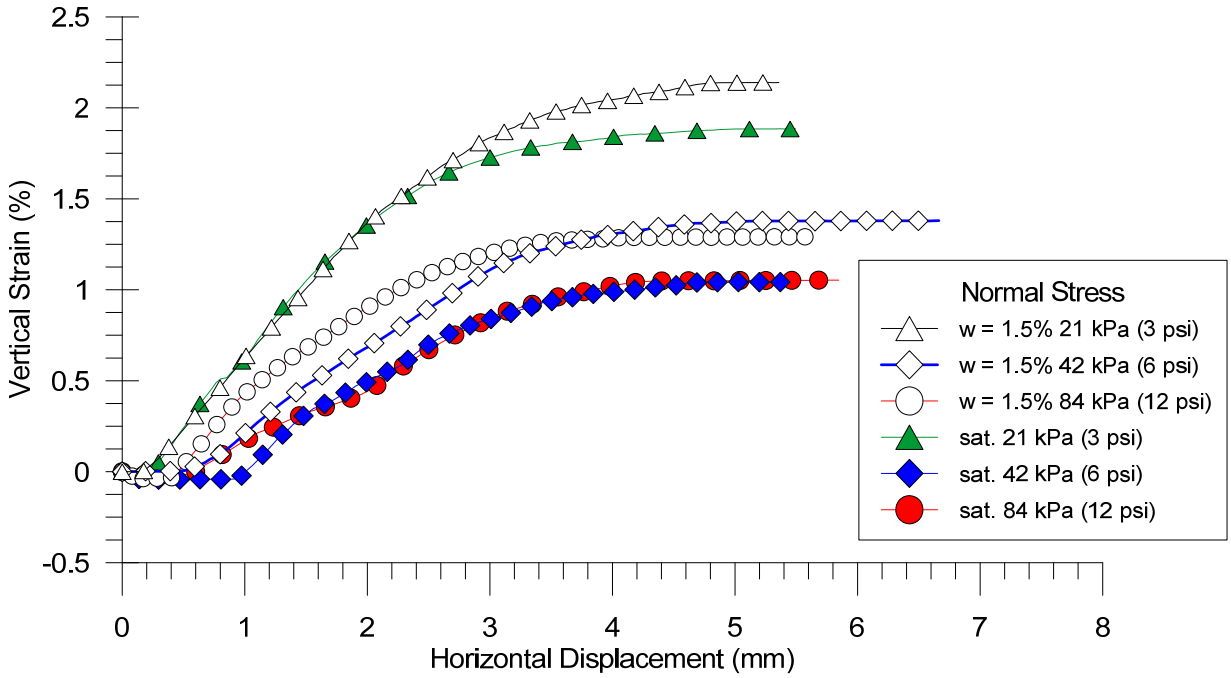


Figure 3.5: Vertical strain data from direct shear tests with Monterey sand with a water content of 1.5 % and saturated with water. Positive values indicate dilation.

### 3.3.2 DIRECT SHEAR TESTS WITH FUSED QUARTZ

The particles of crushed fused quartz were sieved to minimize their interaction with the sleeve of the front wall during pullout tests. Accordingly, the $D_{max}$ of the fused quartz used in the direct shear tests was 4.75 mm (0.187 in). This also adjusted the $D_{max}$ of fused quartz to conform to the recommendations of the ASTM 3080 for ratios between the $D_{max}$ and the dimensions of the direct shear box. The crushed fused quartz was tested in a rectangular shear box of dimensions equal to 76.2 x 76.2 x 30 mm (3.0 x 3.0 x 1.18 in.) corresponding to width, length and thickness, respectively.

The direct shear tests with fused quartz were conducted in three different groups: fused quartz with a water content of 1.5 %, saturated with water and saturated with the mineral oil mix. The average dry unit weight of the fused quartz in these series of tests was 12.8, 13.1, and 13.0 $kN/m^3$, respectively. The correspondent relative densities were 76, 78, and 77 %. The average relative densities are similar to the ones in the transparent pullout tests.

Similar to the direct shear tests with sand, tests with fused quartz were conducted with initial normal stresses of 21, 42 and 84 kPa (3, 6 and 12 psi). Additionally, tests were repeated for each confining pressure since the fused quartz is a new material.

The tests saturated with mineral oil mix were prepared with similar procedures adopted for the transparent pullout tests. First, the direct shear box was flooded with the mineral oil mix until the final height of the first lift. Then, the calculated mass of dry fused quartz for the lift was placed into the box and air bubbles were allowed to rise. Next, the soil was carefully stirred and then manually compacted by hand tampering with a 32 mm (1.25 in.) diameter steel rod. Afterwards, the surface of the soil lift was carefully scarified. Additional air bubbles were allowed to rise before pouring the mineral oil mix

for the next lift. This process is repeated until the desired soil sample height is achieved. The final soil sample height is composed of three compaction lifts.

The failure envelopes for the three series of tests are presented in Figure 3.6. As observed in this figure, the friction angles are virtually the same, independent of the pore fluid. The largest difference between friction angles is only $2^o$, which is within the expected precision of direct shear tests of 2 to 3 degrees. Therefore, it can be concluded that the peak shear strength is not affected by the pore fluid. Similar results were reported by Ezzein and Bathurst (2011a).

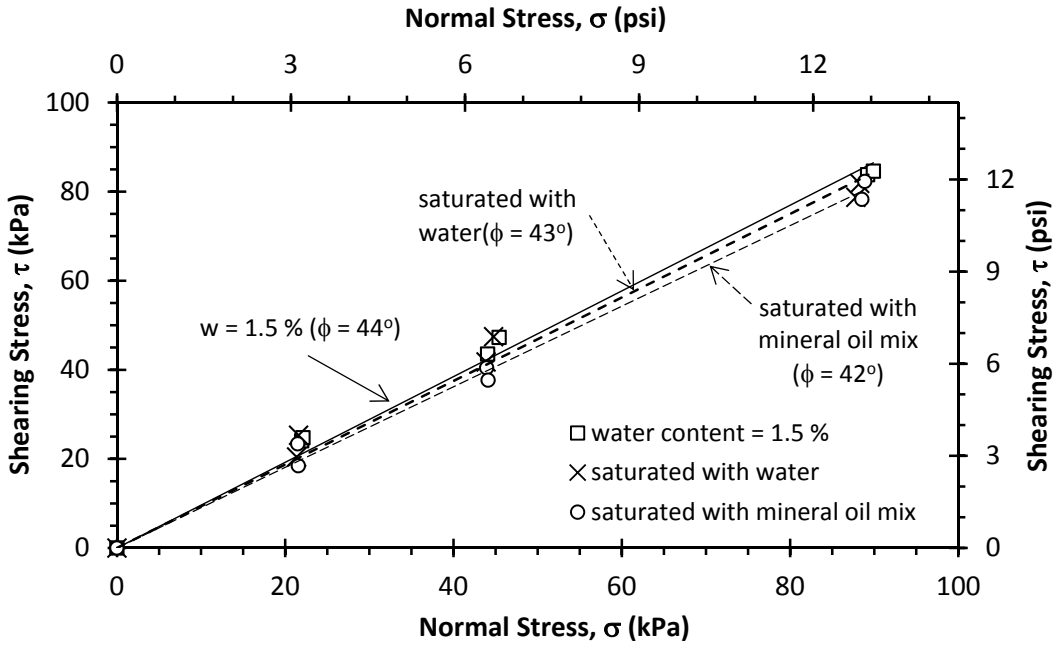


Figure 3.6: Failure envelopes for direct shear tests with crushed fused quartz.

#### 3.3.2.1 Tests of Fused Quartz with a water content of 1.5 %

The data of the direct shear tests using fused quartz with a water content of 1.5 % are presented in Figure 3.7. The data in this figure show that the shear stresses on the fused quartz tend to level to a maximum value with no distinct peak. The Monterey sand shows similar behavior for the normal stresses of 21 and 42 kPa (3 and 6 psi) at the same water content of 1.5 %. However, for the normal stresses of 84 kPa (12 psi), Monterey sand and the fused quartz behave differently. The Monterey sand shows a smooth peak and a gradual decrease of the shear stress after the peak (Figure 3.4). The fused quartz shows a tendency to reach a nearly constant value of maximum shear stress for larger deformations (Figure 3.7).

The coarse fused quartz tested by Ezzein and Bathurst (2011a) in dry conditions had particle sizes in the range of coarse sand, similar to the fused quartz used in this study. Ezzein and Bathurst (2011a) tested the fused quartz with a dry density of 12.4 $kN/m^3$, which is similar to the dry density of 12.8 $kN/m^3$ utilized in this study. However, the results of direct shear tests reported by Ezzein and Bathurst (2011a) showed curves with a smooth peak and a gradual decrease of shear stresses for displacements larger than 5 mm (0.20 in.) up to 10 mm (0.39 in.). The authors applied a normal stress of 75 kPa (11 psi) and used a larger direct shear box with dimensions of 100 x 100 x 50 mm (3.9 x 3.9 x 2.0 in.) corresponding to length, width and height, respectively. The difference between the results in this study and the results from Ezzein and Bathurst (2011a) might be due to the difference between the dimensions of the direct shear boxes used for the tests.

The vertical strain data recorded in the direct shear tests with fused quartz are shown in Figure 3.8. In this figure, it is observed that the fused quartz dilates almost linearly with the increase of horizontal deformation in the range of normal stresses and horizontal displacements tested. Different from the behavior of the Monterey sand, no

constant maximum vertical strain was reached. This behavior was also observed in the tests with coarse fused quartz reported by Ezzein and Bathurst (2011a).

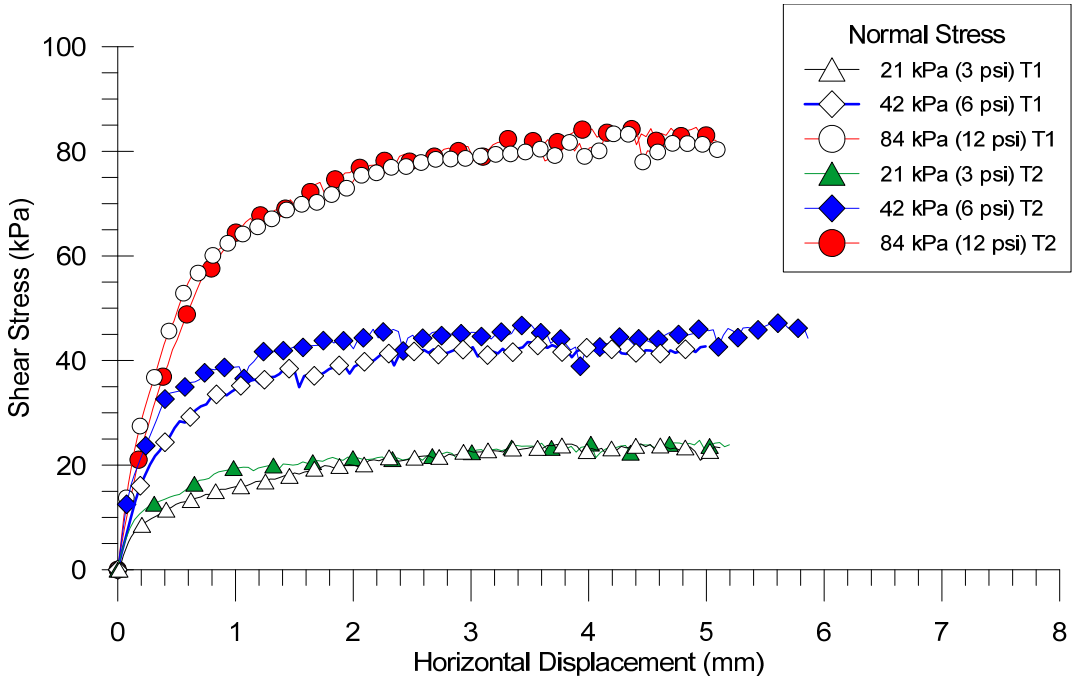


Figure 3.7: Direct shear test data for fused quartz at a water content of 1.5 %. Note: T1 = test 1; T2 = test 2 (repeat of test 1).

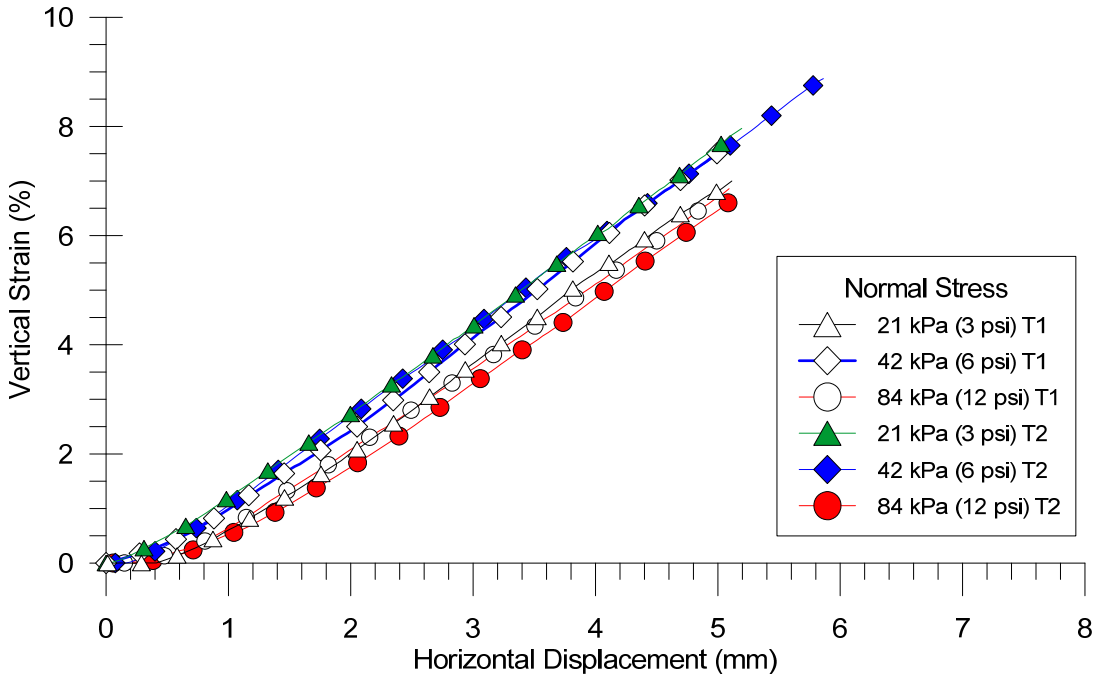


Figure 3.8: Vertical strain data for direct shear test with fused quartz at a water content of 1.5 %.

### 3.3.2.2 Tests of Fused Quartz Saturated with Water

The data of the direct shear tests using fused quartz saturated with water are presented in Figure 3.9. It can be observed in this figure that, in general, the shearing behavior of the fused quartz saturated with water is similar to the behavior with a water content of 1.5 % (Figure 3.7).

The vertical strain data for this series of tests is shown in Figure 3.10. Similar to the behavior with a water content of 1.5 % (Figure 3.8), the fused quartz dilates almost linearly with the increase of horizontal deformation at the range of normal stresses and horizontal displacements tested.

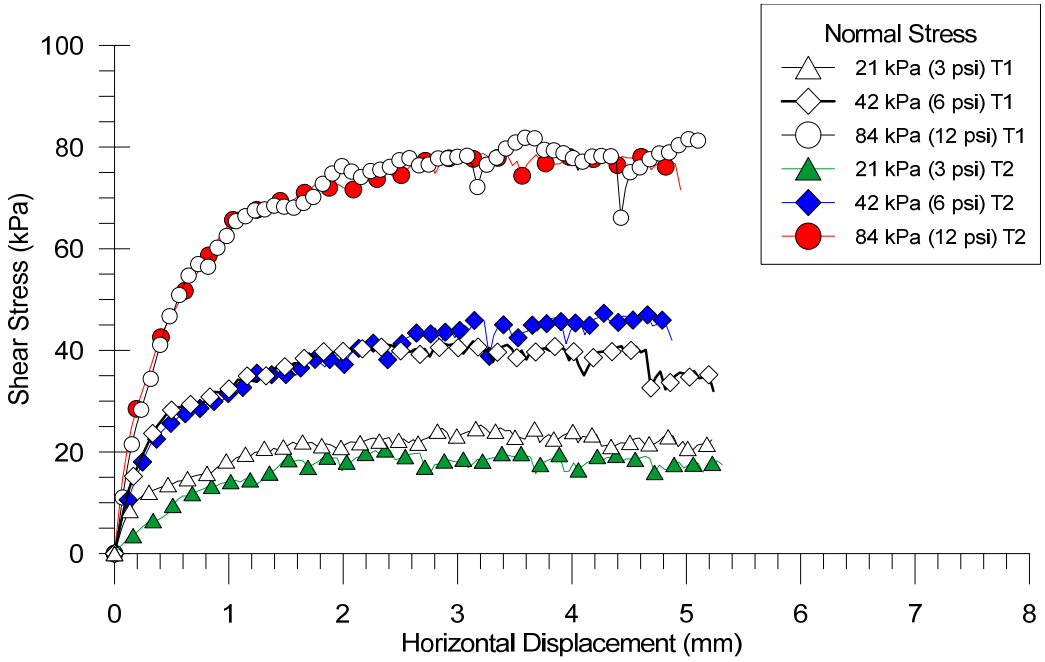


Figure 3.9: Direct shear test data for fused quartz saturated with water. Note: T1 = test 1; T2 = test 2 (repeat of test 1); 84 kPa = 12 psi; 42 kPa = 6 psi; 21 kPa = 3 psi.

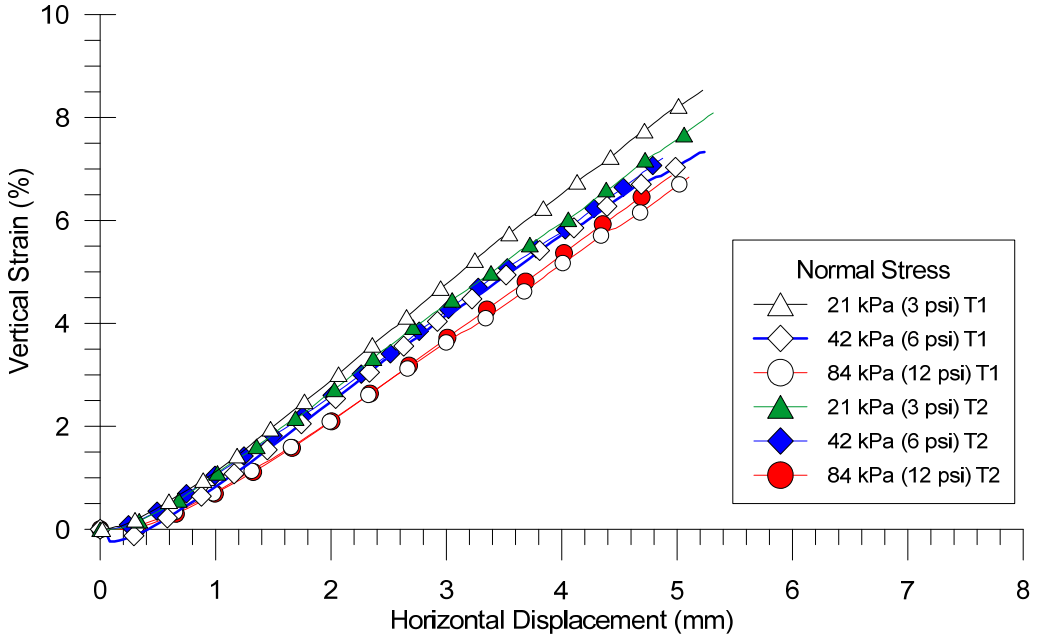


Figure 3.10: Vertical strain data for direct shear tests of fused quartz saturated with water.

#### 3.3.2.3 Tests of Fused Quartz Saturated with Mineral Oil Mix

The data of the direct shear tests using fused quartz saturated with mineral oil mix are presented in Figure 3.11. The slip-stick phenomenon is observed in Figure 3.11, in which cycles of shear stress drop and recovery occur during the test. The load drops are higher for higher normal stresses.

Similar behavior was observed by Ezzein and Bathurst (2011a). The authors attributed the occurrence of these cycles to the alignment of particles while shearing along the principal stress direction, through which inter-particle forces form chains that are in a fragile equilibrium and constantly collapsing and realigning. According to Ezzein and Bathurst (2011a), the collapses are more severe with viscous pore fluid, which allows longer chains to be formed. On the other hand, the mineral oil lubricates the contact between fused quartz particles. This lubrication facilitates the sliding of chains of particles over each other.

The vertical strain data for this series of tests is shown in Figure 3.12. Similar to the behavior observed in the previous series of tests (Figure 3.8 and Figure 3.10), the fused quartz saturated with the mineral oil mix dilates almost linearly with the increase in horizontal deformation, at the range of normal stresses and horizontal displacements tested. However, the vertical strains are smaller than the vertical strains of fused quartz saturated with water and with a water content of 1.5 %.

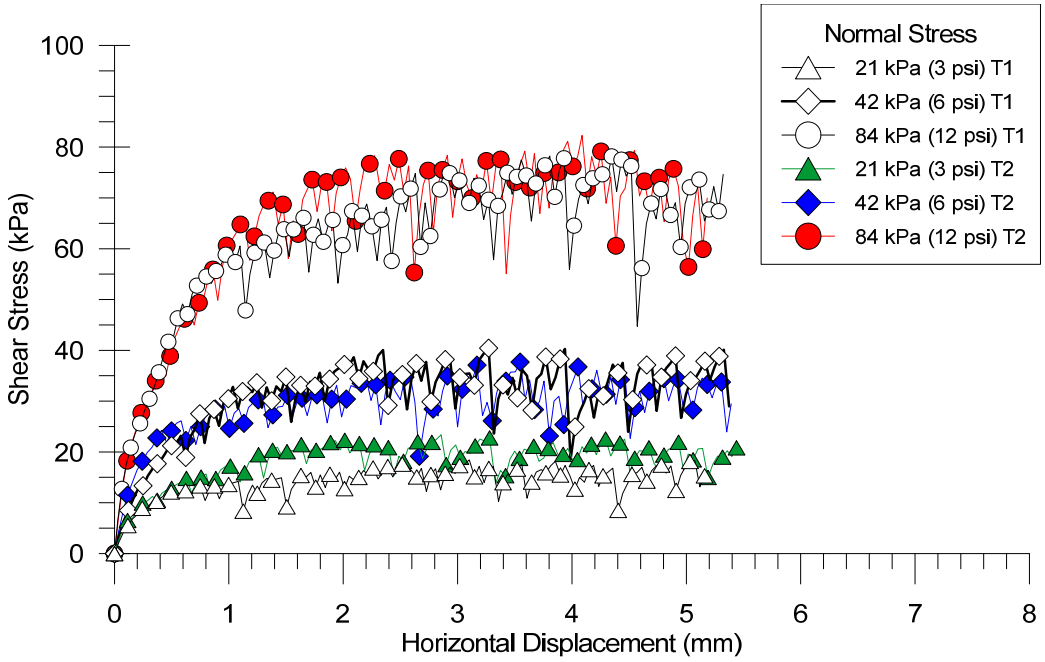


Figure 3.11: Direct shear test data for fused quartz saturated with mineral oil mix. Note: T1 = test 1; T2 = test 2 (repeat of test 1); 84 kPa = 12 psi; 42 kPa = 6 psi; 21 kPa = 3 psi.

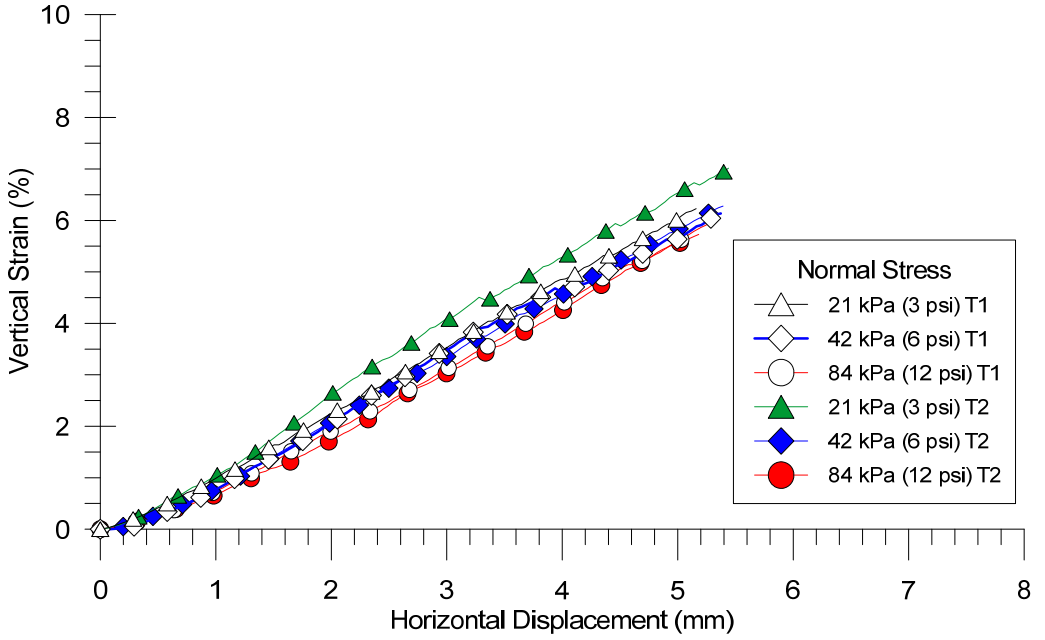


Figure 3.12: Vertical strain data for direct shear tests of fused quartz saturated with mineral oil mix.

## 3.4 Image Data Acquisition and PIV Software

The displacement data throughout the geogrid specimen in transparent pullout tests were obtained from high definition images of the test. The images were acquired with a system composed of two 5 MP cameras synchronized with a load cell and controlled with a LabView program. A data acquisition card manufactured by National Instruments controls the triggering signal of the cameras and the load cell. The images from the camera are transmitted through Gigabit Ethernet (GigE) cables to an external hard drive with a capacity of 3 TB.

### 3.4.1 COMPONENTS OF THE IMAGE DATA ACQUISITION SYSTEM

The image acquisition system is composed of two cameras. The camera named cam0 provided images of the plan view of the geogrid specimen embedded in the transparent soil during pullout testing. Soil markers placed in the direction perpendicular to pullout are also shown in the images from cam0.

The camera named cam1 provided images of the side view of the transparent soil surrounding the geogrid. Images on the plan view are used for measurements of displacements and strains developed throughout the geogrid specimen. Images of the side view are used for measurements of displacement of markers in the soil during pullout.

The cameras are manufactured by Allied Vision Technologies with Sony charge-coupled device (CCD) sensors. The camera named cam0 is a Manta G504B, monochrome camera with resolution of 2,452 x 2,956 pixels (5 MP) and 8-bit pixel format. The pixel format is commonly referred as pixel depth and accounts for the number of different grayscale values that can be distinguished. An 8-bit camera can

record $2^8$ different shades of gray, i.e. 256 gray levels. In this scale, a value equal to zero is the color black and 255 is the color white.

The maximum frame rate of the camera is 9 frames per second (fps). The camera is controlled by a triggering signal sent through an I/O cable with a 12-pin Hirose connector. The data is transmitted by a Gigabit Ethernet (GigE) cable at a rate of 1 GB/sec. The camera is equipped with Kowa C-Mount lens with fixed focal length of 35 mm. Consequently, adjustment of the field of view of the image cannot be made with the lens. Instead, the camera needs to be moved forward or backward to obtain the desired field of view. The focusing range, however, is from 0.2 m (7.9 in.) to infinite. Thus, for a given field of view, objects can be focused at a minimum distance of 0.2 m.

The camera named cam1 is a Manta G504C and was positioned at the side view of the transparent pullout tests. This model has the same specifications as the Manta G504B but it is a color camera. However, the images used for tracking displacement of the soil markers are monochromatic. This camera is equipped with a lens of a fixed focal length of 16 mm.

The same model of lens, Kowa LM35JCM, was installed on both cameras. According to the manufacturer, this lens has only -0.2 % of TV distortion. An illustration of this type of distortion is shown in Figure 3.13. In negative (or barrel) distortion (Ren and Wu, 2012), the length of a straight line at the edge of the image will appear shorter than its true length (Figure 3.13).

In the case of the lenses used in the transparent pullout test setup of this study, a straight line at the edge of the image would be only 0.2 % shorter than its true length. In this study, measurements of the displacement of the geogrid and soil markers were taken near the center of the images. Thus, the errors in displacement measurements caused by lens distortion are assumed to be insignificant for this study.

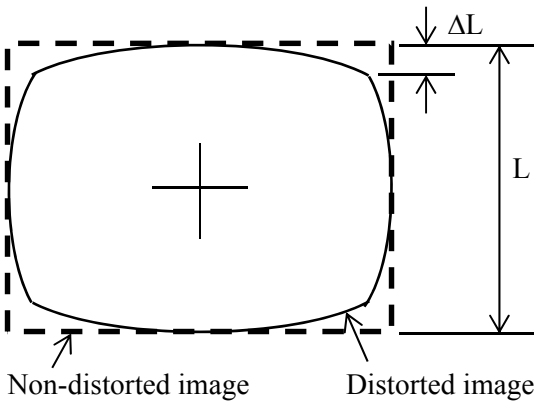


Figure 3.13: Illustration of negative distortion (barrel) in camera lens. (Source: adapted from Ren and Wu, 2012).

### 3.4.2 PIV PROGRAM AND CALIBRATION OF THE PIV CALCULATIONS

The PIV software used for displacement measurements from the images is the DynamicStudio v.2.30 supplied by Dantec Dynamics. Images obtained from the two cameras are pre-processed and analyzed with this software. The calibration of displacements obtained with PIV calculations was performed with images of 512 x 512 pixels cropped from the transparent pullout Test 5.

This calibration was divided in two parts. In the first part, cropped images from cam0 were used. Vertical displacements (dy) were digitally applied to a reference image from cam0 by cropping different images using Adobe® Photoshop Elements offset by the number of pixels desired for the displacement. Displacements of 1, 2, 4, 8, 16 and 32 pixels were used in the calibration. The reference cropped image and the images with vertical displacements of 8, 16 and 32 pixels are presented in Figure 3.14.

The images with the digital displacements were analyzed with the PIV program (DynamicStudio v.2.30) with six different configurations for the parameters of the

adaptive cross-correlation analyses (Table 3.2). These parameters included (i) the size of the final interrogation areas (IA), (ii) the number of refinement steps, and (iii) the overlap between adjacent interrogation areas.

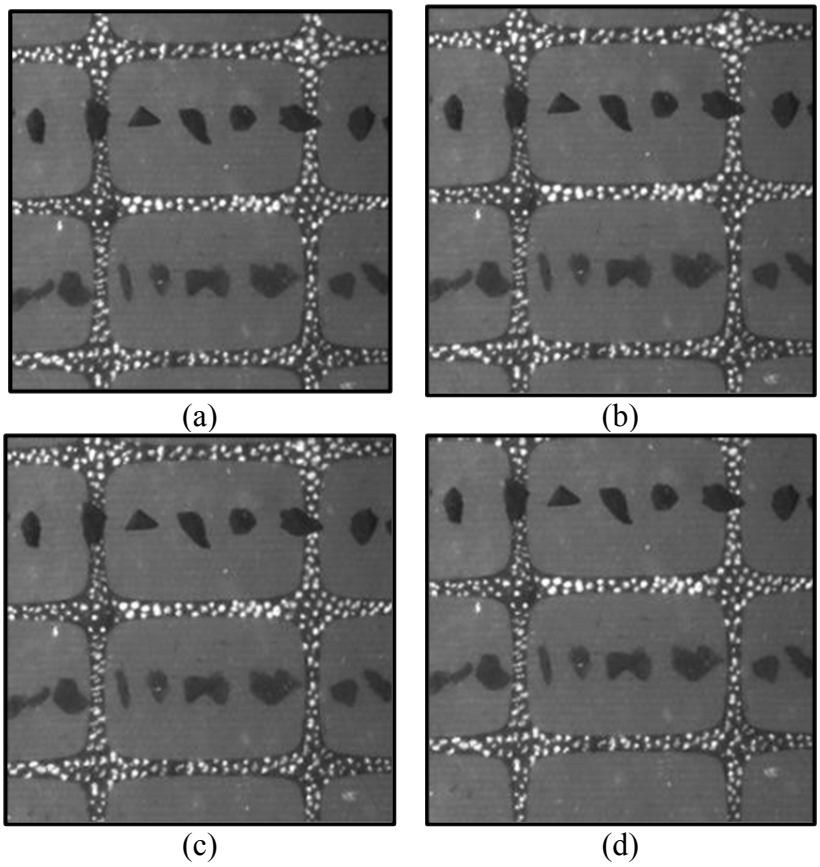


Figure 3.14: Sample of cropped images from cam0 used for calibration of the PIV calculations of displacements of the geogrid: (a) Original image with no vertical displacement (dy = 0). (b) dy = 8 pixels. (c) dy = 16 pixels. (d) dy = 32 pixels.

The number of refinement steps determines the size of the initial IA. For example, a final IA of 16 x 16 pixels and one refinement step leads to an initial IA of 32 x 32 pixels. The addition of a refinement step results in an initial IA of 64 x 64 pixels. The addition of a third refinement step leads to an initial IA of 128 x 128 pixels and so on.

| Scenario # | Final IA (pixels) | Refinement steps # | Initial IA (pixels) | Overlap (%) |
|---|---|---|---|---|
| 1 | 16 x 16 | 2 | 64 x 64 | 25 |
| 2 | 16 x 16 | 3 | 128 x 128 | 25 |
| 3 | 32 x 32 | 2 | 128 x 128 | 25 |
| 4 | 32 x 32 | 3 | 256 x 256 | 25 |
| 5 | 32 x 32 | 2 | 128 x 128 | 50 |
| 6 | 32 x 32 | 3 | 256 x 256 | 50 |

Table 3.2: Different configurations used for calibration of the PIV calculations of displacements in images from cam0 shown in Figure 3.14. Note: IA = Interrogation Area.

The PIV program allows 4 options to be chosen for the overlap between interrogation areas: 0, 25, 50 and 75 %. The overlap of the interrogation areas generates additional displacement vectors due to the resultant oversampling of the image. DynamicStudio allows for overlapping in the horizontal direction, vertical directions, or both directions at the same time. The overlap was used in both directions for all analyses in this study.

The configuration that provided the best results was Scenario 4 in Table 3.2, with a final IA of 32 x 32 pixels, 3 refinement steps (initial IA of 256 x 256 pixels) and an overlap of 25 %. The results obtained with these parameters are shown in Table 3.3. The error reported in Table 3.3 is the difference between the average calculated displacement and the digitally applied displacement.

Table 3.3 shows that the average error, considering displacements between 1 and 32 pixels, is only 0.003 %. The average error considering all displacements, including the case of no displacement, is only 0.00061 pixel. The large c.v. dy of the calculations for

dy equal to zero pixel, is due to the small absolute value of the average dy (0.000007 pixel). The standard deviation for dy equal to zero is only 0.0001 pixel.

However, the average error of the calculations in Table 3.3 should not be considered the standard error for all PIV calculations with images from cam0. These errors were evaluated only for applied integer values of displacements. Sub-pixel displacements result in larger errors because of the need of interpolation of the cross-correlation function for resolutions higher than 1 pixel. Raffel et al. (2007) reported that errors on the order of 0.05 to 0.1 pixel are realistic for interrogation areas of 32 x 32 pixels from 8-bit digital images. White et al. (2003) reported that errors on the order of 0.005 pixel can be achieved.

| Scenario | Applied dy (pixel) | dy | | | | % replaced vectors |
|---|---|---|---|---|---|---|
| | | Avg. dy (pixel) | c.v. dy (%) | Error dy (pixel) | (%) | |
| 4 | 0 | -0.000007 | 1730* | -0.000007 | --- | 0.9 |
| | 1 | 0.999992 | 0.011 | -0.000008 | 0.0008 | 0.7 |
| | 2 | 1.99998 | 0.020 | -0.000020 | 0.0010 | 10.2 |
| | 4 | 3.99996 | 0.012 | -0.000041 | 0.0010 | 10.0 |
| | 8 | 7.99996 | 0.006 | -0.000044 | 0.0006 | 10.2 |
| | 16 | 15.9992 | 0.028 | -0.000778 | 0.005 | 10.9 |
| | 32 | 31.9966 | 0.051 | -0.003372 | 0.011 | 10.9 |

Table 3.3: Results of the selected configuration for the PIV calculations from the scenarios shown in Table 3.2. Note: Avg. = average; dy = vertical displacement; c.v. = coefficient of variation. Note: large c.v. due to the small absolute value of the avg. dy: The standard deviation is only 0.0001 pixel.

In the second part of the calibration of the PIV calculations, cropped images from cam1 were used. Horizontal (dx) and vertical displacements (dy) were digitally applied at the same time to a reference image from cam1 by cropping different images using Adobe® Photoshop Elements offset by the number of pixels desired for the

displacements. Displacements of 1, 2, 4, 8, and 16 pixels were used in the calibration. The reference cropped image and the images with vertical displacements of 8 and 16 pixels are presented in Figure 3.15.

The images with the digital displacements were analyzed with the PIV program (DynamicStudio v.2.30) with five different configurations (Table 3.4) for the same parameters of the adaptive cross-correlation analyses used for the images from cam0 (Table 3.2). The configuration that provided the best results was Scenario 2 in Table 3.4, with a final IA of 16 x 16 pixels, 3 refinement steps (initial IA of 128 x 128 pixels) and an overlap of 25 %. The results obtained with these parameters are shown in Table 3.5 and Table 3.6. The error reported in these tables is the difference between the average calculated displacement and the digitally applied displacement.

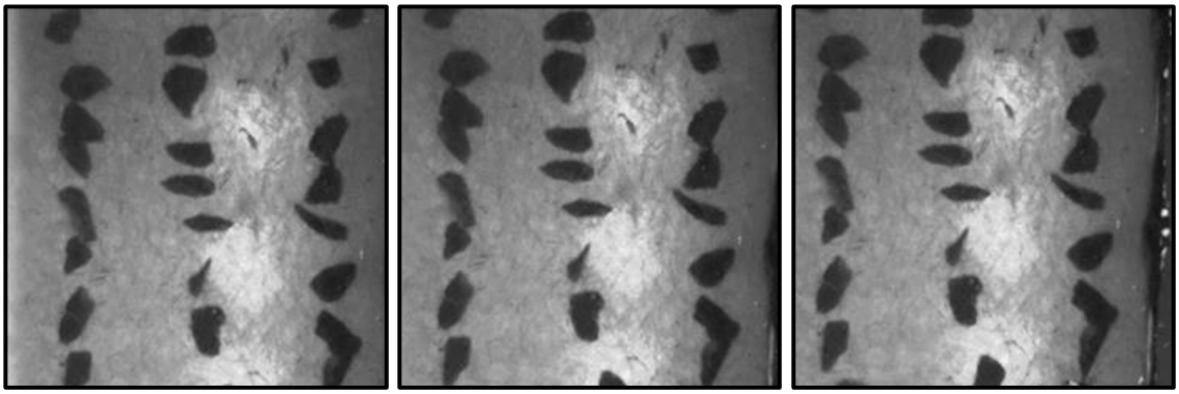

(a) (b) (c)

Figure 3.15: Sample of cropped images from cam1 used for calibration of the PIV calculations of displacements of the geogrid (a) Original image with no horizontal, dx, and vertical displacement, dy (dx = dy = 0). (b) dx = dy = 8 pixels. (c) dx = dy = 16 pixels.

| Scenario # | Final IA (pixels) | Refinement steps # | Initial IA (pixels) | Overlap (%) |
|---|---|---|---|---|
| 1 | 16 x 16 | 2 | 63 x 64 | 0 |
| 2 | 16 x 16 | 3 | 128 x 128 | 25 |
| 3 | 16 x 16 | 3 | 128 x 128 | 50 |
| 4 | 32 x 32 | 2 | 128 x 128 | 50 |
| 5 | 32 x 32 | 3 | 256 x 256 | 50 |

Table 3.4: Different configurations used for calibration of the PIV calculations of displacements in images from cam0 shown in Figure 3.15. Note: IA = Interrogation Area.

| Scenario | Applied dx (pixel) | dx | | | |
|---|---|---|---|---|---|
| | | Avg. dx (pixel) | c.v. dx (%) | Error dx (pixel) | (%) |
| 2 | 0 | 0.0007 | 752 | 0.000695 | --- |
| | -1 | -0.8670 | 33.3 | 0.132962 | -13.3 |
| | -2 | -1.8530 | 15.4 | 0.146954 | -7.3 |
| | -4 | -3.8239 | 8.4 | 0.176107 | -4.4 |
| | -8 | -7.8315 | 5.1 | 0.168501 | -2.1 |
| | -16 | -15.4789 | 10.8 | 0.521117 | -3.3 |

Table 3.5: Results for horizontal displacements of the selected configuration for the PIV calculations from the scenarios shown in Table 3.4. Note: Avg. = average; dx = horizontal displacement; c.v. = coefficient of variation. Negative dx is displacement to the left. The large c.v. dx for dx = 0 pixel is due to the small absolute value of the avg. dx. The standard deviation is only 0.005 pixel.

It can be observed in Table 3.5 and Table 3.6 that the average errors for the calculated displacements of the soil markers in images from cam1 are orders of magnitude higher than the average errors for displacements of the geogrid in images from

cam0. Similar to the results for cam0 (Table 3.3), the errors reported in Table 3.5 and Table 3.6 should not be considered the standard error for all PIV calculations with images from cam1. This is because the errors in Table 3.5 and Table 3.6 were evaluated only for integer values of displacements.

The average error for all horizontal displacements in Table 3.5 is 0.1911 pixel. The average error for all vertical displacements in Table 3.6 is 0.0299 pixel. Thus, the average error for the horizontal displacements of soil markers in cam1 is more than 6 times higher than the average error for the vertical displacements of soil markers in cam1. Moreover, the average error for the vertical displacements of soil markers in cam1 is almost 50 times higher than the average error for the vertical displacements of the geogrid in cam0. These results show that the PIV signal for tracking the displacement of soil markers can be further improved.

| Scenario | Applied dy (pixel) | dy | | | | % replaced vectors |
|---|---|---|---|---|---|---|
| | | Avg dy (pixel) | c.v. dy (%) | Error dy (pixel) | (%) | |
| 2 | 0 | -0.0007 | 478 | -0.000694 | --- | 17.9 |
| | 1 | 0.9971 | 2.8 | -0.002886 | 0.3 | 28.3 |
| | 2 | 1.9645 | 6.9 | -0.035525 | 1.8 | 29.0 |
| | 4 | 3.9661 | 3.4 | -0.033939 | 0.8 | 35.3 |
| | 8 | 7.9658 | 2.6 | -0.034247 | 0.4 | 33.3 |
| | 16 | 15.9280 | 4.0 | -0.072018 | 0.5 | 11.9 |

Table 3.6: Results of vertical displacements of the selected configuration for the PIV calculations from the scenarios shown in Table 3.4. Note: Avg. = average; dy = vertical displacement; c.v. = coefficient of variation. The large c.v. dy for dy = 0 pixel is due to the small absolute value of the avg. dy. The standard deviation is only 0.003 pixel.

## 3.5 Geogrid Product and Validation of the PIV Calculations

An integrally formed, polypropylene geogrid was used in this research. This geogrid is manufactured from punched polypropylene sheets that are oriented in two directions. These sheets form a biaxial geogrid with rectangular apertures.

Ultimate tensile strength tests were performed with this geogrid in the machine direction (MD) following the recommendations of the ASTM 6637. Additional tensile strength tests were conducted with a constant displacement rate of the grip of 1.0 mm/min. (0.04 in./min.), the same displacement rate used in the pullout tests.

#### 3.5.1.1 Geogrid Specifications

The nominal specifications of the geogrid product used in this research are presented in Table 3.7. It can be observed in this table that the geogrid has more ribs per unit width on the cross-machine direction (CD) than on the machine direction (MD). Thus, the geogrid is stronger on the CD.

| Characteristics | | | Geogrid | |
|---|---|---|---|---|
| Mechanical Properties | Tensile Strength (kN/m) at (ASTM 6637) | ε = 2 % | MD<br>CD | 4.1<br>6.6 |
| | | ε = 5 % | MD<br>CD | 8.5<br>13.4 |
| | | Ultimate | MD<br>CD | 12.4<br>19.0 |
| | Junction Efficiency (%) GRI-GG2 | | MD<br>CD | 93<br>--- |
| | Junction Strength (kN/m) calculated from junction efficiency | | MD<br>CD | 11.5<br>--- |
| Geometric Properties | Aperture Dimensions (mm) | | MD<br>CD | 25<br>33 |
| | Minimum Rib Thickness (mm) | | MD<br>CD | 0.76<br>0.76 |
| Polymer and aperture geometry | | | | Polypropylene rectangle |
| Manufacturing process | | | | Integrally formed |

Table 3.7: Nominal specifications of the geogrid used in this research. Note: MD = Machine Direction; CD = Cross Machine Direction.

#### 3.5.1.2 Geogrid Characterization and Validation of PIV Calculations

Two series of ultimate tensile strength tests were conducted with the polypropylene geogrid used in this study. In the first series, the geogrid was tested in the MD following the recommendations of the ASTM 6637. This standard recommends a displacement rate of the grip to be 10 % of the axial strain of the geogrid per min. For the grips used in this study, this recommendation resulted in a displacement rate of approximately 25 mm/min.

In the second series, the geogrid was tested in the MD at a constant displacement rate of the grip of 1.0 mm/min. (0.04 in./min.). All these tests were performed using the new image acquisition system assembled in this research. In order to validate the PIV calculations with the images from the tensile strength tests conducted in this study, the results were validated against the results of the tests conducted by Gupta (2009). The tests from Gupta (2009) were conducted in a commercial laboratory with geogrid specimens from the same lot of the geogrid used in this study.

The results of the tests conducted by Gupta (2009) are presented in Figure 3.16. These tests were conducted following the recommendations of the ASTM 6637. The average ultimate tensile strength of the geogrid measured was 13.8 kN/m with relatively small variation of the results. The average strain of the geogrid at breakage was 16.5 %, with relatively large variation of the results when compared to the results of the tensile force.

The results of the tests with the image acquisition system developed in this study and data from PIV calculations are shown in Figure 3.17. These tests were conducted following the recommendations of the ASTM 6637. The results in Figure 3.17 are similar to the results in Figure 3.16. The average ultimate tensile strength of the geogrid measured was 14.4 kN/m. The average strain of the geogrid at breakage was 16.4 %. The agreement between the results from this study and from Gupta (2009) validates the PIV calculations adopted in this study.

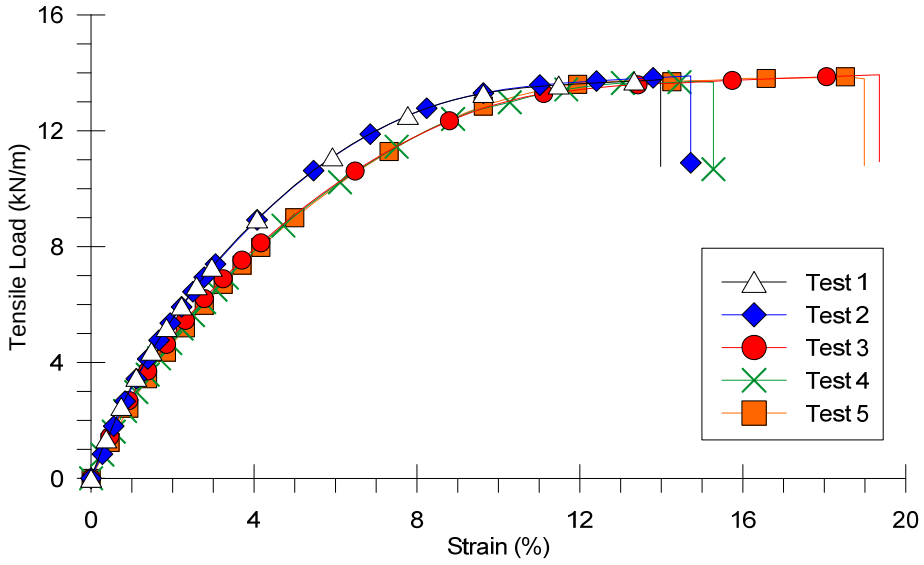


Figure 3.16: ASTM Tensile tests geogrid MD conducted by Gupta (2009) at TRI. Geogrid specimens from a roll of the same lot of the geogrid used in the present study.

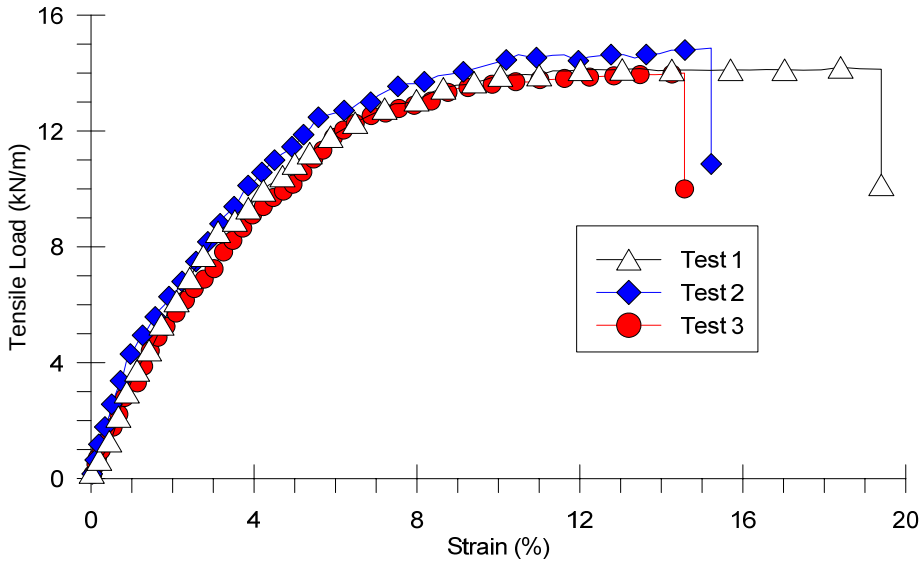


Figure 3.17: ASTM Tensile strength tests using PIV at UT-Austin. Geogrid specimens from the same lot of the specimens tested by Gupta (2009).

A series of ultimate tensile strength tests was conducted with the displacement rate of the grip equal to the displacement of the transparent pullout tests (1.0 mm/min.).

The results of these tests are shown in Figure 3.18, along with the results of the tests performed at the displacement rate recommended by the ASTM 6637. The tests at 1.0 mm/min. presented an average ultimate tensile strength of 13.1 kN/m. These tests also presented an average strain at breakage of 26.1 %. Thus, the average tensile strength of tests conducted at 1.0 mm/min. is near 10 % smaller than the tests conducted at the displacement rate recommended by ASTM 6637.

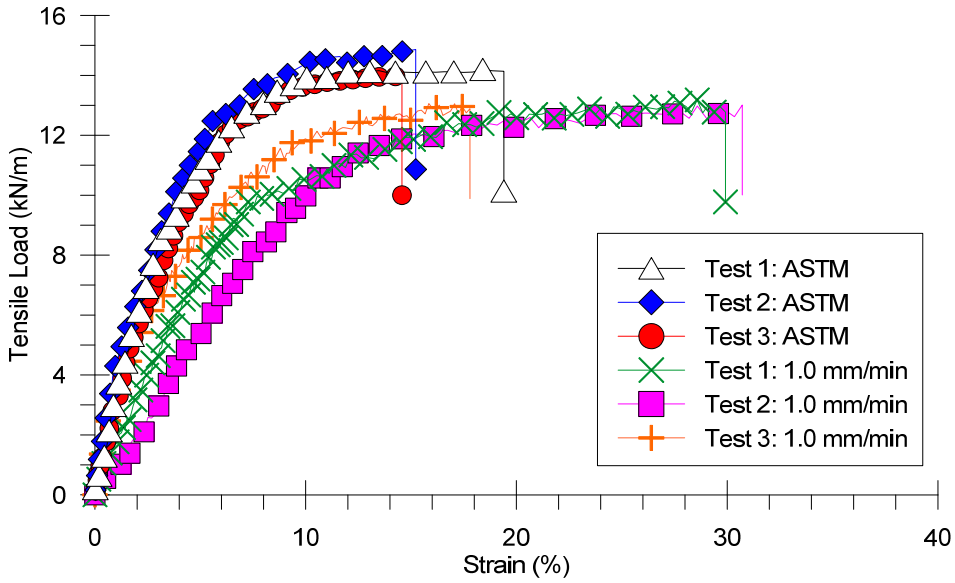


Figure 3.18: Comparison of tensile strength tests conducted at 25 mm/min (ASTM rate) and at 1.0 mm/min.

Additionally, the tensile load of the geogrid becomes steady at larger strains in the tests at 1.0 mm/min. than in the tests conducted at the ASTM displacement rate. The average strains at breakage in these tests were 59 % higher than the average strains at breakage in the test performed at the ASTM displacement rate.

## 3.6 Transparent Pullout Test Apparatus

The transparent pullout test apparatus has the same basic components of traditional pullout equipment recommended in the ASTM D6706. However, there are two main differences. First, the volume of soil used in the transparent pullout test device is only 13.1 % of the volume of soil correspondent to a traditional pullout box with the minimum dimensions suggested in the ASTM D 6706. Second, the transparent pullout test device is used in the vertical position. This apparatus is designed to be compatible with load frames dedicated to wide-width tensile strength tests of geosynthetics (ASTM D 4595 and D 6637).

The differences from large, traditional pullout devices are also the advantages of the small, transparent pullout test device. This new test setup is performed using basic equipment already commonly found in laboratories that perform geosynthetic testing. For the test to be implemented, the only difference is the replacement of the bottom grip of the wide-width tensile strength test by the pullout box and its base frame.

The best advantage of the dimensions of the transparent pullout box is observed in the test procedure. First, the volume of soil is significantly smaller than in traditional tests, so control of compaction is more effective. Second, the transparent pullout box does not need an exclusive device and valuable laboratory space dedicated to it. It can be employed in a testing machine already in use for other geosynthetic testing. Third, the setup of the test with the small pullout box is significantly faster than the setup of a test in a traditional, large pullout box. Finally, as a result of these advantages, the cost of a small pullout test is significantly lower than the cost of a large pullout test.

The design of the transparent pullout apparatus was based on the large amount of experience of the author with small pullout devices of similar dimensions and testing

setup. This concept used in the transparent pullout apparatus was first introduced by Kakuda et al. (2006). However, Kakuda et al. (2006) only measured the pullout force developed in the tests. The author of this dissertation adapted the device from Kakuda et al. (2006) so that displacement readings of two tell-tails attached to the geogrid specimen could be obtained (Ferreira 2007, Ferreira et al. 2008).

Then, the author of this dissertation improved the design of the test setup and further modified the small pullout apparatus used by Ferreira et al. (2008) to use five tell-tails attached along to the geogrid specimen. The aperture of the front wall of the box, where the geogrid specimen exits the box, was also modified to accommodate the use of granular soils in the research project 5-4829 of the Texas Department of Transportation (TxDOT) (Zornberg et al. 2008, Zornberg et al. 2012a, Zornberg et al. 2012b, Zornberg et al. 2013).

The laboratory component of the research project 5-4829 with TxDOT involved testing with five different soils and eleven different geosynthetic products. The geosynthetic products were tested on the MD and on the CD with a minimum of five repetitions for each test. The total number of small pullout tests conducted was 323 including the ones performed during the development of the test setup.

The transparent pullout box is composed of 2 parts: (i) the internal walls and (ii) an external frame designed to reinforce the walls. The internal walls are interchangeable, thus scratched transparent walls can be easily replaced. The side walls are transparent allowing the view of the cross section of the test and displacements of soil markers that can be placed near the interface.

The thickness of the transparent side walls is 12.7 mm (0.50 in.). The material is an abrasion-resistant polycarbonate sheet of high stiffness and strength. The nominal Modulus of Elasticity is 2,344 MPa (340,000 psi), the Ultimate Tensile Strength is 66

MPa (9,500 psi) and the Flexural Strength is 93 MPa (13,500 psi), as reported by the manufacturer[3].

The front wall is composed of top and bottom plates that are 9.5 mm-thick (0.375 in.) and made of stainless steel type 303. The gap between these plates creates the front wall aperture. These plates were machined with 2 different configurations: flat plates and sleeved plates. Sleeved plates have sleeves welded at the ends that extend 15.875 mm (0.625 in.) into the soil mass in the box. A cross-section of the transparent small pullout test setup showing the sleeved front wall is presented in Figure 3.19. The sleeves are used not only to reduce interaction of the soil with the front wall during the test, but also to minimize loss of oil and fused quartz particles during compaction and testing.

The aperture in the front wall is 12.7 mm (0.50 in.) through which the geosynthetic specimen exits the box and is attached to the grip (Figure 3.19). The internal dimensions of the transparent pullout box are 300 x 250 x 150 mm (11.8 x 9.8 x 5.9 in.) corresponding to width x length x height. The dimensions of the embedded portion of the geogrid specimen is 216 x 232 mm (8.50 x 9.13 in.) corresponding to width and length, respectively. The shorter length of the geogrid specimen in relation to the length of the box is due to the presence of the sleeves of the front wall, which extends into the soil mass. Figure 3.20 shows the plan view of the transparent pullout test along with the dimensions of the internal walls of the box.

[3] Manufactured by SABIC Innovative Plastics™ , model Lexan MR10.

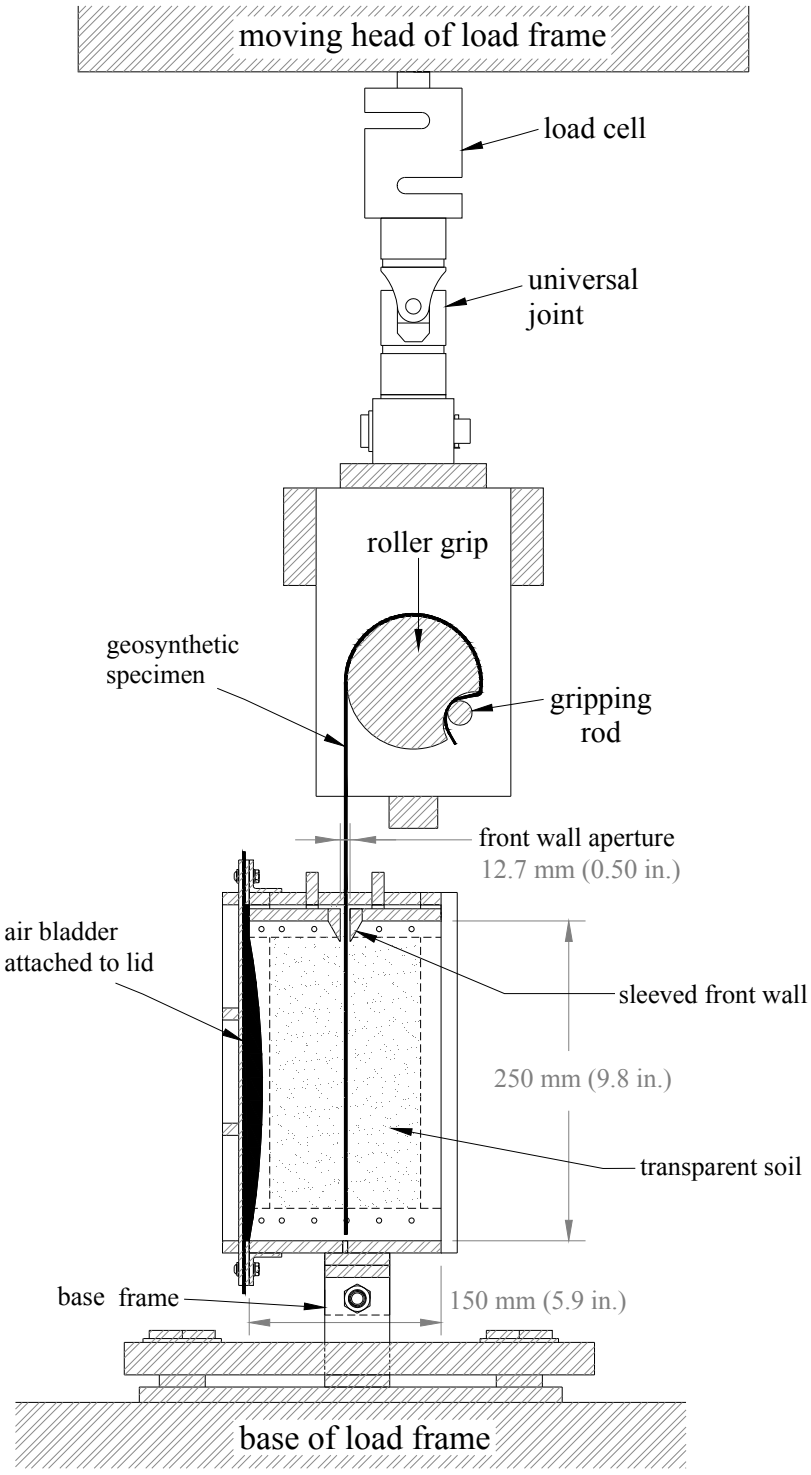


Figure 3.19: Cross-section of the transparent small pullout test setup with sleeved front wall.

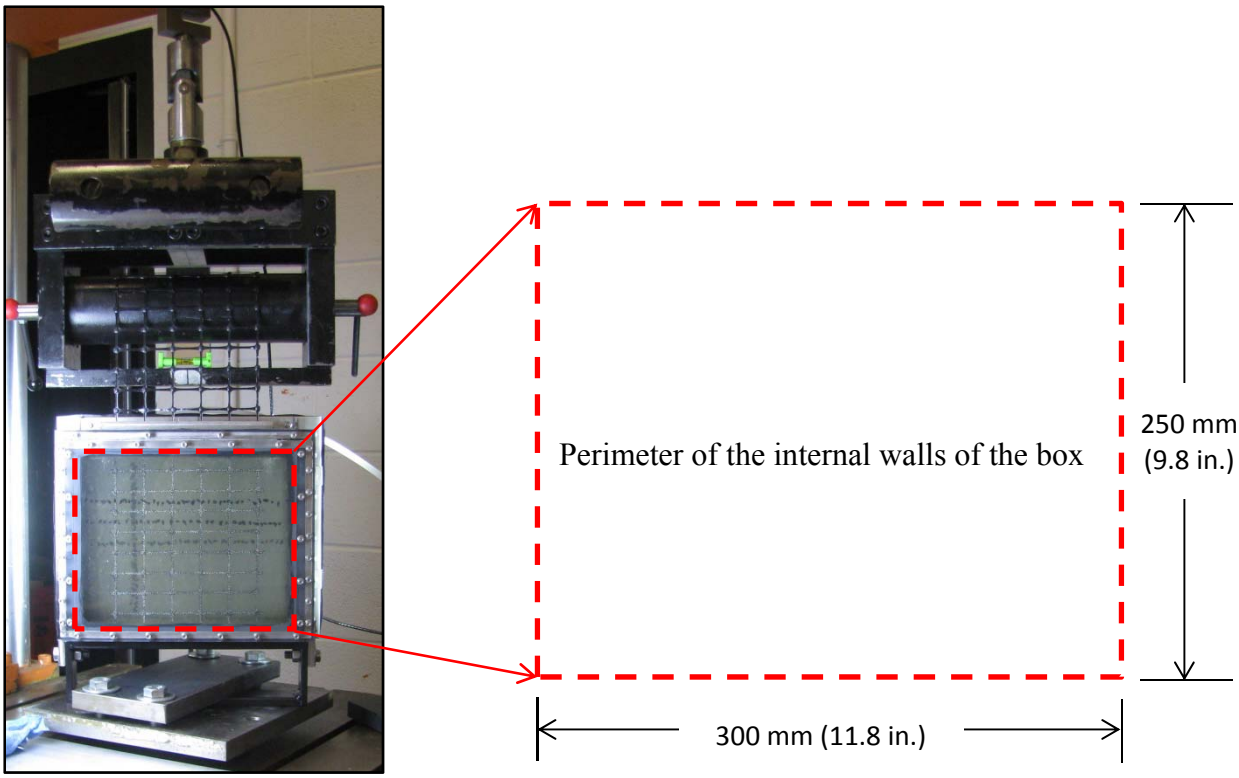


Figure 3.20: Plan view of the transparent pullout test showing the internal dimensions of the pullout box.

The external frame is incorporated with the rear wall and is made of the same material as the plates of the front wall. The rear wall has a slot of 4.0 mm (0.1575 in.) across at mid-height. This allows the use of wires and displacement sensors, for tests without transparent soil to be performed using tell-tails attached at different points along the geogrid specimen. When the transparent soil is used, an external plate is attached to the rear wall. This plate contains a plug machined to fit the slot and prevent oil leakage through the aperture of the rear wall.

The bottom plate of the box is transparent and made of the same material as the side walls. The transparent bottom plate allows for the plan view of the geogrid specimen embedded in transparent soil (Figure 3.20). The pullout box is attached to a base frame

which in turn is attached to the base of the load frame (Figure 3.19 and Figure 3.20). The confining pressure is applied through compressed air supplied to a bag attached to the lid of the box (Figure 3.19).

The load frame is a universal testing machine from SATEC Systems with maximum capacity of 267 kN (60,000 lbf). The load frame was modified to be powered and controlled with National Instruments SCXI hardware and LabVIEW software system. The pullout force is recorded with an Omega S-type load cell of 22 kN (5,000 lbf) of capacity.

## 3.7 Procedure for Pullout Testing with Monterey Sand and Dry Fused Quartz

In this section, the procedure adopted in preparing the pullout tests with Monterey sand and fused quartz with a target water content of 1.5 % is described. The compaction of the bottom layer is executed in four lifts by hand, tampering with a steel rod of 32 mm (1.25 in.) in diameter. The mass of soil for each lift required for the target dry density is measured on a scale prior to placement of the soil into the box. After compaction of each lift, the surface of the soil is scarified before placement of the mass of soil of the next lift.

Following completion of the bottom layer, the geogrid specimen is placed and the wires attached to it passed through the aperture of the rear wall. Then, the top layer of soil is compacted in four lifts with the same procedure used for the compaction of the bottom layer. A gap of 5 mm (0.20 in.) is left between the soil surface and the top of the box. This gap is to accommodate a piece of non-woven geotextile that is placed on the soil surface to protect the air bladder of the lid from puncturing. Finally, the lid is secured and the confining pressure is applied to the soil through the air bladder.

Only after application of the confining pressure, the box is positioned in a vertical position and attached to the base frame on the load frame. The displacement sensors are then aligned to the wires of the tell-tails connected to the geogrid and locked in place in the base frame. Finally, the geogrid is attached to the grip and a pre-load of 0.13 kN (30 lbf) applied.

## 3.8 Procedure for Pullout Testing with the Transparent Soil

In this section, the procedure adopted in preparing the pullout tests with the transparent soil is described. Before compaction, the transparent box is cleaned and placed in a tray. The function of the tray is to recover mineral oil losses that may occur during compaction of the transparent soil. The front wall aperture is sealed with a piece of rubber prior to compaction of the soil.

First, the mineral oil mix is poured in the transparent box up to the final height of a compaction lift, 19 mm (0.75 in.). Then, the weighted proper dry mass of fused quartz particles is pluviated into the box in 3 steps. After each step, the soil is visually inspected and non-transparent particles are individually retrieved with tweezers to maintain the transparency quality.

Fused quartz particles that do not become transparent when immersed in the mineral oil mix have the appearance of a cloud with a dense concentration of white dots. This lack of transparency is caused by small air bubbles entrapped in the interior of the fused quartz particles during production of the material. An optical microscope was used to obtain a detailed image of a particle of fused quartz that has entrapped air bubbles in its interior Figure 3.21.

Figure 3.21: Optical microscopic view of a fused quartz particle with entrapped air bubbles.

After all of the dry mass of fused quartz of the lift is immersed in the oil mix; a glass pipette is used to carefully stir the transparent soil causing air bubbles in the oil mix to rise. Next, the soil is hand tamped with a 32 mm (1.25 in.) diameter steel rod to the desired final height. Remaining air bubbles are allowed to rise after tamping. Afterwards, the surface of the soil is carefully scarified and additional oil mix is poured. This compaction process is repeated until completion of the bottom layer at the mid-height of the box. The bottom layer is formed by four compaction lifts.

Next, the rubber seal is unplugged from the front wall aperture of the box and the geogrid specimen placed. Due to this operation, a small amount of oil is lost from the box and collected in the tray where the box rests. Modeling clay is applied on the front wall aperture and around the geogrid ribs to reseal the front wall aperture and allow for compaction of transparent soil to the final height of the box.

After sealing the front wall aperture with modeling clay, the recovered mineral oil of the bottom layer that leaked out is carefully replaced. The fused quartz becomes

transparent again without disturbing the compacted layer below the geogrid. Finally, the top layer of transparent soil is compacted in 4 lifts following the aforementioned steps.

A gap of approximately 5 mm (0.20 in.) is left between the soil surface and the top of the box to accommodate a piece of white woven geotextile and a piece of non-woven geotextile. The white geotextile is used to create a background contrast with the black geogrid specimen. All the geogrid products used in this research are black. Finally, the piece of non-woven geotextile is used to provide additional protection to the air bladder against puncture from the angular fused quartz particles.

The next step is to apply a confining pressure of 6.9 kPa (1.0 psi) with compressed air supplied into the air bladder of the lid of the box. This initial confinement is to minimize disturbance in the soil-geogrid system when positioning the pullout box in the vertical position. After positioning the pullout box in the vertical position, the modeling clay is removed and the final confining pressure desired for the test is applied. Then, the pullout box is placed on the base frame attached to the load frame and secured in place.

The following step is to attach the geogrid to the grip. Then the cameras and lighting system are carefully positioned and aligned with the pullout box. Next, a pre-load of 0.15 kN (30 lbf) is applied to the geogrid. Finally, the test starts with synchronized data and image acquisitions from the load cell and cameras. The setup of the transparent pullout tests is shown in Figure 3.22.

After the test is finished, the geogrid is disconnected from the grip and the pullout box is put aside on a separate table without moving the position of the cameras. Next, the calibration box shown in Figure 3.2 is placed on the base frame of the pullout box, and calibration images are obtained with the cameras used in the pullout test. These images

are used to relate measurements in the image space (pixels) to measurements in the object space (mm).

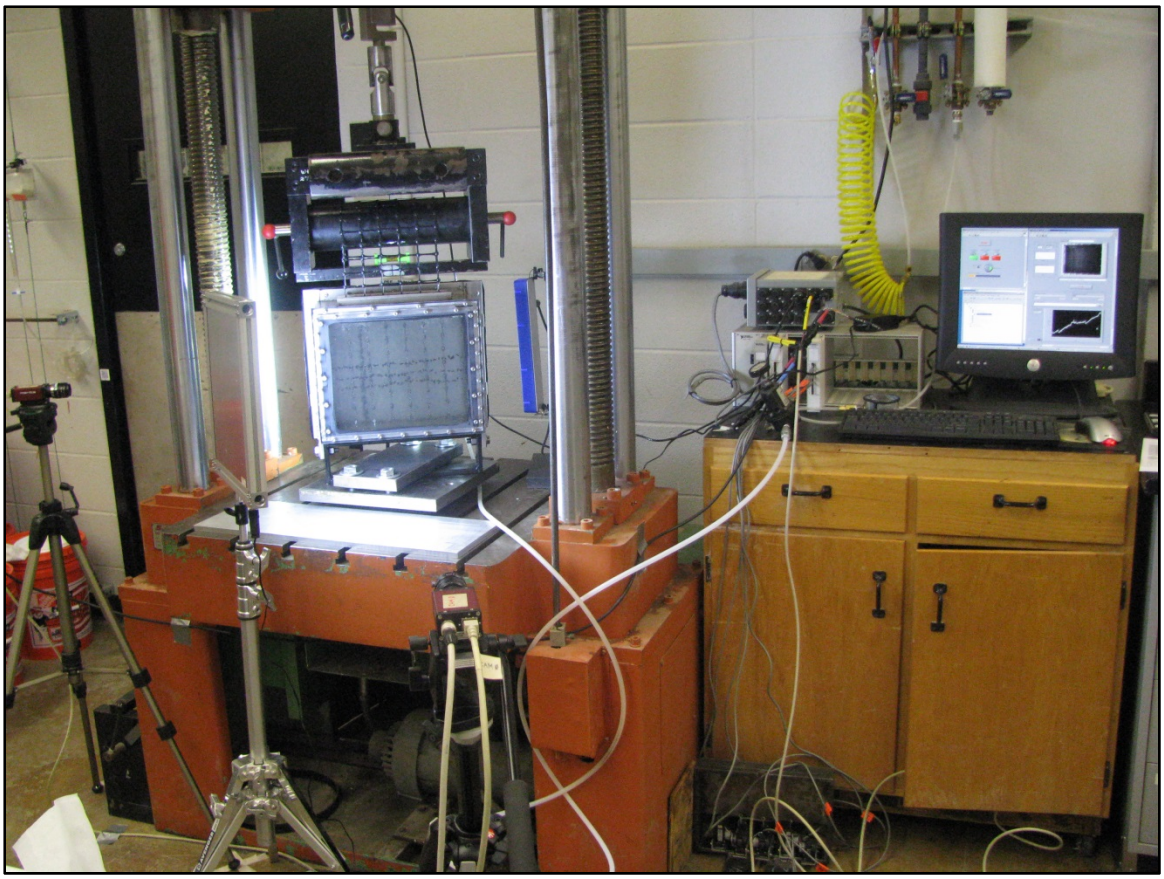

Figure 3.22: Setup of the transparent pullout test.

# 4 PRESENTATION OF THE RESULTS

The data from the small pullout tests conducted in this research are presented in this chapter in the traditional layout found in the literature: plots of pullout force against displacement of a limited number of points along the geogrid specimen. Discussion of the results of the pullout tests in this chapter is limited to the evaluation of the pullout forces and displacements of five points along the geogrid specimen of the different tests.

The procedure used for fitting the displacement data obtained with the PIV program is explained at the end of this chapter. Source of errors in the PIV calculations and in the data fitting process related to the testing setup are also explained in the end of this chapter. Detailed analyses of displacement profiles obtained using PIV and calculations of strains along the geogrid in different tests are presented in Chapter 5 "Discussion of the Results". Qualitative evaluation of the displacements of the soil markers embedded in the transparent soil is also presented in Chapter 5.

## 4.1 Testing Matrix

The testing matrix of this research is separated into two sets of pullout tests (Table 4.1). In the first set of tests, the geogrid was used in the cross-machine direction (CD) and the confining pressure was 21 kPa (3 psi). The soils used were Monterey sand, crushed fused quartz, and crushed fused quartz saturated with the white mineral oil mix (i.e. the transparent soil). This configuration for tests was chosen to allow future comparisons of these results to the results obtained by Zornberg et al. (2013).

| Test set | Geogrid | | Soil | Confining pressure |
|---|---|---|---|---|
| | Orientation | Configuration | | |
| I | CD | 1st transverse cut | Monterey sand at w = 1.5 % | 21 kPa (3 psi) |
| | CD | 1st transverse cut | Fused quartz at w = 1.5 % | 21 kPa (3 psi) |
| | CD | 1st transverse cut | Transparent soil | 21 kPa (3 psi) |
| II | MD | No transverse rib | Transparent soil | 35 kPa (5 psi) |
| | MD | One transverse rib | Transparent soil | 35 kPa (5 psi) |
| | MD | Two closely spaced transverse ribs | Transparent soil | 35 kPa (5 psi) |
| | MD | Two largely spaced transverse ribs | Transparent soil | 35 kPa (5 psi) |
| | MD | No modifications (eight closely spaced transverse ribs) | Transparent soil | 35 kPa (5 psi) |

Table 4.1: Testing matrix adopted in this research. Note: CD – Cross-machine Direction; MD – Machine Direction; Transparent soil – fused quartz saturated with the mineral oil mix.

The objective of the first set of tests is to evaluate the influence on the results of the artificial soil composed by particles of fused quartz when compared to tests with Monterey sand. Also, the influence of the white mineral oil on the results is evaluated in relation to the test with only fused quartz.

In the second set of tests, the geogrid was used in the machine direction (MD) and in different configurations. The confining pressure was 35 kPa (5 psi). All of these tests were conducted using the transparent soil. The discussion of the results in this chapter is focused on the effects of the different configurations of the geogrid on the shape of the pullout force x displacement curves. Detailed analysis of this set of tests is presented in Chapter 5 with displacement and strain profiles of the geogrid specimens at different stages of the tests.

## 4.2 Comparison of Pullout Tests with Monterey Sand, Fused Quartz and Transparent Soil

A small pullout test was conducted using Monterey sand and the geogrid in the cross-machine direction (CD). The confining pressure was 21 kPa (3 psi). The sand was compacted at a water content of 1.33 % and dry unit weight of 15.9 kN/m$^3$ (99 pcf). This corresponds to a relative density (RD) of 54 %. Displacements along the geogrid were monitored with tell-tails at 5 different junctions distributed along the geogrid specimen as shown in Figure 4.1. The terminology adopted for the test setup of this research is also presented in Figure 4.1. The distances of the measurement points along the embedded portion of the geogrid are shown in Table 4.2. The embedded length of the geogrid is 232 mm for all pullout tests.

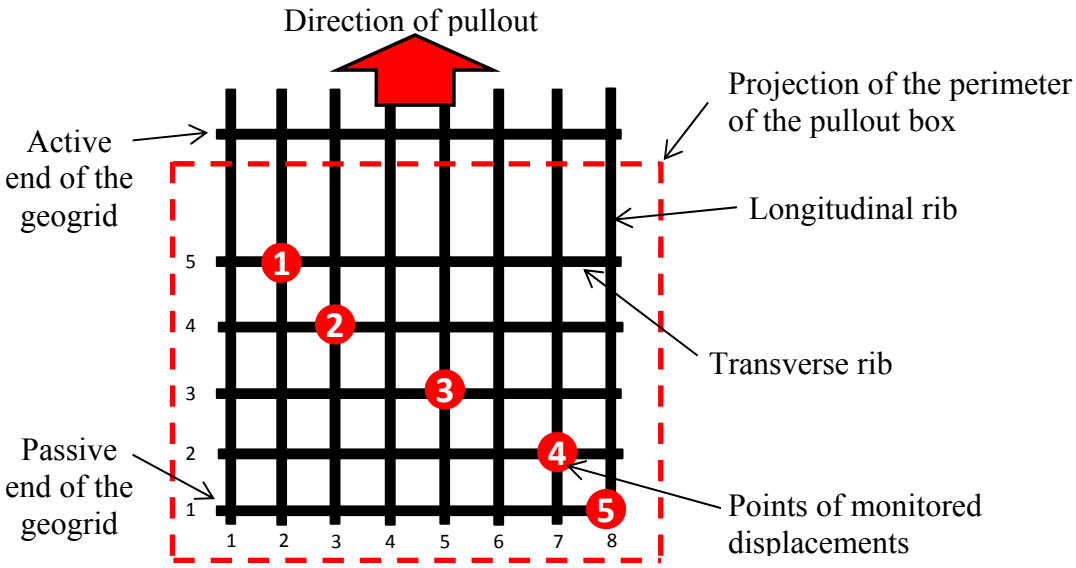


Figure 4.1: Terminology adopted for the pullout tests and location of the points (junctions) along the geogrid with monitored displacements in the tests conducted with the geogrid oriented in the CD.

| Displacement sensor # | Distance from the active end of the geogrid | | |
|---|---|---|---|
| | (mm) | (inch) | % L (mm/mm) |
| 1 | 58 | 2.3 | 0.25 |
| 2 | 98 | 3.9 | 0.42 |
| 3 | 138 | 5.4 | 0.59 |
| 4 | 179 | 7.0 | 0.77 |
| 5 | 219 | 8.6 | 0.94 |

Table 4.2: Locations of points of monitored displacements along the geogrid specimen during small pullout testing. Note: L – total length of the geogrid.

The transverse rib that would be closest to the exit of the box was cut prior placement of the geogrid in the pullout box. This was done because this rib would be extremely close to the sleeve at the exit of the box. This could cause additional loads to be applied to the geogrid due to friction resistance developed by the displaced soil in contact with the surfaces of the sleeve when exiting the box. This friction increases with the dilation of the soil particles created by the cutting action of the transverse rib exiting the box.

The data of this small pullout test is presented in Figure 4.2. The maximum pullout force obtained was 6.8 kN/m (465 lbf/ft). Cycles of sudden drops in the pullout load, followed by load recovery are also observed in Figure 4.2. At the same time when the load drops, the entire geogrid moves at once. The load recovery occurs with relatively small displacements. These cycles started when near 65 % of the maximum pullout was reached. Nakamura et al. (2003) reported pullout results with similar cycles of drops and recovery of the pullout load in tests with a fine sand and pullout box with dimensions comparable to the one used in the present study. However, the cycles of load drops and recovery in the results of Nakamura et al. (2003) start only after the maximum pullout force is reached.

(a)

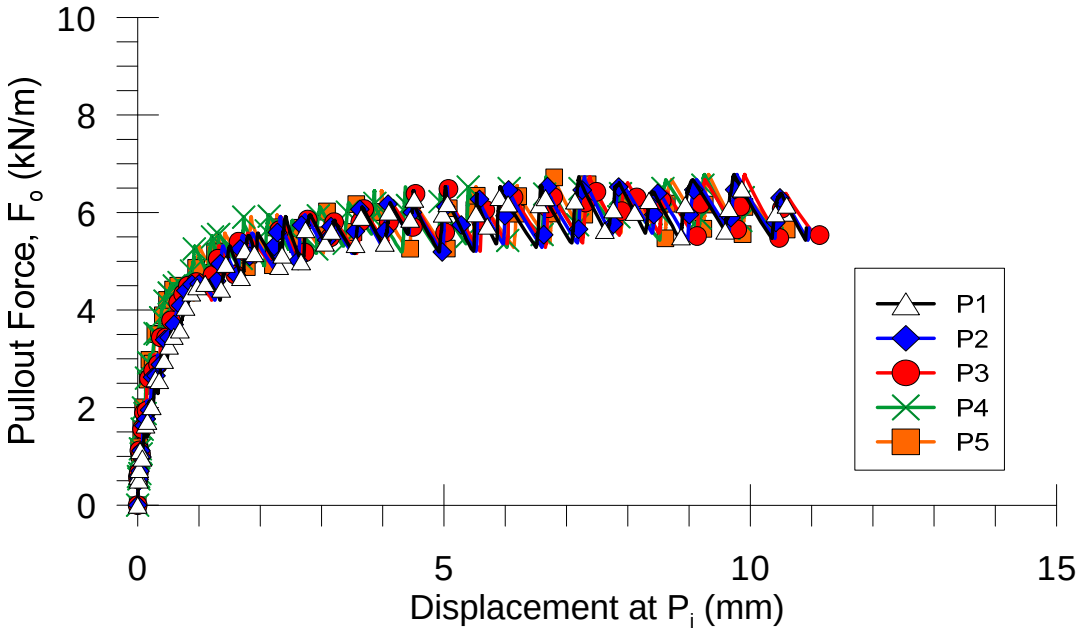


(b)

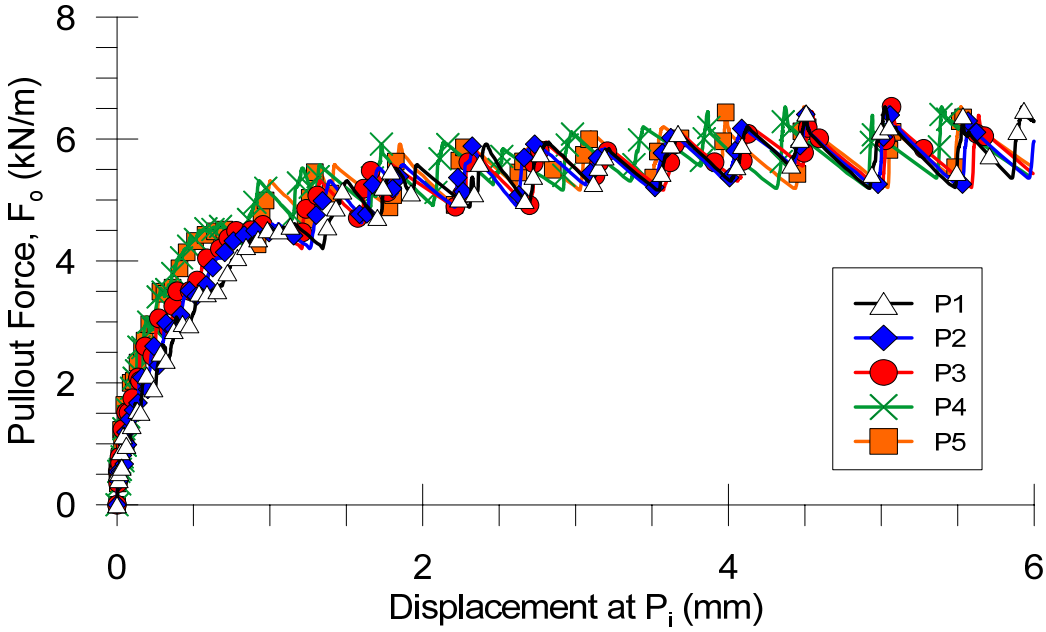


Figure 4.2: Data from small pullout test with Monterey sand, geogrid CD, and confining pressure of 21 kPa (3 psi): (a) Data from the entire test. (b) View of the data up to 6 mm of displacement.

Zornberg et al. (2013) reported similar results for pullout tests with Monterey sand in a small pullout box of the same internal dimensions to the transparent pullout box used in the present study. The only difference between the pullout boxes is that the transparent box has a sleeve and a smaller aperture in the wall where the geogrid exits the box.

The results in Figure 4.2 show that there is a slip-stick phenomenon at the interface of the fine Monterey sand with the geogrid, although this phenomenon was not observed in the direct shear tests of the Monterey sand. This slip-stick phenomenon occurs when chains of particles are formed to support the load. As the load increases, the chains of particles slide over each other, thus causing the load to drop. Then, new chains of particles start to form and the load increases again until the chains of particles collapse once more (Alshibli and Roussel 2006, Duttine et al. 2008).

Alshibli and Roussel (2006) reported the slip-stick behavior for triaxial tests with uniform, fine glass beads. Duttine et al. (2008) observed this behavior in direct shear tests with a uniform, fine sand and uniform, fine glass beads. This behavior occurred until the end of the pullout test.

Figure 4.3 presents the results for the pullout test performed with crushed fused quartz compacted at a water content of 1.26 % and dry unit weight of 12.6 kN/m$^3$ (79 pcf). This corresponds to a RD of 46 %, similar to the RD of 54 % used in the pullout test with Monterey sand. Displacements along the geogrid were monitored with tell-tails at the 5 junctions illustrated in Figure 4.1. The distances of the monitored points along the geogrid were similar to the ones for the test with Monterey sand reported in Table 4.2.

Similar to the test with the Monterey sand, the transverse rib that would be closest to the exit of the box was cut prior to placement of the geogrid in the pullout box. However, this measure did not completely eliminate the generation of additional loads to

the geogrid due to friction resistance developed by the displaced soil in contact with the surfaces of the sleeve when exiting the box (Figure 4.4). On the other hand, additional loads to the geogrid were generated only at large displacements, higher than 6 mm (Figure 4.3).

It can be noted in Figure 4.3a that the pullout force increases until reaching and holding a constant value of 12.5 kN/m, then the pullout force starts to increase again until breakage of the geogrid at 19 kN/m. The value of 12.5 kN/m, at which the pullout force was initially steady, is considered the maximum pullout force of the test. The increase of the pullout force after that is due to the friction resistance developed by the displaced soil in contact with the surfaces of the sleeve when exiting the box. The crushed fused quartz is highly dilative (see direct shear tests in Chapter 3), so additional friction was created against the surfaces of the sleeve of the box since they restrain the dilation of the soil.

Thus the pullout curve considered for this test is the one shown in Figure 4.3b. The shape of this plot is similar to plots of pullout test results reported in the literature (Farrag et al. 1993, Gupta 2009, Palmeira and Milligan 1989, Ochiai et al. 1996, Teixeira et al. 2007).

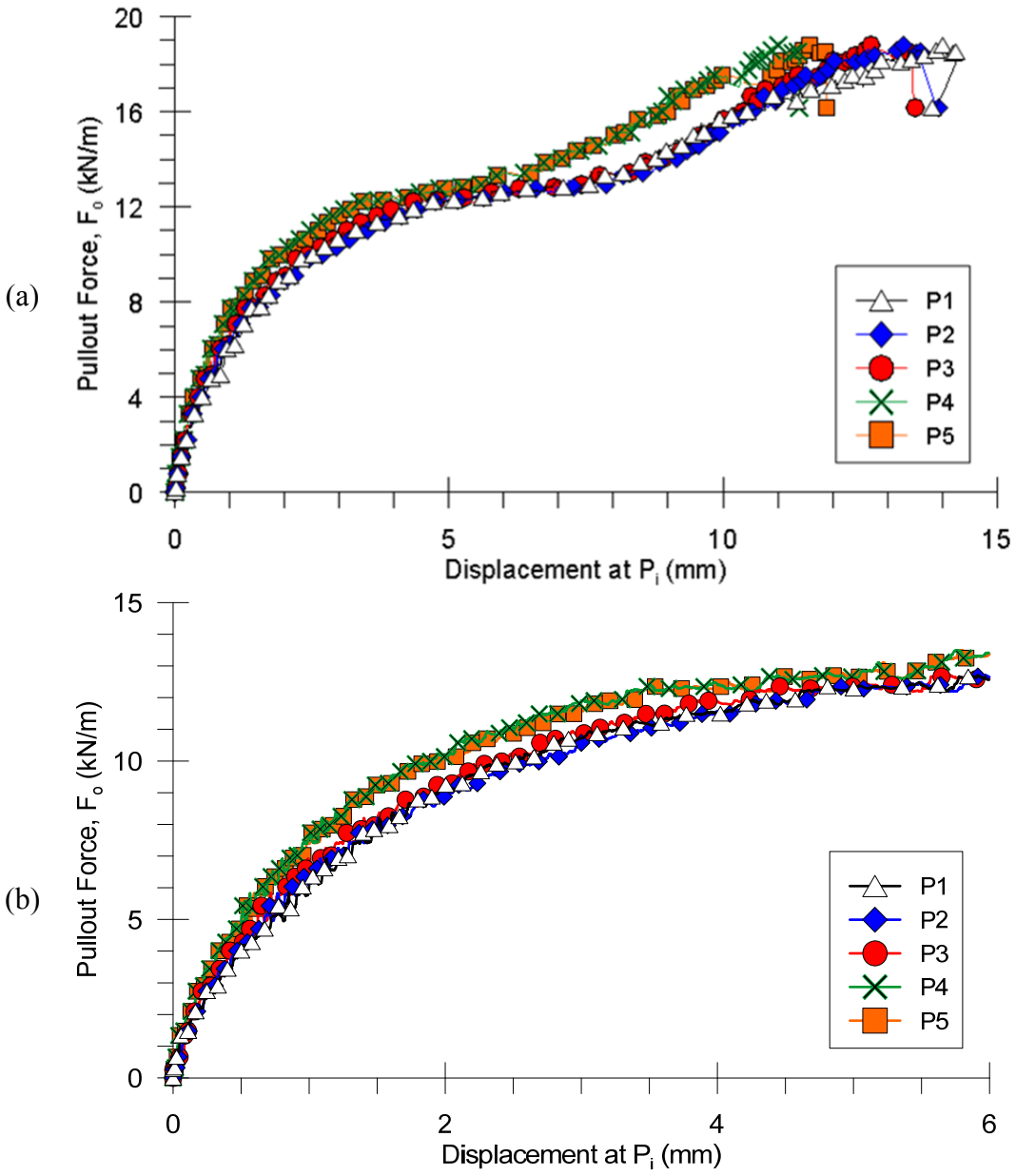


Figure 4.3: Data from small pullout test with fused quartz, geogrid CD and confining pressure of 21 kPa (3 psi): (a) Data from the entire test. (b) View of the data up to 6 mm of displacement.

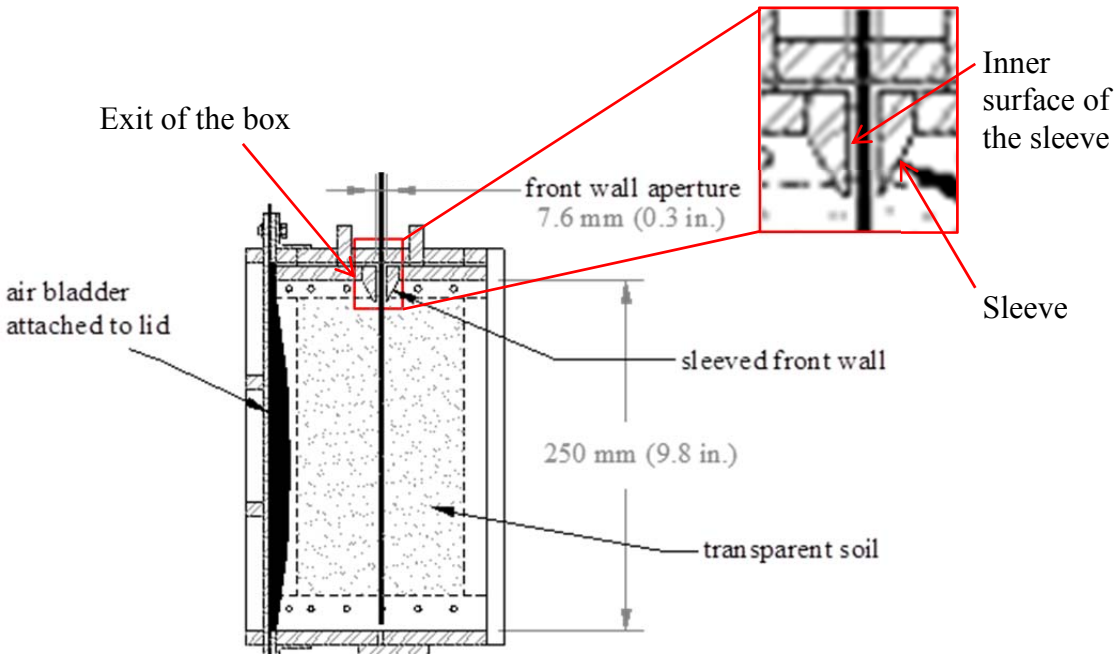


Figure 4.4: Details of the sleeve of the pullout box.

Figure 4.5 presents the results for the pullout test performed with the transparent soil, i.e. crushed fused quartz saturated with the mineral oil mix. The dry unit weight of the transparent soil in this test was 12.7 kN/m3. This corresponds to a RD of 60 %. A lower RD was difficult to achieve because compaction of the fused quartz is facilitated with the presence of the mineral oil mix. The oil lubricates the contact between the particles, thus the mass of fused quartz is densified with minimum compaction effort.

Displacements along the geogrid were monitored at the 5 junctions illustrated in Figure 4.1 by analyzing the images of the geogrid with the PIV program. The distances of the monitored points along the geogrid were similar to the ones in the previous tests (Table 4.2). It is observed in Figure 4.5a that once the pullout force reaches a constant value, it remains steady. Thus, it can be concluded that the oil also lubricates the contact

of the fused quartz along the surfaces of the sleeve when the particles exit the box. As a result, no additional pullout load is generated.

The slip-stick behavior observed in the pullout test with Monterey sand (Figure 4.2) is also observed in the pullout test with the transparent soil (Figure 4.5). However, the slip-stick phenomenon was not observed in the test with fused quartz at the water content of 1.5 % (Figure 4.3). Therefore, it can be concluded that the slip-stick behavior observed in Figure 4.5 is caused by the presence of mineral oil on the contact between fused quartz particles.

This lubrication prevents larger chains of particles from forming that would support the load. As the load increases, the chains of particles slide over each other more easily, thus the slip-stick phenomenon occurring at small pullout loads and displacements. Figure 4.5b shows that slip-stick starts at only 30 % of the maximum pullout force.

Nevertheless, the overall shape of the displacements shown in Figure 4.5 is similar to curves reported in the literature (Farrag et al. 1993, Gupta 2009, Palmeira and Milligan 1989, Ochiai et al. 1996, Teixeira et al. 2007). Additionally, comparison of the results in Figure 4.5 to the results in Figure 4.3 show that saturation of the particles of fused quartz in mineral oil decrease the pullout forces generated throughout a test.

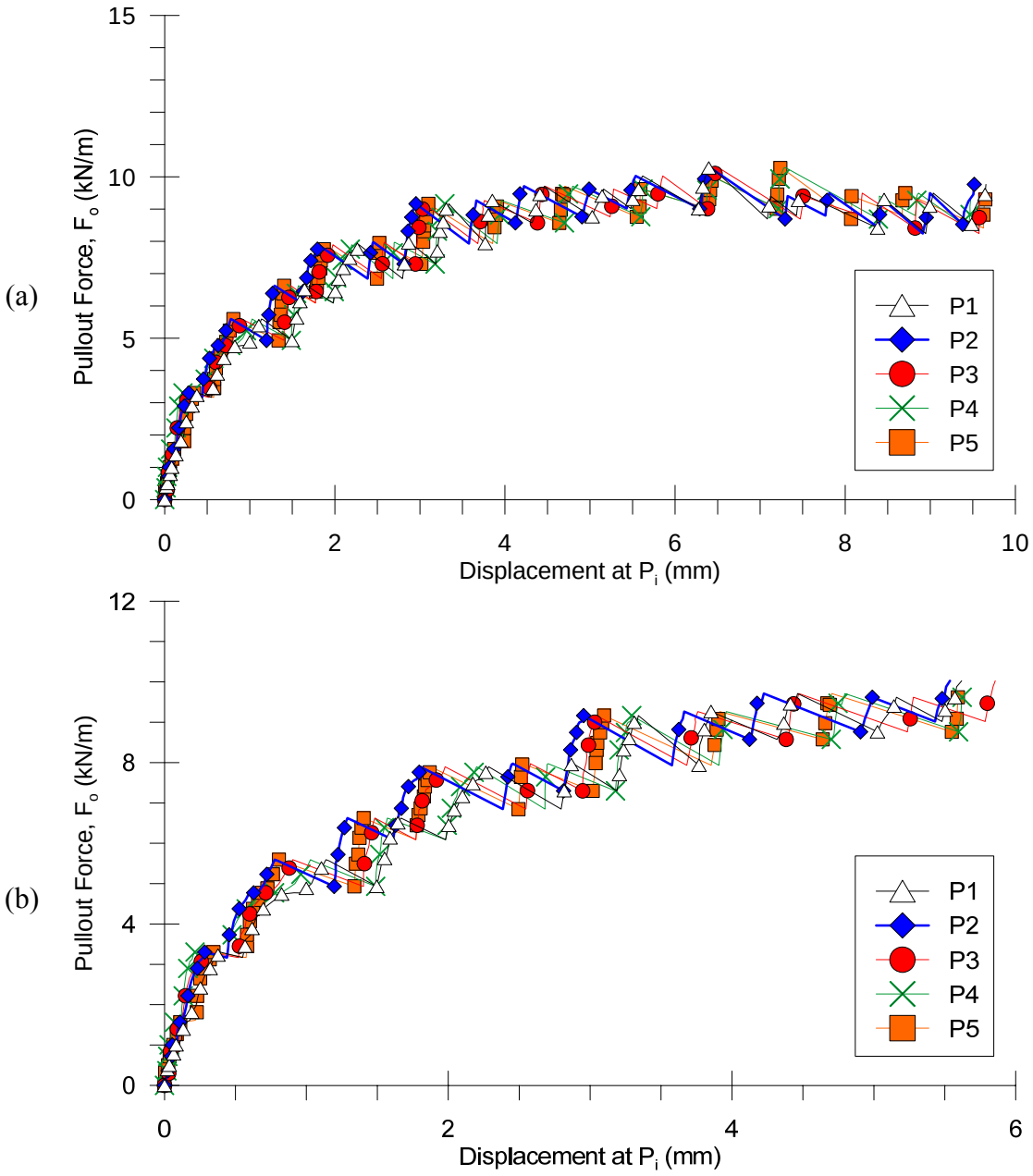


Figure 4.5: Data from small pullout test with fused quartz saturated with the mineral oil mix (transparent soil), geogrid CD and confining pressure of 21 kPa (3 psi): (a) Data from the entire test. (b) View of the data up to 6 mm of displacement.

## 4.3 Transparent Pullout Tests

In this set of pullout tests, the target relative density of the transparent soil and the confining pressure were higher than the values used in the previous set of tests. The transparent soil was compacted with a dry density of 12.9 kN/m$^3$, corresponding to a relative density of 74 %. A confining pressure of 35 kPa (5 psi) was used. The higher density and confining pressure were adopted aiming at inducing larger strains in the geogrid during the tests. Additionally, the geogrid was tested in the MD instead of the CD used in the previous set of tests. This change of the orientation of the geogrid was adopted so that larger deflections in the transverse ribs could be measured. This is because the distance between ribs along the MD is larger than the distance between ribs along the CD for the geogrid product used in this study. Thus, the length between junctions of the ribs perpendicular to the pullout direction is greater when the geogrid is tested on the MD than on the CD.

Five tests were conducted in this series of tests. Each test had a different configuration for the geogrid. In the first test, the geogrid had no transverse ribs. In the second test, the geogrid had one transverse rib. In the third test, the geogrid had two closely spaced transverse ribs. In the fourth test, the geogrid had two largely spaced transverse ribs. In the last test, the geogrid had no modifications, with transverse ribs equally distributed along the entire length of the geogrid. Consequently, the geogrid had eight closely spaced transverse ribs.

### 4.3.1 Test 1: Geogrid With No Transverse Ribs

The geogrid specimen in this test had no transverse ribs. The pullout curves for this test are reported for five junctions distributed along the geogrid in similar pattern

than the previous tests (Figure 4.6). The distances of the measurement points shown in Figure 4.6 along the embedded portion of the geogrid are shown in Table 4.3.

| Monitored point | Distance from the active end of the geogrid | | |
|---|---|---|---|
| | (mm) | (inch) | % L (mm/mm) |
| P1 | 42 | 1.7 | 0.18 |
| P2 | 72 | 2.8 | 0.31 |
| P3 | 130 | 5.1 | 0.56 |
| P4 | 193 | 7.6 | 0.83 |
| P5 | 220 | 8.7 | 0.95 |

Table 4.3: Locations of points of monitored displacements along the geogrid specimen during small pullout testing. Note: L – total length of the geogrid.

This test was conducted until pullout failure was reached. Pullout failure is considered when a maximum value of the pullout force is observed and becomes steady with increasing displacements. In the case of pullout tests with the transparent soil, it is the value of the pullout force on the load recovery in the slip-stick cycles that is used in the failure criterion. Figure 4.7 presents the pullout curves of this test with the pullout force plotted with the displacements of the five points shown in Figure 4.6.

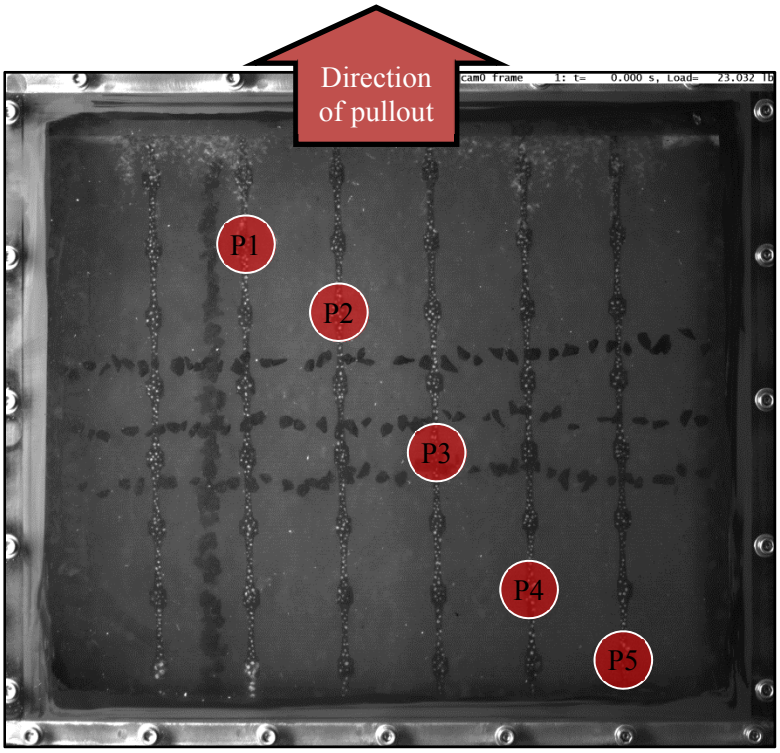


Figure 4.6: Points on the geogrid with reported displacements for traditional pullout curves.

Figure 4.7a is the data for the entire test and Figure 4.7b is the same data but for displacements until 4 mm. It can be observed in Figure 4.7b that the slip-stick phenomenon starts when 50 % of the maximum pullout force is reached. The maximum pullout force develops near 6 mm of displacement is observed for P3.

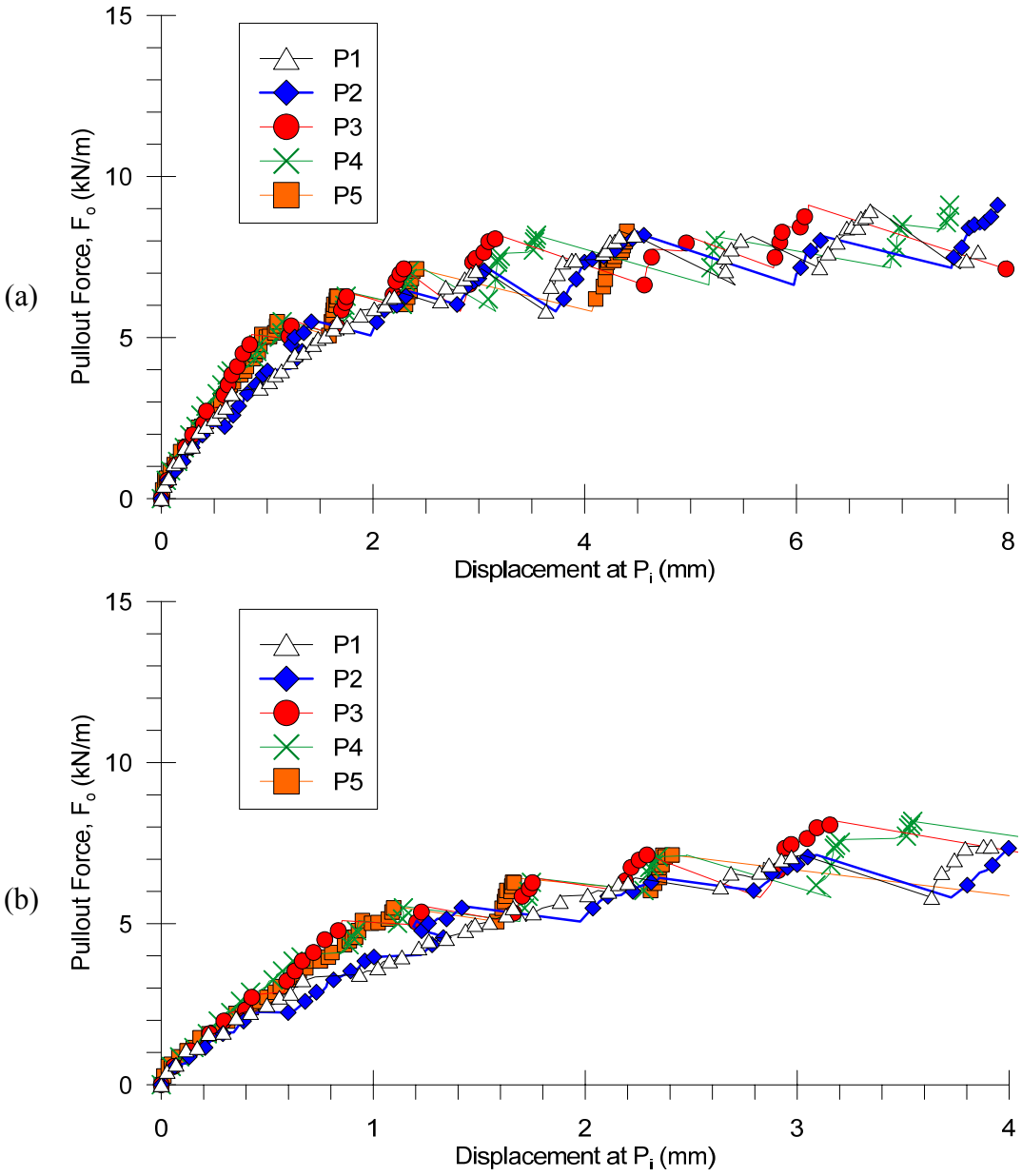


Figure 4.7: Test 1: Data from small pullout test with transparent soil, geogrid MD with no transverse ribs and confining pressure of 35 kPa (5 psi): (a) Data from the entire test. (b) View of the data up to 6 mm of displacement.

### 4.3.2 TEST 2: GEOGRID WITH ONE TRANSVERSE RIB

The geogrid specimen in this test had one transverse rib located near the middle of the specimen at 0.46L. The pullout curves for this test are reported for five junctions distributed along the geogrid in similar pattern than the previous test (Figure 4.6). The distances of the measurement points along the embedded portion of the geogrid are similar to ones in the previous test (Table 4.3).

This test was conducted until breakage of the geogrid occurred in the confined portion of the geogrid, at the junction of the longitudinal rib L5 closest to the exit of the box. This failure of the geogrid specimen was unexpected since it occurred for a maximum value for the pullout force of 10.5 kN/m. This is only 80% of the ultimate tensile strength of 13.1 kN/m measured in the tensile strength tests reported in Chapter 3.5.1.2 (see Figure 3.18). Moreover, if the pullout force would have reached a value near 13 kN/m, the breakage of the geogrid would be expected to occur in the portion outside of the pullout box, where the geogrid is unconfined.

A picture of the geogrid specimen retrieved after the test is presented in Figure 4.8 with a close view of the failed junction. This figure shows that the entire row of junctions closest to the exit of the box in the confined portion of the geogrid experienced large plastic deformations. Similar failures and patterns of deformations were observed in these junctions in Tests 3 and 4. The failures in the row of junctions closest to the exit of the box, and not in junctions further away, is because the loads are higher near the active end of the geogrid, where the pullout force is applied. The premature failure of these junctions may be explained by the combination of several factors.

First, the strength and stiffness of the junctions may be smaller than the strength and stiffness of the ribs due, to the manufacturing process of this geogrid. The first step in the process is to produce a sheet of polypropylene, which is then punched and drawn in

two perpendicular directions (Koerner 2012), giving form to the geogrid. Drawing induces the alignment of molecules and segments of molecules in the direction parallel to the stresses generated (Hertzberg et al. 2012). As a consequence, the stiffness and strength of the polypropylene in the ribs of the geogrid significantly increase (Koerner 2012, Hertzberg et al. 2012).

However, alignment of the molecules and segments of molecules does not occur in the junctions of the geogrid in the same manner as in the ribs. This is because the junctions are where the perpendicular ribs of the geogrid are connected. Thus, alignment of the molecules in the junctions in one direction is constrained by the connection to the rib in the perpendicular direction. As a result, the stiffness and strength and lower in the junctions than in the ribs. Consequently, the junctions are the weak points in the geogrid. Moreover, cutting the transverse ribs eliminates the constraint on the junctions due to the connection to the transverse ribs.

Second, cutting transverse ribs allows for more heterogeneity in the loads applied to each longitudinal rib due to material variability intrinsic to the manufacturing process. The presence of transverse ribs improves the distribution of the loads among longitudinal ribs because the transverse ribs connect the longitudinal ribs. Thus, the probability of a concentration of loads in a longitudinal rib increases as the number of transverse ribs decreases. This concentration of loads can lead to the premature failure of a rib.

Finally, the junctions of the geogrid may be more susceptible to piercing by the sharp particles of fused quartz than the ribs. This is due to the greater thickness of the junctions in relation to the ribs. As the geogrid moves, the particles of fused quartz may slide along the ribs, but get momentarily trapped where the rib ends and the junction starts. As a consequence, the particles of fused quartz are thrust against the surface of the junction thus piercing the geogrid and inducing failure of the geogrid at the junction.

Figure 4.9 presents the pullout curves of this test with the pullout force plotted with the displacements of the five points in similar positions as shown in Figure 4.6. Figure 4.9a is the data for the entire test and Figure 4.9b is the same data but for displacements until 4 mm. It can be observed in Figure 4.9a that the maximum pullout force is reached at 3.5 mm of displacement of P3, before breakage of the junction in L5 at displacements of 6.5 mm. The slip-stick phenomenon starts at near 45 % of the maximum pullout force (Figure 4.9b).

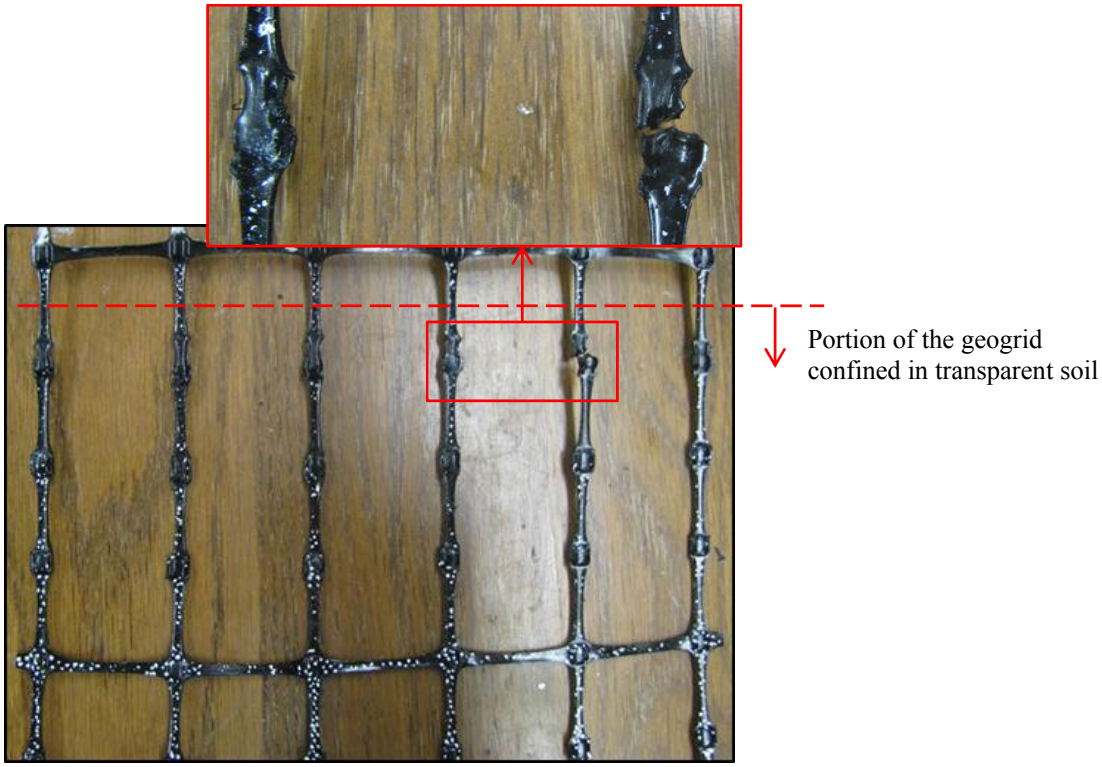


Figure 4.8: Test 2: geogrid retrieved after the test showing breakage at the junction of L5 closest to the exit of the box.

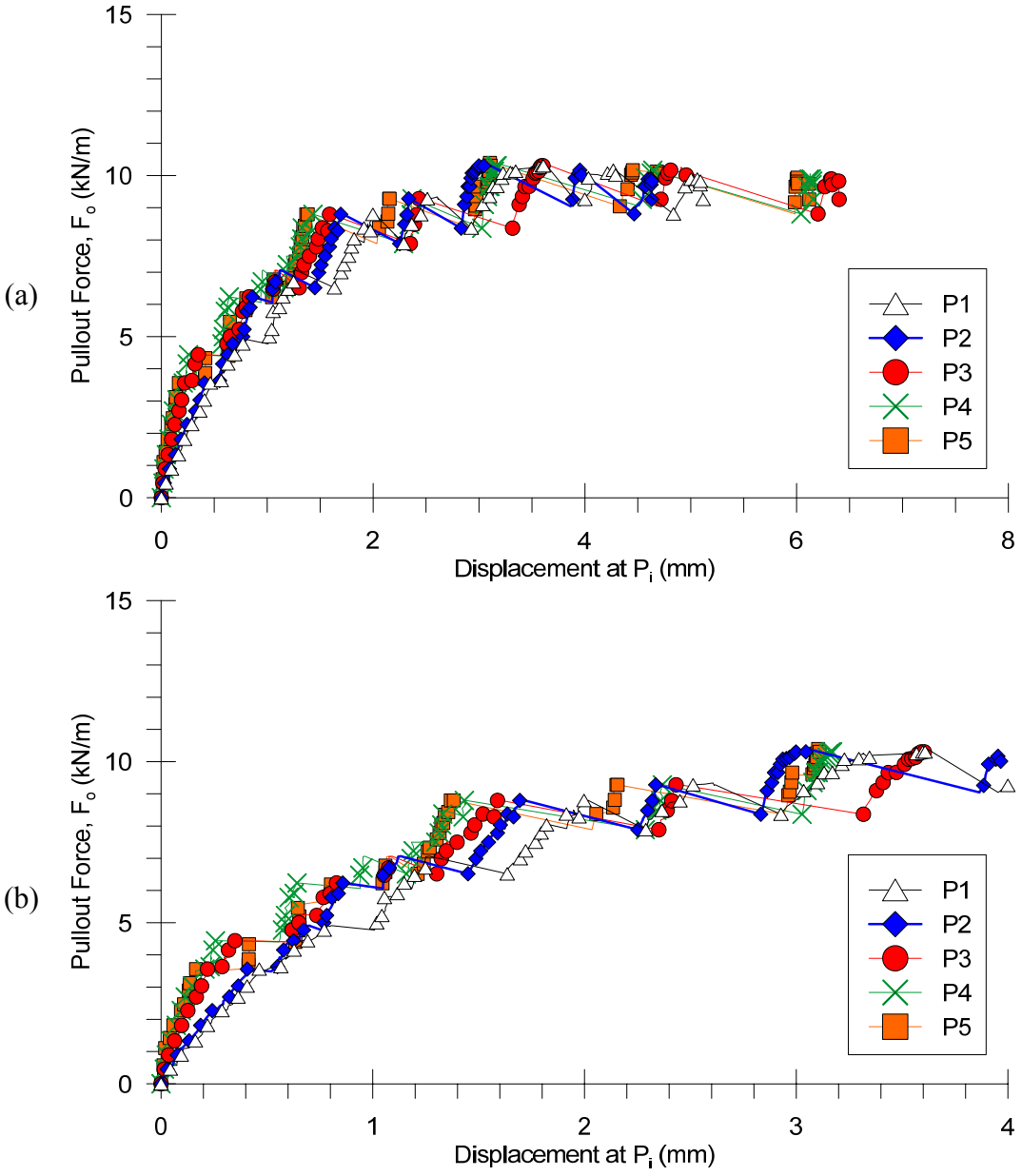


Figure 4.9: Test 2: Data from small pullout test with transparent soil, geogrid MD with one transverse rib and confining pressure of 35 kPa (5 psi): (a) Data from the entire test. (b) View of the data up to 6 mm of displacement.

### 4.3.3 TEST 3: GEOGRID WITH TWO CLOSELY SPACED TRANSVERSE RIBS

The geogrid specimen in this test had two closely spaced transverse ribs, 21 mm apart. This is the original aperture size of the geogrid along the machine direction. The ratio aperture size over the $D_{50}$ of the soil is 5.5 for the region between the transverse ribs. The first transverse rib is located at 0.35L. The second transverse rib is located at 0.46L, which is the same location of the transverse rib in Test 2. The pullout curves for this test are reported for five junctions distributed along the geogrid in similar pattern than the previous tests (Figure 4.6). The distances of the measurement points along the embedded portion of the geogrid are similar to ones in the previous test (Table 4.3).

This test was conducted until breakage of the geogrid occurred in the embedded portion of the geogrid, at the junction of the longitudinal rib L3 closest to the exit of the box. The geogrid specimen was retrieved after the test for inspection of the geogrid. The breakage occurred in similar fashion as it occurred in Test 2 (Figure 4.8). The only difference is that the failure was in L3 in Test 3 and in L5 in Test 2. Similar to Test 2, the entire row of junctions closest to the exit of the wall embedded in soil experienced large plastic deformations.

Figure 4.10 presents the pullout curves of this test with the pullout force plotted with the displacements of the five points in similar positions as shown in Figure 4.6. Figure 4.10a is the data for the entire test and Figure 4.10b is the same data but for displacements until 4 mm. It can be observed in Figure 4.10a that the maximum pullout force is reached near 3.0 mm of displacement of P3, before breakage of the junction in L3 at 5.5 mm of displacements. The slip-stick phenomenon starts at near 30 % of the maximum pullout force (Figure 4.10b).

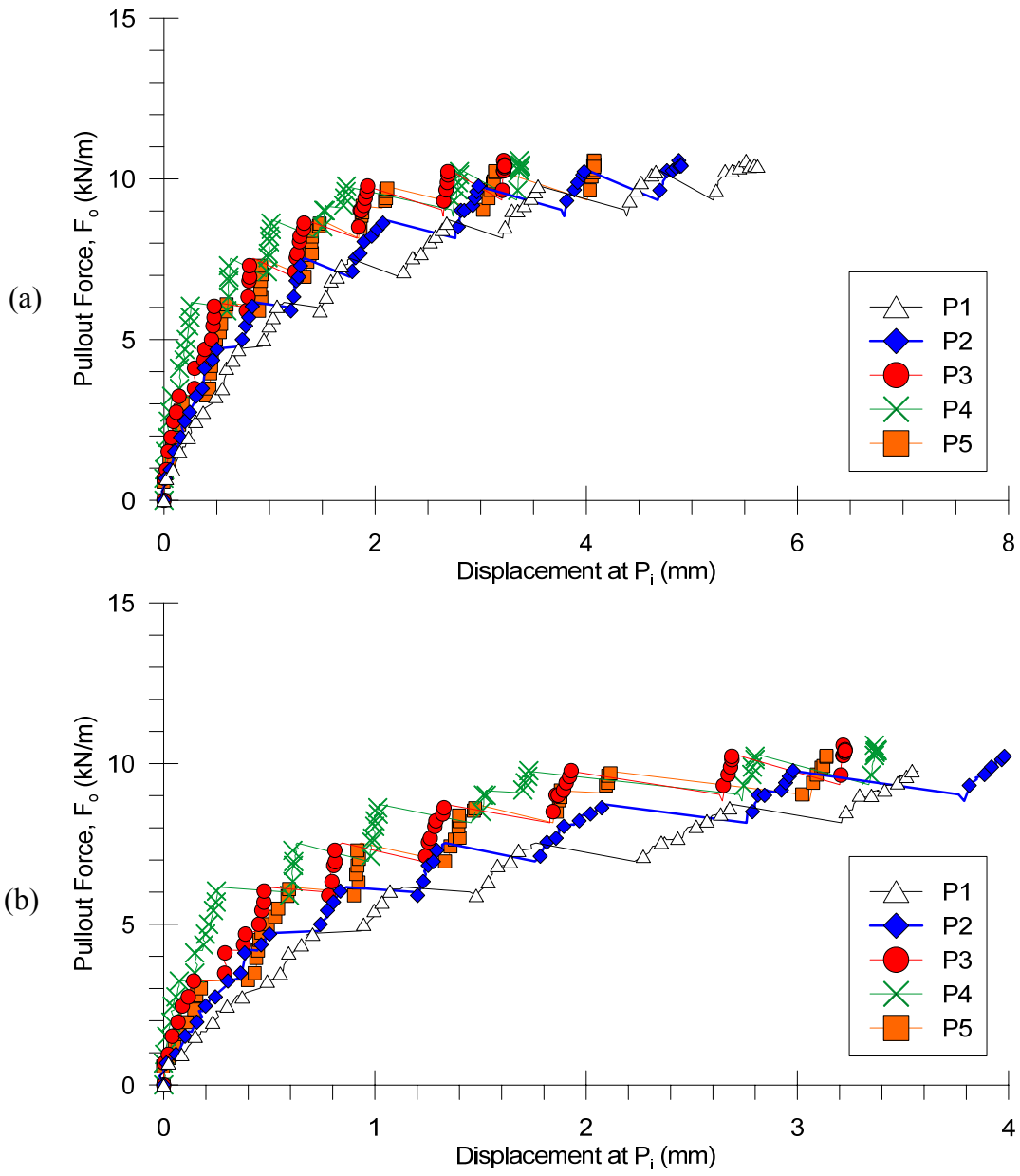


Figure 4.10: Test 3: Data from small pullout test with transparent soil, geogrid MD with two closely spaced transverse ribs and confining pressure of 35 kPa (5 psi): (a) Data from the entire test. (b) View of the data up to 6 mm of displacement.

### 4.3.4 TEST 4: GEOGRID WITH TWO LARGELY SPACED TRANSVERSE RIBS

The geogrid specimen in this test had two largely spaced transverse ribs, 49 mm apart. The ratio aperture size over the $D_{50}$ of the soil is 12.9 in the region between the transverse ribs. The first transverse rib is located at 0.34L, the same position of the first transverse rib in Test 3. The second transverse rib is located at 0.58L. The pullout curves for this test are reported for five junctions distributed along the geogrid in similar pattern than the previous tests (Figure 4.6). The distances of the measurement points along the embedded portion of the geogrid are similar to ones in the previous test (Table 4.3).

This test was conducted until breakage of the geogrid occurred in the embedded portion of the geogrid, at the junction of the longitudinal rib L2 closest to the exit of the box. The geogrid specimen was retrieved after the test for inspection of the geogrid. The breakage occurred in similar fashion as occurred in Tests 2 and 3 (Figure 4.8). The only difference is that the failure was in L2 in Test 4, in L3 in Test 3, and in L5 in Test 2. Similar to Tests 2 and 3, the entire row of junctions closest to the exit of the wall embedded in soil experienced large plastic deformations. The random location of the failed junctions confirms that the action of cutting off transverse ribs from the geogrid creates weak spots at the junctions. The junction that fails is determined by heterogeneities intrinsic to the production of the geogrid itself, not by damage from a specific sharp point in the sleeve of the pullout box.

Figure 4.11 presents the pullout curves of this test with the pullout force plotted with the displacements of the five points in similar positions as shown in Figure 4.6. Figure 4.11a is the data for the entire test and Figure 4.11b is the same data but for displacements until 4 mm. The shape of the curves in Figure 4.11a suggests that the maximum pullout force was not achieved before breakage of the junction in L2 at

displacement of 3.5 mm. The slip-stick phenomenon starts at a pullout force of 5 kN/m (Figure 4.11b), 50 % of the pullout force when breakage of the junction in L2 occurred.

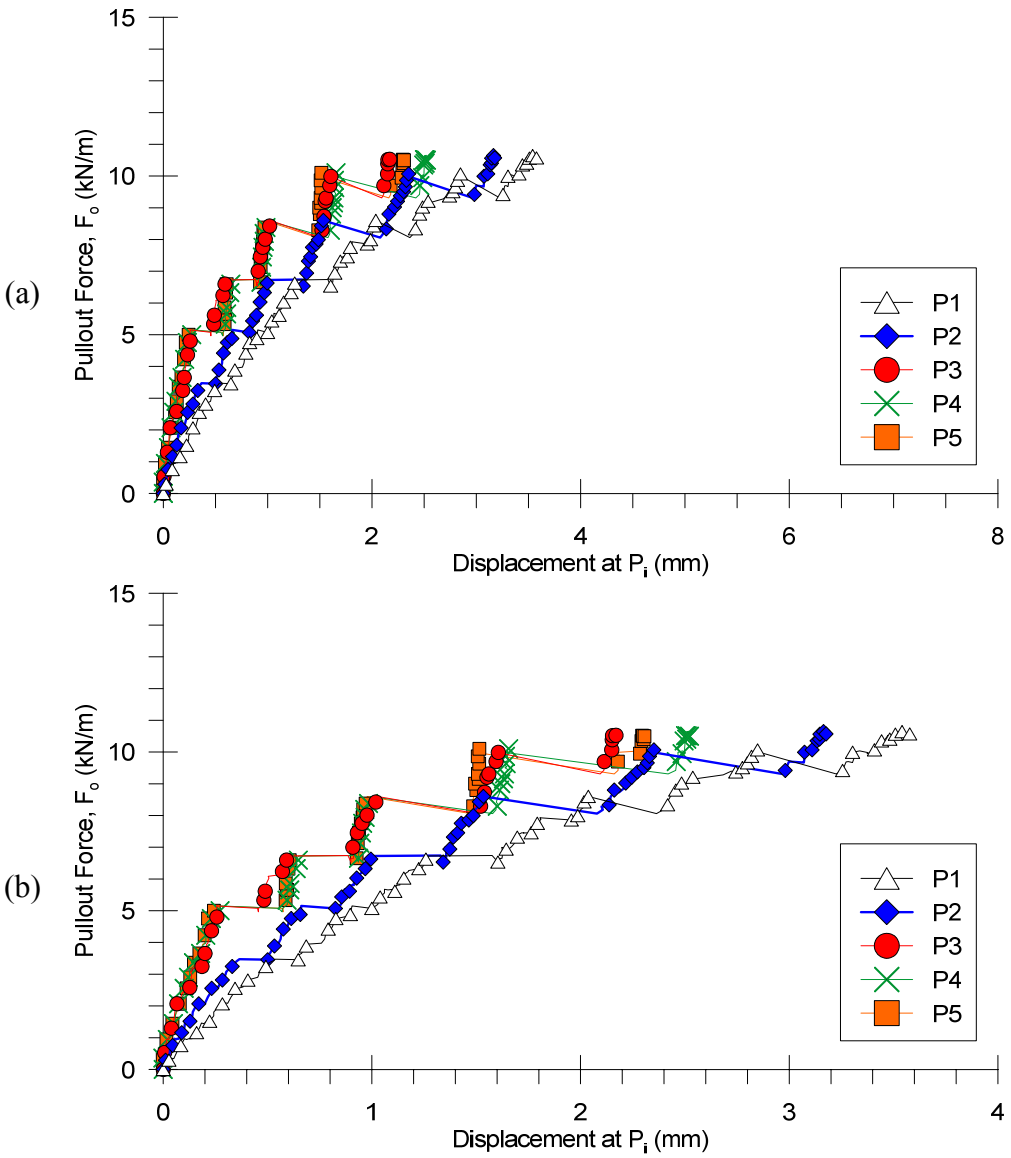


Figure 4.11: Test 4: Data from small pullout test with transparent soil, geogrid MD with two largely spaced transverse ribs and confining pressure of 35 kPa (5 psi): (a) Data from the entire test. (b) View of the data up to 6 mm of displacement.

### 4.3.5 TEST 5: GEOGRID WITH EIGHT CLOSELY SPACED TRANSVERSE RIBS

The geogrid in this test was used with no modifications. The transverse ribs were present along the entire length of the geogrid specimen with its original aperture size of 21 mm between transverse ribs. The ratio aperture size over the $D_{50}$ of the soil is 5.5. The geogrid in this test has a total of eight transverse ribs. The pullout curves for this test are reported for five junctions distributed along the geogrid in similar pattern than the previous tests (Figure 4.6). The distances of the measurement points along the embedded portion of the geogrid are similar to ones in the previous test (Table 4.3).

This test was conducted until failure of the geogrid outside the pullout box (Figure 4.12). The breakage of the geogrid occurred at a pullout force of 12.2 kN/m in the unconfined portion of the specimen as opposed to the breakages in the confined portion occurred in Tests 2 to 4 (Figure 4.8). The location of the failure of the geogrid observed in Test 5 is the one that would be expected since no transverse ribs were cut off of the geogrid: in the unconfined portion of the geogrid specimen at values of pullout force near the ultimate tensile strength of the geogrid of 13 kN/m.

Figure 4.13 presents the pullout curves of this test with the pullout force plotted with the displacements of the five points in similar positions as shown in Figure 4.13. Figure 4.13a is the data for the entire test and Figure 4.13b is the same data but for displacements until 4 mm. The shape of the curves in Figure 4.13a suggests that the maximum pullout force was not achieved before breakage of the geogrid at displacements of 3.5 mm. The slip-stick phenomenon starts at a pullout force of 5 kN/m (Figure 4.11b), 40 % of the pullout force when breakage of the geogrid occurred.

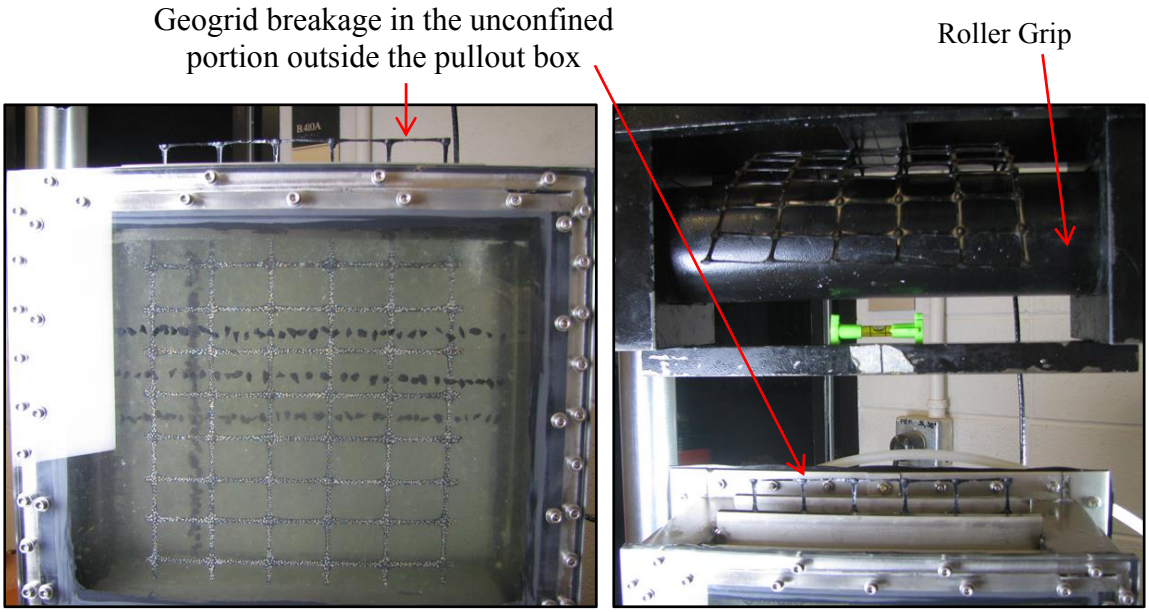


Figure 4.12: Test 5: Geogrid breakage during pullout test: (a) View of the unconfined (outside the pullout box) and confined (embedded in the transparent soil) portions of the geogrid. (b) View of the entire unconfined portion of the geogrid.

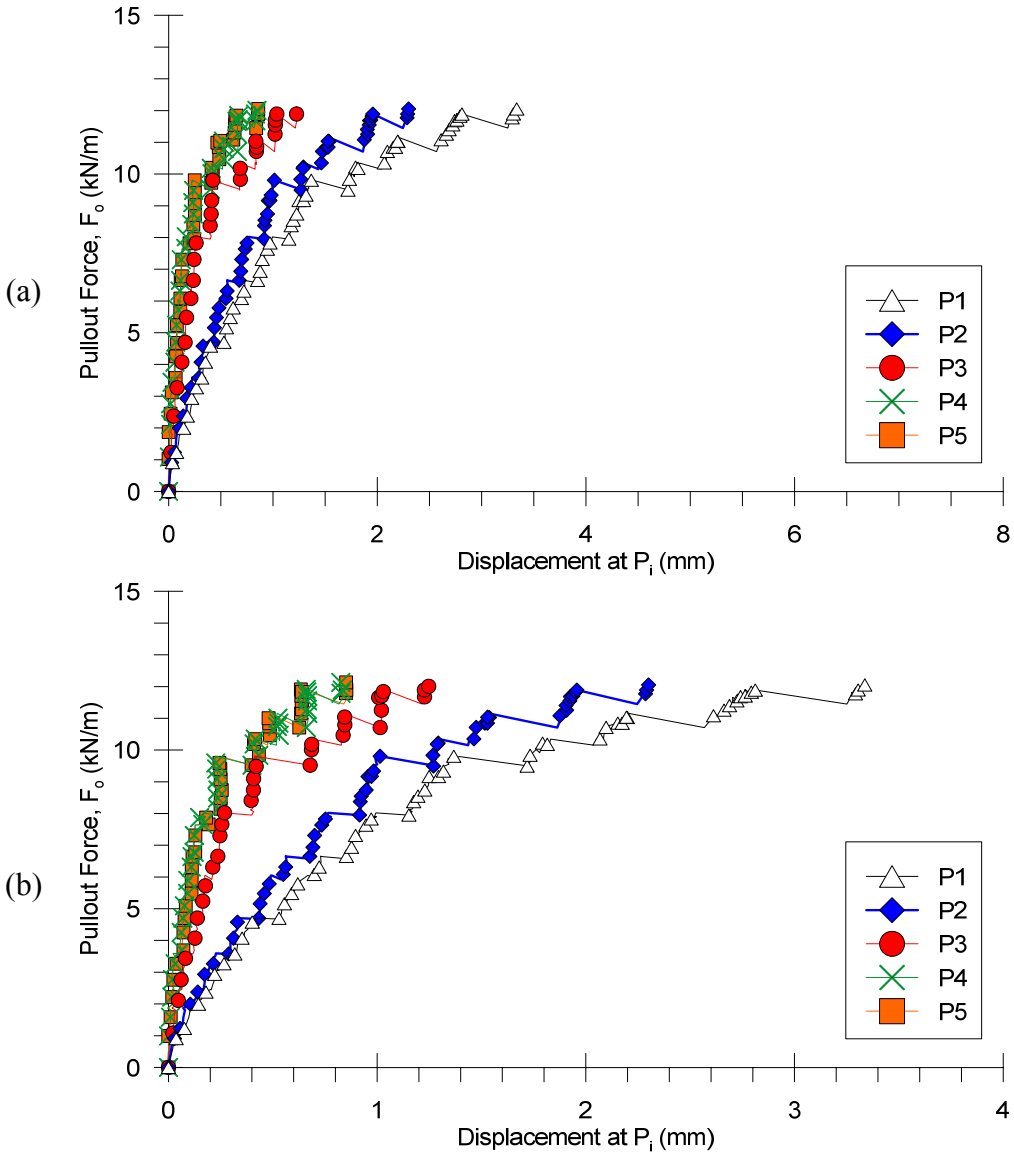


Figure 4.13: Test 5: Data from small pullout test with transparent soil, geogrid MD with eight closely spaced transverse ribs and confining pressure of 35 kPa (5 psi): (a) Data from the entire test. (b) View of the data up to 6 mm of displacement.

## 4.4 Procedure for Fitting the Data of Displacement Profiles and Calculating Strains along Geogrid Specimens

Displacement profiles along the geogrid specimens in the transparent pullout tests were obtained with PIV calculations. These displacement data were found to be well explained by using an exponential equation. The derivative of the exponential equation provided the calculated strains along the geogrid specimens.

The displacement data from L3 in Test 5 were first used in the data fitting process because these are the best quality data, with points close to the active end of the geogrid. However, Test 5 was the one with the smallest displacements observed. Thus, data from L3 in Test 4 were also used in the data fitting process to choose the best equation that describes the measured displacements. Several equations were plotted with the data in Figure 4.14 and Figure 4.15 in order to determine which equation is the best candidate. The equation chosen to fit the displacement data of all transparent pullout tests is the following exponential equation:

$$y = \alpha + \beta e^{(-x/\gamma)} \tag{4.1}$$

Where $x$ is any point along the geogrid length (L) and $\alpha$, $\beta$, and $\gamma$ are the experimental parameters to be determined. The values of $x$ are normalized to the length of the geogrid specimen $L$. Thus, $x$ varies from 0 to 1, where $x$ equals to zero is the active end of the geogrid, which is the point closest the exit of the pullout box. Where $x$ equals to one is the passive end of the geogrid, which is the point furthest away from the exit of the box.

Equation 4.1 was chosen using three criteria. First, the equation meets the boundary conditions of the pullout tests conducted in this study. Since the passive end of the geogrid ($x$ = 1.00L) is free to move, the strain of the geogrid at $x$ = 1.00L must be

zero. Thus, the derivative of the equation at this value of *x* must be zero. Consequently, the plot of the equation needs to be horizontal or near horizontal at *x* = 1.00L.

Second, the equation needs to intersect the y-axis. This is because the strains at the active end of the geogrid are limited to the strains at the ultimate tensile strength of the material as shown in Figure 3.17. Thus, equations with a power form ($y = \alpha x^{-\beta}$), reciprocal form ($y = \alpha + \beta/x$) and logarithmic form ($y = \alpha + \beta \cdot \log(x)$) were excluded since the value of *y* at *x* = 0 tends to infinite in these equations.

Third, the equation needs to be simple enough so that an equation for the derivative can be found. Additionally, preference was given to equations that could be linearized in order to facilitate the evaluation of the equation for the best fit for a regression model.

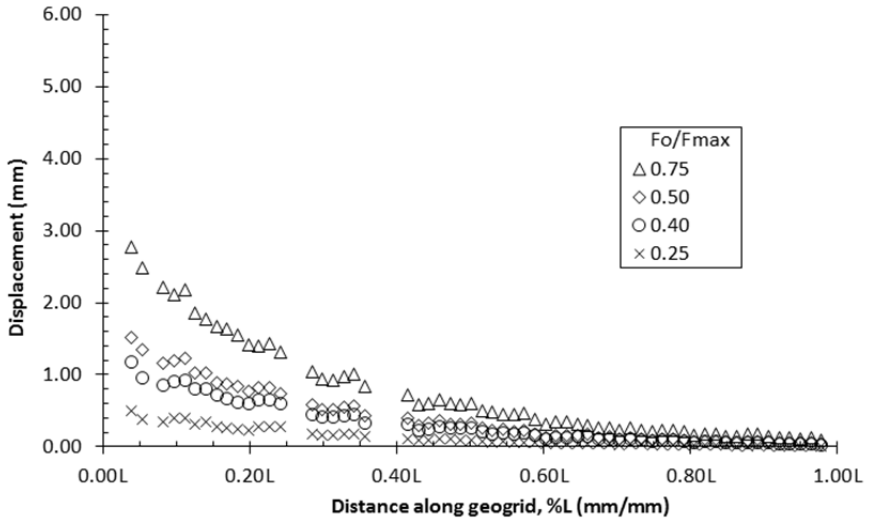


Figure 4.14: Data from displacements along longitudinal rib L3 in Test 5.

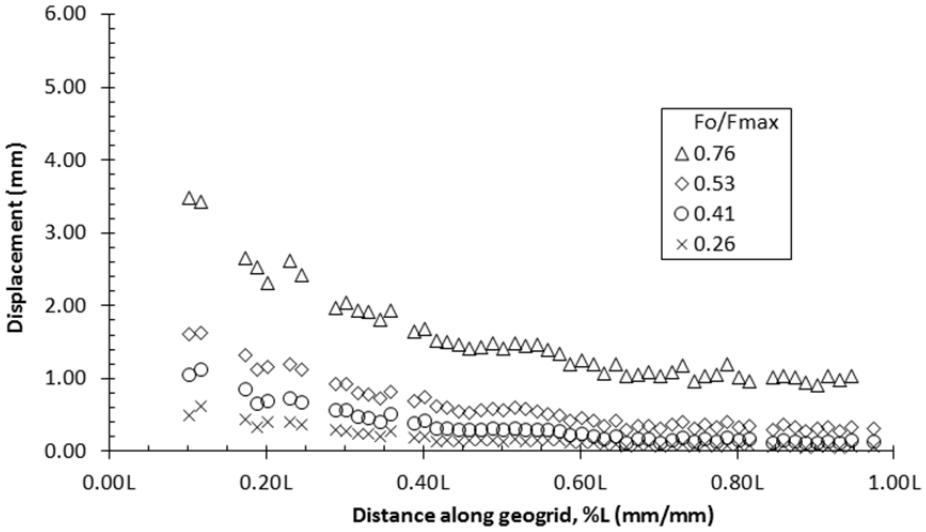


Figure 4.15: Data from displacements along longitudinal rib L3 in Test 3.

It can be noted in Equation 4.1 that the parameter $\alpha$ controls the distance of the curve from the *x*-axis. The parameter $\beta$ controls the inclination of the entire curve. The parameter $\gamma$ controls the concavity of the curve.

The procedure followed to find the parameters to fit Equation 4.1 to the data shown in Figure 4.14 involves a transformation of the horizontal axis, so that Equation 4.1 becomes linear. The transformation of the horizontal axis is as follows:

$$x' = e^{(-x/\gamma)} \tag{4.2}$$

Thus, Equation 4.1 becomes:

$$y = \alpha + \beta\, x' \tag{4.3}$$

Accordingly, parameters $\alpha$ and $\beta$ can be found with Equation 4.3 by fitting a straight line to the data plotted against the transformed horizontal axis *x'*. However, the parameter $\gamma$ is inherent to *x'*. Consequently, the solution to find the values of $\alpha$, $\beta$, and $\gamma$

that provides the best fit is iterative. The best fit was evaluated using the method of the least squares. The following steps were adopted to find the best fit for the parameters $\alpha$, $\beta$, and $\gamma$:

1. Adopt initial values for $\alpha$, $\beta$, and $\gamma$ and plot $y$ against $x'$.
2. Calculate $\sum(y_i - \hat{y}_i)^2$ , where $y_i$ is a data point and $\hat{y}_i$ is the predicted value for the data point.
3. Use the tool "solver" in Microsoft® Excel to minimize $\sum(y_i - \hat{y}_i)^2$ by changing the values of $\alpha$, $\beta$, and $\gamma$.
4. Plot a straight line to fit the data in the plot of $y$ against $x'$.
5. Visually inspect whether the data falls into a straight line and check the value of the coefficient of determination $r^2$.
6. Adopt different values for $\alpha$, $\beta$, and $\gamma$ than the values used in Step 1.
7. Repeat Steps 2 to 5 and check whether the new solution by "solver" converges to the same values found in Step 3.

Steps 6 and 7 are necessary because the "solver" tool in Excel is an algorithm that finds a local optimum for the problem being analyzed (Fylstra et al. 1998). Thus, it is necessary to use different starting values for $\alpha$, $\beta$, and $\gamma$ to verify whether the solution provided by "solver" converged to the most probable best solution (i.e. the global optimum). The solution given by "solver" can also be verified by comparing the values of $\alpha$ and $\beta$ provided by "solver" to the coefficients $m$ and $n$ of a regression line $y = n + mx'$ for the data plotted in $y$ vs. $x'$. If the best solution is found, then the value of $\alpha$ provided by "solver" should be the same as $n$, and the value of $\beta$ should be the same as $m$. This was the case when the best fit was for positive values of $\alpha$ as shown in Figure 4.16.

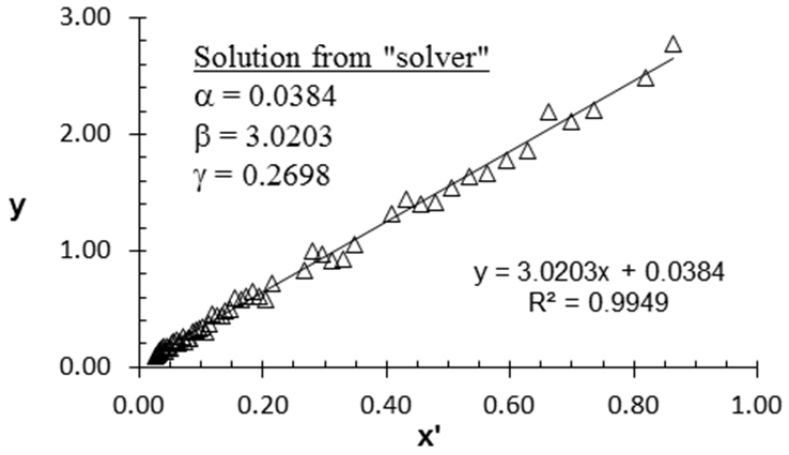


Figure 4.16: Example of solution obtained with the "solver" tool in Microsoft® Excel when the least squares are found ($\alpha$ and $\beta$ coincide with the coefficients of the regression line).

However, "solver" does not find the best solution for the least squares when the value of $\alpha$ for the best fit is negative. In this case, the value of $\alpha$ returned by "solver" is zero. Also, the values of $\alpha$ and $\beta$ do not coincide with the values of *n* and *m* as shown in Figure 4.17.

For the example shown in Figure 4.17, the value of $\sum(y_i - \hat{y}_i)^2$ with the coefficients $\alpha$ and $\beta$ provided by "solver" is 0.074 mm$^2$. The value of $\sum(y_i - \hat{y}_i)^2$ decreases to 0.073 mm$^2$ when $\alpha$ and $\beta$ are replaced with the values of *n* and *m* provided by the regression line. Small decreases of $\sum(y_i - \hat{y}_i)^2$ such as the one in the example above were observed for all instances when the solution provided by "solver" had $\alpha$ equal to zero. It was observed that, although negative, the values of *n* were always close to zero. Consequently, replacing the values of $\alpha$ with the values of *n* still resulted in predicted values of $y_i$ equal to or larger than zero for $x$ = 1.00L.

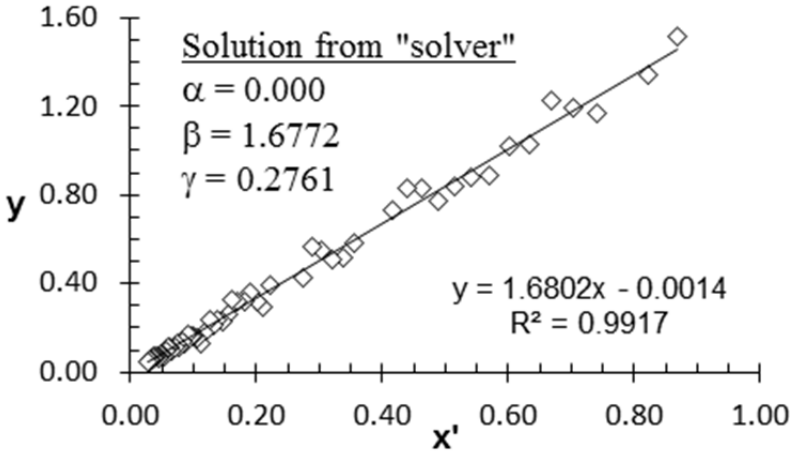


Figure 4.17: Example of solution obtained with the "solver" tool in Microsoft® Excel when the least squares are not found ($\alpha$ and $\beta$ do not coincide with the coefficients of the regression line).

Figure 4.18 and Figure 4.19 show the curves fitted to the data in the examples shown in Figure 4.14 and Figure 4.15 using the procedure described above. The solid lines of different colors are the curves fitted to data of different percentages of the maximum pullout force. The dashed lines are the extrapolation of these curves to the intersection with the y-axis.

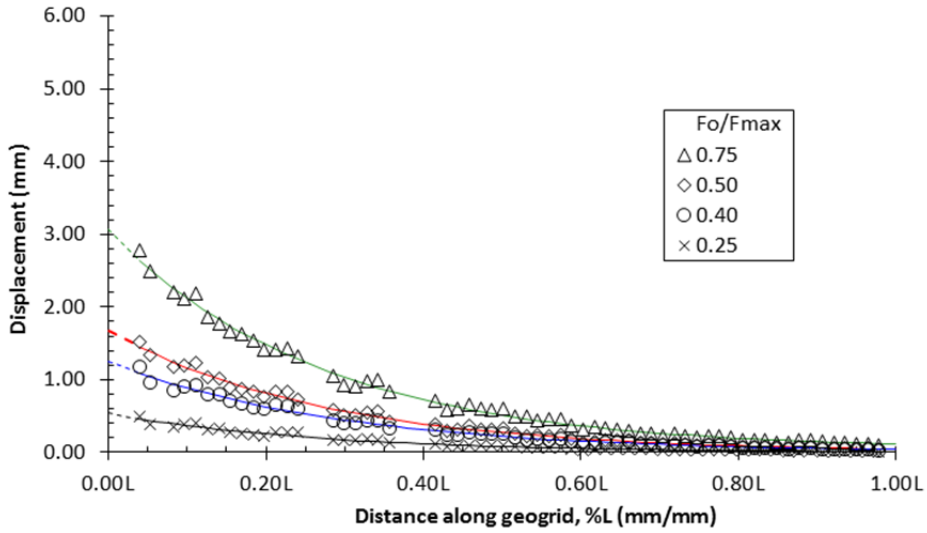


Figure 4.18: Curves fitted to the data shown in Figure 4.14.

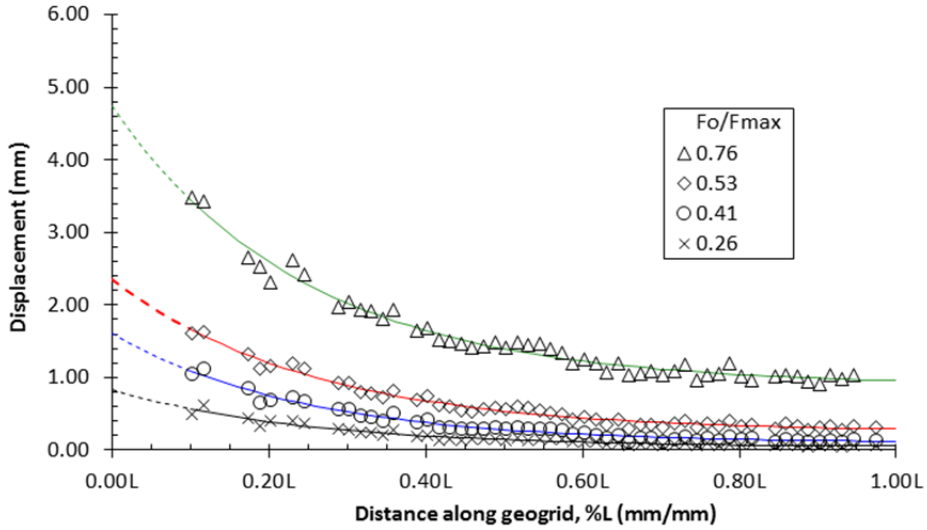


Figure 4.19: Curves fitted to the data shown in Figure 4.15.

Larger errors may exist in the curves fitted to the displacement data in Figure 4.19 than in Figure 4.18. This is due to the lack of data points in Figure 4.19 near the origin of the horizontal axis, which is the active end of the geogrid. Data points in this region have

significant influence in determining the parameter $\gamma$ in Equation 4.1, which determines the curvature of the model fit.

The residual plots of the fitted curves in Figure 4.18 and Figure 4.19 are shown in Figure 4.20 and Figure 4.21, respectively. In the residual plots, the residual $y - \hat{y}_i$ is plotted on the vertical axis against predicted displacement, $\hat{y}_i$, on the horizontal axis. It can be observed in Figure 4.20 and Figure 4.21 that the residuals increase with displacements, showing the importance of the data points near the active end of the geogrid.

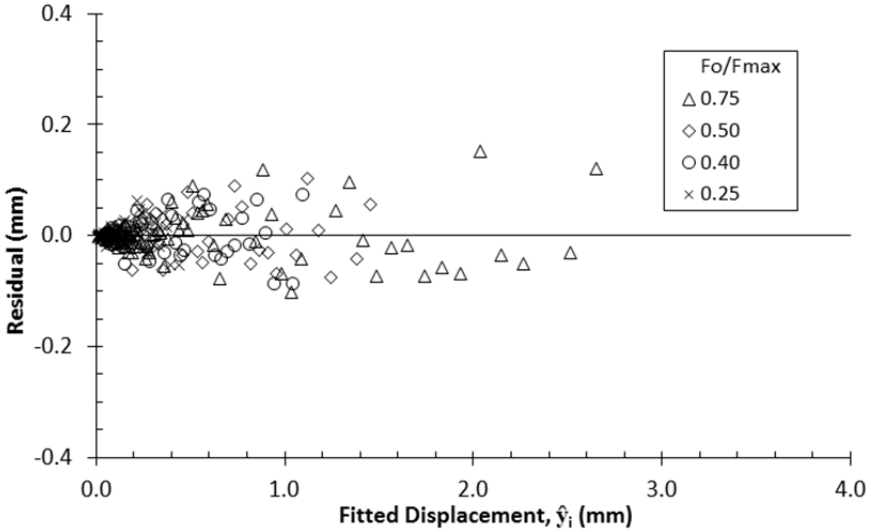


Figure 4.20: Residuals plot of the fitted curves in Figure 4.18.

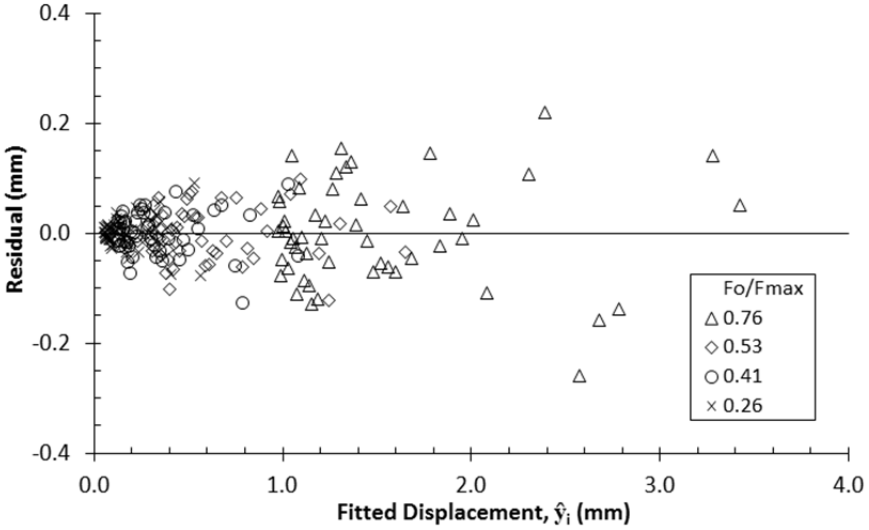


Figure 4.21: Residuals plot of the fitted curves in Figure 4.19.

The next step in the analysis is to calculate the strains along the geogrid at the different percentages of the maximum pullout force. Strains are obtained with the derivative of Equation 4.1:

$$\frac{dy}{dx} = \frac{d}{dx}\left(\alpha + \beta \cdot e^{(-x/\gamma)}\right) = 0 + \beta \frac{d}{dx}\left(e^{(-x/\gamma)}\right) \tag{4.4}$$

Applying the chain rule in Equation 4.4 leads to the following solution:

$$\frac{dy}{dx} = \beta \cdot e^{(-x/\gamma)} \cdot \frac{d}{dx}\left(-\frac{1}{\gamma}x\right) = -\frac{\beta}{\gamma}e^{(-x/\gamma)} \tag{4.5}$$

The derivative of Equation 4.1 is negative as shown in Equation 4.5. However, the geogrid deforms in tension in the pullout tests used in this study. Convention in engineering assigns a positive sign to tensile strains in geosynthetic materials. Consequently, the sign of Equation 4.5 was inverted to follow convention and the tensile strains, $\varepsilon$, along the geogrid were calculated using the following equation:

$$\varepsilon = \frac{\beta}{\gamma} e^{(-x/\gamma)} \tag{4.6}$$

The strain distributions calculated with Equation 4.6 from the data fitted in Figure 4.18 and Figure 4.19 are shown in Figure 4.22 and Figure 4.23, respectively. The derivative of Equation 4.6 provides the rate that the strains along the geogrid change (i.e. strain gradient). Equation 4.7 is the derivative of Equation 4.6:

$$\Delta\varepsilon = -\frac{\beta}{\gamma^2} e^{(-x/\gamma)} \tag{4.7}$$

The strain gradients obtained from the strain distributions in Figure 4.22 are shown in Figure 4.24. These plots facilitate comparisons of how much the strains vary along the geogrid for the different configurations used in the pullout tests performed in this study.

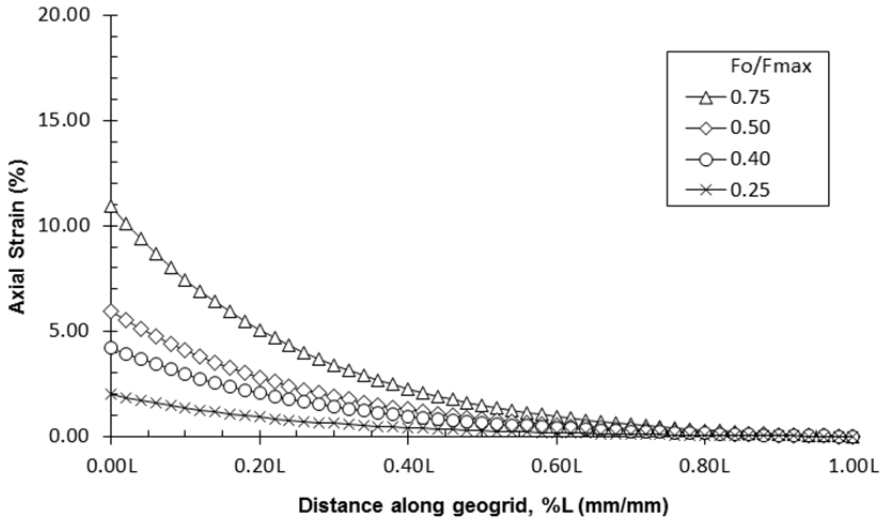


Figure 4.22: Strain distribution along the geogrid calculated from the curves fitted to the displacement data in Figure 4.18.

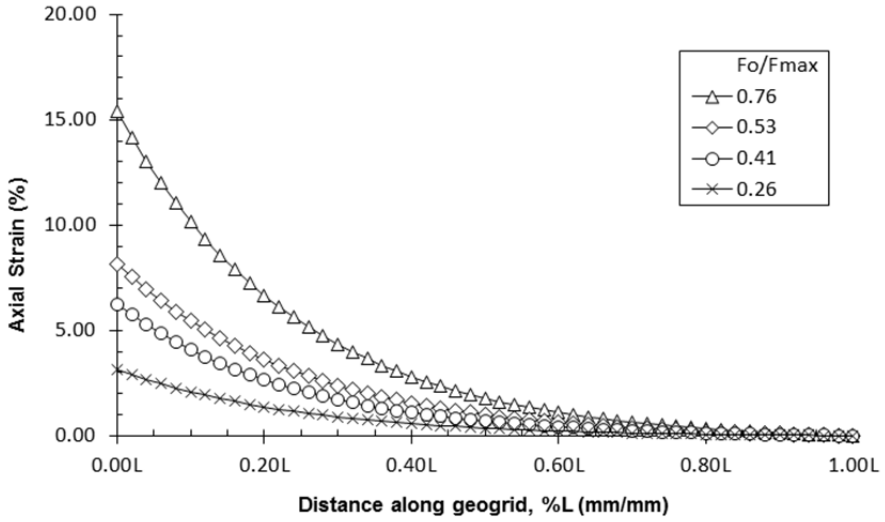


Figure 4.23: Strain distribution along the geogrid calculated from the curves fitted to the displacement data in Figure 4.19.

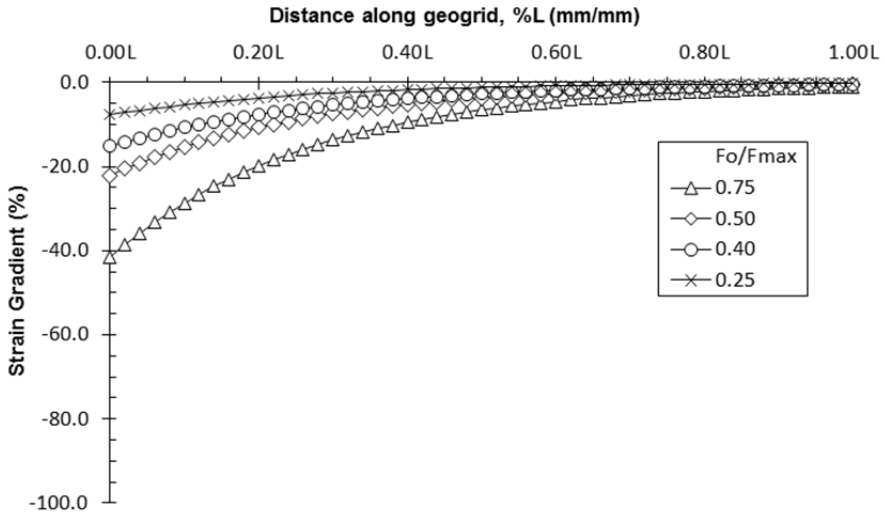


Figure 4.24: Strain gradient obtained from the strains calculated in Figure 4.22.

## 4.5 Source of errors in the PIV calculations and data fitting

Additional errors in the PIV calculations arise from the white dots painted on the geogrid starting to unbind from it during the pullout tests. This occurs due to friction between particles of fused quartz and the surface of the geogrid. Fused quartz particles are angular and scratch the white dots when the geogrid moves. Also, the presence of mineral oil weakens the bond between the white dots and the geogrid. Figure 4.25 shows an example of a white dot unbinding from the geogrid during a pullout test.

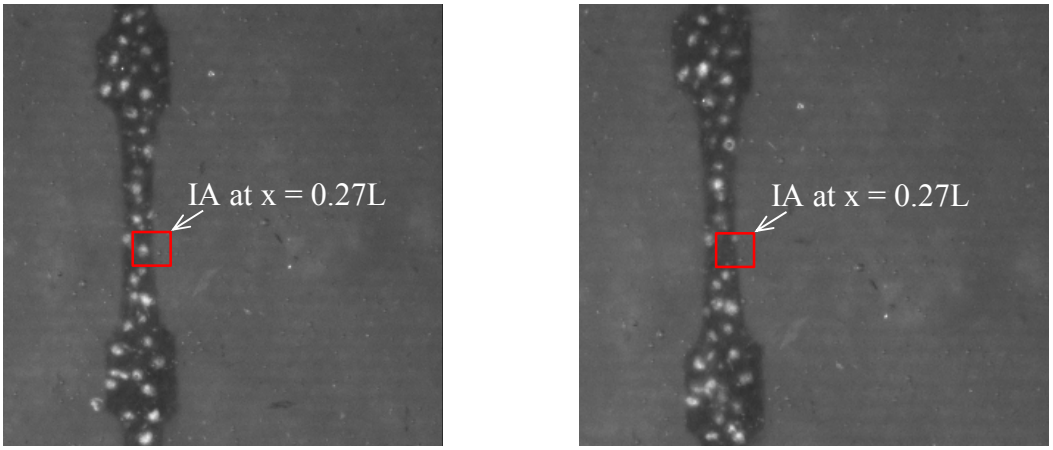


Figure 4.25: Example of white dot unbinding from geogrid: (a) Original dot at 0.00 Fo/Fmax. (b) Lost dot at 0.75 Fo/Fmax. Note: IA – Interrogation Area.

Additional errors occur due to variations of the intensity of the light from the lighting source. This leads to change in the reflection of the white dots and reflections on the transparent plate of the box. Another source of errors in the PIV calculations is the presence of soil markers covering the geogrid. Figure 4.26 shows soil markers covering different Interrogation Areas at different stages of a pullout test due to displacement of

the geogrid and no displacement of the soil markers. This causes errors in PIV calculation because the patterns of white dots that were being tracked by the PIV program in the beginning of the tests become hidden behind the soil markers.

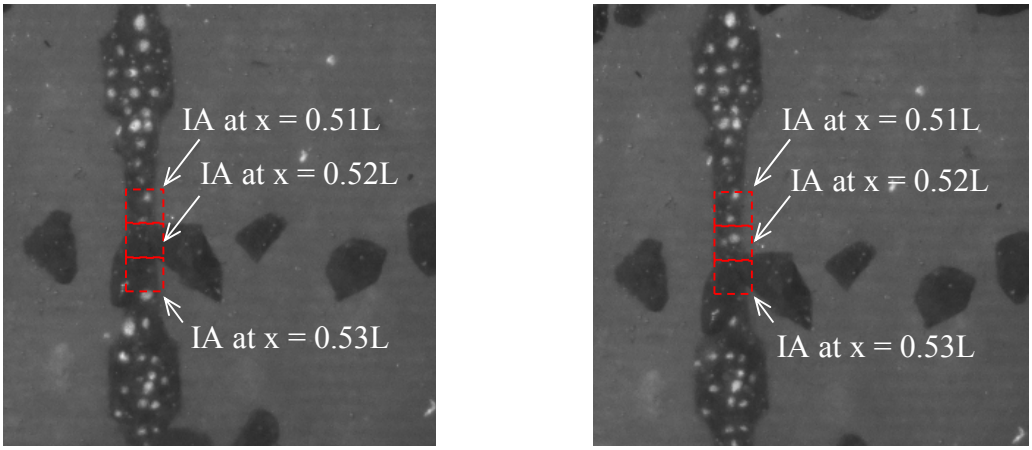


(a) (b)

Figure 4.26: Soil markers covering geogrid: (a) 0.00 Fo/Fmax. (b) 0.75 Fo/Fmax. Note: IA – Interrogation Area.

The contamination of the transparent soil with the remaining modeling clay used in the preparation of the test also introduces errors to the PIV calculations. The nature of this problem is similar to the problems of soil markers covering the geogrid. Lumps of white clay particles may cover parts of the geogrid near the active end of the geogrid. These lumps of clay do not move with the geogrid, thus covering different white dots at different stages of the test. Figure 4.27 shows an example of the lumps of modeling clay covering parts of the longitudinal ribs of the geogrid near the exit of the pullout box.

The consequence of the problems mentioned above is the lack of data points in certain regions of the geogrid specimen that can potentially impair the fitting of the entire displacement curve. This problem is more prominent in the case of lumps of modeling clay covering the geogrid because it occurs near the exit of the box. The displacement

data points near the exit of the box have significant influence on the curvature of the model equation because they are important for determining the parameter $\gamma$ in Equation 4.1.

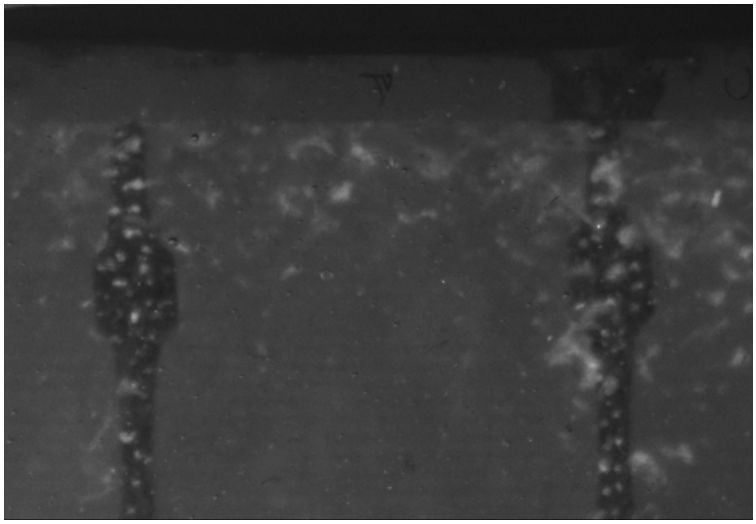

Figure 4.27: Lumps of modeling clay (white pieces) covering the geogrid near the active end of the geogrid at the exit of the box.

# 5 DISCUSSION OF THE RESULTS

The focus of this chapter is the analysis of the geogrid displacements and strains during the transparent pullout tests. The images used for these analyses were obtained from the cam0 (Figure 5.1). White dots were painted throughout the geogrid specimen to improve the PIV signal and track displacements along the geogrid more accurately. Images from cam0 also show soil markers placed in the direction perpendicular to the pullout and at different depths from the interface (Figure 5.1).

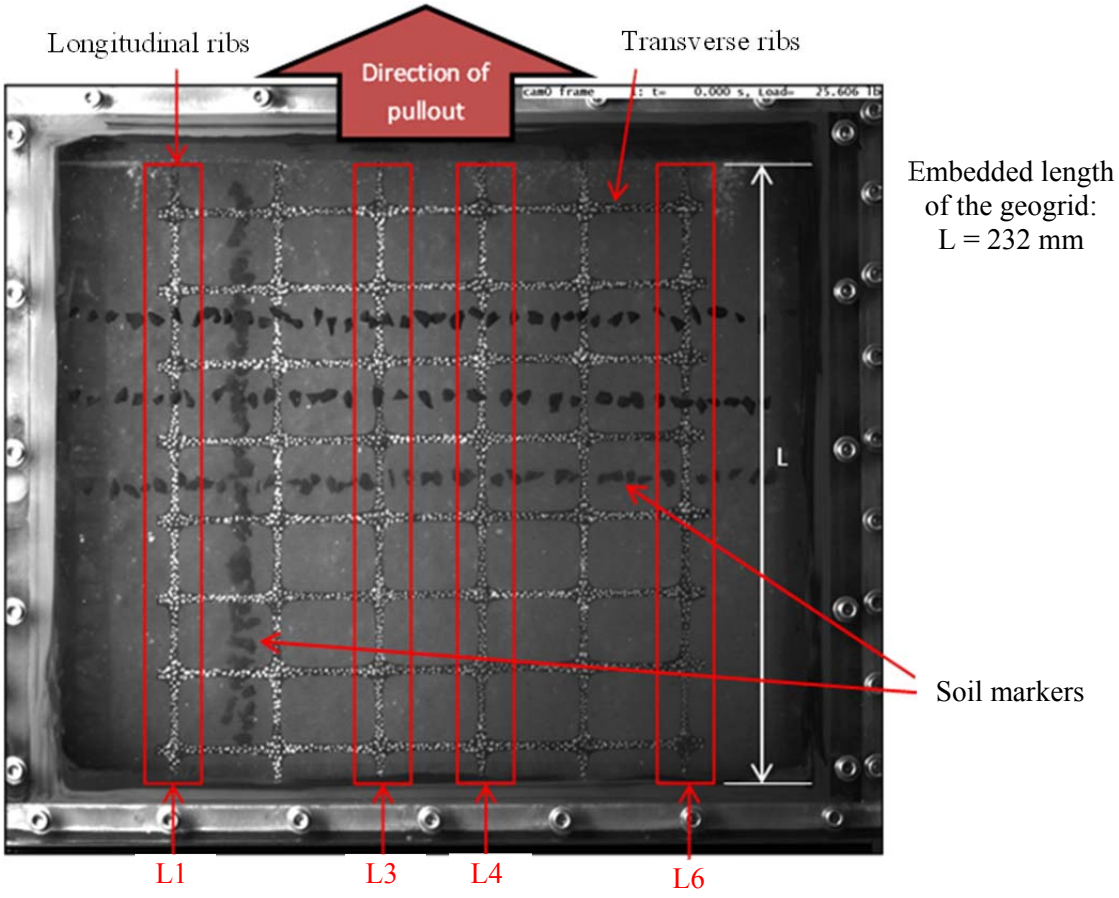


Figure 5.1: Image from cam0 (plan view of the test) with the terminology adopted for the transparent pullout tests.

Lines of markers were also placed in the direction parallel to the pullout at different distances from the interface and the images were captured with cam1 (Figure 5.2). Box movement during the tests resulted in problems with the PIV signal for tracking the markers. Explanations of the observed movements of the box and of the effects on the displacement data of the soil markers are presented at the end of this chapter. Also, a qualitative evaluation is presented on the displacements of the soil markers, along with recommendations to improve the test setup to obtain accurate data. The displacement data from the soil markers and displacement of the pullout box during the tests are presented in Appendix A.

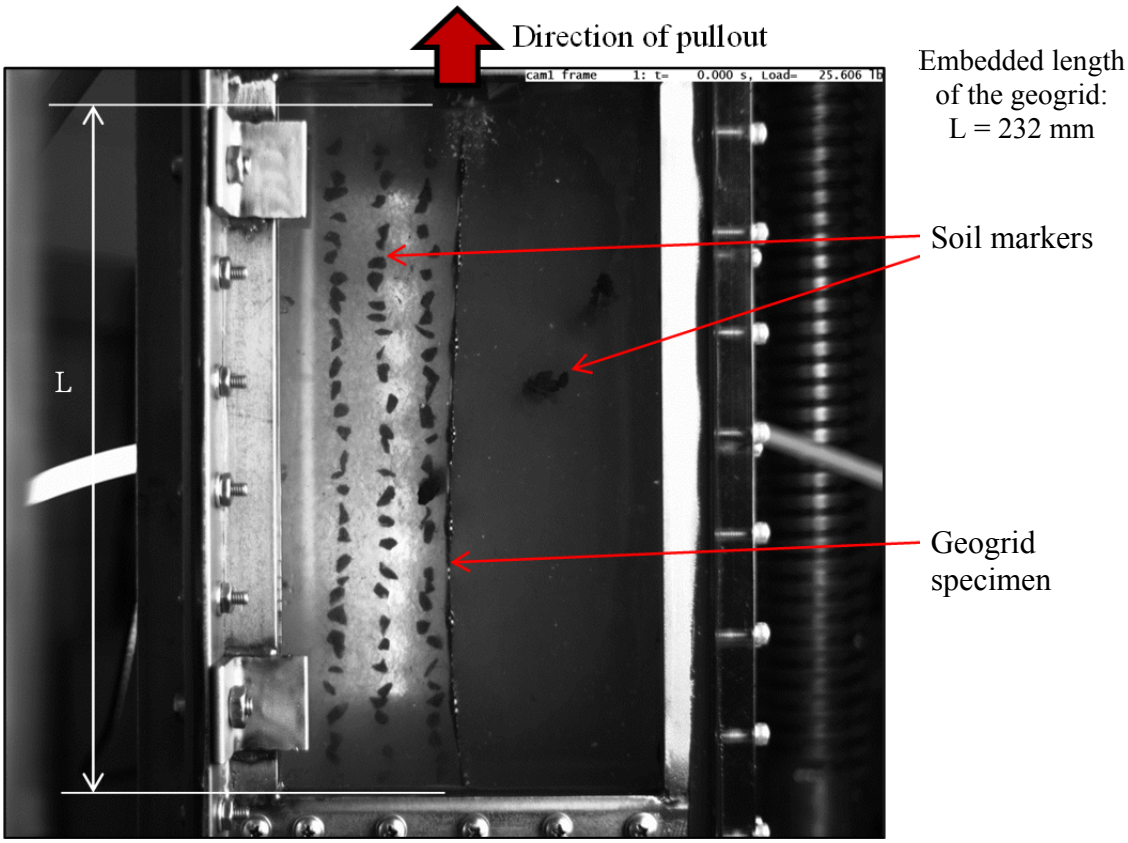


Figure 5.2: Image from cam1 (side view of the test) with the terminology adopted for the transparent pullout tests.

As explained in Chapter 4, the displacement data along the geogrid length were fitted using the following exponential equation for all tests:

$$y = \alpha + \beta\, e^{(-x/\gamma)} \tag{5.1}$$

Where $y$ is the axial displacement of the geogrid at a location $x$ along the geogrid. The independent variable, $x$, is normalized to the length $L$ of the geogrid specimen and varies from 0 to 1.00L. The parameters $\alpha$, $\beta$ and $\gamma$ are obtained through the iterative data fitting process explained in Chapter 4.

The strains along the geogrid length are obtained as the first derivative of Equation 5.1 as follows:

$$\varepsilon = \frac{dy}{dx} = \frac{\beta}{\gamma} e^{(-x/\gamma)} \tag{5.2}$$

Where $\varepsilon$ is the axial strain of the geogrid at a location $x$ along the geogrid. Note that the first derivative of Equation 1 is negative. However, the sign was inverted to conform the results with convention of positive strain on geosynthetic materials corresponding to tensile strains.

The second derivative of Equation 5.1 provides the rate at which the strain varies (i.e. strain gradient) along the geogrid:

$$\frac{d^2y}{dx^2} = -\frac{\beta}{\gamma^2} e^{(-x/\gamma)} \tag{5.3}$$

Note that the second derivative of Equation 5.1 is positive, but due to the sign change in Equation 5.2, the sign was also changed for Equation 5.3 for consistency.

The analyses of the tests were performed using data obtained from the central longitudinal ribs L3 and L4 for each test (Figure 5.1). The central ribs are expected to be

less affected by boundary conditions. The edges of the geogrid specimen in pullout tests are more affected by boundary conditions, especially near the exit of the box, due to the tendency for necking of the geogrid specimen in the unconfined portion with large loads. Moreover, measurements on L3 and L4 are the least affected by the distortion created by the lens of the camera since these ribs are near the center of the images.

The data shown in this chapter corresponds to different stages of the pullout tests. Four stages were chosen to be used: (i) approximately 25 % of the maximum pullout force (0.25 Fo/Fmax), (ii) approximately 40 % of the maximum pullout force (0.40 Fo/Fmax), (ii) approximately 50 % of the maximum pullout force (0.50 Fo/Fmax), and (ii) approximately 75 % of the maximum pullout force (0.75 Fo/Fmax). The data at maximum pullout force (1.00 Fo/Fmax) could not be analyzed. This is because at percentages of the maximum pullout force beyond 0.80 Fo/Fmax, the white dots used for tracking displacements along the geogrid become severely scratched by the sharp edges of the particles of fused quartz during movement of the geogrid. This introduced large errors in the PIV signal, impairing the results.

## 5.1 Analysis of Test 1: Geogrid without transverse ribs

The geogrid specimen in this test was used without its transverse ribs (Figure 5.3). The objective of this test is to evaluate the mobilization of the interface friction along the longitudinal members of the geogrid. The results of this test will be compared to the results from Test 2, in which the geogrid specimen had one transverse rib. The comparison allows for evaluations of the effects of the bearing mechanism on the mobilization of the geogrid that develops along the transverse rib.

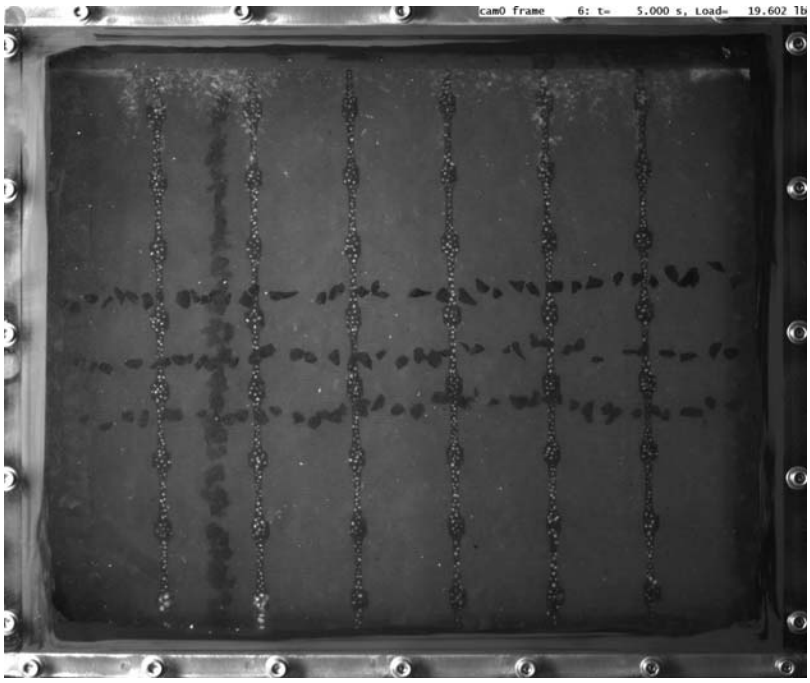


Figure 5.3: Test 1: Geogrid without transverse ribs (cam0) and 3 lines of soil markers placed perpendicular to the pullout direction.

Displacements along the longitudinal rib L3 are shown in Figure 5.4. In this figure, symbols are data points, solid lines are the curves fitted to the data using Equation 5.1, and dashed lines are the extrapolation of the fitted curves until intersection with the vertical axis. The plots used to obtaining the parameters $\alpha$, $\beta$ and $\gamma$ through linear transformation of Equation 5.1 are presented in Appendix B.

Figure 5.4 does not show the data point at 0.04L of the curve for 0.74 Fo/Fmax. This is because the white dot at this location of the geogrid was lost during the test sometime when Fo/Fmax was between 0.52 and 0.74. This issue with the white dots painted on the geogrid specimens was discussed in details in Chapter 4.5. Accordingly, the curve was extrapolated for values of the horizontal axis smaller than 0.13L for 0.74 Fo/Fmax. The other curves were extrapolated for values of the horizontal axis smaller than 0.04L.

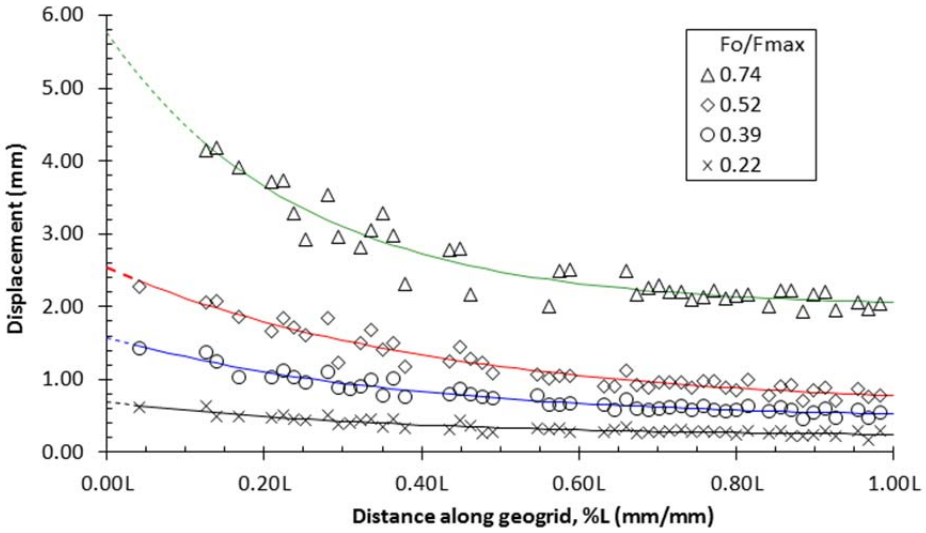


Figure 5.4: Displacement profile along the longitudinal rib L3 in Test 1 (geogrid with no transverse ribs).

Displacements along the longitudinal rib L4 are shown in Figure 5.5. Similarly to Figure 5.4, symbols are data points, solid lines are the curves fitted to the data using Equation 5.1, and dashed lines are the extrapolation of the fitted curves until intersection with the vertical axis. The plots used to obtaining the parameters $\alpha$, $\beta$ and $\gamma$ through linear transformation of the Equation 5.1 are presented in Appendix B.

All curves were extrapolated from values of the horizontal axis smaller than 0.15L. The curves for L4 (Figure 5.5) are similar to the curves for L3 (Figure 5.4) until Fo/Fmax equals 0.52. The differences in displacement data for L3 and L4 at 0.74 Fo/Fmax may be due to the following factors: variation of the response of each rib, errors in PIV calculations and lack of data points near the active end of the geogrid (values of the horizontal axis near zero).

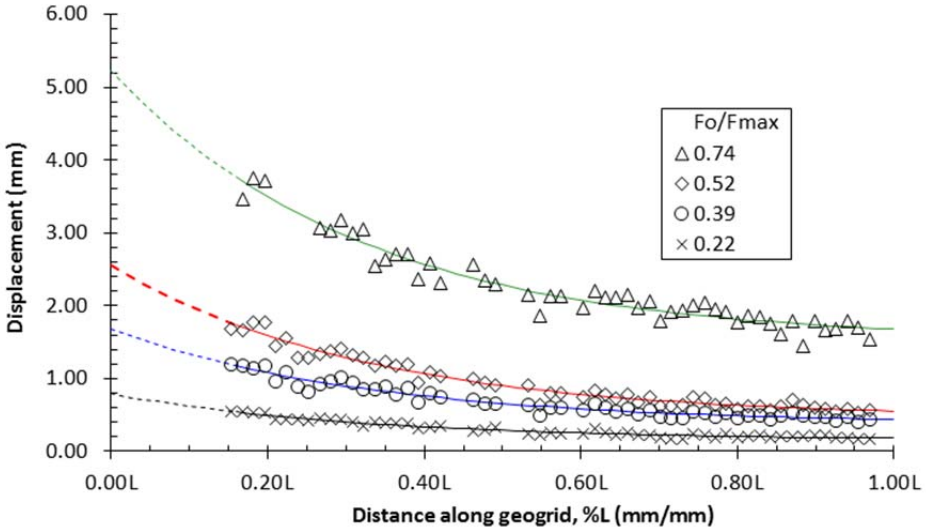


Figure 5.5: Displacement profile along the longitudinal rib L4 in Test 1 (geogrid with no transverse ribs).

The strains calculated with Equation 5.2 along the ribs L3 and L4 are shown in Figure 5.6 and Figure 5.7, respectively. Similar responses of these ribs are noted until 0.52 Fo/Fmax. Differences of 20 to 35 % between the results are observed for 0.74 Fo/Fmax and values of the horizontal axis smaller than 0.15L. This difference seems to be due to errors in data fitting of the displacement curves that arise from the lack of data points for values of the horizontal axis smaller than 0.15L. However, the strain profiles at 0.74 Fo/Fmax are similar for values of the horizontal axis higher than 0.15L.

Average strains along the geogrid specimen (Figure 5.8) were obtained from the strains calculated for L3 and L4 (Figure 5.6 and Figure 5.7). The average strains in Figure 5.8 are used for comparison of the results from Test 1 to results from Tests 2 to 5. It can be observed from Figure 5.8 that the distribution of strains becomes more nonlinear at 0.74 Fo/Fmax.

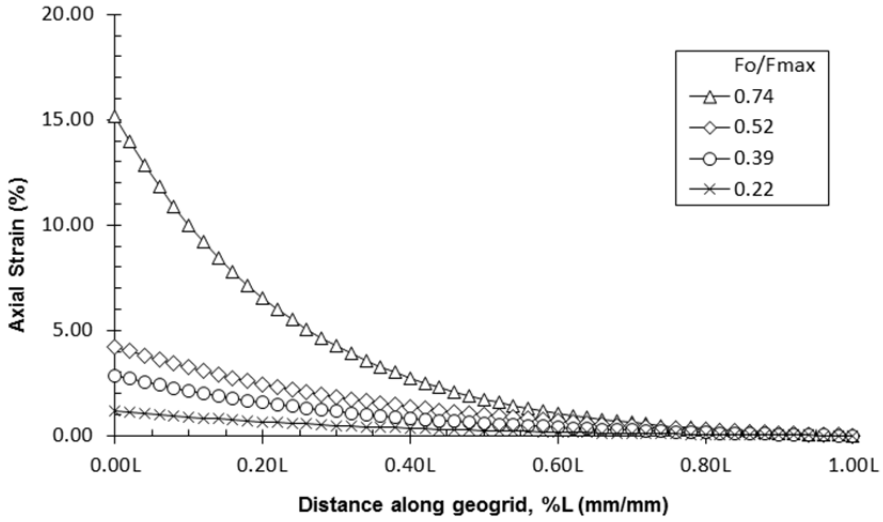


Figure 5.6: Strain profile along the longitudinal rib L3 in Test 1 (geogrid with no transverse ribs).

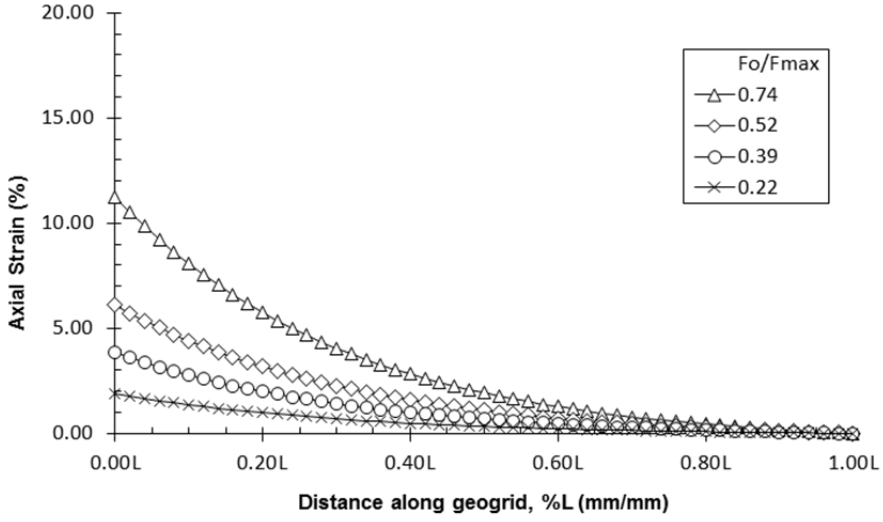


Figure 5.7: Strain profile along the longitudinal rib L4 in Test 1 (geogrid with no transverse ribs).

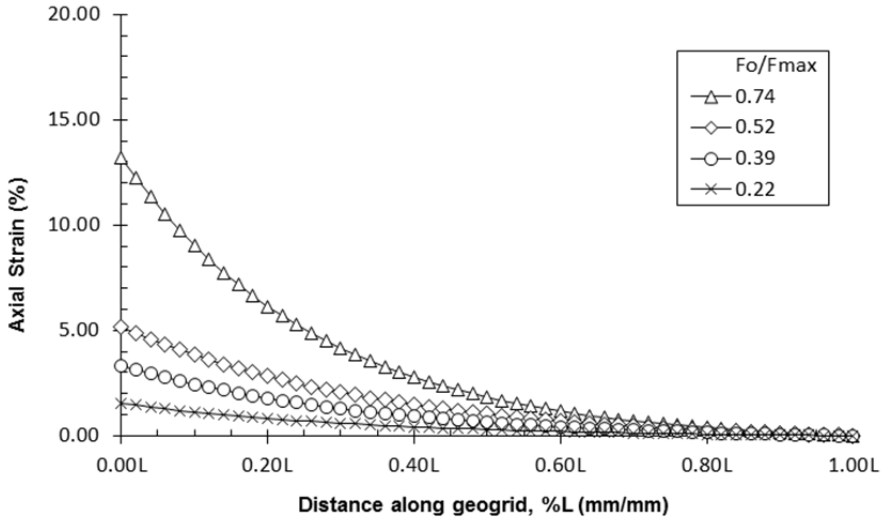


Figure 5.8: Average strain profile of the central longitudinal ribs L3 and L4 in Test 1 (geogrid with no transverse ribs).

Figure 5.9 shows the rate of variation of the strains along the geogrid, i.e. strain gradient (Equation 5.3), calculated from the average strains in Figure 5.8. As shown by the steeper curve for 0.74 Fo/Fmax, higher variations of the mobilized strains along the geogrid were observed at larger pullout loads.

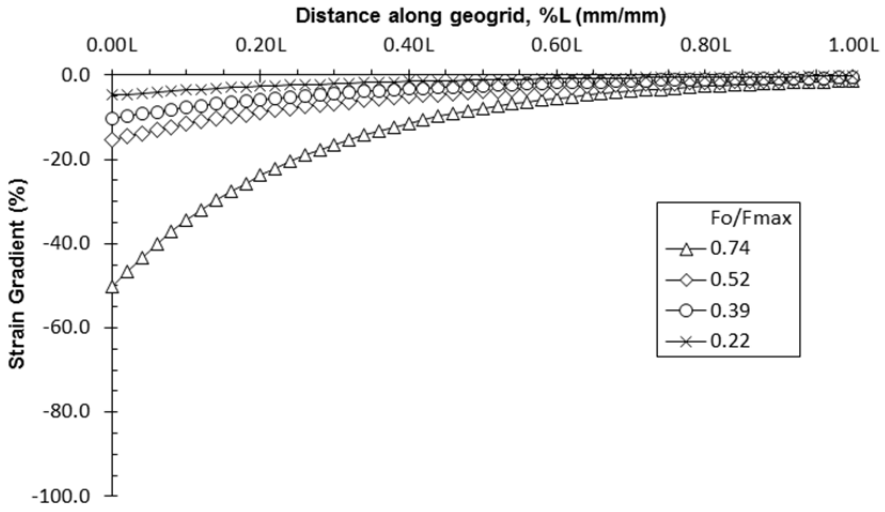


Figure 5.9: Average strain gradient along the central longitudinal ribs L3 and L4 in Test 1 (geogrid with no transverse ribs).

## 5.2 Analysis of Test 2: Geogrid with one transverse rib

The geogrid specimen in this test included one transverse rib (Figure 5.10). The transverse rib is located near the middle of the length of the geogrid ($x$ = 0.46L). The objective of this test was to evaluate the effects of the presence of a transverse rib. This evaluation involves the comparison of the results of this test with the results of Test 1, in which the geogrid has no transverse rib.

The presence of the transverse rib in Test 2 allows for the contribution of the bearing mechanism to the soil-geogrid interaction. Thus, both the interface friction and the bearing mechanism may develop in Test 2. In Test 1, only the interaction mechanism of interface friction along the longitudinal ribs of the geogrid is present, since there was no transverse rib in Test 1.

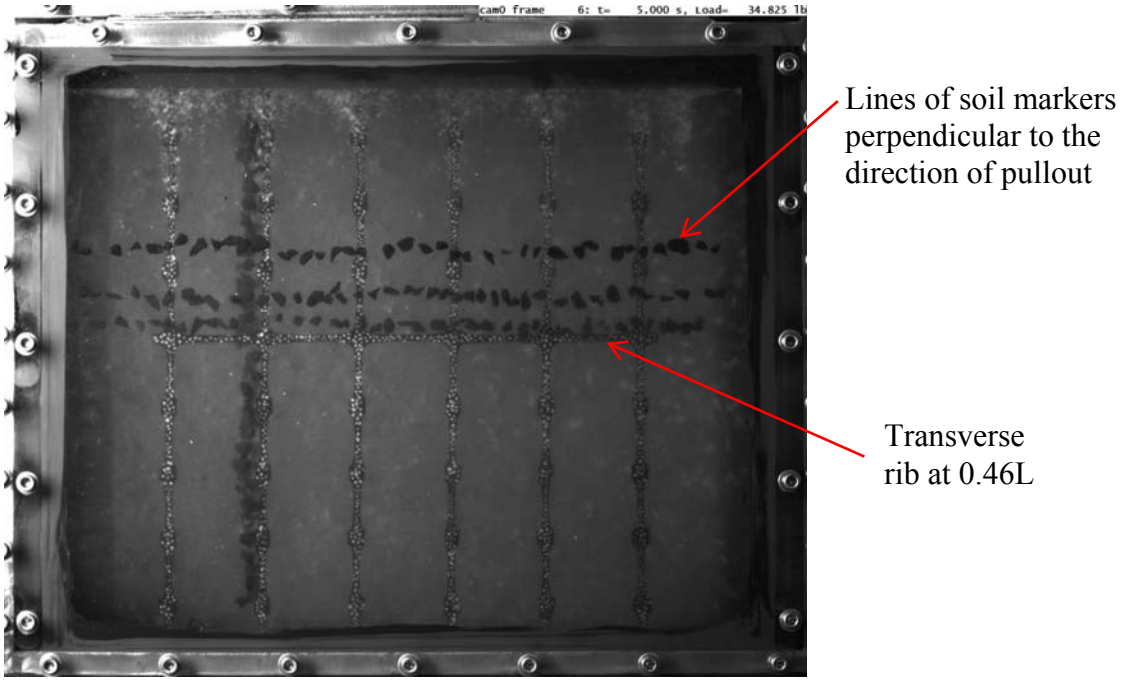


Figure 5.10: Test 2: geogrid with one transverse rib at 0.46L (cam0).

### 5.2.1 STRAINS ALONG THE GEOGRID IN TEST 2

Displacements along the longitudinal rib L3 are shown in Figure 5.11. The plots used to obtaining the parameters $\alpha$, $\beta$ and $\gamma$ through linear transformation of the Equation 5.1 are presented in Appendix B. Displacements along L3 in this test are smaller than along L3 in Test 1 (Figure 5.4) for all percentages of the maximum pullout forces.

Displacements along the longitudinal rib L4 are shown in Figure 5.12. The plots used to obtaining the parameters $\alpha$, $\beta$ and $\gamma$ through linear transformation of the Equation 5.1 are presented in Appendix B. Comparison between Figure 5.12 and Figure 5.11 shows similar displacements along L3 and L4. No local, sudden change in the

displacement profiles of L3 and L4 was observed at 0.46L due to the presence of the transverse rib at this location.

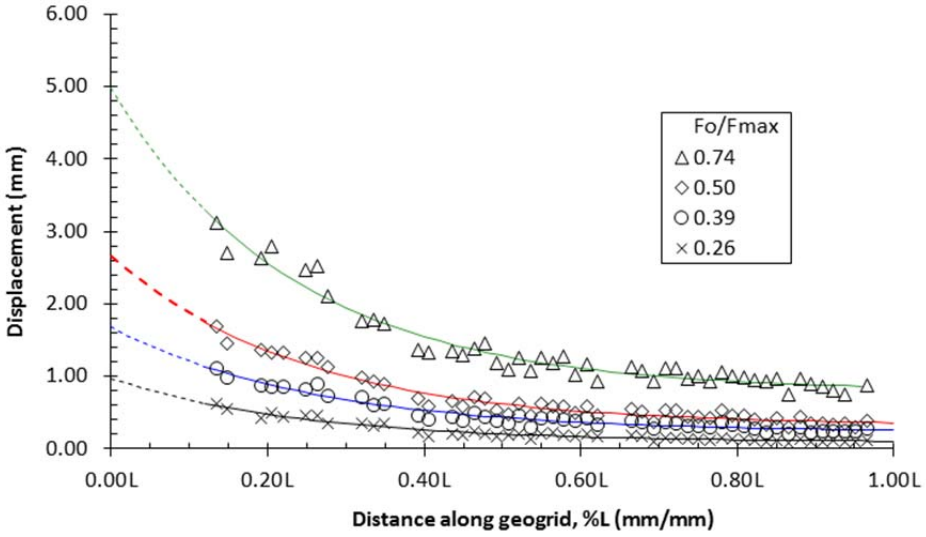


Figure 5.11: Displacement profile along the longitudinal rib L3 in Test 2 (geogrid with one transverse rib at 0.46L).

Smaller displacements along L4 in Test 2 (Figure 5.12) are observed for the same percentage of the maximum pullout forces of L4 in Test 1 (Figure 5.5). Comparing the displacement profiles obtained in Test 1 (Figure 5.4 and Figure 5.5) and Test 2 (Figure 5.11 and Figure 5.12) shows that the soil-geogrid interaction is improved with the presence of the transverse rib. The transverse rib seems to create an "anchoring effect" on the geogrid. These results show that higher pullout loads were required for a given displacement of a geogrid with a transverse rib than one without it.

The strains calculated with Equation 5.2 along the ribs L3 and L4 are shown in Figure 5.13 and Figure 5.14, respectively. Similar results are observed between the strain profiles on these figures.

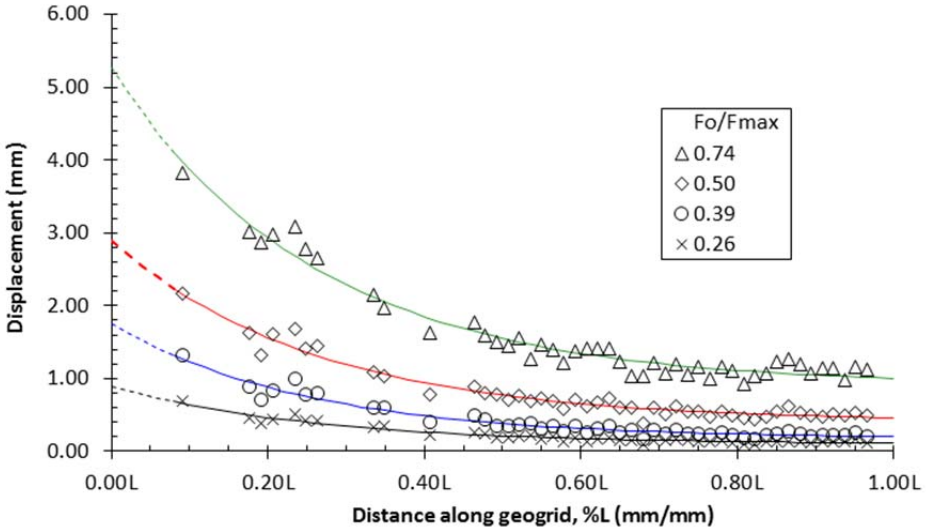


Figure 5.12: Displacement profile along the longitudinal rib L4 in Test 2 (geogrid with one transverse rib at 04.6L).

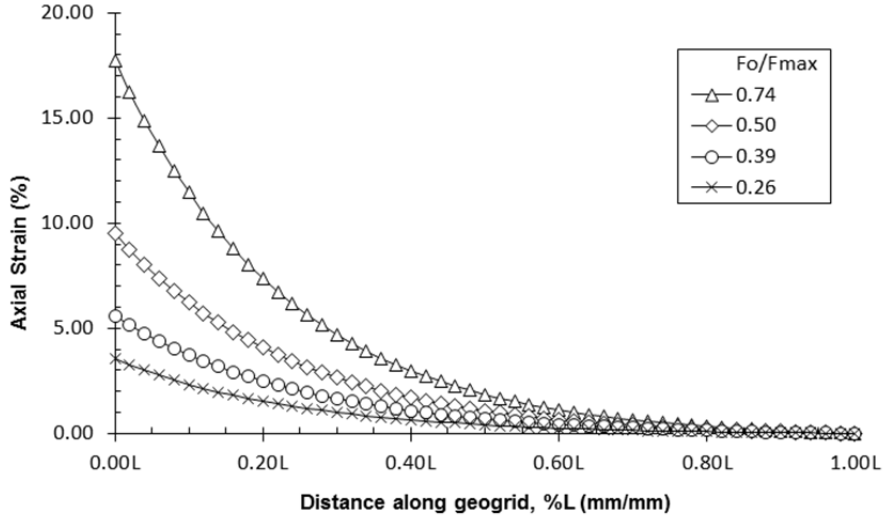


Figure 5.13: Strain profile along the longitudinal rib L3 in Test 2 (geogrid with one transverse rib at 0.46L).

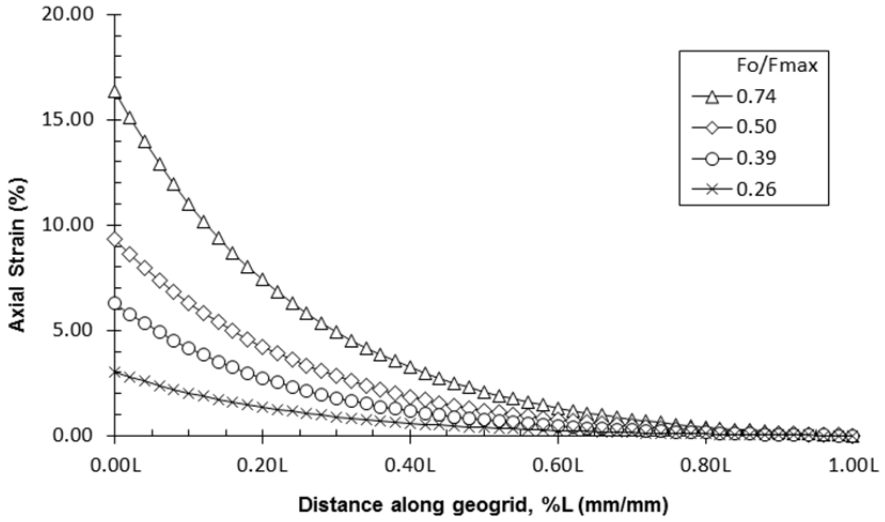


Figure 5.14: Strain profile along the longitudinal rib L4 in Test 2 (geogrid with one transverse rib at 0.46L).

Average strains along the geogrid specimen (Figure 5.15) were obtained from the strains calculated for L3 and L4 (Figure 5.13 and Figure 5.14). There are higher strains for all percentages of the maximum pullout force when compared to the average strain profile for Test 1 (Figure 5.8). These results show that the presence of the transverse rib improves the soil-geogrid interaction, thus increasing the engagement of the longitudinal ribs starting at 0.26 Fo/Fmax.

Table 5.1 shows the pullout forces generated in Tests 1 and 2 at different stages of the tests. If the bearing mechanism along the transverse rib would only developed for relatively large displacements (Farrag et al. 1993, Palmeira 2004, Teixeira et al. 2007), the forces in Tests 1 and 2 would be similar at the early stages of the test. However, this is not observed in Table 5.1. The loads generated in Test 2 are higher than the loads generated in Test 1 for all percentages of the maximum pullout forces.

This improvement of the soil-geogrid interaction at 0.26 Fo/Fmax with the presence of a transverse rib is for displacements along the geogrid smaller than 1.0 mm (Figure 5.11 and Figure 5.12). Specifically, the displacement of the junctions with the transverse rib in L3 and L4 at 0.46L are only 0.20 mm at 0.26 Fo/Fmax (Figure 5.11 and Figure 5.12). Thus, these results show that the contribution of the transverse rib to the pullout force starts at relatively small displacements.

| Percentage (%) of Fmax | Generated pullout force (kN/m) | | |
|---|---|---|---|
| | Test 1 (geogrid with no transverse rib) | Test 2 (geogrid with one transverse rib) | Ratio Test 2/Test 1 |
| 25 | 2.0 | 2.7 | 1.35 |
| 40 | 3.5 | 4.2 | 1.20 |
| 50 | 4.8 | 5.2 | 1.08 |
| 75 | 6.7 | 7.8 | 1.16 |
| 100 | 9.1 | 10.5 | 1.15 |

Table 5.1: Comparison of pullout forces generated in Tests 1 and 2.

Figure 5.16 shows the average strain gradient along the geogrid calculated from the average strains in Figure 5.15. Results in Figure 5.16 show that there are higher variations of the mobilized strains along the geogrid due to the presence of the transverse rib when compared to Test 1 (Figure 5.9).

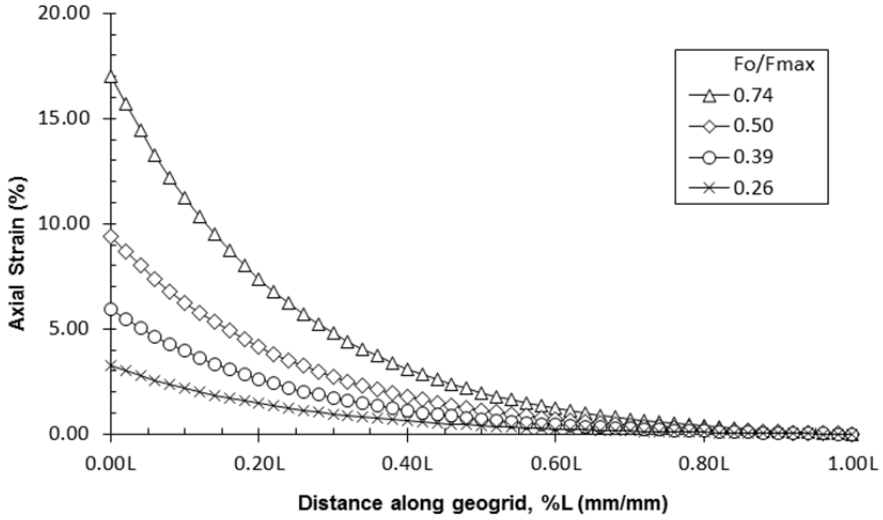


Figure 5.15: Average strain profile of the central longitudinal ribs L3 and L4 in Test 2 (geogrid with one transverse rib at 0.46L).

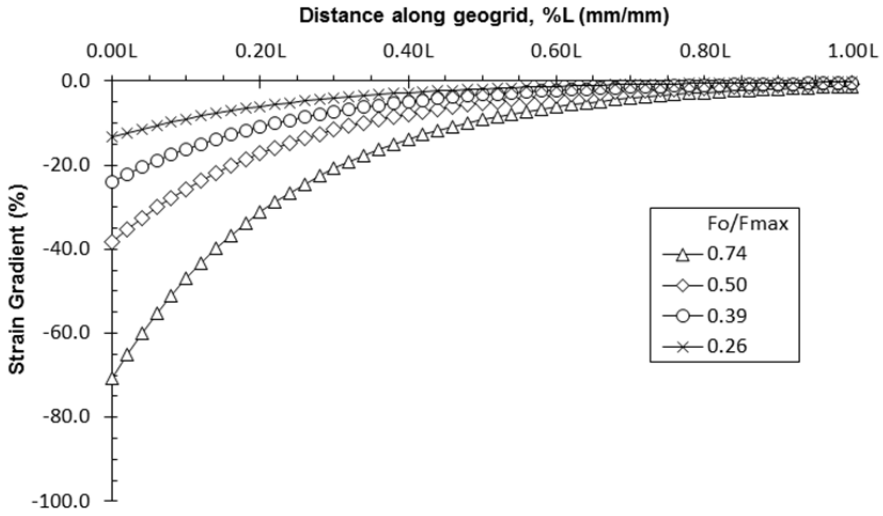


Figure 5.16: Average strain gradient along the central longitudinal ribs L3 and L4 in Test 2 (geogrid with one transverse rib at 0.46L).

### 5.2.2 DISPLACEMENT PROFILE OF THE TRANSVERSE RIB

The displacements along the transverse rib between the longitudinal ribs L3 and L4 are shown in Figure 5.17. The distance from L3 to L4 is normalized to the spacing W, which is 36.6 mm in this geogrid. Thus 0.00W on the horizontal axis is at L3 and 1.00W is at L4. Data for 0.74 Fo/Fmax were not obtained because soil markers were partially covering the transverse rib (Figure 5.18). As a consequence, errors were introduced into the PIV calculations due to this proximity of the transverse rib to the soil markers.

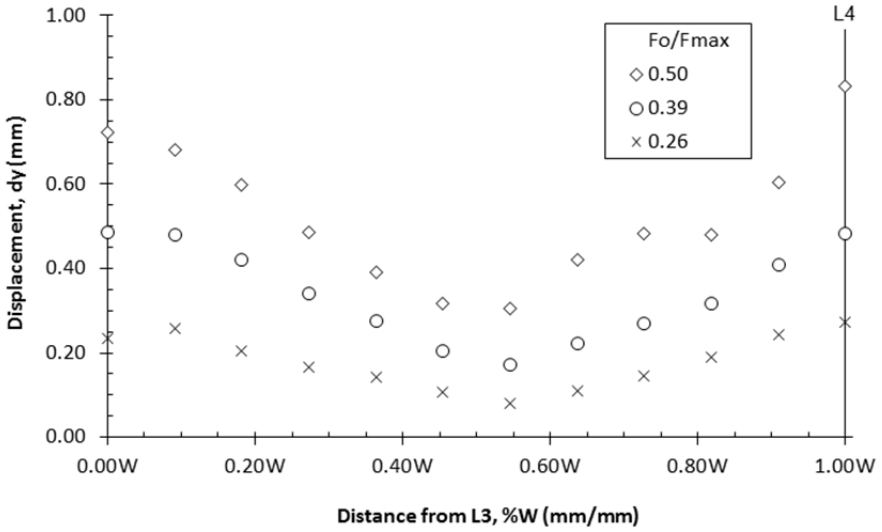


Figure 5.17: Displacement profile of the transverse rib located at 0.46L in Test 2 (geogrid with one transverse rib at 0.46L).

Figure 5.17 shows significant deflections of the transverse rib for small displacements, smaller than 1.0 mm. Figure 5.19 shows the deflections along the transverse rib measured in relationn to the junction of the transverse rib in L3. This figure shows that there are continuously higher deflections at larger percentages of the maximum pullout force. Engagement of the transverse rib is first observed at 0.26 Fo/Fmax with a deflection of 0.153 mm.

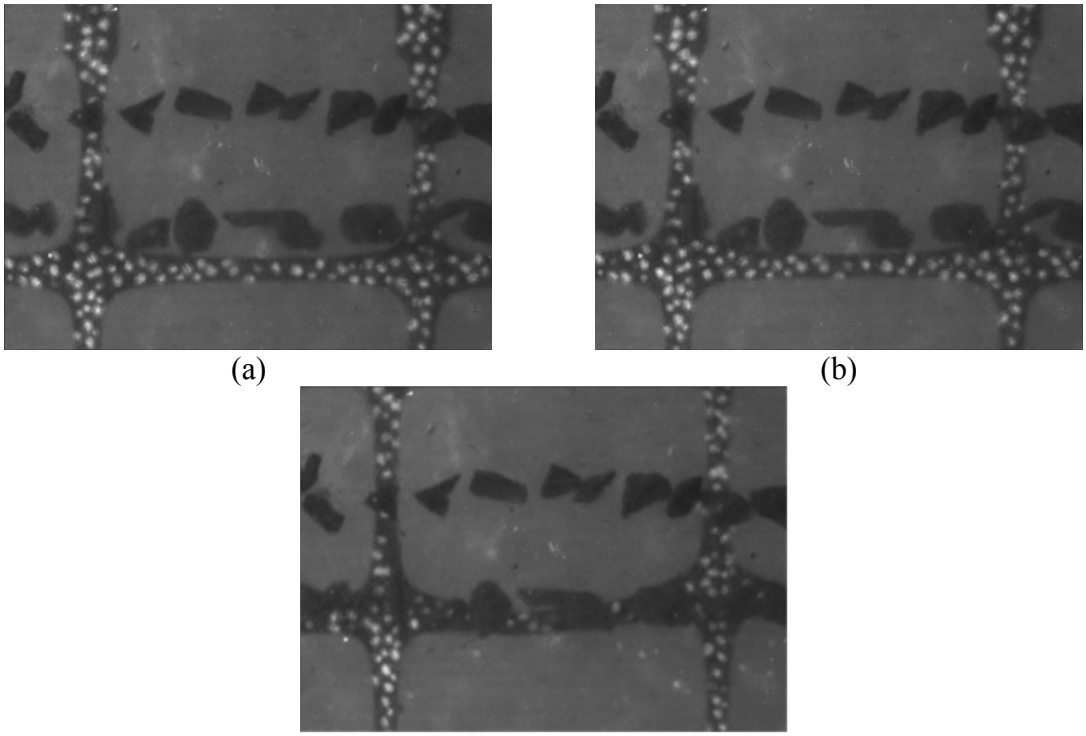


Figure 5.18: Close view of the transverse rib in Test 2 at different stages of the test: (a) 0.00 Fo/Fmax. (b) 0.50 Fo/Fmax. (c) 1.00 Fo/Fmax.

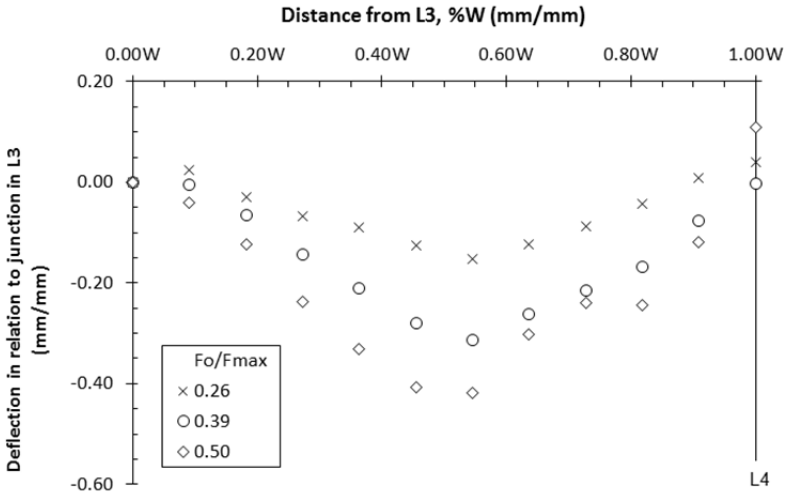


Figure 5.19: Test 1: Deflections along the transverse rib in relation to the junction in L3.

The contribution of the bearing mechanism along the transverse rib at small displacements can be better evaluated by comparing the pullout forces generated in Tests 1 and 2 with the displacement of a reference point in the geogrid. Figure 5.20 shows the pullout forces generated in Tests 1 and 2 with the displacement of the point P3 in the geogrid (see Figure 4.6). This point was chosen because it is at the middle of the length of the geogrid specimens. It can be observed in Figure 5.20 that the pullout forces in Test 2 are higher than in Test 1 for the entire curve of displacement of the point P3.

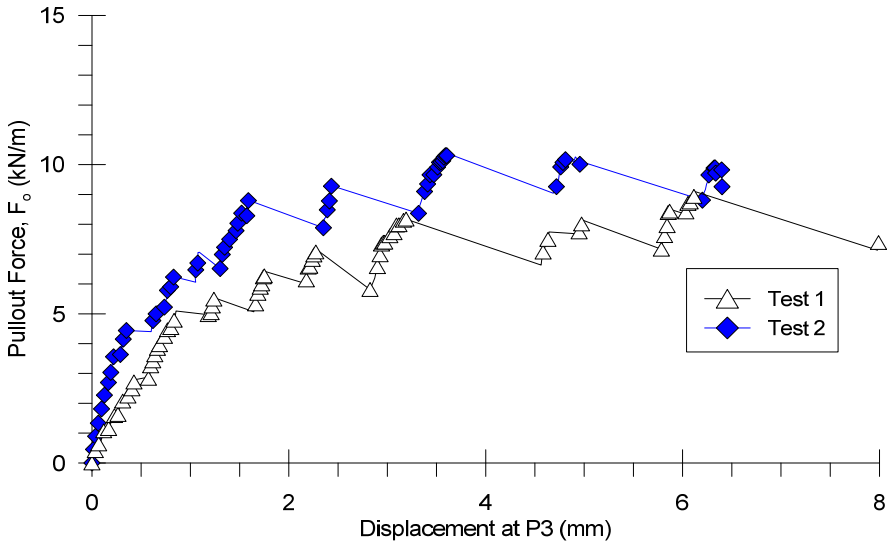


Figure 5.20: Comparison of pullout forces generated in Tests 1 and 2 with displacements of point P3 in the geogrids.

Table 5.2 shows the pullout forces in Tests 2 and 1 for small displacements of P3. This table shows that the contribution of the bearing mechanism is observed for displacements as low as 0.20 mm (0.008 in.). With the data from Tests 1 and 2, it can be concluded that the bearing mechanism develops at small displacements. It was first observed at 0.26 Fo/Fmax.

| Displacement of P3 (mm) | Generated pullout force (kN/m) | | |
|---|---|---|---|
| | Test 1 (geogrid with no transverse rib) | Test 2 (geogrid with one transverse rib) | Ratio Test 2/Test 1 |
| 0.20 | 1.5 | 3.3 | 2.20 |
| 0.50 | 2.8 | 4.4 | 1.57 |
| 1.00 | 5.0 | 6.1 | 1.22 |

Table 5.2: Comparison of pullout forces generated in Tests 1 and 2 with small displacements of point P3 in the geogrids.

These findings are contrary to the findings of Teixeira et al. (2007). The authors found that the contribution of the bearing mechanism of transverse ribs only develops at relatively large displacements. However, their findings were based on tests with a geogrid made of polyester, differently than the polypropylene geogrid used in the present study. Thus, more research is needed to verify the engagement of transverse ribs composed of different polymers at different percentages of the maximum pullout force and relatively small displacements.

## 5.3 Analysis of Test 3: Geogrid with two closely spaced transverse ribs

The geogrid specimen in this test included two closely spaced transverse ribs, 21 mm apart (Figure 5.21). This is the original aperture size of the geogrid along the machine direction. The ratio between the aperture size and the $D_{50}$ of the soil is 5.5 for the region between the transverse ribs. The first transverse rib is located at 0.35L. The second transverse rib is located at 0.46L, which is the same location of the transverse rib in Test 2.

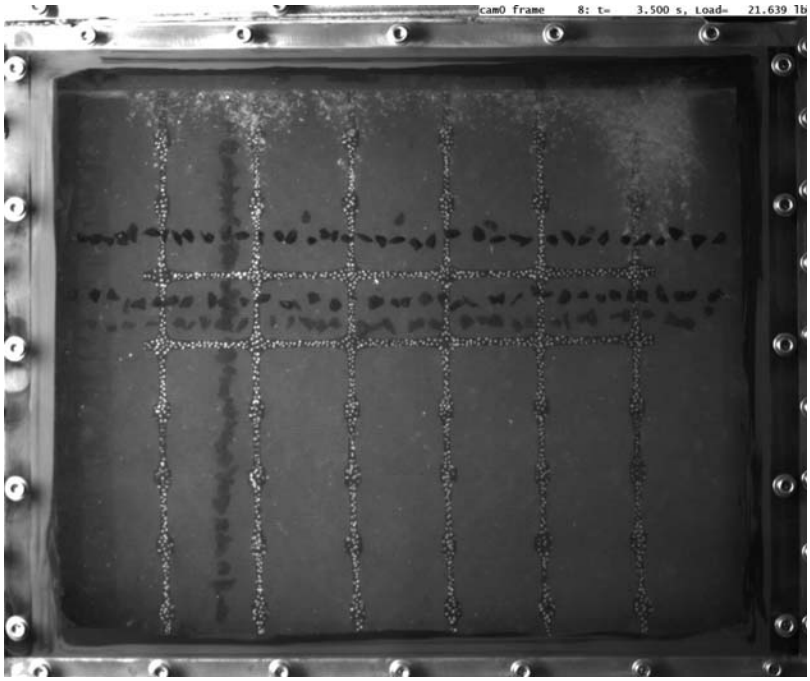


Figure 5.21: Test 3: geogrid with two closely spaced transverse ribs at 0.35L and 0.46L (cam0).

The primary objective of this test was to evaluate the potential interference of each rib on the bearing mechanism developed along them. Moreover, it is analyzed how the presence of two transverse ribs contribute to the overall engagement of the geogrid, as opposed to when there is only one transverse rib. This will be achieved by comparing the results of this test to results from Test 2.

### 5.3.1 STRAINS ALONG THE GEOGRID IN TEST 3

Displacements along the longitudinal rib L3 are shown in Figure 5.22. The plots used for obtaining the parameters $\alpha$, $\beta$ and $\gamma$ through linear transformation of the Equation 5.1 are presented in Appendix B. Displacements along L3in Test 3 are similar

for all percentages of the maximum pullout force than the displacements in Test 2 (Figure 5.11).

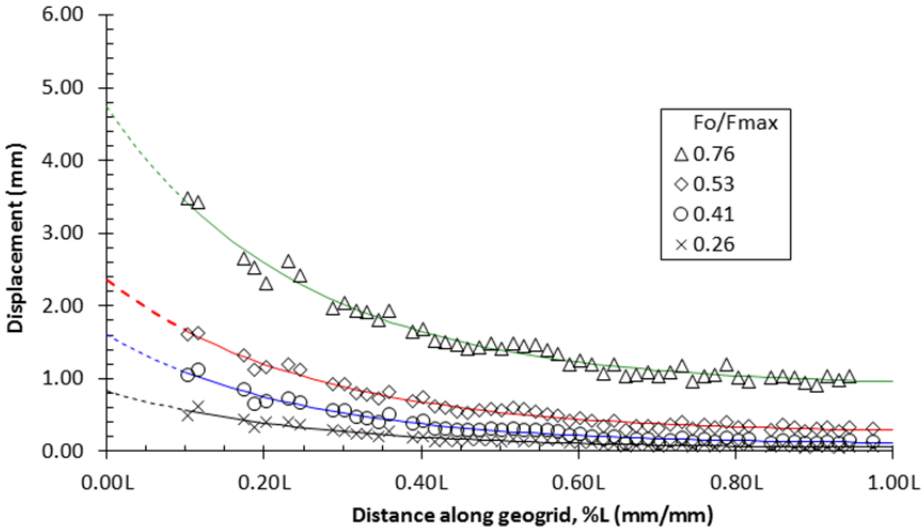


Figure 5.22: Displacement profile along the longitudinal rib L3 in Test 3 (geogrid with two closely spaced transverse ribs at 0.35L and 0.46L).

Displacements along the longitudinal rib L4 are shown in Figure 5.23. The plots used for obtaining the parameters $\alpha$, $\beta$ and $\gamma$ through linear transformation of the Equation 5.1 are presented in Appendix B. Slightly larger displacements along L4 are observed than along L3 (Figure 5.22). No local, sudden changes in the displacement profiles of L3 and L4 were observed at 0.35 and 0.46L due to the presence of the transverse ribs at these locations.

The strains calculated with Equation 5.2 along the ribs L3 and L4 are shown in Figure 5.24 and Figure 5.25, respectively. Significant difference is observed between the strains along L3 and the strains along L4 up to 0.20L, especially for 0.53 and 0.76 Fo/Fmax. On the other hand, strains along the ribs are similar for $x$ larger than 0.20L. This variation in results may be due to errors of the PIV signal in tracking the white dots on the geogrid. As explained before, these dots start to unbind from the rib during the

tests due to the presence of mineral oil and movement of the geogrid. The white dots are scratched by the angular corners of particles of fused quartz at the interface. Moreover, additional errors are introduced especially near the exit of the box with the presence of lumps of remaining modeling clay used when assembling the test. As a result, additional variations are introduced to the process of data fitting.

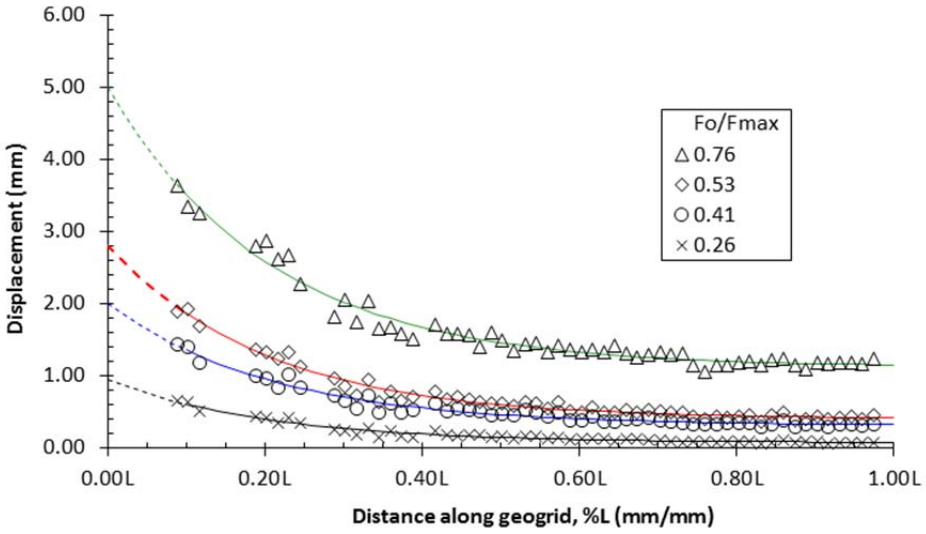


Figure 5.23: Displacement profile along the longitudinal rib L4 in Test 3 (geogrid with two closely spaced transverse ribs at 0.35L and 0.46L).

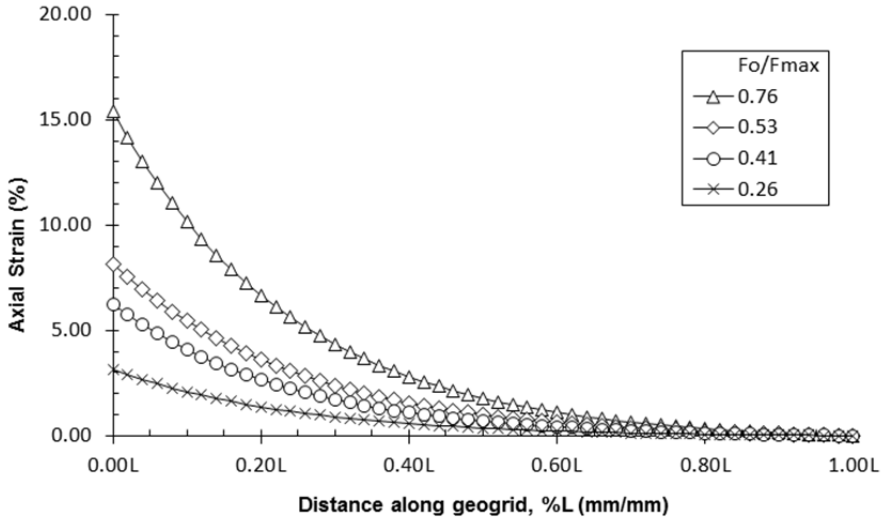


Figure 5.24: Strain profile along the longitudinal rib L3 in Test 3 (geogrid with two closely spaced transverse ribs at 0.35L and 0.46L).

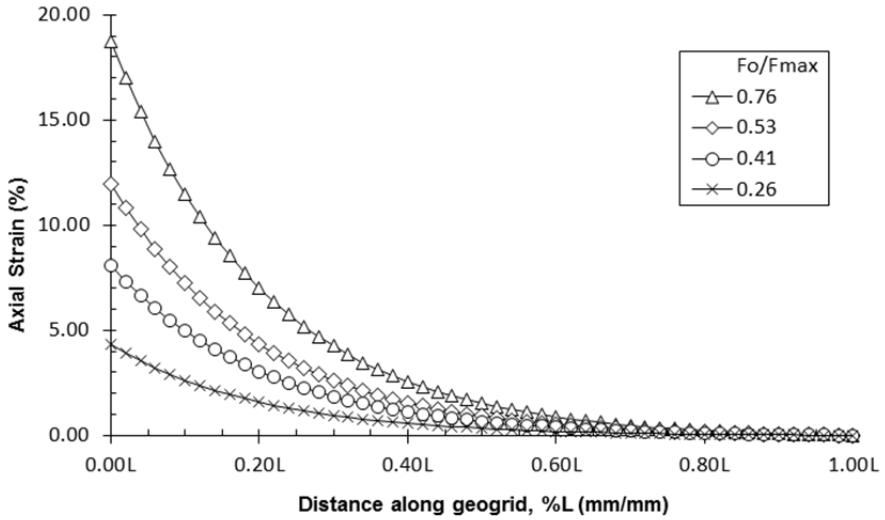


Figure 5.25: Strain profile along the longitudinal rib L4 in Test 3 (geogrid with two closely spaced transverse ribs at 0.35L and 0.46L).

Figure 5.26 shows the average strains along the geogrid specimen obtained from the strains calculated for L3 and L4. The average strains along the central longitudinal

ribs in this test are similar to the average strains along the central longitudinal ribs in Test 2 (Figure 5.15) for all percentages of the maximum pullout force. Similar pullout forces were also generated in both tests throughout the duration of the tests (Table 5.3). These results suggest that there is large interference between the transverse ribs in Test 3. Accordingly, there is insignificant contribution of the bearing mechanism from the additional transverse rib to the soil-geogrid interaction.

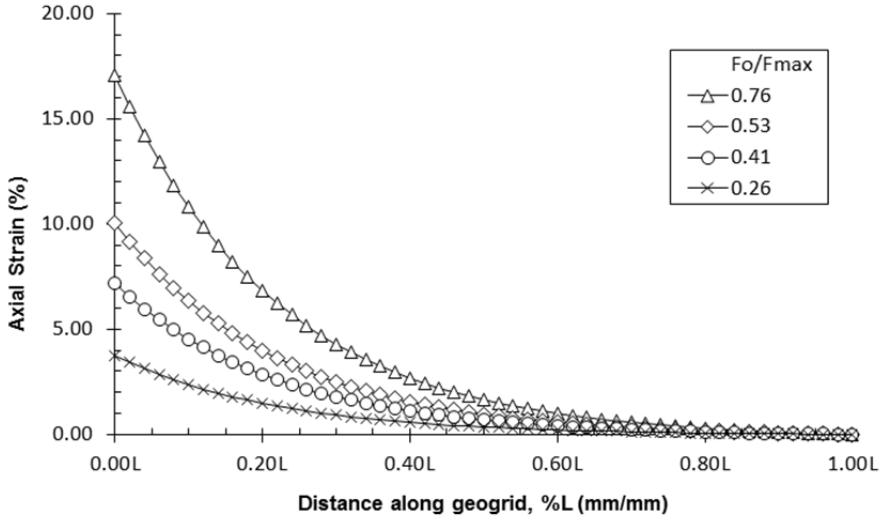


Figure 5.26: Average strain profile of the central longitudinal ribs L3 and L4 in Test 3 (geogrid with two closely spaced transverse ribs at 0.35L and 0.46L).

| Percentage (%) of Fmax | Generated pullout force (kN/m) | | |
|---|---|---|---|
| | Test 2 (geogrid with one transverse rib) | Test 3 (geogrid with two closely spaced transverse ribs) | Ratio Test 3/Test 2 |
| 25 | 2.7 | 2.7 | 1.00 |
| 40 | 4.2 | 4.4 | 1.05 |
| 50 | 5.2 | 5.7 | 1.10 |
| 75 | 7.8 | 8.1 | 1.04 |
| 100 | 10.5 | 10.7 | 1.02 |

Table 5.3: Comparison of pullout forces generated in Tests 2 and 3.

Figure 5.27 shows the average strain gradient along the geogrid calculated from the average strains in Figure 5.26. Results in Figure 5.27 show that the variation of strains along the geogrid with two closely spaced transverse ribs is slightly higher than the variation of strains along the geogrid with one transverse rib (Figure 5.16). This result suggests that the presence of two closely spaced transverse ribs does not improve the distribution of strains throughout the longitudinal ribs of the geogrid. It has the same effect as when only one transverse rib is present.

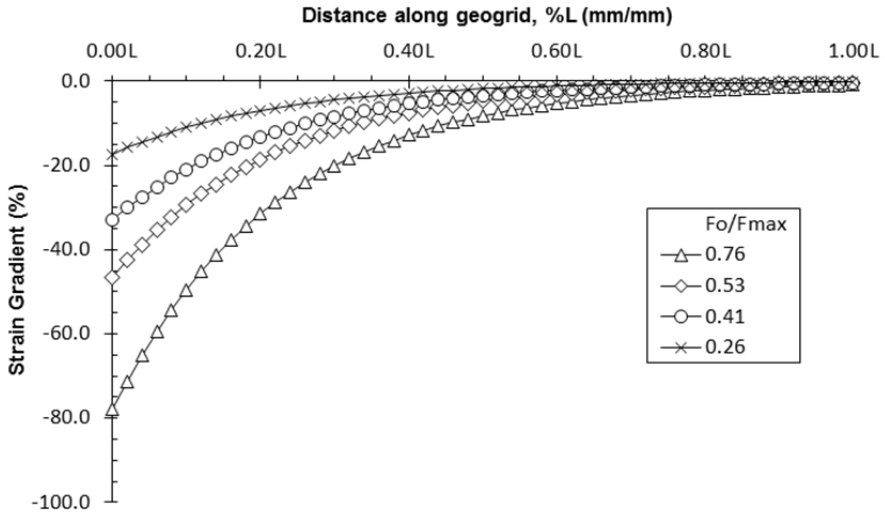


Figure 5.27: Average strain gradient of the central longitudinal ribs L3 and L4 in Test 3 (geogrid with two closely spaced transverse ribs at 0.35L and 0.46L).

### 5.3.2 DISPLACEMENT PROFILE OF THE TRANSVERSE RIBS

The ratio of the spacing between the transverse ribs (S) over the thickness of the transverse ribs (B) is 24 in Test 3. Figure 5.28 and Figure 5.29 show the displacements along the transverse ribs at 0.35L and 0.46L, respectively. Larger deflections are

observed in the transverse rib at 0.35L (Figure 5.28) than in the transverse rib at 0.46L (Figure 5.29). Insignificant deflections are observed in the transverse rib at 0.46L (Figure 5.29) for all percentages of the maximum pullout force.

To properly evaluate the interference between the transverse ribs, deflections of these ribs need to be analyzed for similar levels of displacements of the ribs. The deflection of the transverse rib at 0.35L is 0.38 mm (0.015 in.) for near 1.5 mm (0.06 in.) of displacement of the junctions (Figure 5.28). The deflection of the transverse rib at 0.46L is only 0.08 mm (0.003 in.) for near 1.5 mm (0.06 in.) of displacement of the junctions (Figure 5.29).

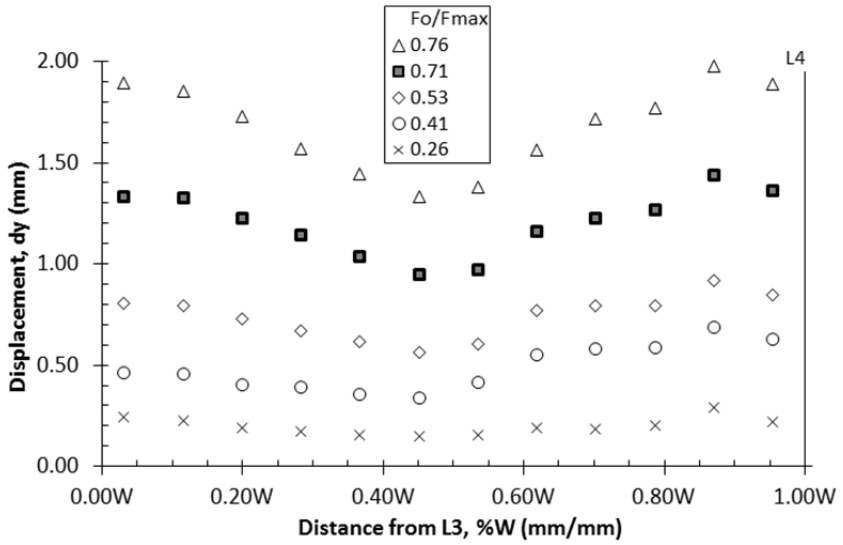


Figure 5.28: Displacement profile of the transverse rib located at 0.35L in Test 3 (geogrid with two closely spaced transverse ribs at 0.35L and 0.46L).

Thus, as stated above, it can be concluded that there is significant interference of the transverse rib at 0.35L into the engagement of the rib at 0.46L. This finding is in agreement with the findings of Dyer (1985) and Palmeira and Milligan (1989). Dyer

(1985) showed large interference between closely spaced transverse ribs in photo-elastic pullout tests with steel grids. Palmeira and Milligan (1989) reported that there is high interference between members for rations S/B smaller than 50.

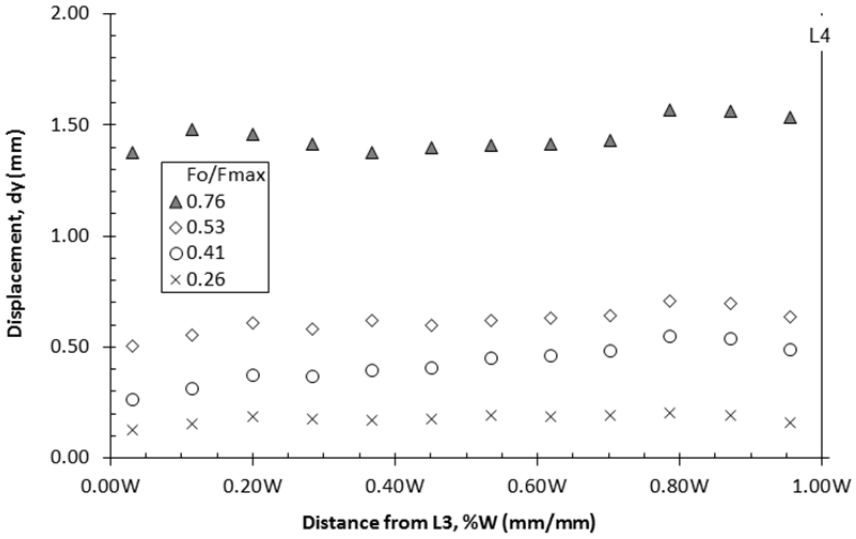


Figure 5.29: Displacement profile of the transverse rib located at 0.46L in Test 3 (geogrid with two closely spaced transverse ribs at 0.35L and 0.46L).

Figure 5.30 shows the pullout forces generated in Tests 3 and 2 with the displacement of the point P3 in the geogrid. It can be observed in Figure 5.30 that the pullout forces in Test 3 become slightly higher than the forces in Test 2 after small displacements. Table 5.4 shows the comparison of pullout forces generated in Tests 2 and 3 for displacements of point P3 up to 1.0 mm.

It can be observed in Table 5.4 that the pullout forces are similar for 0.20 mm of displacement of P3, but the pullout force in Test 3 is larger than the pullout force in Test 2 for 0.50 and 1.00 mm of displacement of P3. The higher pullout forces in Test 3 indicate engagement of the transverse rib at 0.46L.

The largest difference between the pullout forces is at 0.50 mm. The decrease of the difference in pullout forces after 0.50 mm of displacement of P3 suggests the start of the interference between the transverse ribs. This level of displacement of P3 corresponds to 0.58 Fo/Fmax. Thus, it can be concluded that the interference between transverse ribs is first observed to start at near 60 % of the maximum pullout force.

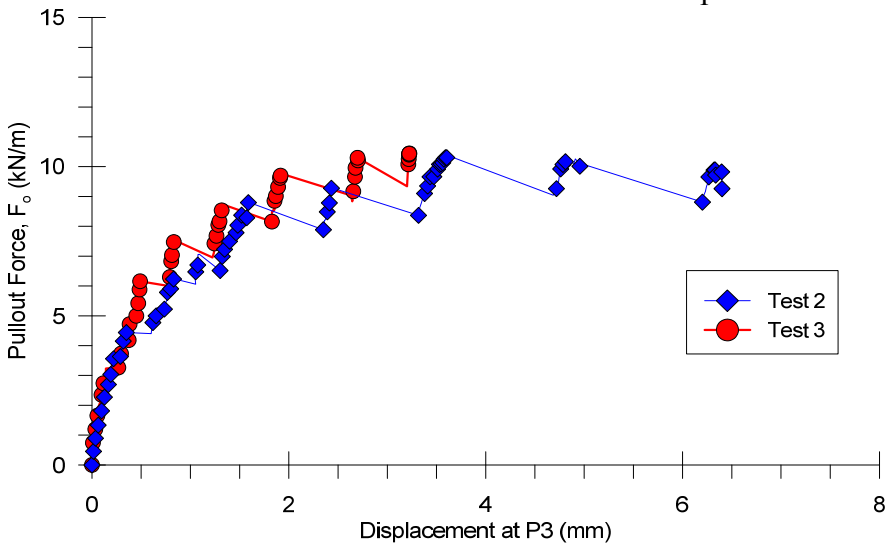


Figure 5.30: Comparison of pullout forces generated in Test 2 and 3 with displacement of point P3 in the geogrids.

| Displacement of P3 (mm) | Generated pullout force (kN/m) | | |
|---|---|---|---|
| | Test 2 (geogrid with no transverse rib) | Test 3 (geogrid with two closely spaced transverse ribs) | Ratio Test 3/Test 2 |
| 0.20 | 3.3 | 3.2 | 0.97 |
| 0.50 | 4.4 | 6.2 | 1.41 |
| 1.00 | 6.1 | 7.2 | 1.18 |

Table 5.4: Comparison of pullout forces generated in Tests 2 and 3 with small displacements of point P3 in the geogrids.

Figure 5.31 presents detailed views of both transverse ribs at different stages of the test: (a) at the beginning of test, (b) at 0.76 Fo/Fmax, and (c) at maximum pullout load at the end of the test. Insignificant deflection of the transverse rib at 0.46L is observed in Figure 5.31, thus insignificant engagement of this transverse rib even at maximum pullout load (Figure 5.31c).

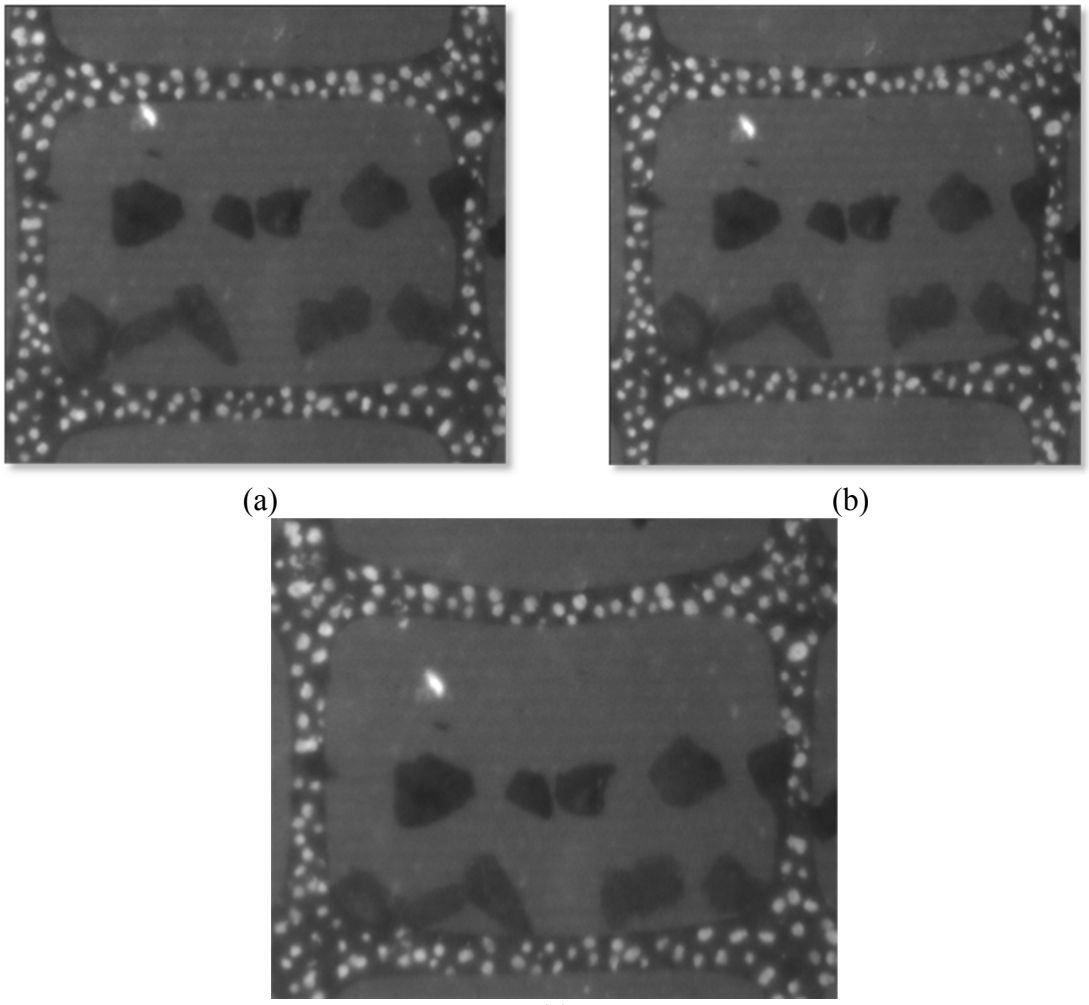

(a) (b)

(c)

Figure 5.31: Close view of the two closely spaced transverse ribs in Test 3 at different stages of the test: (a) 0.00 Fo/Fmax. (b) 0.76 Fo/Fmax. (c) 1.00 Fo/Fmax.

## 5.4 Analysis of Test 4: Geogrid with two largely spaced transverse ribs

The geogrid in this test was used with two largely spaced transverse ribs, 49 mm apart (Figure 5.32). The ratio between the aperture size and the $D_{50}$ of the soil is 12.9 in the region between the transverse ribs. The first transverse rib is located at 0.34L, the same position of the first transverse rib in Test 3. The second transverse rib is located at 0.58L.

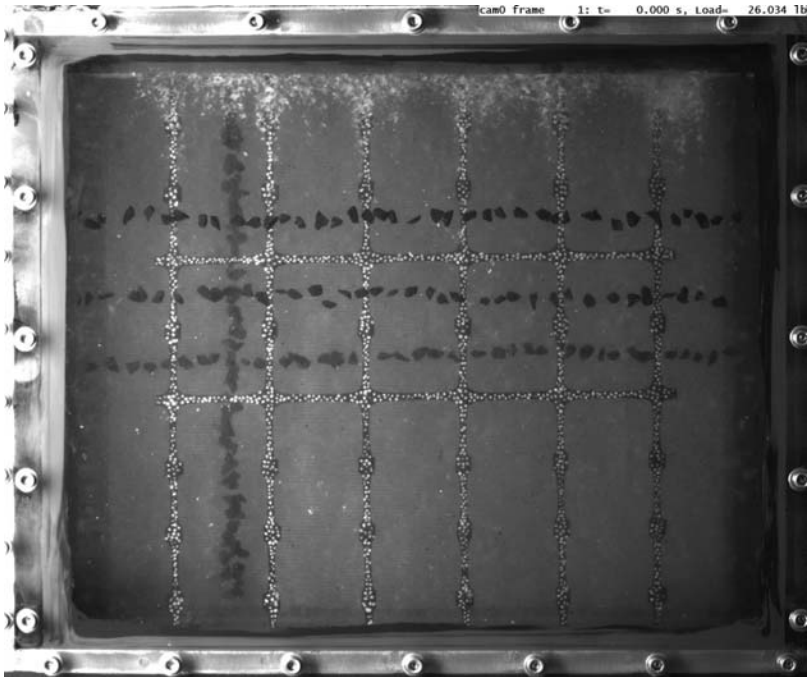


Figure 5.32: Test 4: geogrid with two largely spaced transverse ribs (cam0).

The objective of this test was to evaluate the degree of interference between two largely spaced transverse ribs. This is achieved by comparing the overall engagement of the geogrid and pullout forces generated in this test to the results from Test 3.

### 5.4.1 STRAINS ALONG THE GEOGRID IN TEST 4

Displacements along the longitudinal rib L3 are shown in Figure 5.33. The plots used to obtaining the parameters $\alpha$, $\beta$ and $\gamma$ through linear transformation of the Equation 5.1 are presented in Appendix B.

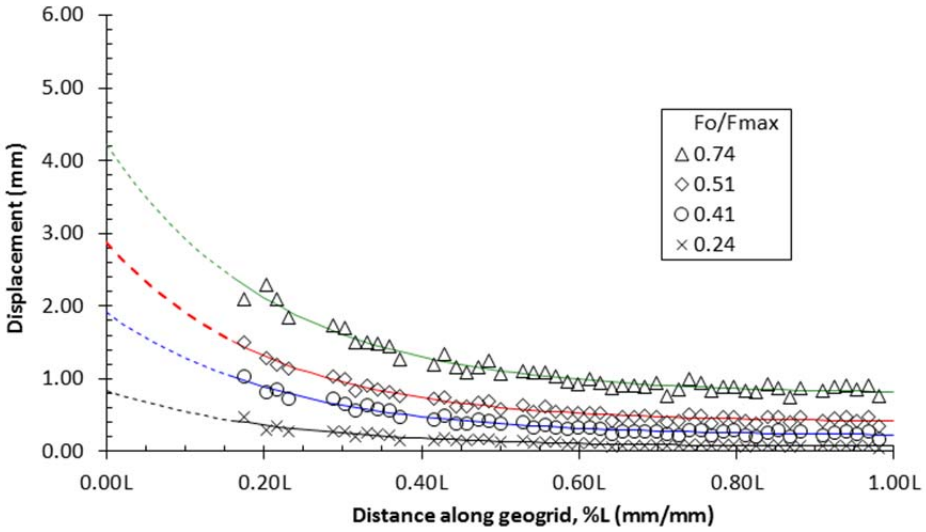


Figure 5.33: Displacement profile along the longitudinal rib L3 in Test 4 (geogrid with two largely spaced transverse ribs). Note: L is the length of the geogrid.

Displacements along the longitudinal rib L4 are shown in Figure 5.34. The plots used to obtaining the parameters $\alpha$, $\beta$ and $\gamma$ through linear transformation of the Equation 5.1 are presented in Appendix B. The displacements observed along L4 (Figure 5.34) are similar to the ones along L3 (Figure 5.33).

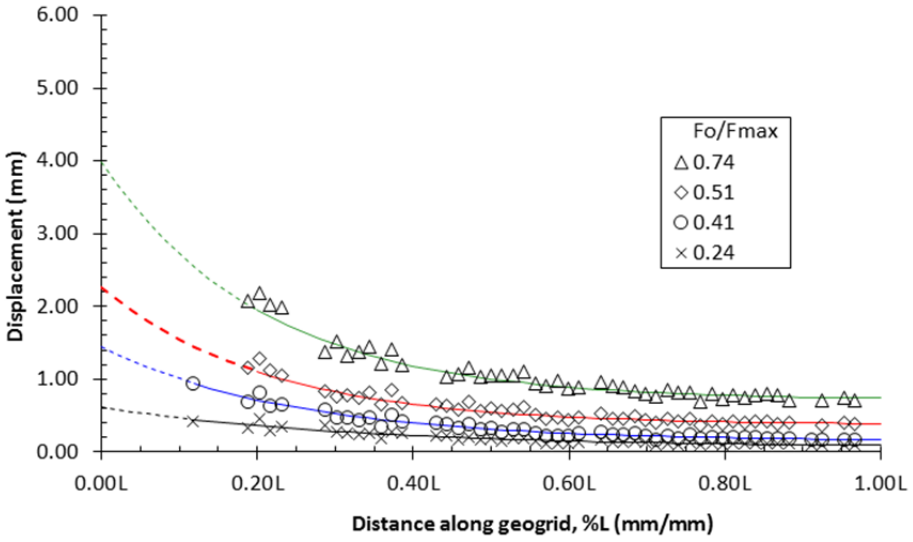


Figure 5.34: Displacement profile along the longitudinal rib L4 in Test 4 (geogrid with two largely spaced transverse ribs). Note: L is the length of the geogrid.

The strains calculated with Equation 5.2 along the ribs L3 and L4 are shown in Figure 5.35 and Figure 5.36, respectively. Differences of strains along L3 and L4 are observed for percentages of the maximum pullout force up to 0.51 Fo/Fmax. On the other hand, similar strains are observed for 0.74 Fo/Fmax.

Figure 5.37 shows the average strains along the geogrid specimen obtained from the strains calculated for L3 and L4. Slightly lower strains are observed in Test 4 (Figure 5.37) than in Test 3 (Figure 5.26). These differences in strains might have been caused by engagement of the second transverse rib in Test 4, which is at 49 mm from the first transverse rib as opposed to the 21 mm between the transverse ribs in Test 3.

Figure 5.38 shows the average strain gradient along the geogrid calculated from the average strains in Figure 5.37. Similar variation of strains in Test 4 and Test 3 are observed for all percentages of the maximum pullout force.

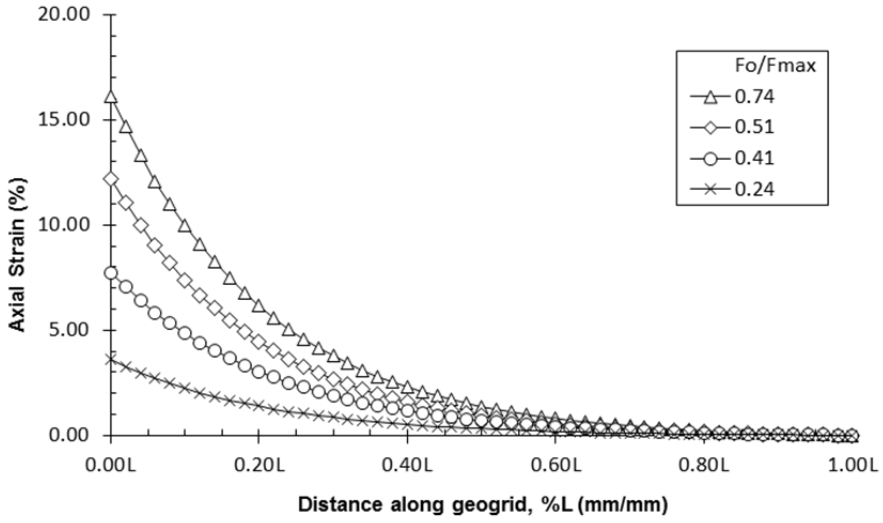


Figure 5.35: Strain profile along the longitudinal rib L3 in Test 4 (geogrid with two largely spaced transverse ribs).

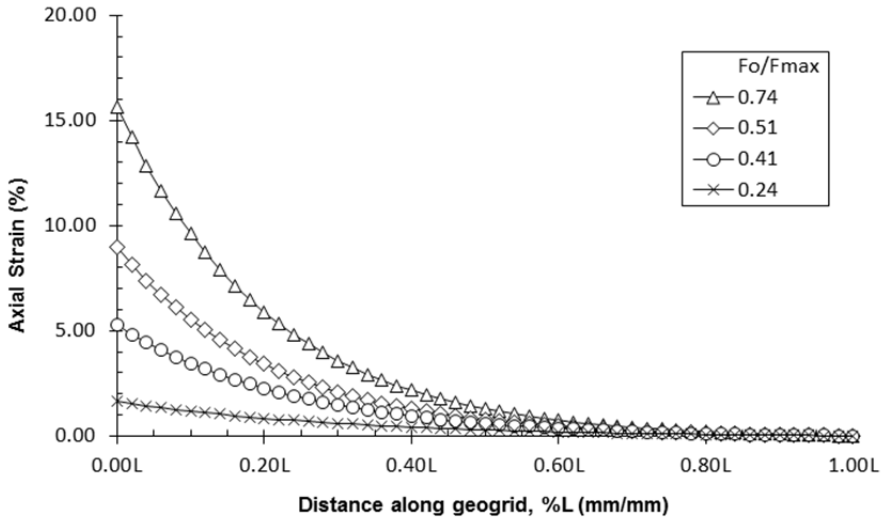


Figure 5.36: Strain profile along the longitudinal rib L4 in Test 4 (geogrid with two largely spaced transverse ribs).

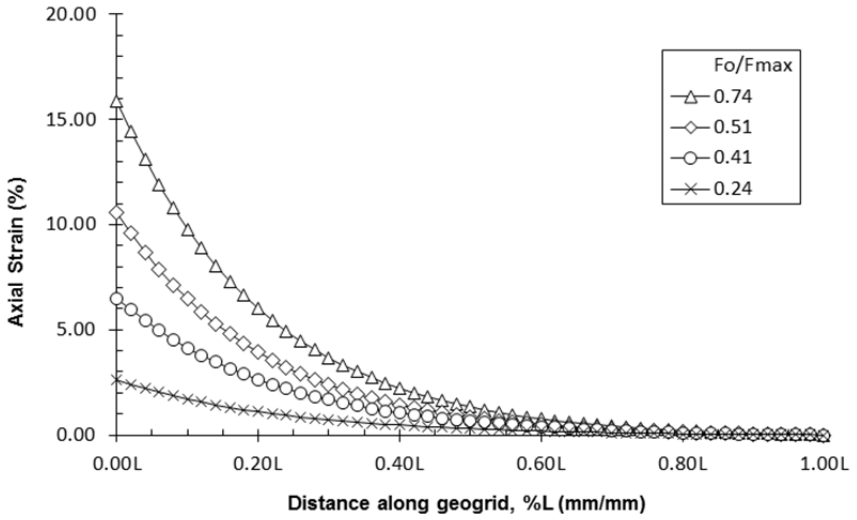


Figure 5.37: Average strain profile of the central longitudinal ribs L3 and L4 in Test 4 (geogrid with two largely spaced transverse ribs).

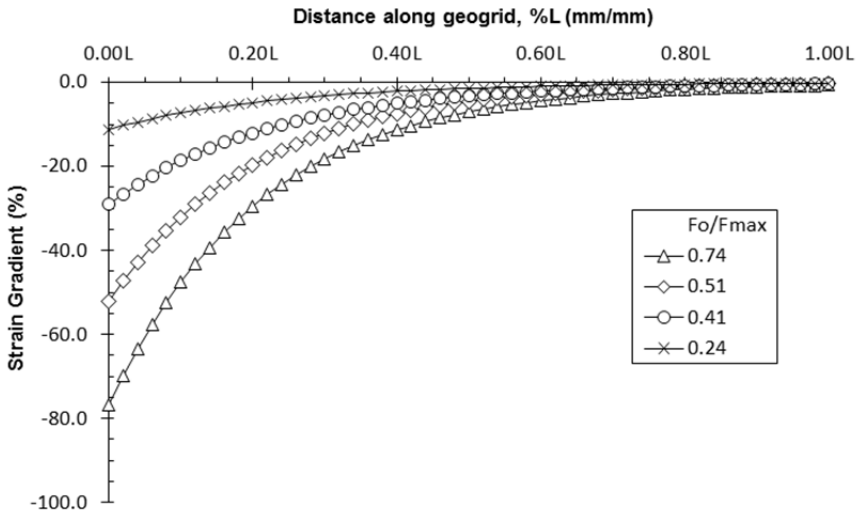


Figure 5.38: Average strain gradient of the central longitudinal ribs L3 and L4 in Test 4 (geogrid with two largely spaced transverse ribs).

### 5.4.2 DISPLACEMENT PROFILE OF THE TRANSVERSE RIBS

Figure 5.39 and Figure 5.40 show the displacements along of the transverse rib at 0.34L and along the transverse rib at 0.58L, respectively. Besides the noise in the measurements of the rib at 0.34L (Figure 5.39), especially at 0.74 Fo/Fmax, the comparison of the displacement profiles of both figures shows larger deflections in the transverse rib at 0.34 L. Small deflections of the transverse rib at 0.58L are observed in Figure 5.40.

To properly evaluate the interference between the transverse ribs, deflections of these ribs need to be analyzed for similar levels of displacements of the ribs. The deflection of the transverse rib at 0.34L is 0.35 mm (0.0138 in.) for near 1.0 mm (0.04 in.) of displacement of the junctions (Figure 5.39). The deflection of the transverse rib at 0.58L is 0.36 mm (0.0142 in.) for near 1.5 mm (0.06 in.) of displacement of the junctions (Figure 5.40). Thus, the transverse ribs behave as isolated ribs and similar deflections are observed in the transverse ribs for similar levels of displacement of the junctions.

Table 5.5 shows a comparison of the pullout forces generated in each for different stages of the tests. It would be expected that the pullout force in Test 4 to be larger than the pullout force in Test 3 for the later stages of Test 4, when displacements start to occur at the junction of the transverse rib at 0.58L. However, the forces are similar for all stages of the tests (Table 5.5).

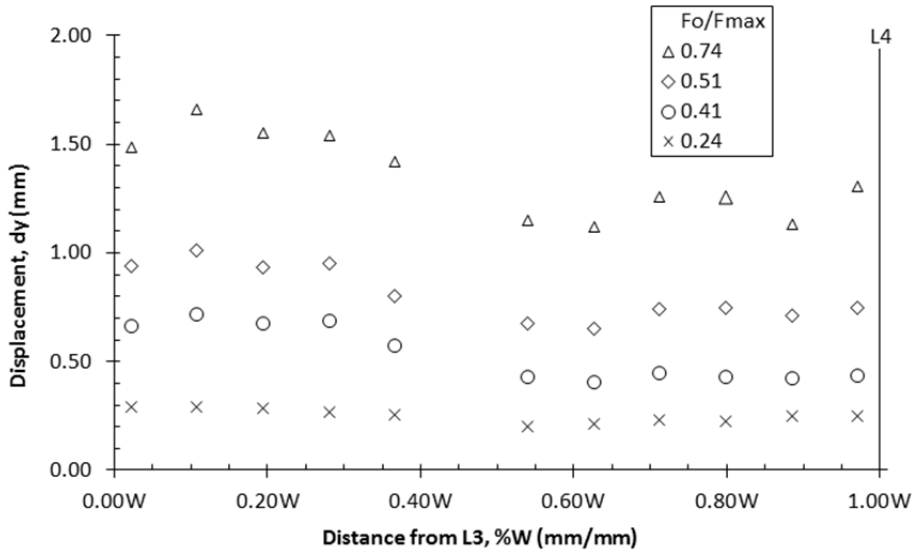


Figure 5.39: Displacement profile of the transverse rib located at 0.34L in Test 4 (geogrid with two largely spaced transverse ribs). Note: W is the distance between the longitudinal ribs L3 and L4.

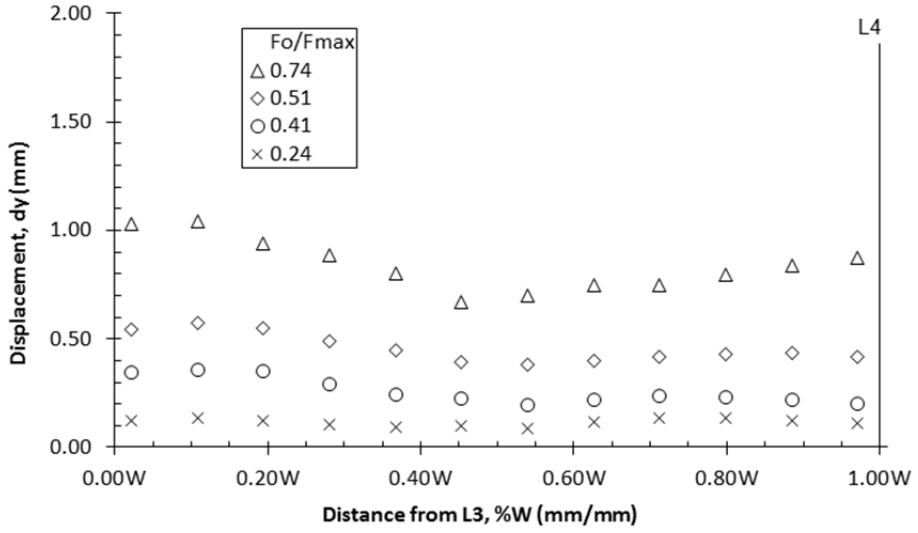


Figure 5.40: Displacement profile of the transverse rib located at 0.58L in Test 4 (geogrid with two largely spaced transverse ribs). Note: W is the distance between the longitudinal ribs L3 and L4.

| Percentage (%) Fmax | Generated pullout force (kN/m) | | |
|---|---|---|---|
| | Test 3 (geogrid with two closely spaced transverse ribs) | Test 4 (geogrid with two largely spaced transverse ribs) | Ratio Test 4/Test 3 |
| 25 | 2.7 | 2.6 | 0.96 |
| 40 | 4.4 | 4.4 | 1.00 |
| 50 | 5.7 | 5.4 | 0.95 |
| 75 | 8.1 | 8.0 | 0.99 |
| 100 | 10.7 | 10.7 | 1.00 |

Table 5.5: Comparison of pullout forces generated in Tests 3 and 4.

A better comparison of the pullout forces generated in both tests may be obtained by analyzing the force generated for displacements of the reference point P3 in the geogrid in both tests (Figure 5.41). It can be observed in this figure that the pullout force in Test 4 becomes slightly larger than the pullout force in Test 3 with increasing displacements of P3. Table 5.6 shows the comparison of pullout forces generated in Tests 3 and 4 for displacements of P3 up to 1.0 mm.

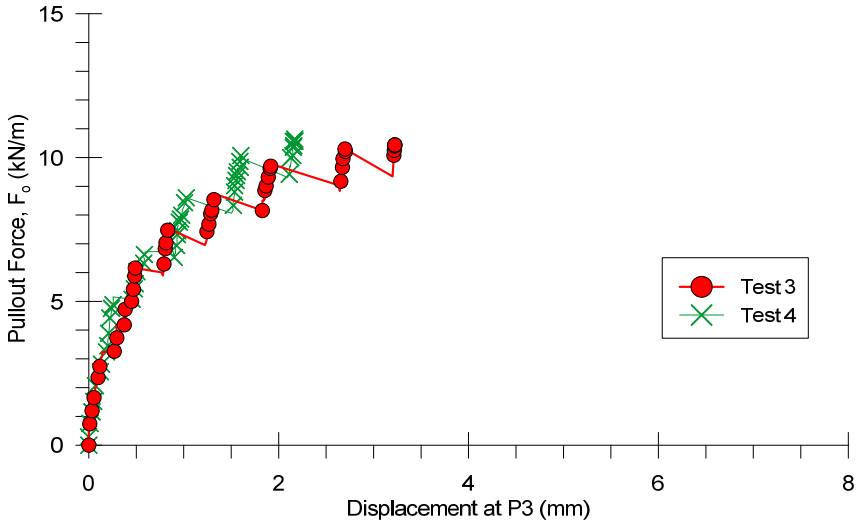


Figure 5.41: Comparison of pullout forces generated in Tests 4 and 3 with displacement of point P3 in the geogrids.

| Displacement of P3 (mm) | Generated pullout force (kN/m) | | |
|---|---|---|---|
| | Test 3 (geogrid with two closely spaced transverse ribs) | Test 4 (geogrid with two largely spaced transverse ribs) | Ratio Test 4/Test 3 |
| 0.20 | 3.2 | 3.5 | 1.09 |
| 0.50 | 6.2 | 6.1 | 0.98 |
| 1.00 | 7.2 | 8.3 | 1.15 |

Table 5.6: Comparison of pullout forces generated in Tests 4 and 3 with small displacements of point P3 in the geogrids.

It can be observed in Table 5.6 that the pullout forces are similar up to 0.50 mm of displacement of P3, and the force in Test 4 becomes larger than in Test 3 for 1.00 mm of displacement of P3. These results show the contribution of the transverse rib at 0.58L to the pullout force generated in Test 4 starting at 1.00 mm of displacement of P3.

Although the maximum pullout forces generated in both tests were similar (10.7 kN/m for 1.00 Fo/Fmax in Table 5.5), the shape of the pullout curves for Test 4 (Figure 5.42a) suggests that a higher pullout force could be generated, had the premature breakage of the junction of L2 not occurred. This is not the case for Test 3, in which the maximum pullout force for this test was reached before breakage of the junction of L3 (Figure 5.42b). Additionally, similar pullout forces and strains along the geogrid were generated in Test 4 and Test 3, but for smaller displacements in Test 4 than in Test 3.

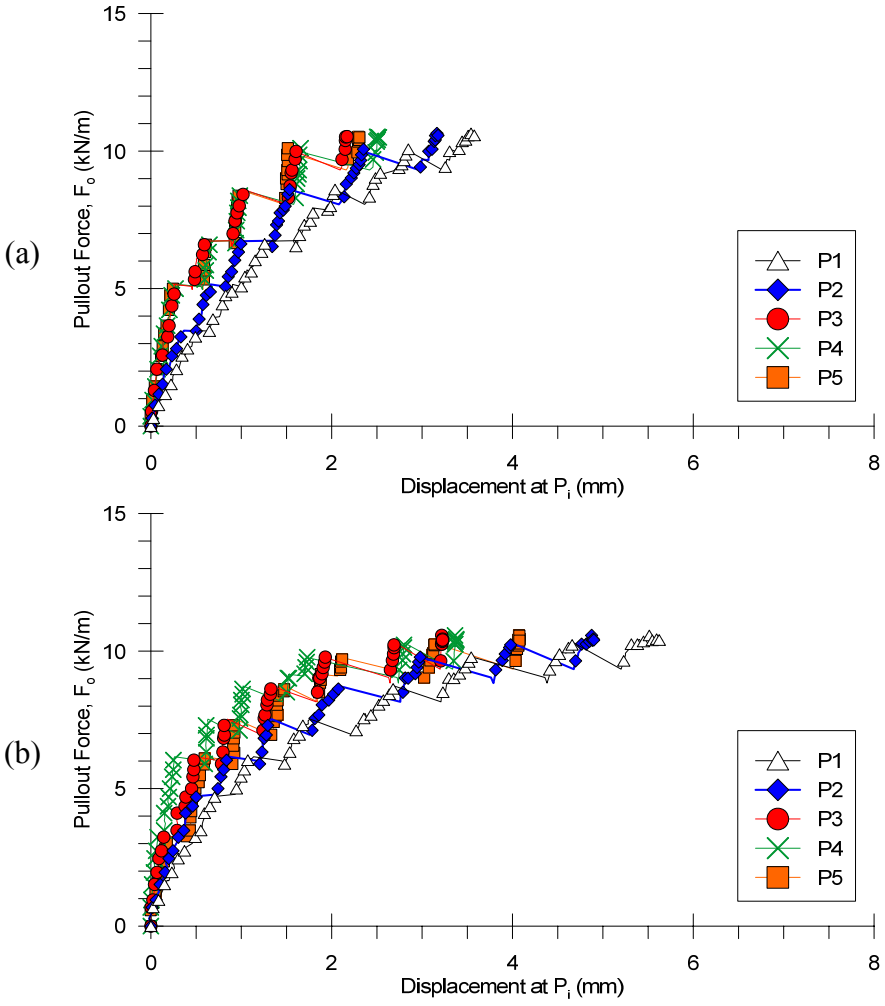


Figure 5.42: Pullout curves from (a) Test 4 (geogrid with two largely spaced transverse ribs) and (b) Test 3 (geogrid with two closely spaced transverse ribs).

These results show that the soil-geogrid interaction was more efficient in Test 4 than in Test 3. Thus, it can be concluded that insignificant interference between the transverse ribs was observed in Test 4, in which the ratio of spacing between transverse ribs (S) over the $D_{50}$ of the soil is12.9. The average measured thickness of the transverse ribs (B) is 0.86 mm. Thus, the ratio S/B is 57.

This insignificant interference between transverse ribs for a S/B ratio of 57 observed in Test 4 agrees with the suggestion by Palmeira and Milligan (1989) that the

interference would become negligible for S/B ratios above 50. Therefore, the transverse ribs in Test 4 behave as isolated ribs.

Figure 5.43 shows a detailed view of the transverse ribs at different stages of the test: (a) at the beginning of the test, (b) at 0.74 Fo/Fmax, and (c) at the end of the test. It can be observed in this figure the small deflection of the transverse at 0.58L when the maximum pullout force of the test is reached (Figure 5.43c). Significantly larger deflections are observed in the transverse rib at 0.34L because larger displacements occur at the junctions of this rib (Figure 5.43).

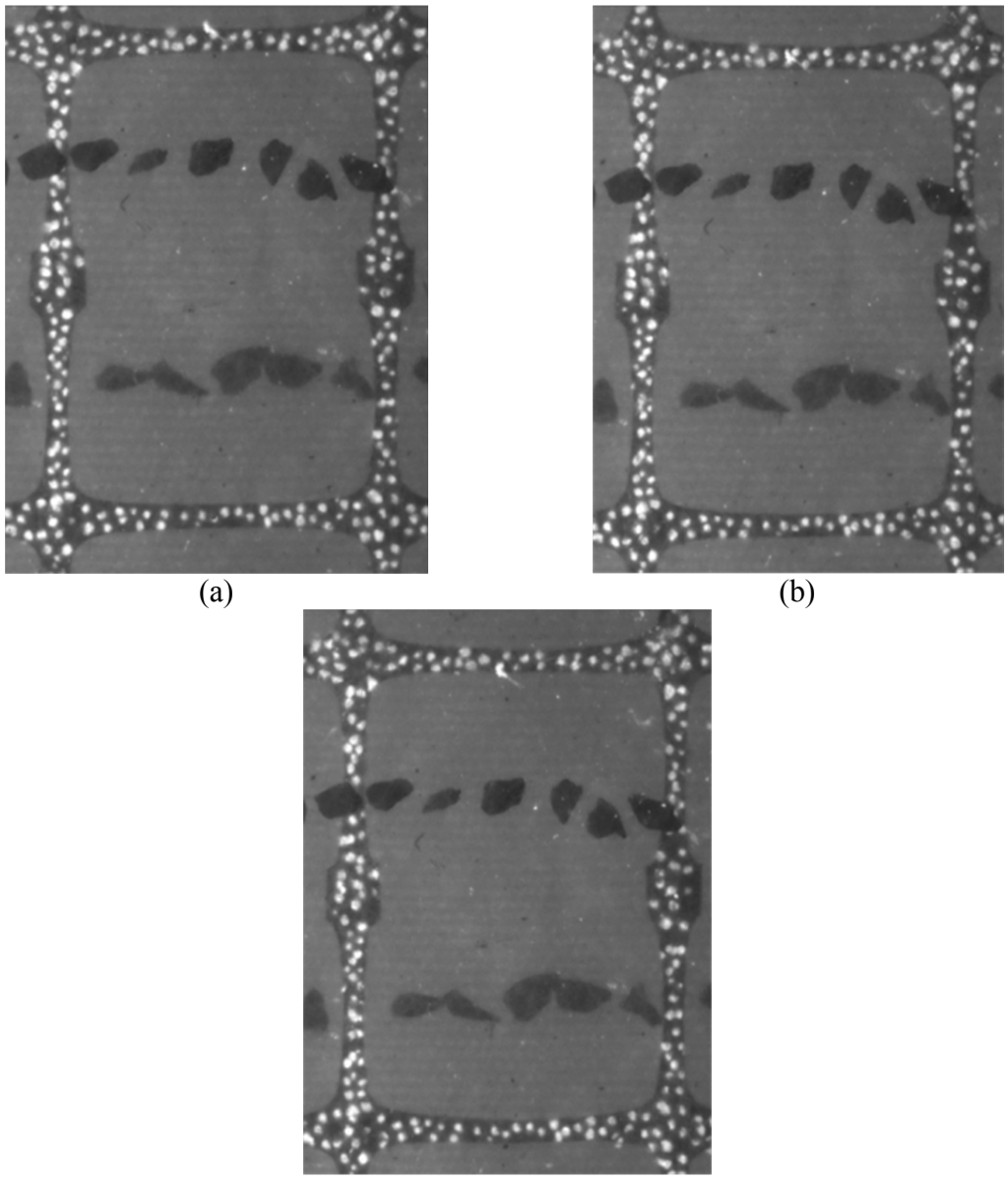

(a) (b)

(c)

Figure 5.43: Detailed view of the two largely spaced transverse ribs in Test 4 at 0.34L and 0.58L at different stages of the test: (a) 0.00 Fo/Fmax. (b) 0.74 Fo/Fmax. (c) 1.00 Fo/Fmax.

## 5.5 Analysis of Test 5: Geogrid with 8 closely spaced transverse ribs

The geogrid in this test was used with no modifications. The transverse ribs were present along the entire length of the geogrid specimen with its original aperture size of 21 mm between transverse ribs. The ratio between the aperture size and the $D_{50}$ of the soil is 5.5. The geogrid in this test had a total of eight transverse ribs (Figure 5.44).

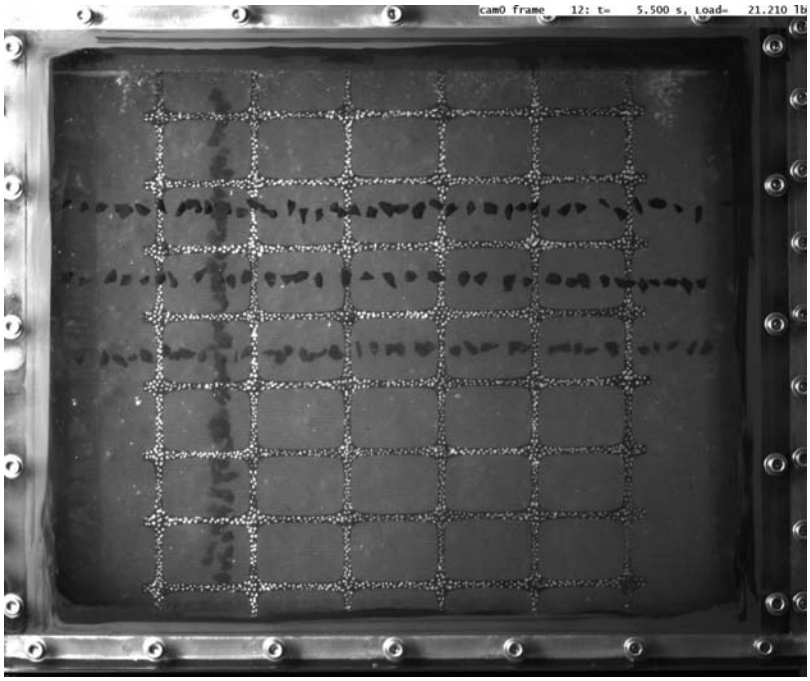


Figure 5.44: Test 5: geogrid with eight closely spaced transverse ribs along the entire geogrid specimen (cam0).

The objective of this test was to evaluate the behavior of a geogrid in conditions that would normally be tested (without modifications) and to compare its behavior to the behavior observed in the previous tests.

### 5.5.1 STRAINS ALONG THE GEOGRID IN TEST 5

Displacements along the longitudinal rib L3 are shown in Figure 5.45. The plots used to obtaining the parameters $\alpha$, $\beta$ and $\gamma$ through linear transformation of the Equation 5.1 are presented in Appendix B. Significant smaller displacements were observed in Test 5 than all other tests for all percentages of the maximum pullout force.

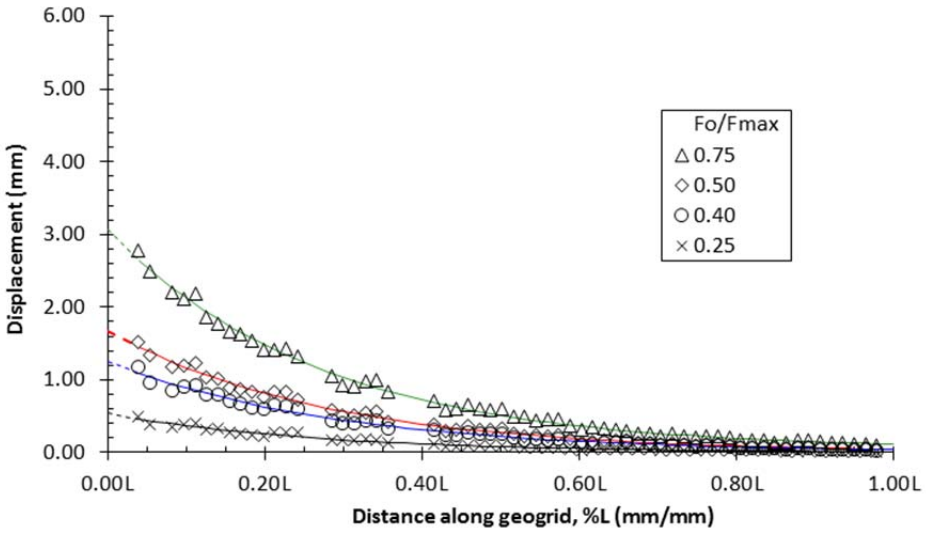


Figure 5.45: Displacement profile along the longitudinal rib L3 in Test 5 (geogrid with eight closely spaced transverse ribs).

Displacements along the longitudinal rib L4 are shown in Figure 5.46. The plots used to obtaining the parameters $\alpha$, $\beta$ and $\gamma$ through linear transformation of the Equation 5.1 are presented in Appendix B. Smaller variations were observed between displacements along L3 and L4 than for all other tests. These smaller variations may be due to the continuous, good quality data obtained near the active end of the geogrid, and especially at L3 (Figure 5.45).

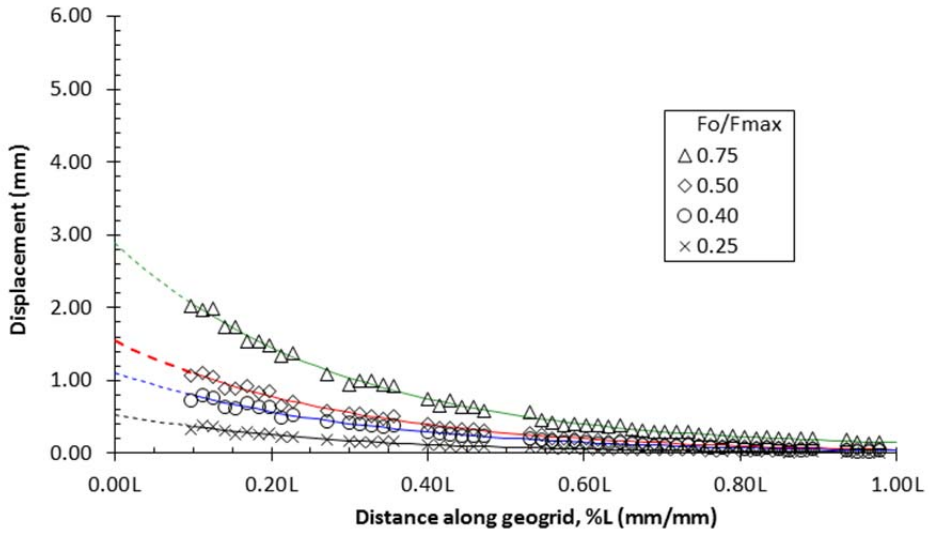


Figure 5.46: Displacement profile along the longitudinal rib L4 in Test 5 (geogrid with eight closely spaced transverse ribs).

The strains calculated with Equation 5.2 along the ribs L3 and L4 are shown in Figure 5.47 and Figure 5.48, respectively. Similar results are observed in Figure 5.47 and Figure 5.48. Figure 5.49 shows the average strains along the geogrid specimen obtained from the strains calculated for L3 and L4.

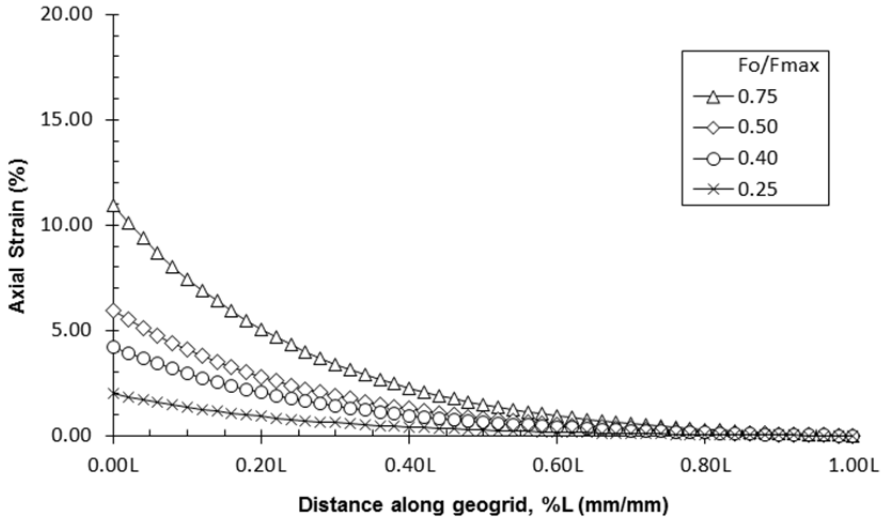


Figure 5.47: Strain profile along the longitudinal rib L3 in Test 5 (geogrid with eight closely spaced transverse ribs).

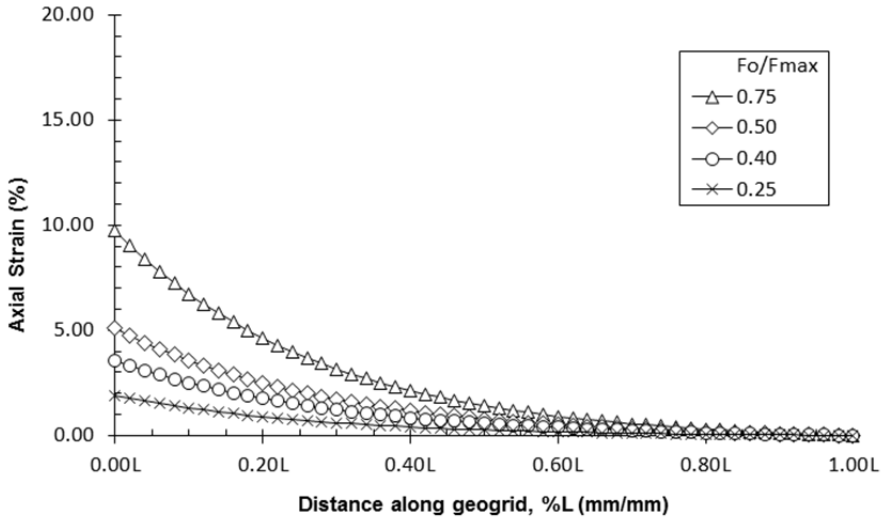


Figure 5.48: Strain profile along the longitudinal rib L4 in Test 5 (geogrid with eight closely spaced transverse ribs).

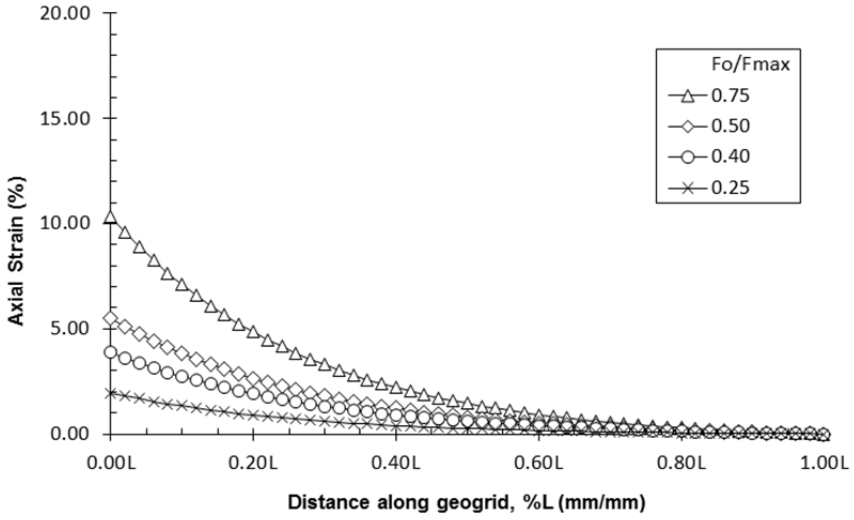


Figure 5.49: Average strain profile of the central longitudinal ribs L3 and L4 in Test 5 (geogrid with eight closely spaced transverse ribs).

Significant smaller strains are observed in Test 5 than all other tests, mainly at the higher percentages of the maximum pullout force of 0.50 and 0.75 Fo/Fmax. Smaller strains in Test 5 than all other tests are also observed for 0.40 Fo/Fmax. This shows the improvement of soil-geogrid interaction with the presence of transverse ribs along the entire length of the geogrid specimen. The improvement of this interaction translates into more stresses being transmitted to the surrounding soil through shearing stress onto the soil mass.

Figure 5.50 shows the average strain gradient along the geogrid calculated from the average strains in Figure 5.49. The strain gradient observed in this test was significantly smaller than all other tests.

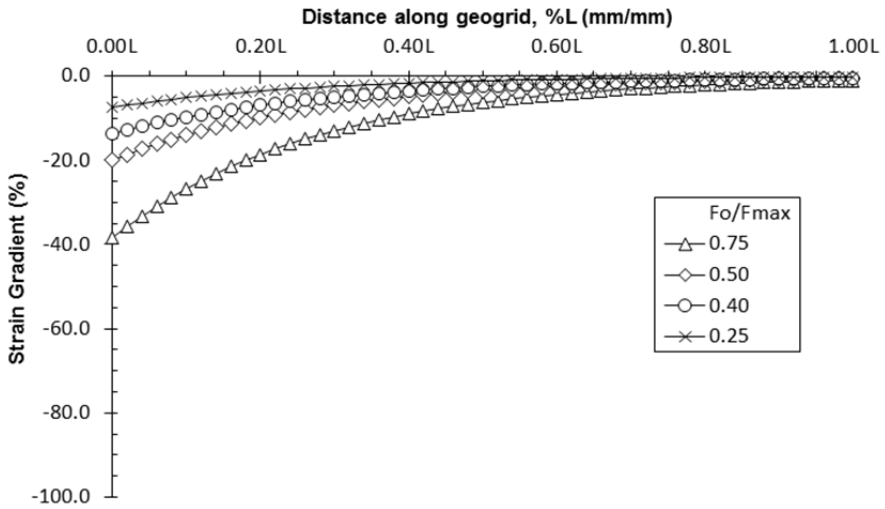


Figure 5.50: Average strain gradient of the central longitudinal ribs L3 and L4 in Test 5 (geogrid with eight closely spaced transverse ribs).

### 5.5.2 DISPLACEMENT PROFILE OF THE TRANSVERSE RIBS

Figure 5.51 to Figure 5.55 show the displacement profiles of the transverse ribs located from 0.08L to 0.57L. Higher scatter is observed on the displacement data from the transverse rib at 0.08L because this is the transverse rib subjected to the largest displacements. Thus, this rib is more susceptible to scratching and unbinding of the white dots on the rib due to friction against the sharp edges of the adjacent fused quartz particles.

At 0.75 Fo/Fmax, the transverse rib at 0.08L (Figure 5.51) deflects more than the transverse rib at 0.20L (Figure 5.52); which in turn deflects more than the transverse rib at 0.33L (Figure 5.53). However, this transverse rib at 0.33L (Figure 5.53) deflects less than the transverse rib at 0.44L (Figure 5.54) despite the larger displacements observed for the transverse rib at 0.33L. Then, the initial pattern of smaller deflections observed in

ribs further away from the active end of the geogrid is observed again. The transverse rib at 0.44L (Figure 5.54) deflects more than the rib at 0.57L (Figure 5.55).

These observations from Figure 5.51 to Figure 5.55 exemplify the complexity involving soil-geogrid interaction and the interference between transverse ribs. These results show that there is high interference between transverse ribs when they are closely spaced, as it was observed in Test 3. However, the pattern of this interference is complex. It was expected that the further away a transverse rib is from the active end of the geogrid, the smaller is the deflection on the rib. This was not observed when comparing Figure 5.53 (transverse rib at 0.33L) to Figure 5.54 (transverse rib at 0.44L). The transverse rib at 0.44L (Figure 5.54) had greater deflection than the transverse rib at 0.33L (Figure 5.53), in spite of the smaller displacements of the rib at 0.44L.

These results suggest that, for closely spaced transverse ribs, there is a decrease in the size of the disturbed zone behind the ribs located further away from the active end of the geogrid (in this case, ribs located from 0.08L to 0.33L). Then, after a certain point, this zone behind a transverse rib becomes significantly less disturbed, so that the next transverse rib becomes more engaged (in this case, the transverse ribs at 0.44L). After that, this transverse rib that is more engaged than the previous one, leaves behind a disturbed zone of soil that prevents the transverse rib after (in this case, rib at 0.57L) to fully develop its bearing stress capacity.

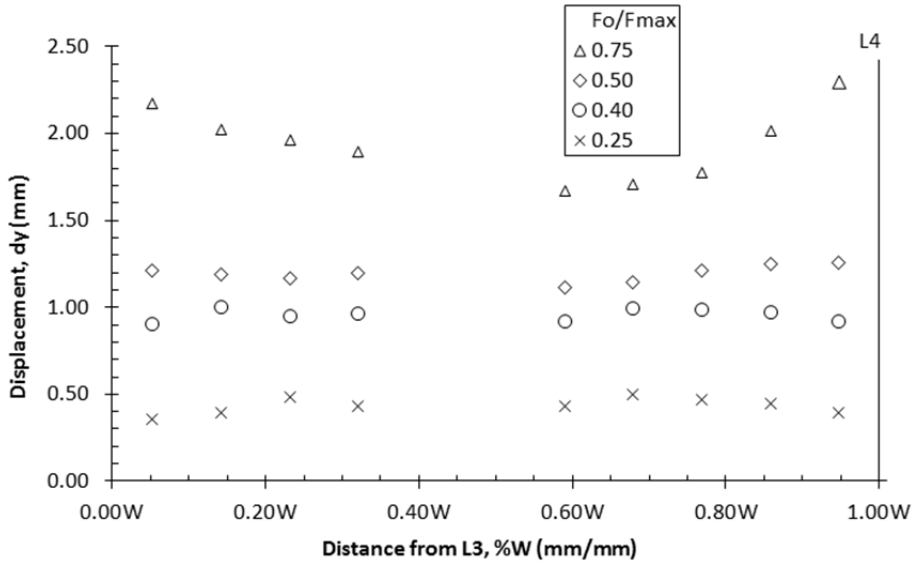


Figure 5.51: Displacement profile of the transverse rib located at 0.08L in Test 5 (geogrid with eight closely spaced transverse ribs). Note: Lack of data points between 0.35W and 0.55W due to lumps of modeling clay covering the rib.

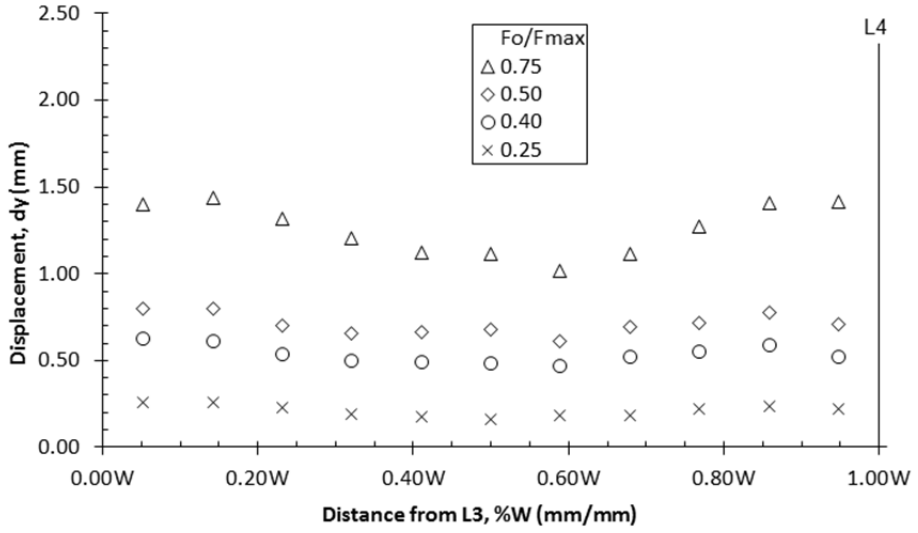


Figure 5.52: Displacement profile of the transverse rib located at 0.20L in Test 5 (geogrid with eight closely spaced transverse ribs).

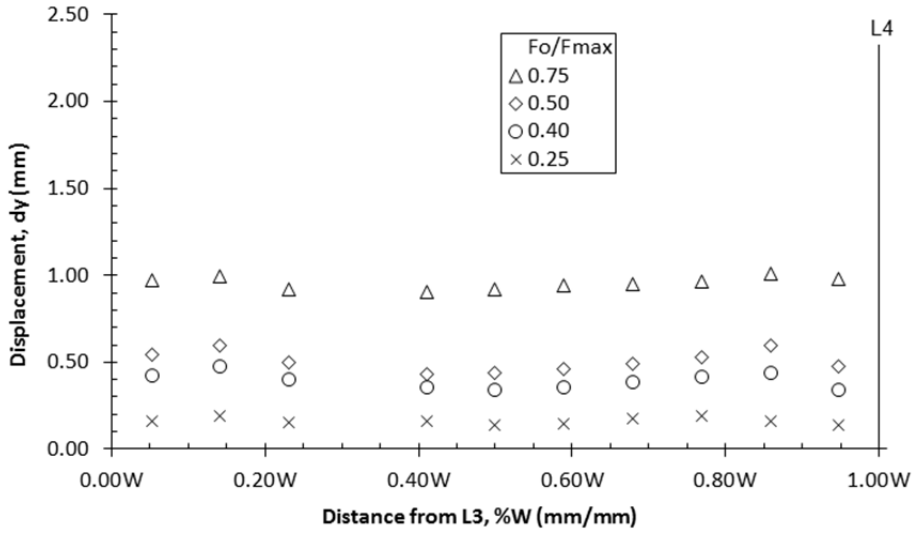


Figure 5.53: Displacement profile of the transverse rib located at 0.33L in Test 5 (geogrid with eight closely spaced transverse ribs).

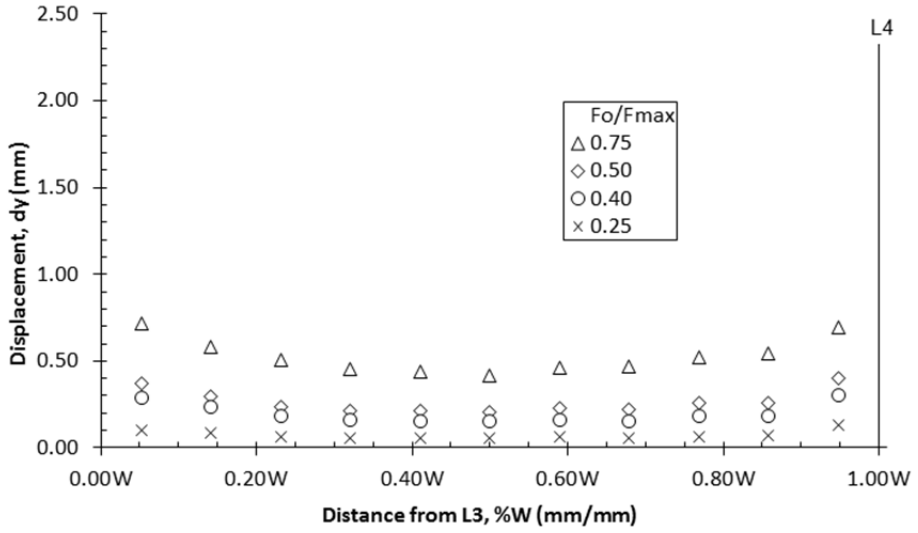


Figure 5.54: Displacement profile of the transverse rib located at 0.44L in Test 5 (geogrid with eight closely spaced transverse ribs).

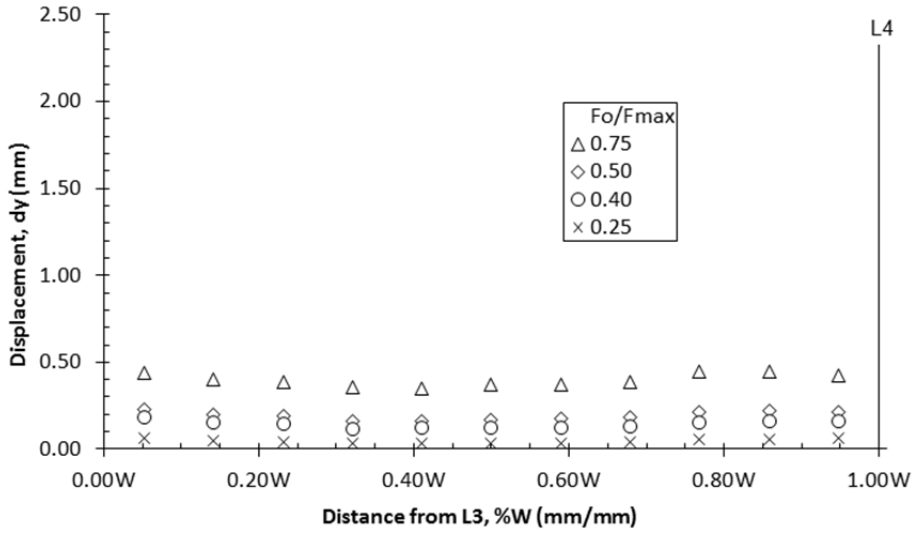


Figure 5.55: Displacement profile of the transverse rib located at 0.57L in Test 5 (geogrid with eight closely spaced transverse ribs).

It should be emphasized that the observations above are for the higher percentages of the maximum pullout force of 0.75 Fo/Fmax. Small deflections are observed for all transverse ribs at 0.40 and 0.50 Fo/Fmax. Insignificant deflections were observed at 0.25 Fo/Fmax.

Figure 5.56 presents a detailed view of transverse ribs located from 0.08L to 0.57L at different stages of the test: (a) at 0.00 Fo/Fmax, (b) at 0.75 Fo/Fmax, and (c) at 1.00 Fo/Fmax. The larger deflections of the first two transverse ribs (ribs at 0.08L and 0.20L) are observed starting at 0.75 Fo/Fmax (Figure 5.56b and Figure 5.56c). The different deflections between transverse ribs at 0.33L and 0.44L (third and fourth rib from top-down in Figure 5.56) are not visually distinguishable in the images.

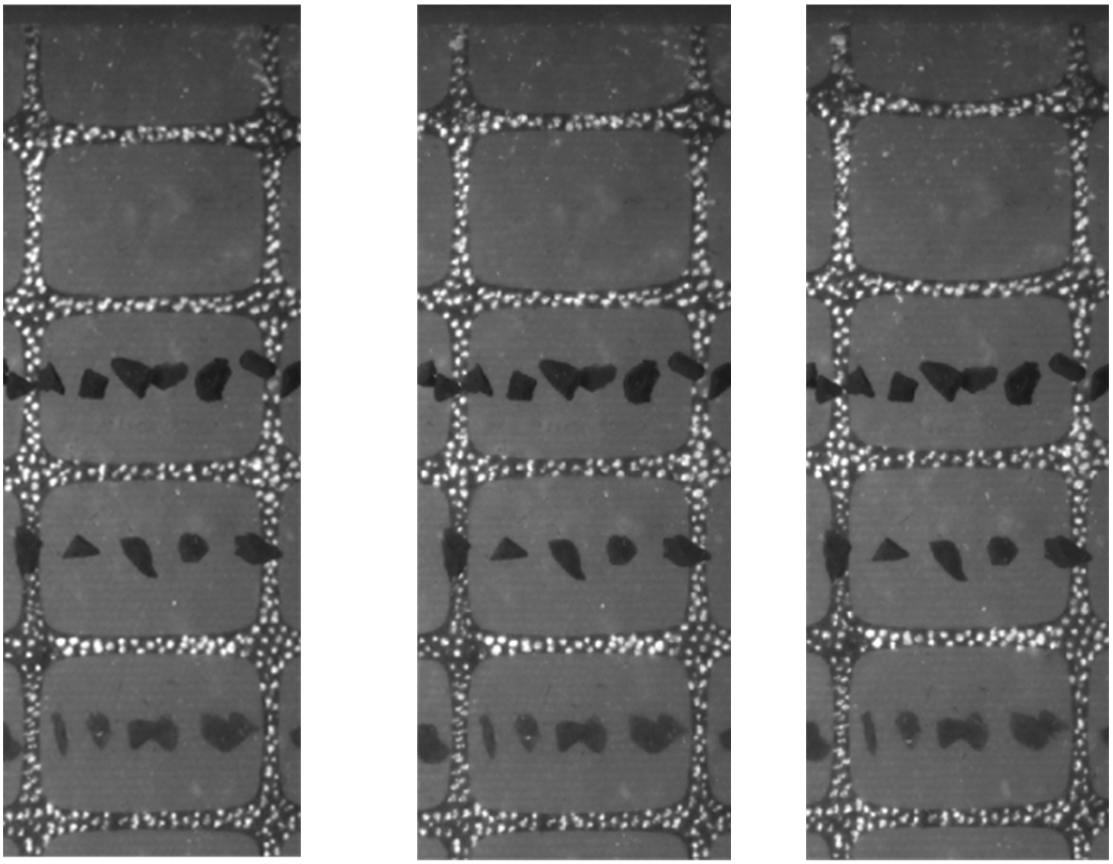

(a) (b) (c)

Figure 5.56: Close view of the transverse ribs located from $x$ = 0.08L to $x$ = 0.57L at different stages of the test: (a) 0.00 Fo/Fmax. (b) 0.75 Fo/Fmax. (c) 1.00 Fo/Fmax.

Additionally, besides the high interference between the eight closely spaced transverse ribs in Test 5, the soil-geogrid interaction is better in Test 5 than in Test 4, which had two largely spaced transverse ribs. Figure 5.57 shows the pullout forces generated in both tests with the displacement of the point P3 in the geogrids (see Figure 4.6). The pullout forces generated in Test 5 are significantly larger than the forces

generated in Test 4 for all ranges of displacement of P3. This difference is better observed with the data shown in Table 5.7.

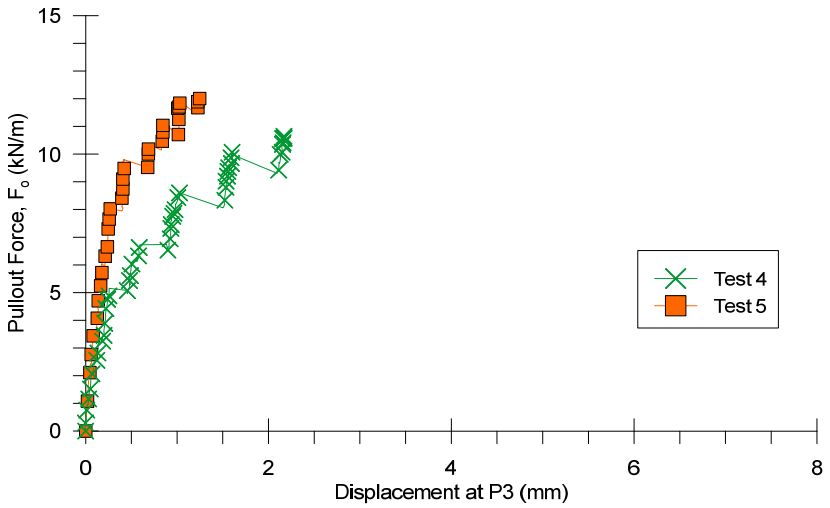


Figure 5.57: Comparison of pullout forces generated in Tests 5 and 4 with displacement of point P3 in the geogrids.

It can be observed in Table 5.7 that the pullout forces in Test 5 are significantly larger than the forces in Test 4, but this difference decreases with displacement of P3. This decrease can be explained by the higher interference between the transverse ribs in Test 5 with larger displacements of the geogrid. As the displacement increase, larger zones of disturbed soil are generated.

| Displacement of P3 (mm) | Generated pullout force (kN/m) | | |
|---|---|---|---|
| | Test 4 (geogrid with two largely spaced transverse ribs) | Test 5 (geogrid with eight closely spaced transverse ribs) | Ratio Test 5/Test 4 |
| 0.20 | 3.5 | 5.9 | 1.69 |
| 0.50 | 6.1 | 9.6 | 1.57 |
| 1.00 | 8.3 | 10.7 | 1.29 |

Table 5.7: Comparison of pullout forces generated in Tests 5 and 4 with small displacements of point P3 in the geogrids.

## 5.6 Additional Remarks

The average strain profiles for all tests are assembled together in Figure 5.58. The strains along the geogrid length were calculated with the following exponential equation:

$$\varepsilon = \frac{\beta}{\gamma} e^{(-x/\gamma)} \quad (5.2)$$

Where $\beta$ and $\gamma$ are parameters obtained for each percentage of the maximum pullout force by fitting Equation 5.1 to the displacement profile data, and $x$ is the location along the geogrid specimen.

The shape of the strain profile of the geogrids calculated for the transparent pullout tests conducted in this research is different than the strain profiles reported by Chang et al. (1995), Ezzein and Bathurst (2011b) and Palmeira (2009). Chang et al. (1995) reported a triangular distribution of strains along the geogrid. However, the strains were obtained in only 3 points along a HDPE uniaxial geogrid specimen.

The boundary conditions of the tests performed by Ezzein and Bathurst (2011b) are significantly different than the ones in the present study. The authors tested geogrids with the passive end of the specimen (the one furthest away from the application of the pullout force) attached to a rear grip. Thus, strains are developed at the passive end of the geogrid in their tests. There are no strains developed at the passive end of the geogrid of the present study since it is free to move. Also, the dimensions of the transparent pullout apparatus performed by Ezzein and Bathurst (2011b) are several orders of magnitude larger than the dimensions of the apparatus used in the present study.

The strain distribution along geogrids reported by Palmeira (2009) is the one that approximates the most to the strain distribution calculated in the present research. This occurred in spite of the significantly different dimensions between the setup of the test

from Palmeira (2009) and the transparent pullout tests in the present research. The pullout test reported by Palmeira (2009) was conducted in a 1 $m^3$ (35 $ft^3$) pullout box, and a HDPE uniaxial geogrid specimen that was 600 mm long embedded in dense sand. The transparent tests were conducted in a 0.011 $m^3$ (0.39 $ft^3$) pullout box, and polypropylene biaxial geogrids that were 232 mm long embedded in the transparent soil that can be compared to dense coarse sand. Another difference between the results is that Palmeira (2009) showed only 5 data points and no curve was fitted to the data.

The test setup of the strain profile reported by Palmeira (2009) has dimensions comparable to those recommended by the ASTM D6706 for traditional, large pullout tests. Thus, the relative degree of similarity between the strain profiles from the present research, and the strain profile reported by Palmeira (2009), creates a positive prospect on extrapolating the results from tests with the developed transparent pullout test setup to tests with natural soils. However, more research is needed to verify this possibility.

Figure 5.58 shows that the strains developed along the geogrid are smaller in Test 5 than for all other tests starting around 0.75 Fo/Fmax. This shows the improvement of soil-geogrid interaction with the presence of transverse ribs along the entire geogrid length. This decrease in strains is also due to the increase in rigidity of the geogrid specimen because of the presence of more transverse ribs equally distributed along the geogrid.

For the intermediate percentages of the maximum pullout force, around 0.40 and 0.50 Fo/Fmax, Figure 5.58 shows that the strains developed along the geogrid are significantly smaller in Test 5 than for all other tests, except for Test 1. On the other hand, strains are similar for the lower percentages of the maximum pullout force near 0.25 Fo/Fmax.

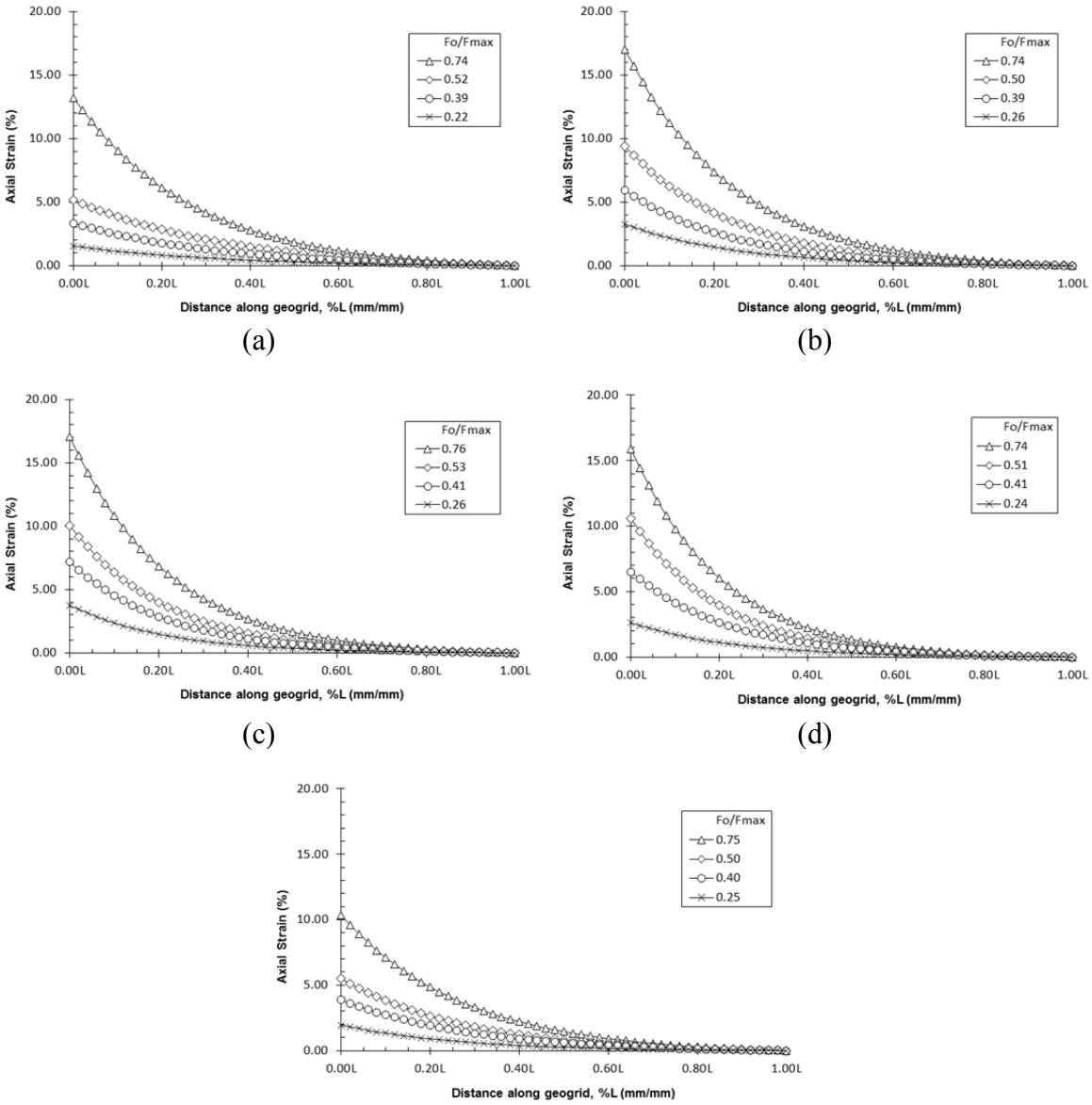


Figure 5.58: Average strain profiles of (a) Test 1, (b) Test 2, (c) Test 3, (d) Test 4, and (e) Test 5.

It can be noted in Figure 5.58 that strains developed in Test 5 (Figure 5.58e) are similar to strains developed in Test 1 (Figure 5.58a) for percentages of the maximum pullout force up to near 0.50 Fo/Fmax. Ignoring the results from Tests 2 to 4 and doing a direct comparison of the results in Test 1 and 5, would suggest that only the interface friction mechanism along the longitudinal ribs develops at lower percentages of the maximum pullout force; with the bearing stress mechanism against the transverse ribs developing only at the higher percentages of the maximum pullout force of 0.75 Fo/Fmax. However, such conclusions would ignore the gain in stiffness of the geogrid specimen in Test 5 due to the presence of several transverse ribs.

Comparing the results from Tests 2 to 4 (Figure 5.58b to d) with the results of Test 1 (Figure 5.58a), it is observed that the transverse ribs also contribute to soil-geogrid interaction also at low percentages of the maximum pullout force. This observation is supported by the deflections observed in the displacement profiles of the transverse ribs in Tests 2 to 4 (Figure 5.17, Figure 5.28, Figure 5.29, Figure 5.39 and Figure 5.40). The presence of one or two transverse ribs improves soil-geogrid interaction at the percentages of the maximum pullout force near 0.25 Fo/Fmax and 0.40 Fo/Fmax. The presence of the transverse ribs requires more shear strength to be applied to the surrounding soil for the geogrid to move. As a result, the engagement of the longitudinal ribs shown by the larger strains developed along the geogrid in Tests 2 to 4 are better than those in Test 1 (Figure 5.58b to Figure 5.58d).

Contrary to the results of this research, Chang et al. (1995), Farrag et al. (1993), Palmeira (2004) and Teixeira et al. (2007) concluded that the bearing mechanism against transverse ribs start to develop only at relatively large displacements. These studies concluded that the interface friction mechanism is the most responsible for soil-geogrid interaction at low percentages of the maximum pullout force. However, Palmeira (2004)

and Teixeira et al. (2007) pointed out that the bearing mechanism against transverse ribs interferes with the mechanism of interface friction along longitudinal ribs. However, none of the studies specified at what percentages of the maximum pullout force starts to occur the interference between different mechanisms.

On the other hand, the results in the present study are in agreement with the studies mentioned above in that the bearing mechanism interferes with the interface friction mechanism. The difference between the findings of this study and the aforementioned studies is that this interference was first observed to occur at 60 % of the maximum pullout force.

Also, Chang et al. (1995), Farrag et al. (1993), Palmeira (2004) and Teixeira et al. (2007) seem to not have taken into account the gain in in-plane stiffness of a geogrid specimen composed of several transverse ribs in relation to a geogrid specimen composed only of longitudinal ribs. Evidence of this gain in stiffness and mobilization of bearing mechanism is shown by comparing the strain profiles of Tests 5 and 1 (Figure 5.58e and Figure 5.58a) and the absolute pullout forces generated in both tests (Table 5.8) at the same percentages of the maximum pullout force.

| Percentage (%) of Fmax | Pullout Force (kN/m) | | |
|---|---|---|---|
| | Test 1 | Test 5 | Ratio Test 5/Test 1 |
| 25 | 2.0 | 3.1 | 1.55 |
| 40 | 3.5 | 4.8 | 1.37 |
| 50 | 4.8 | 6.1 | 1.27 |
| 75 | 6.7 | 9.2 | 1.37 |

Table 5.8: Comparison of pullout forces between Tests 1 and 5.

Although the strains developed along the geogrid are similar in Tests 5 and 1 up to 0.50 Fo/Fmax (Figure 5.58e and Figure 5.58a), the pullout forces generated in Test 5

are significantly higher than forces generated in Test 1 (Table 5.8). This is also shown in Figure 5.59, where the pullout forces generated with the displacements of P3 in the geogrids in Tests 5 and 1 are shown for the duration of the tests. Table 5.9 shows that the pullout forces in Test 5 are at least more than two times larger than the forces in Test 1.

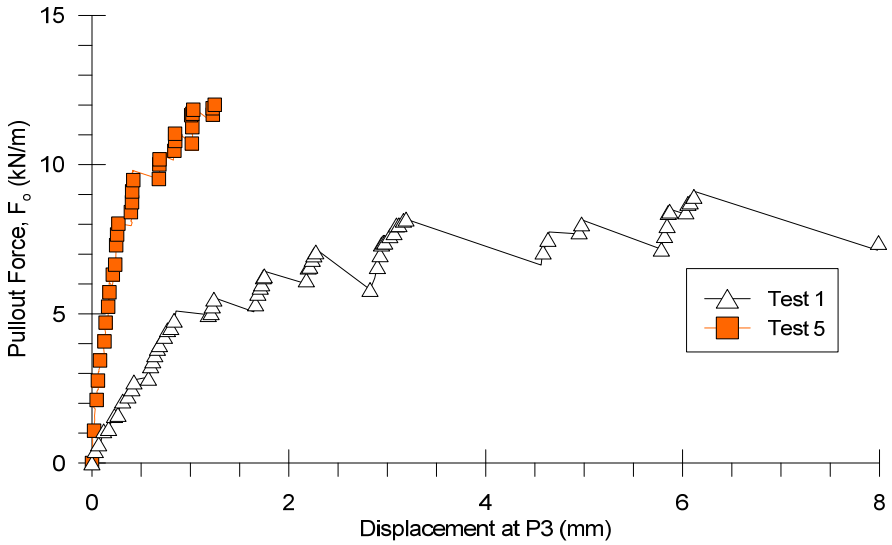


Figure 5.59: Comparison of pullout forces generated in Tests 5 and 1 with displacement of point P3 in the geogrids.

| Displacement of P3 (mm) | Generated pullout force (kN/m) | | |
|---|---|---|---|
| | Test 1 (geogrid with no transverse ribs) | Test 5 (geogrid with eight closely spaced transverse ribs) | Ratio Test 5/Test 1 |
| 0.20 | 1.5 | 5.9 | 3.93 |
| 0.50 | 2.8 | 9.6 | 3.42 |
| 1.00 | 5.0 | 10.7 | 2.14 |

Table 5.9: Comparison of pullout forces generated in Tests 5 and 1 with small displacements of point P3 in the geogrids.

The low percentage of the maximum pullout force of 0.25 Fo/Fmax showed the largest difference in the generated absolute pullout forces between Tests 5 and 1 (Table 5.8); but strains generated in the geogrid specimens of these tests are similar. Insignificant deflections were observed on the transverse ribs in Test 5 at this percentage of the maximum pullout force (Figure 5.51 to Figure 5.55). Thus, these results suggest that the higher stiffness of the geogrid specimen in Test 5 is the main cause of this difference in pullout forces, although there may be some contribution of the bearing mechanism to the soil-geogrid interaction.

The intermediate percentage of the maximum pullout force of 0.40 Fo/Fmax showed smaller differences between pullout forces generated in Tests 5 and 1 (Table 5.8). Small deflections were observed on the transverse ribs in Test 5 (Figure 5.51 to Figure 5.54), but the strain profile of the geogrid in both tests are similar (Figure 5.58e and Figure 5.58a).

These results suggest a larger contribution of the bearing mechanism to the generation of the pullout force in comparison to the 0.25 Fo/Fmax; although there may be contribution of the higher stiffness of the geogrid specimen. However, small deflections on the transverse ribs generate disturbed zones in the soil as these ribs move. The disturbances in the surrounding soil degrade the interface friction along the longitudinal ribs. Consequently, there may be interference between the bearing mechanism and the interface friction, and also among transverse ribs.

The intermediate percentage of the maximum pullout force of 0.50 Fo/Fmax showed the smallest difference between pullout forces generated in Test 5 and 1 (Table 5.8). Deflections observed on the transverse ribs in Test 5 were similar to the deflections observed at 0.40 Fo/Fmax (Figure 5.51 to Figure 5.54). The strains developed in the

geogrid specimen in Test 5 are similar to the strains observed in Test 1 (Figure 5.58e and Figure 5.58a).

However, displacements of the transverse ribs in Test 5 are larger at 0.50 Fo/Fmax than at 0.40 Fo/Fmax. Larger displacements of the transverse ribs generate larger zones of disturbed soil. Thus, interference among transverse ribs is larger at 0.50 Fo/Fmax than at 0.40 Fo/Fmax. As a result, the difference between the pullout forces in Tests 5 and 1 is smaller at 0.50 Fo/Fmax than at 0.40 Fo/Fmax.

The difference between pullout forces generated in Test 5 and Test 1 starts to increase again at 0.75 Fo/Fmax (Table 5.8). The largest difference between strains along the geogrid specimens in Test 5 and Test 1 is also observed at 0.75 Fo/Fmax (Figure 5.58e and Figure 5.58a). The pullout force in Test 5 is 37 % higher than the pullout force in Test 1. On the other hand, the strains calculated in Test 5 are 30 to 40 % smaller than the strains calculated in Test 1 depending on the location along the geogrid specimens. These results show the excellent gain in soil-geogrid interaction with the presence of transverse ribs closely spaced along the entire geogrid specimen; in spite of the high interference among the bearing mechanisms developed on the transverse ribs.

It should be emphasized that these conclusions were observed for the test setup and materials used in this study. Thus, additional research is needed to confirm these findings for other materials tested. The displacement and strain profiles might change for biaxial geogrids of similar geometry but composed of materials other than polypropylene.

Additionally, the findings related to the bearing mechanism and interference between transverse ribs may change for other geogrid products. The behavior of transverse ribs depends not only on the distance between them, but also on their stiffness and the stiffness of their junctions (Brown et al. 2007 and Palmeira 2009). Factors related

to the stiffness of transverse ribs include: (i) polymer, (ii) shape, (iii) thickness, (iv) width, and (v) length of the transverse ribs.

The smallest distance between two transverse ribs used in this study provided a ratio between the aperture size and the $D_{50}$ of the soil equal to 5.5. Smaller ratios might improve the results. Brown et al. (2008) found that a ratio of 1.4 provides the best soil-geogrid interaction for their tests. The stiffness of the polymer may also influence the response of transverse ribs. Polymers commonly used to manufacture geogrids include polypropylene, polyester, and high and low density polyethylene.

Deflections of transverse ribs, like beams, depend on the moment of inertia of these ribs in relation to the pullout movement (Palmeira 2004). The moment of inertia depends on the geometry of the transverse ribs. Shapes of transverse ribs can be circular, rectangular or square. Rectangular shapes can have different relationships between thickness and width of transverse ribs. Palmeira and Milligan (1989) showed that these factors impact the engagement of transverse ribs and, consequently, on soil-geogrid interaction. The length of transverse ribs is determined by the distance between longitudinal ribs.

Additionally, the efficiency of the engagement of transverse ribs may be related to the stiffness of the junctions. Flexible and weak junctions may limit the maximum potential deflection of transverse ribs. As a consequence, the development of the bearing mechanism would be affected thus impairing the overall engagement of the geogrid.

## 5.7 Qualitative evaluation of the displacements of the soil markers

Particles of crushed fused quartz were spray-painted with a black color and used as soil markers in the mass of transparent soil compacted in the pullout box. These soil markers were placed on the surface of compaction lifts after the lifts were scarified. The transparent soil was compacted in a total of eight compaction lifts. The geogrid specimen was placed at the surface of the fourth compaction lift.

The soil markers were placed along lines that were perpendicular and parallel to the direction of pullout. Displacements of the markers in lines perpendicular to the direction of pullout are observed from cam0, which provided images of the plan view of the pullout box (Figure 5.60a). Displacements of the markers in lines parallel to the direction of pullout are observed from cam1, which provided images of the side view of the pullout box (Figure 5.60b).

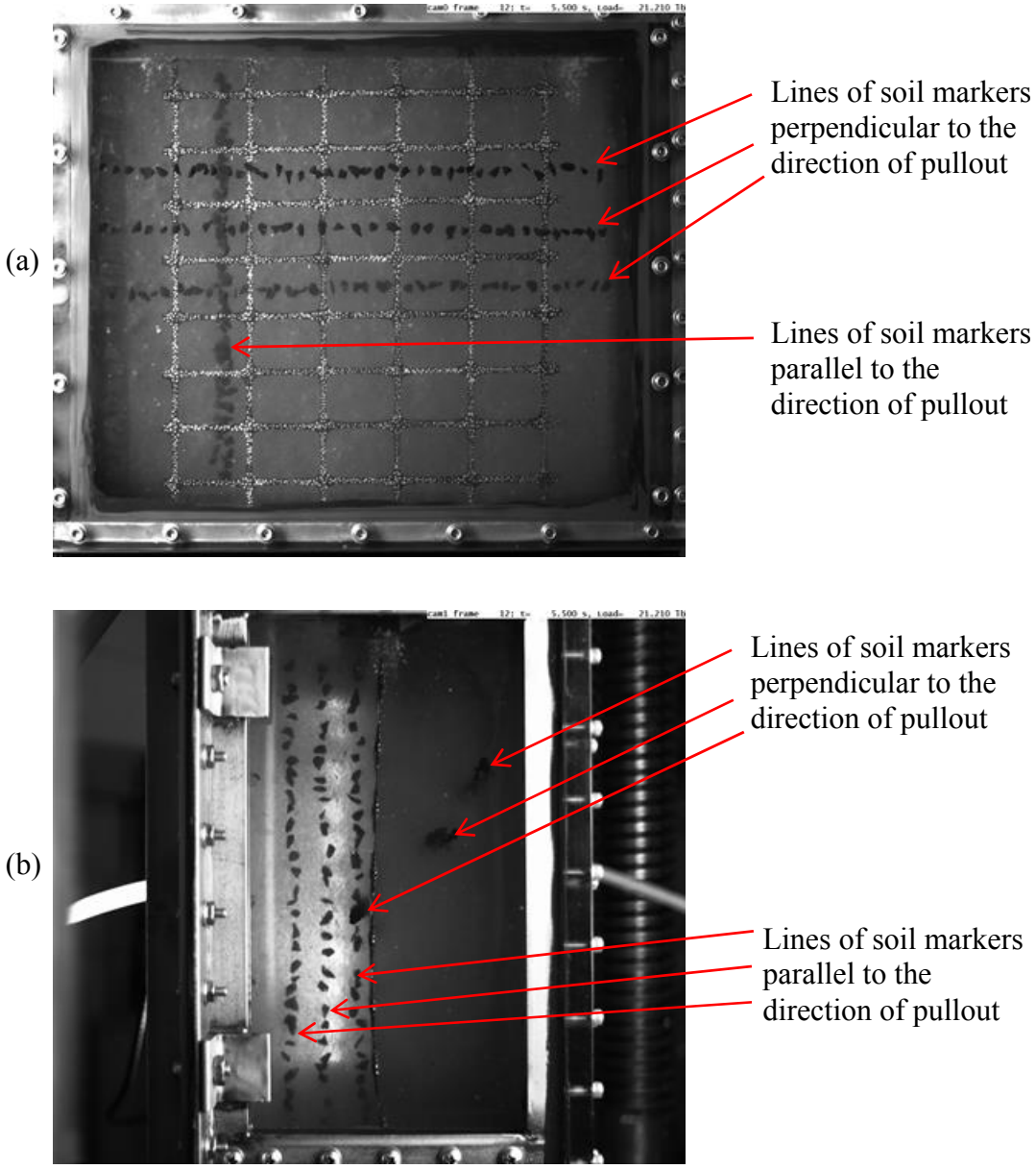


Figure 5.60: Lines of soil markers placed in the transparent soil compacted in the pullout box: (a) Plan view of the box (cam0). (b) Side view of the box (cam1).

Tracking of the soil markers and PIV calculations of the displacements of the soil markers were affected by movement of the pullout box during the tests. The movement of the box was not continuous and occurred in incremental steps that coincided with the

drops of pullout force accompanied with sudden displacement of the entire geogrid specimen. This movement was noticeable starting when near 80 % of the maximum pullout force was reached for all tests.

Images from the side view of the test (cam1) show that the pullout box rotated around the base frame in the clockwise direction (Figure 5.61). Measurements of the displacements of soil markers from images of cam1 were the most affected by the movement of the box.

The movement of the box was also observed in the images from cam0. The rotation of the box in the clockwise direction observed from the side view of the test (Figure 5.61) was a rotation of the box towards cam0. Thus, the box became closer to cam0 as it rotated. This movement created a magnification effect on the images from cam0. The magnification of the box was more noticeable near the active end of the geogrid, in the top portion of the images, where the rotation of the box was greater (Figure 5.61b).

The effect of the rotation of the box towards cam0 is the apparent downward displacement of the box observed in the images from cam0. At the same time, the right edge of the box has an apparent movement to the right. Concurrently, the left edge of the box has an apparent movement to the left. These movements were not symmetrical. There was also a translational movement of the box observed in the images from cam0.

This translational movement occurs because the surface of the base frame, on which the pullout box is resting on, is not perfectly flat. Thus, the rotation of the box is accompanied by a re-accommodation of the box on the base frame. Figure 5.62 shows two images from cam0 from the beginning and the end of Test 5 with an illustration of this movement of the box.

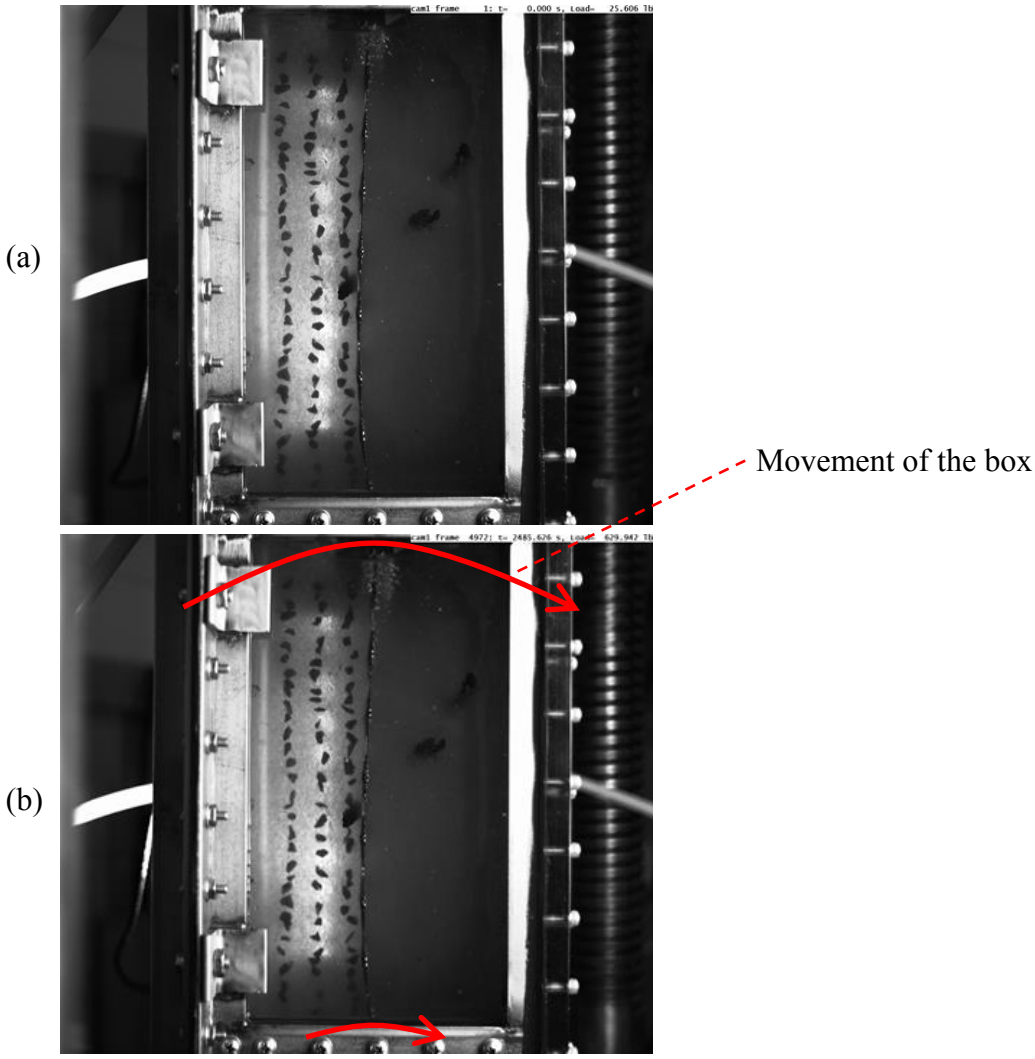


Figure 5.61: Side view of the box observed from cam1 with illustration of the rotation in the clockwise direction around the base: (a) Image at the beginning of the test (0.0 Fo/Fmax). (b) Image at the end of the test (1.0 Fo/Fmax). Note: Arrows are not on scale.

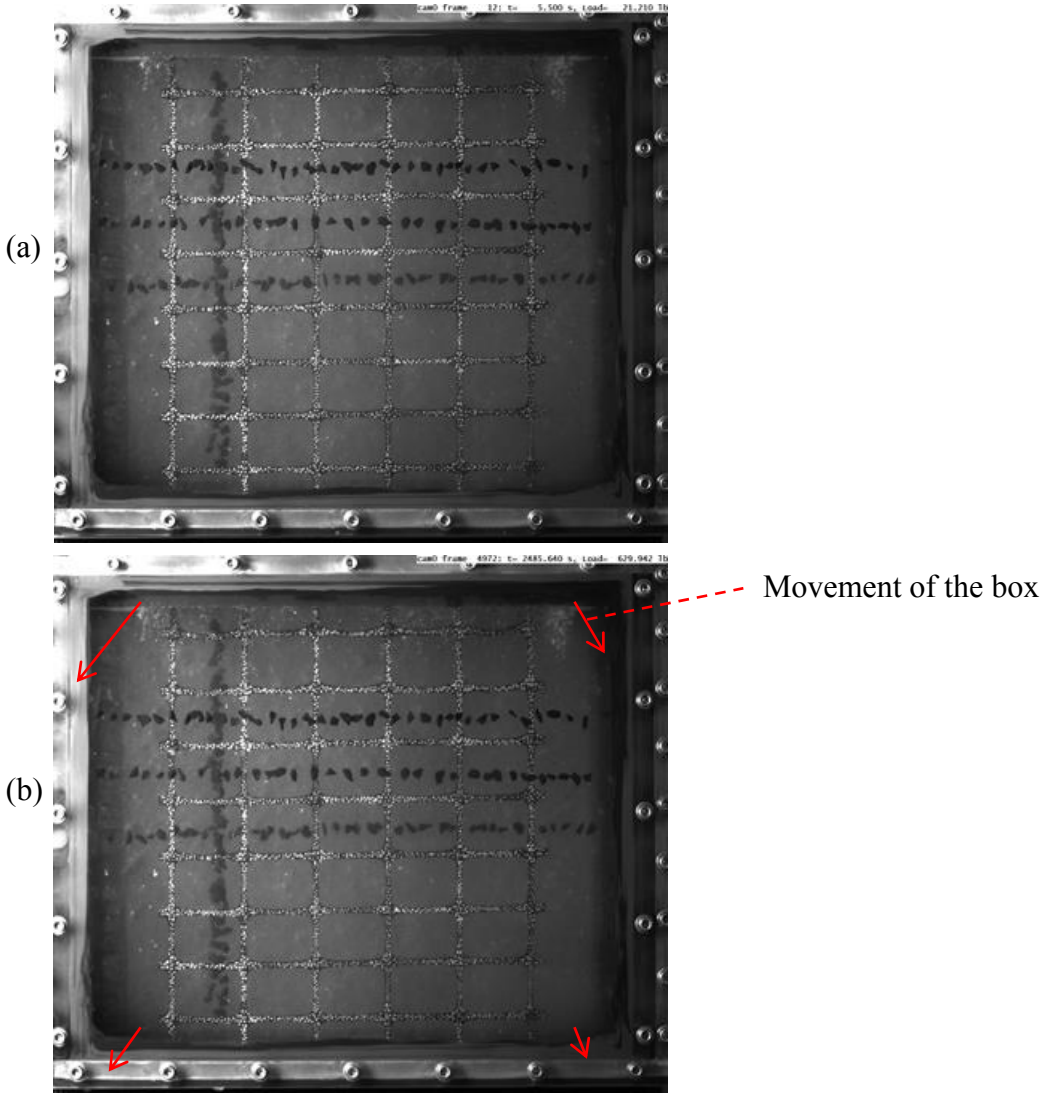


Figure 5.62: Plan view of the box observed from cam0 with illustration of the observed movements: (a) Image at the beginning of the test (0.0 Fo/Fmax). (b) Image at the end of the test (1.0 Fo/Fmax). Note: Arrows are not on scale.

The movement of the box observed in the images from cam0 (Figure 5.62) was orders of magnitude smaller than the displacements of the geogrid during the test. Consequently, the influence of the box movements in the displacement data of the geogrid was insignificant. However, the displacement data of the soil markers were affected by the box movements, since they were in the same order of magnitude.

Correction of the displacements of the soil markers was attempted by tracking the displacements of the pullout box in the images from both cameras. The measured displacement of the pullout box was discounted from the displacement data of the soil markers. However, the displacements of the box could not be isolated from the displacements of the soil markers. A detailed explanation of these calculations performed to correct the data from the soil markers is presented in Appendix A.

Because of these issues with the data from the soil markers, a limited qualitative analysis is presented in this chapter. This analysis is limited to the images from cam0 since the movement of the box observed from these images was smaller than the movement observed in the images from cam1. Only the displacements of the lines of soil markers placed perpendicular to the pullout direction are qualitatively evaluated in this chapter.

### 5.7.1 TEST 1: GEOGRID WITH NO TRANSVERSE RIB

The geogrid specimen in this test had no transverse rib. Images from cam0 at different stages of the pullout test are shown in Figure 5.63. The image at the beginning of the test is shown in Figure 5.63a. The image at 0.74 Fo/Fmax is shown in Figure 5.63b. The image at the end of the test is shown in Figure 5.63c.

The lines of soil markers placed perpendicular to the pullout direction were at distances of 38 mm (1.50 in.), 17 mm (0.67 in.), and 2 mm (0.08 in.) from the interface. These distances correspond, respectively, to the lines of markers in the top, middle and bottom shown in Figure 5.63a.

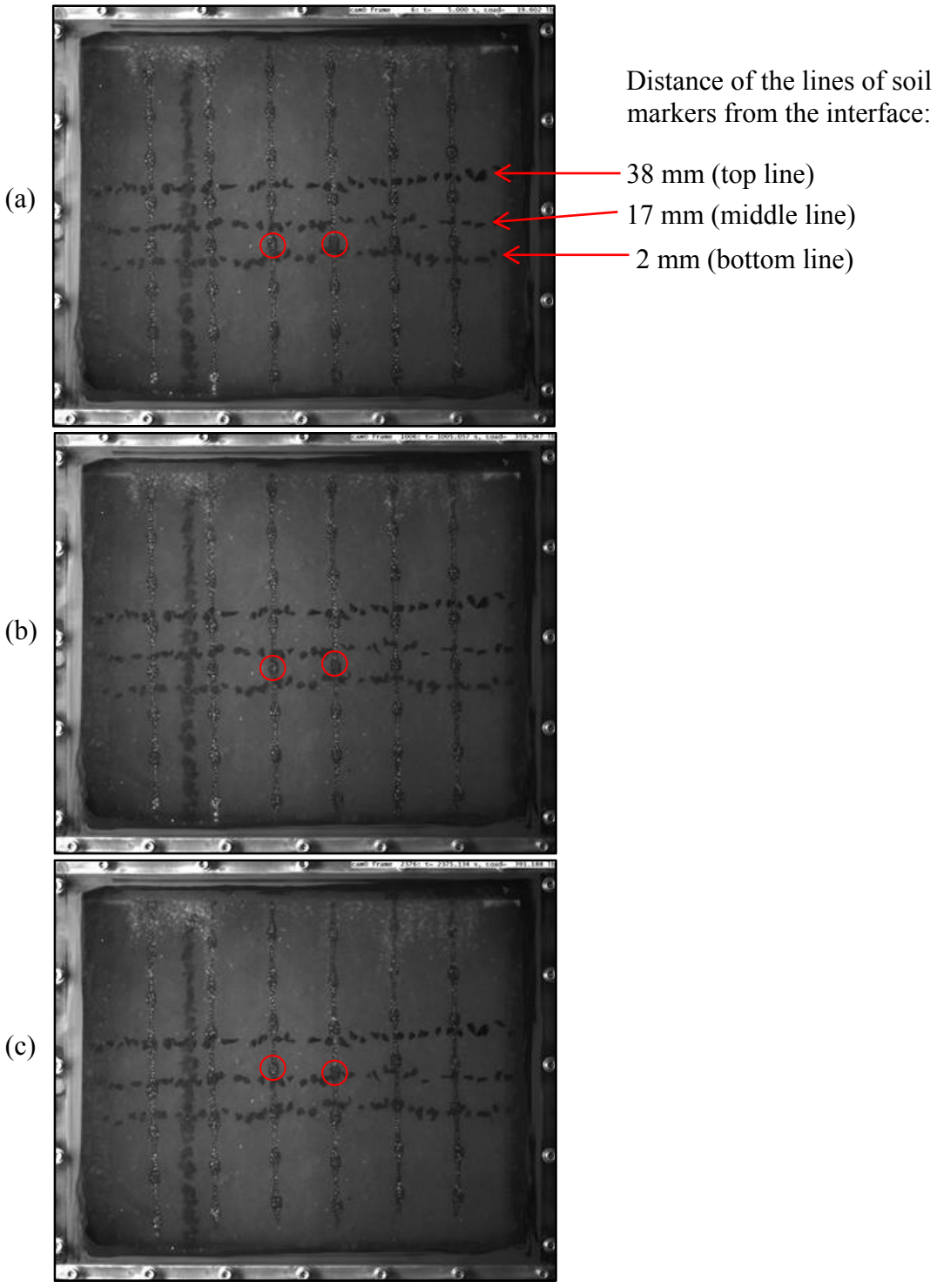


Figure 5.63: Test 1: Images from cam0 at (a) 0.00 Fo/Fmax, (b) 0.74 Fo/Fmax, and (c) 1.00 Fo/Fmax.

No displacement is observed of the soil markers at distances of 38 mm (1.50 in.) and 17 mm (0.67 in.) from the interface throughout the test (Figure 5.63). No displacement is observed of the soil markers in the line at a distance of 2 mm (0.08 in.) from the interface up to 0.74 Fo/Fmax (Figure 5.63b). However, displacements of the soil markers in this line of markers closest to the geogrid can be observed towards the end of the test, between 0.74 Fo/Fmax (Figure 5.63b) and 1.00 Fo/Fmax (Figure 5.63c).

Nevertheless, the displacement of the geogrid is orders of magnitude higher than the displacements of the soil markers in the line of markers closest to the geogrid. This can be observed by the relative position between the highlighted junctions of the geogrid and the soil markers in Figure 5.63. At 0.74 Fo/Fmax (Figure 5.63b), the highlighted junctions are slightly above than the bottom line of soil markers. At 1.00 Fo/Fmax (Figure 5.63c), the highlighted junctions are slightly above than the middle line of soil markers.

On the other hand, little change is noticed in the vertical distance between the bottom and the middle lines of markers in the images from 0.74 and 1.00 Fo/Fmax (Figure 5.63b and Figure 5.63c). Thus, for the setup in Test 1 and large displacements occurring towards pullout failure, the soil particles adjacent to the interface do not move together with the geogrid.

### 5.7.2 TEST 2: GEOGRID WITH ONE TRANSVERSE RIB

The geogrid specimen in this test had one transverse rib located near the middle of the geogrid length at 0.46 L. Images from cam0 at different stages of the pullout test are shown in Figure 5.64. The image at the beginning of the test is shown in Figure 5.64a.

The image at the 0.74 Fo/Fmax is shown in Figure 5.64b. The image at the end of the test is shown in Figure 5.64c.

The lines of soil markers placed perpendicular to the pullout direction were at distances of 47 mm (1.85 in.), 25 mm (0.98 in.), and 10 mm (0.39 in.) from the interface. These distances correspond, respectively, to the lines of markers in the top, middle and bottom shown in Figure 5.64a.

No displacements are observed for the top and middle lines of soil markers throughout the test (Figure 5.64). No displacements are observed for the bottom line of soil markers, which is the one closest to the interface, until 0.74 Fo/Fmax. On the other hand, small displacements are noticeable between 0.74 and 1.00 Fo/Fmax (Figure 5.64b and Figure 5.64c, respectively).

Nevertheless, the relative displacement between the geogrid and the lines of soil markers is significant, especially towards the end of the test between 0.74 and 1.00 Fo/Fmax (Figure 5.64b and Figure 5.64c, respectively). Thus, similar to Test 1, it can be concluded in Test 2 that the soil particles adjacent to the interface do not move together with the geogrid.

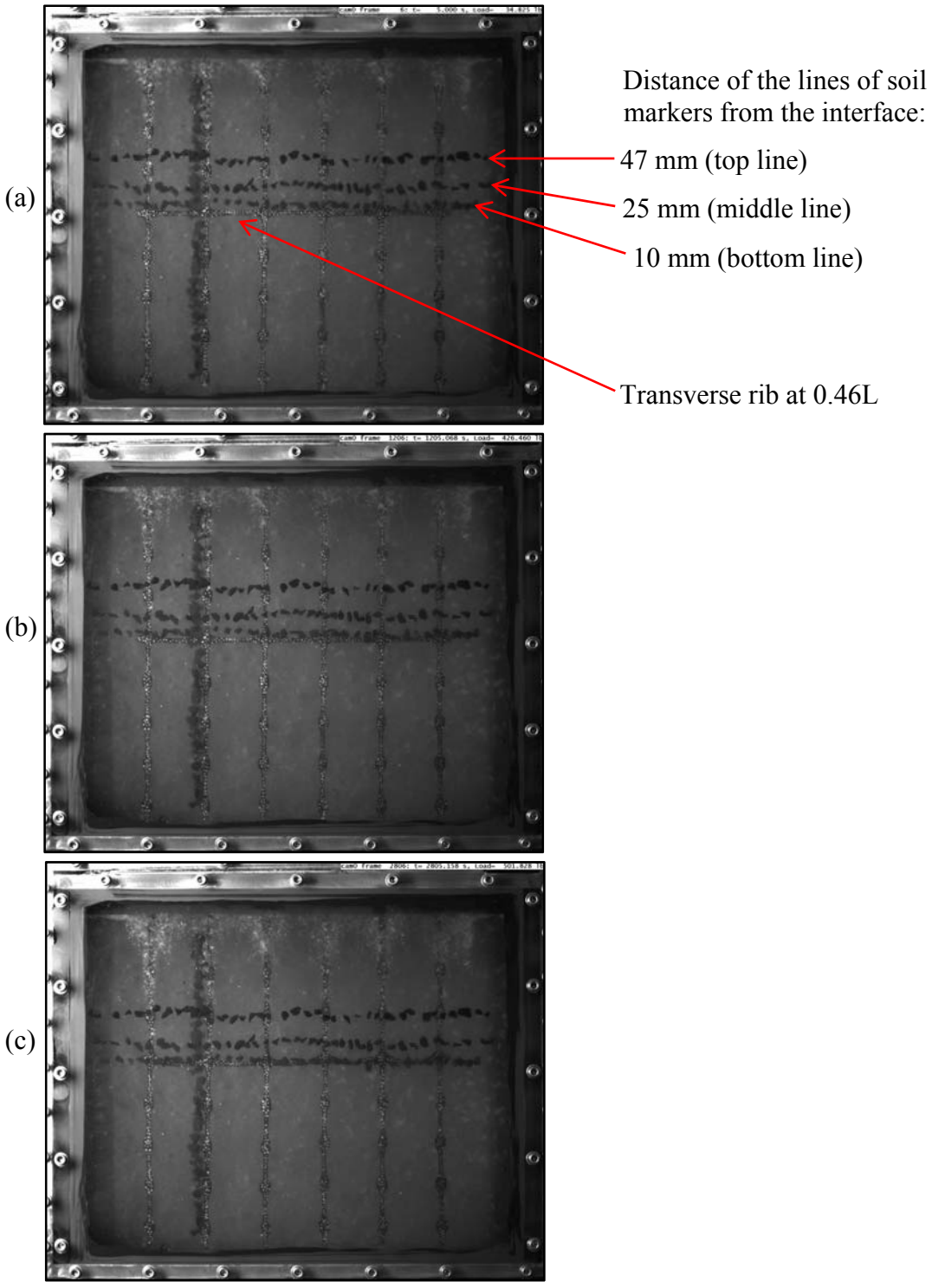


Figure 5.64: Test 2: Images from cam0 at (a) 0.00 Fo/Fmax, (b) 0.74 Fo/Fmax, and (c) 1.00 Fo/Fmax.

### 5.7.3 TEST 3: GEOGRID WITH TWO CLOSELY SPACED TRANSVERSE RIBS

The geogrid specimen in this test had two closely spaced transverse ribs located at 0.35L and 0.46L. Images from cam0 at different stages of the pullout test are shown in Figure 5.65. The image at the beginning of the test is shown in Figure 5.65a. The image at 0.76 Fo/Fmax is shown in Figure 5.65b. The image at the end of the test is shown in Figure 5.65c.

The lines of soil markers placed perpendicular to the pullout direction were at distances of 45 mm (1.77 in.), 25 mm (0.98 in.), and 8 mm (0.31 in.) from the interface. These distances correspond, respectively, to the lines of markers in the top, middle and bottom shown in Figure 5.65a.

No displacement is observed of the soil markers at distances of 45 mm (1.77 in.) and 25 mm (0.98 in.) from the interface throughout the test (Figure 5.65). On the other hand, displacements of the soil markers closest to the interface (bottom line in Figure 5.65a) are observed throughout the duration of the test. The distance between the bottom and the middle line of soil markers decreases between the images of the different stages of the test (Figure 5.65).

However, the relative displacement between the geogrid and the line of soil markers closest to the geogrid is significant, especially towards the end of the test between 0.76 and 1.00 Fo/Fmax (Figure 5.65b and Figure 5.65c). Thus, similar to Tests 1 and 2, it can be concluded in Test 3 that the soil particles adjacent to the interface do not move together with the geogrid.

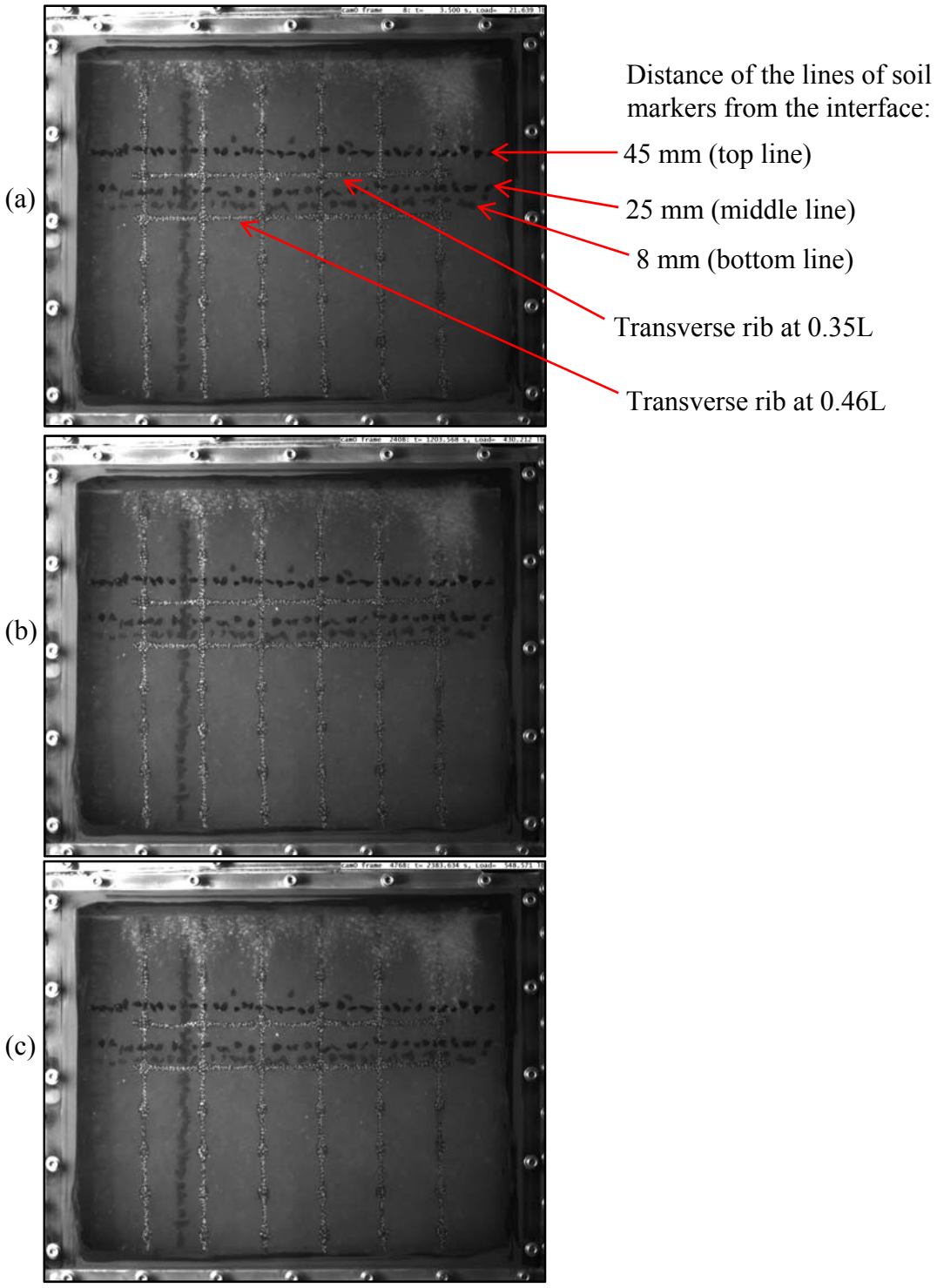


Figure 5.65: Test 3: Images from cam0 at (a) 0.00 Fo/Fmax, (b) 0.76 Fo/Fmax, and (c) 1.00 Fo/Fmax.

### 5.7.4 TEST 4: GEOGRID WITH TWO LARGELY SPACED TRANSVERSE RIBS

The geogrid specimen in this test had two largely spaced transverse ribs located at 0.34L and 0.58L. Images from cam0 at different stages of the pullout test are shown in Figure 5.66. The image at the beginning of the test is shown in Figure 5.66a. The image at 0.74 Fo/Fmax is shown in Figure 5.66b. The image at the end of the test is shown in Figure 5.66c.

The lines of soil markers placed perpendicular to the pullout direction were at distances of 43 mm (1.69 in.), 25 mm (0.98 in.), and 11 mm (0.43 in.) from the interface. These distances correspond, respectively, to the lines of markers in the top, middle and bottom shown in Figure 5.66a.

No displacement is observed of the soil markers at distances of 43 mm (1.69 in.) and 25 mm (0.98 in.) from the interface throughout the test (Figure 5.66). On the other hand, displacements of the soil markers closest to the interface (bottom line in Figure 5.66a) are observed throughout the duration of the test. The distance between the bottom and the middle line of soil markers decreases between the images of the different stages of the test, especially towards the end between 0.74 and 1.00 Fo/Fmax (Figure 5.66b and Figure 5.66c).

However, the relative displacement between the geogrid and the line of soil markers closest to the geogrid is significant, especially towards the end of the test between 0.76 and 1.00 Fo/Fmax (Figure 5.66b and Figure 5.66c). Thus, similar to Tests 1 to 3, it can be concluded in Test 4 that the soil particles adjacent to the interface do not move together with the geogrid.

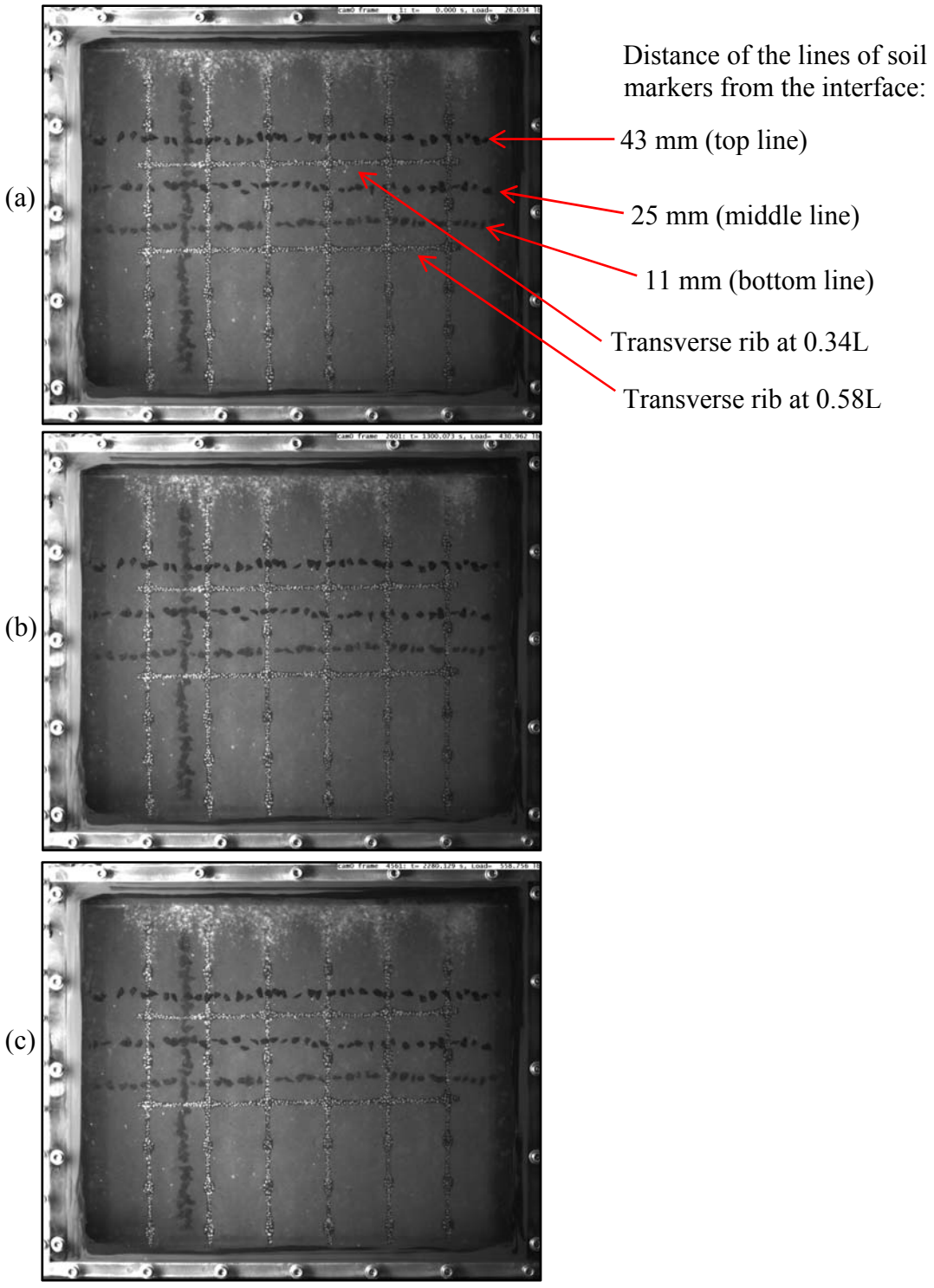


Figure 5.66: Test 4: Images from cam0 at (a) 0.00 Fo/Fmax, (b) 0.74 Fo/Fmax, and (c) 1.00 Fo/Fmax.

### 5.7.5 TEST 5: GEOGRID WITH EIGHT CLOSELY SPACED TRANSVERSE RIBS

The geogrid in this test was used with no modifications. The transverse ribs were present along the entire length of the geogrid specimen with its original aperture size. The geogrid in this test had a total of eight transverse ribs. Images from cam0 at different stages of the pullout test are shown in Figure 5.67. The image at the beginning of the test is shown in Figure 5.67a. The image at 0.74 Fo/Fmax is shown in Figure 5.67b. The image at the end of the test is shown in Figure 5.67c.

The lines of soil markers placed perpendicular to the pullout direction were at distances of 51 mm (2.01 in.), 31 mm (1.22 in.), and 7 mm (0.28 in.) from the interface. These distances correspond, respectively, to the lines of markers in the top, middle and bottom shown in Figure 5.67a.

No displacements are observed of the soil markers at distances of 51 mm (2.01 in.) and 31 mm (1.22 in.) from the interface throughout the test (Figure 5.67). No displacements are observed of the soil markers closest to the interface (bottom line in Figure 5.67a) until 0.75 Fo/Fmax. On the other hand, relatively small displacements of these markers are observed between 0.75 and 1.00 Fo/Fmax (Figure 5.67b and Figure 5.67c, respectively).

Nevertheless, the relative displacement between the geogrid and the line of soil markers closest to the geogrid is relatively large throughout the test. These observations are similar to all transparent pullout tests analyzed above. In all tests, no displacements were observed on the top and middle lines of soil markers throughout the tests (Figure 5.63 to Figure 5.67).

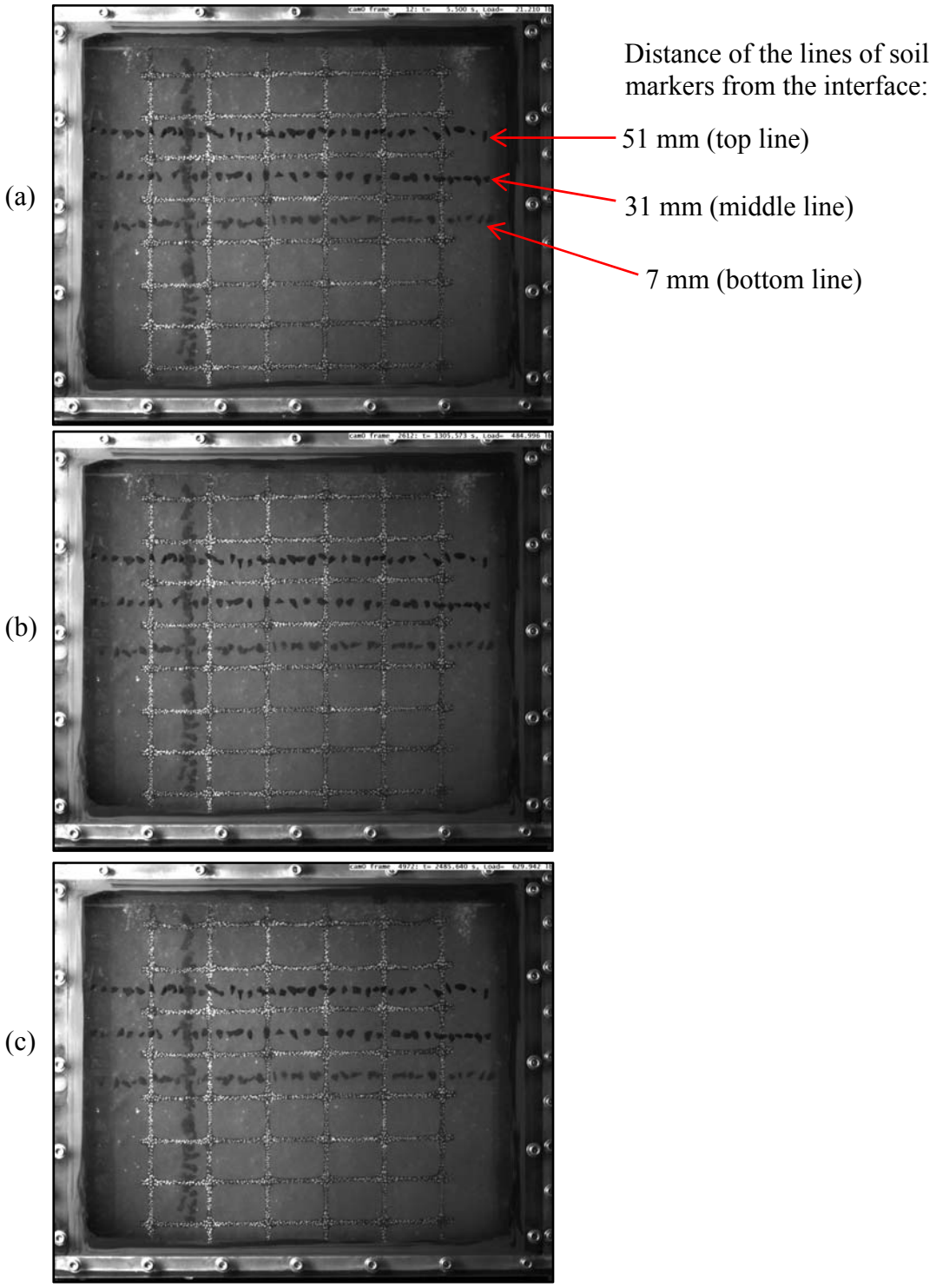


Figure 5.67: Test 5: Images from cam0 at (a) 0.00 Fo/Fmax, (b) 0.75 Fo/Fmax, and (c) 1.00 Fo/Fmax.

On the other hand, displacements were observed in the line of soil markers closest to the interface in all tests. Thus, it can be concluded that for the transparent soil and polypropylene geogrid used in this research, the observed boundary of the zone of influence of the geogrid is between 11 and 25 mm from the interface. This is equivalent to between 3 and 7 times the $D_{50}$ of the soil. The ratio between the $D_{50}$ of the soil and the thickness of the transverse ribs is 4.4.

It should be emphasized that these results are based on qualitative evaluations in tests with an artificial soil. The shape and rugosity of the particles of fused quartz are extremely different than those of soils used in the construction of the base of pavements and in earth retaining walls. Moreover, the viscosity and lubrication effect of the mineral oil make it more difficult to compare these results with data reported in the literature.

# 6 CONCLUSION

This research aimed at understanding the mechanisms of soil-geogrid interaction at different stress levels. This was achieved with the analysis of the results of a series of tests on a transparent pullout device using transparent soil. These tests allowed continuous measurement of displacements along the geogrid specimens. Strains along the geogrid specimens were calculated from the displacement data. The analyses included calculation of the strains along the geogrid specimens at different stages of the transparent pullout tests.

## 6.1 Summary and main conclusions

The setup of the transparent pullout tests was assembled by designing a new transparent pullout box and image acquisition system, and by using crushed fused quartz saturated in a mix of white mineral oil. A series of direct shear and small pullout tests were conducted to compare the results of the tests with fused quartz to the results of tests with Monterey sand. It was concluded that the transparent soil of the present study can be used as a surrogate for sands.

Particle Image Velocimetry (PIV) was used to obtain displacement data of the geogrid and soil markers throughout the transparent pullout tests. The software used in the PIV calculations was DynamicStudio v.2.30 provided by Dantec Dynamics. Calibration of the PIV data was performed with a series of cropped images from transparent pullout tests. Displacement increments were digitally applied to the images using Photoshop Elements by Adobe.

Validation of the PIV calculations was performed with data from ultimate tensile strength tests of the polypropylene geogrid used in this study. This type of test was conducted with the new image acquisition system and PIV program. The results were compared to the results of the tests conducted by Gupta (2009) with geogrid specimens from the same lot at a commercial laboratory. Good agreement was found between the results.

The test setup adopted in this study allowed for obtaining high resolution images of the plan view of the entire geogrid specimen throughout the duration of the test. Soil markers were placed in the transparent soil, so movements of soil particles within the soil mass and near the geogrid could be tracked. Unfortunately, movement of the pullout box during the test was observed, especially at stress levels above 80 % of the maximum pullout force. The influence of the movement of the box on tracking the displacements of the geogrid was insignificant. On the other hand, this influence was significant in tracking displacements of the soil markers. Recommendations are suggested for changes in the test setup to minimize movement of the box during tests.

The testing program was grouped in 2 sets of pullout tests. The first group of pullout tests included tests with Monterey sand, crushed fused quartz with 1.5 % water content, and crushed fused quartz saturated with a mix of white mineral oil (transparent soil). The objective of the first group of tests was to evaluate the influence on the results of the artificial soil composed by particles of fused quartz when compared to tests with Monterey sand. Also, the influence of the white mineral oil on the results was evaluated in relation to the test with only fused quartz. Analysis of the results of these tests led to the following conclusions:

1. The transparent soil can be used as a surrogate for natural soils.

2. The general shape of the pullout curves with transparent soil agrees well with data reported in the literature.

However, the slip-stick phenomenon was observed in direct shear tests and at relatively small displacements in pullout tests with the transparent soil. More research is needed to assess the influence of this phenomenon on the results before the results of tests with transparent soil can be extrapolated to natural soils.

The second group of pullout tests included 5 transparent pullout tests with different configurations of the geogrid specimen: (i) geogrid with no transverse ribs, (ii) geogrid with one transverse rib, (iii) geogrid with two closely spaced transverse ribs, (iv) geogrid with two largely spaced transverse ribs, and (v) geogrid with eight closely spaced transverse ribs.

Analysis of the results of these tests led to the following conclusions:

1. Displacements along the polypropylene geogrid used in this study are well represented by an exponential function in the form of $y = \alpha + \beta\, e^{(-x/\gamma)}$, where $x$ is the location along the geogrid and $\alpha$, $\beta$, and $\gamma$ are experimental parameters obtained through data fitting.
2. The bearing mechanism along the transverse ribs starts contributing to soil-geogrid interaction at small displacements and strains. This contribution was first observed at displacements of 0.20 mm (0.008 in.) and 25% of the maximum pullout force.
3. Interference between transverse ribs was first observed at approximately 60% of the maximum pullout force.

4. Interference between transverse ribs is significant for a ratio of spacing between transverse ribs (S) over the thickness of these ribs (B) equal to 24 (S/B = 24).
5. Insignificant interference between transverse ribs was observed for a ratio of S/B equal to 57.
6. The boundary of the zone of influence of the geogrid was observed to be at a distance from the interface (d) between 3 to 7 times the $D_{50}$ of the soil (boundary of zone of influence at $3 < d/D_{50} < 7$).
7. The displacements of the geogrid are orders of magnitude larger than the displacements of soil particles at $d/D_{50}$ equal to 3.

## 6.2 Recommendations for Future Work

The new transparent pullout test setup developed in this study allows for the visualization and displacement measurements throughout the entire geogrid specimen with great detail and non-invasively. The deformed shape of entire transverse ribs can be, for the first time, visualized. Also, deflections can be reliably measured in the transverse ribs.

Countless combinations of geogrid configurations can be used in the transparent pullout test setup developed in this study. Thus, the influence of the geometric and physical characteristics of geogrids on soil-geogrid interaction can be properly evaluated. Geometric characteristics of geogrids include the distance between transverse ribs, the distance between longitudinal ribs, the shape of the aperture of the geogrid (square, rectangular or triangular); and the thickness and width of transverse and longitudinal ribs.

Physical characteristics of geogrids include stiffness and strength of the different types of polymers that constitute geogrids; and stiffness and strength of the junctions.

The new transparent pullout test setup developed in this study has some limitations that must be taken into account in the analysis of the results. The dimensions of the pullout box limit the aperture size of geogrids and the size of the soil particles that can be utilized. The shape and rugosity of the surface of the particles of crushed fused quartz is not found in particles of natural soil. The viscosity and lubrication effect of the mineral oil mix influences the results.

Several improvements can be made to the test setup. The most important improvement is to minimize movements of the pullout box during the test. This can be achieved by enlarging the base frame on which the pullout box rests. The top surface of this base frame can also be leveled-off so that the pullout box rests on a flatter surface.

The connection of the box to the base frame should also be enlarged. Three screws in a triangular form should be used to attach the pullout box to the based frame, instead of only one screw in the current setup. This would minimize rotation and translation of the pullout box during the test. Additionally, targets should be placed near the corners of the pullout box to allow accurate measurements of the movement of the pullout box during the test that might still occur.

The PIV signal for tracking the soil markers can be improved by doing an incomplete paint job with white spray paint on the soil markers. The soil markers are particles of fused quartz spray-painted in black color. Thus, this paint job would create a high contrast with unique patterns of white dots on the surface of the black soil markers. This contrast should be better than the contrast of the edges of the soil markers against the light through the transparent soil mass used for the images from cam1. The contrast

should also be better than the contrast of the edges of the soil markers against the white woven geotextile in the background of the images from cam0.

Displacements throughout the entire soil mass in the developed transparent pullout test could be measured with the use of a laser light sheet generator. This would greatly increase accuracy and resolution of the displacement data within the soil mass when compared to using soil markers.

# Appendix A: Displacement of soil markers

The developed transparent pullout testing apparatus allows for not only the plan view of the geogrid, but also the side view of the soil-geogrid interface. Thus, displacements within the soil mass can be visualized by tracking the movement of soil markers. Soil markers were placed adjacent to the geogrid and at different distances above and below the interface.

The displacement data from the soil markers would give additional insight into the soil-geogrid interaction by allowing the visualization of the zone of influence of the geogrid at different stages of the test. Unfortunately, movement of the pullout box was observed during the tests. Consequently, only a limited qualitatively analysis of the displacement of the soil markers could be performed.

This appendix is organized in two sections. In the first section, suggestions are recommended to improve the test setup and minimize the movement of the pullout box during tests. Recommendations are also made to improve the PIV signal for tracking the displacements of soil markers. In the second section, the data of the displacements of the box and soil markers are presented.

## SUGGESTED IMPROVEMENTS FOR THE TEST SETUP

Simple improvements on the test setup can minimize the movements of the pullout box during tests. The base frame on which the pullout box rests should be enlarged. The top surface of the base frame can also be leveled-off so that the pullout box rests on a flatter surface.

The connection of the box to the base frame can also be enlarged. Three screws in a triangular form should be used to attach the pullout box to the based frame, instead of

only one screw in the current setup. This would minimize rotation and translation of the pullout box during the test. Additionally, targets should be placed near the corners of the pullout box to allow accurate measurements of the movement of the pullout box during the test that might still occur.

The PIV signal for tracking the soil markers can be improved by doing an incomplete paint job with white spray paint on the soil markers. The soil markers are particles of fused quartz spray-painted in black color. Thus, this paint job would create a high contrast with unique patterns of white dots on the surface of the black soil markers. This contrast should be better than the contrast of the edges of the soil markers against the light through the transparent soil mass used for the images from cam1. The contrast should also be better than the contrast of the edges of the soil markers against the white woven geotextile in the background of the images from cam0.

### DISPLACEMENT OF THE BOX AND SOIL MARKERS DURING THE PULLOUT TESTS

Displacements of the pullout box were calculated from the images of both cameras. In the images from cam0 (plan view of the test), the used references to track displacements of the box were the screws on the right and left edges of the bottom plate of the box. In the images from cam1 (side view of the test), the used references to track displacements of the box were the corners of the L-shaped plates welded to the external frame of the box, which secure the lid of the box in place.

These references did not provide accurate measurements. Thus, the displacements of the box could not be isolated from the measured displacements of the soil markers. Horizontal displacements measured for the soil markers in all tests were within the

average margin of error estimated in Chapter 3.4.2. Thus, no conclusion could be made from these measurements.

The data of horizontal and vertical displacements measured for the pullout box in images from cam0 were highly scattered. The data of horizontal and vertical displacements in images from cam1 were fitted to straight lines, since the rotation of the box (Figure 5.55) is the rotation of a rigid body. However, this not provided better results.

It was observed in the data of all tests that the displacements of all lines of markers followed a pattern that was clearly influenced by the displacement of the box. It is observed in the data of most tests in which displacements of the soil markers furthest away from the interface being larger than the displacements of the soil markers closest to the interface. Visual inspection of the images of the tests showed that this is erroneous.

The data of the displacements of the pullout box and soil markers obtained from the images of both cameras is presented along this appendix.

**Test 1**

***Images from cam0 (plan view of the test)***

The images from cam0 provide the plan view of the test. In these images, the line of markers perpendicular to the pullout direction are observed (Figure A. 1). The top, middle and bottom lines of soil markers in Figure A. 1 are at 38 mm (1.50 in.), 17 mm (0.67 in.), and 2 mm (0.08 in.) from the interface, respectively.

The data of the horizontal and vertical displacements of the pullout box are shown in Figure A. 2 and Figure A. 3, respectively. The data of the horizontal and vertical displacements of the soil markers are shown from Figure A. 4 to Figure A. 9.

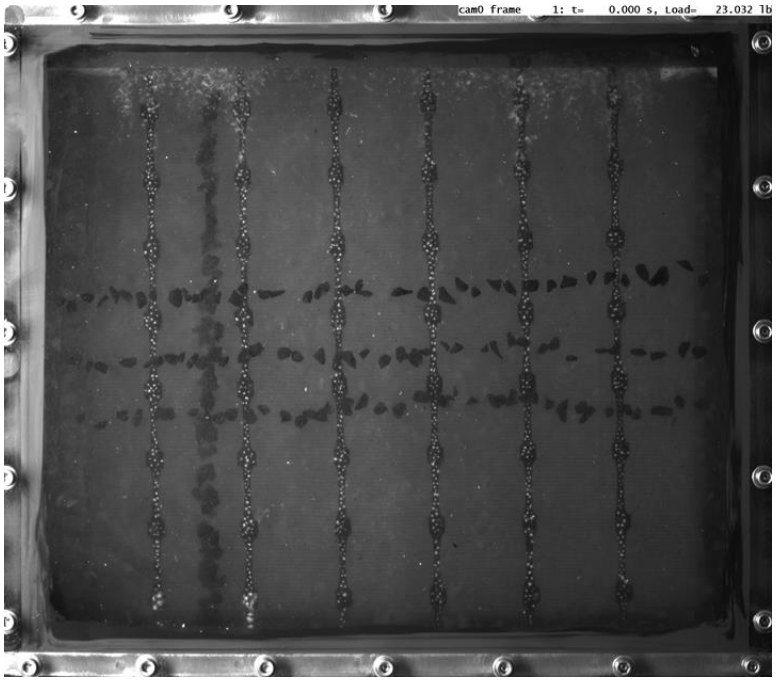


Figure A. 1: Test1: Image of the plan view of the box (cam0) and lines of soil markers placed perpendicular to the pullout direction.

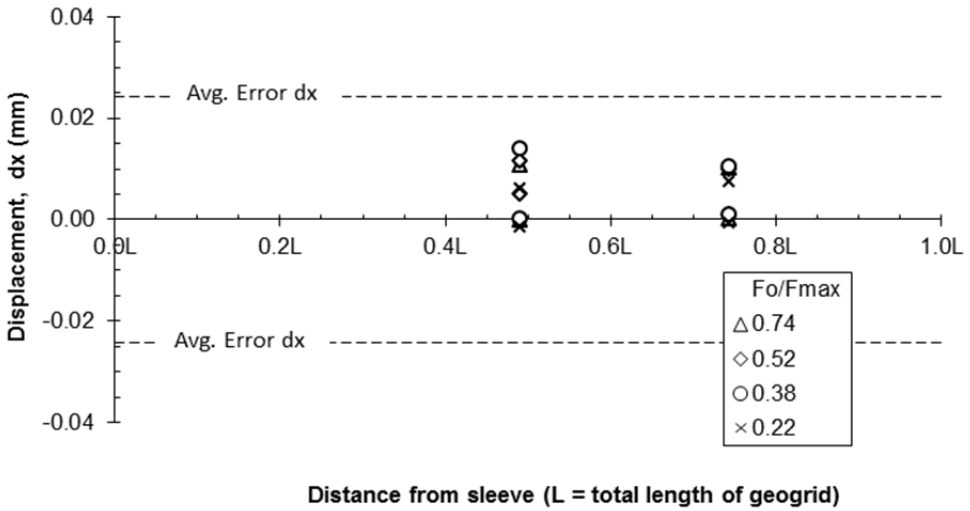


Figure A. 2: Test 1: Horizontal movement of the box calculated with the PIV software with images from cam0 (plan view).

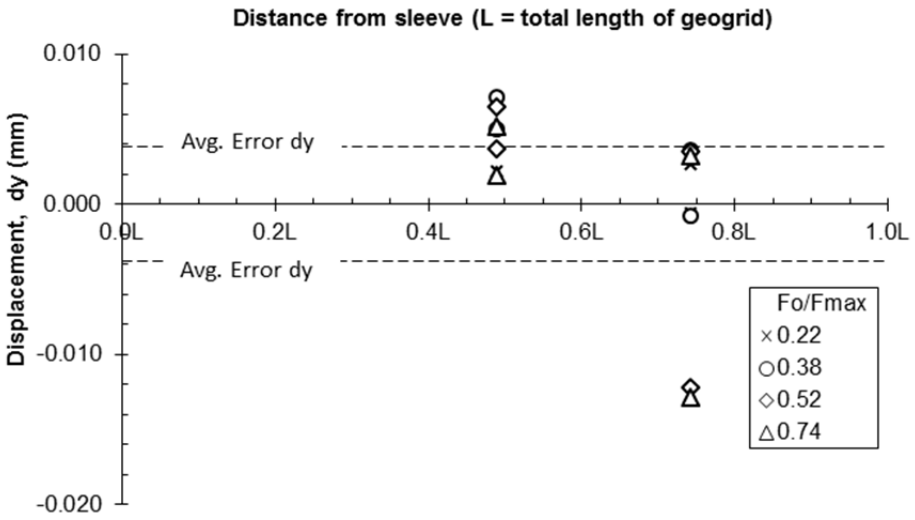


Figure A. 3: Test 1: Vertical movement of the box calculated with the PIV software with images from cam0 (plan view).

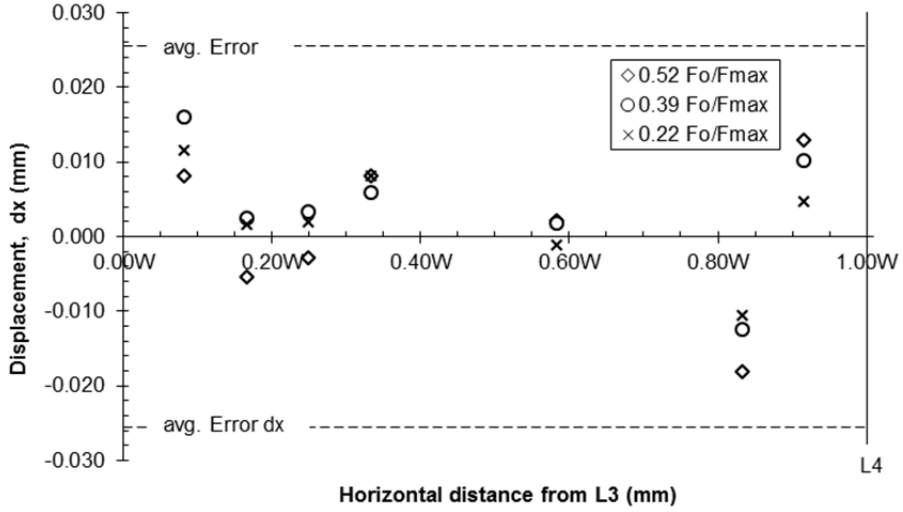


Figure A. 4: Test 1: Horizontal displacement of soil markers between L3 and L4 at 38 mm from the interface.

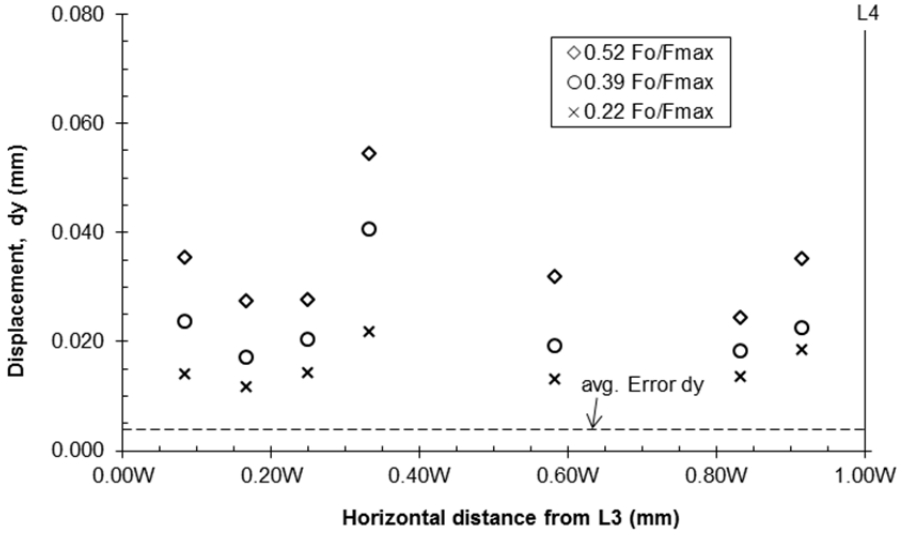


Figure A. 5: Test 1: Vertical displacement of soil markers between L3 and L4 at 38 mm from the interface.

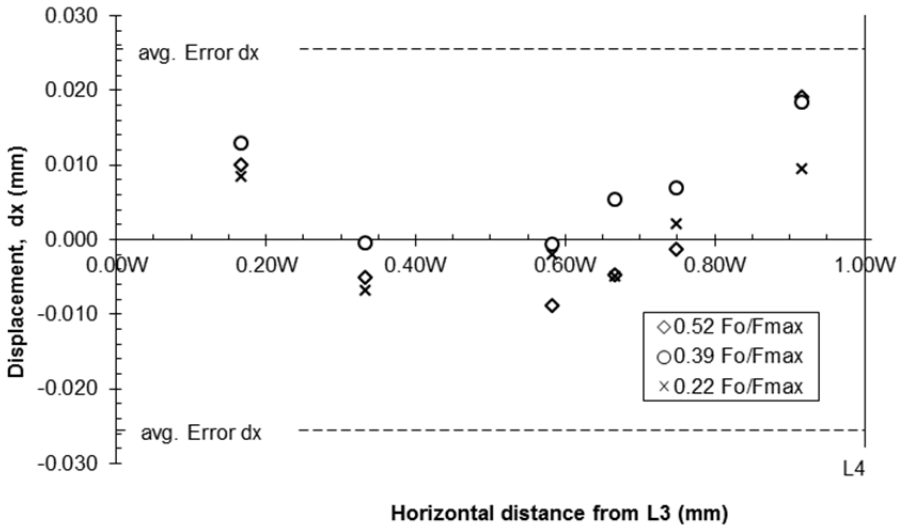


Figure A. 6: Test1: Horizontal displacement of soil markers between L3 and L4 at 17 mm from the interface.

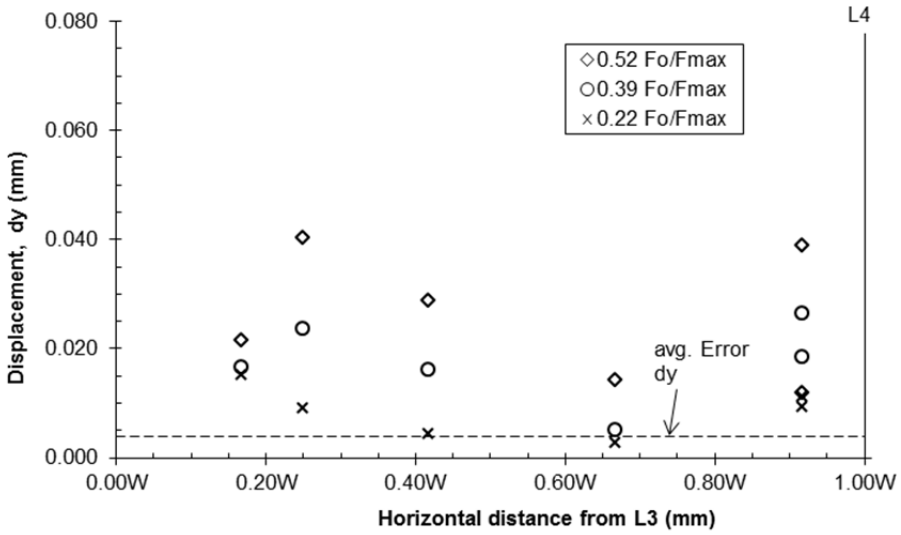


Figure A. 7: Test1: Vertical displacement of soil markers between L3 and L4 at 17 mm from the interface.

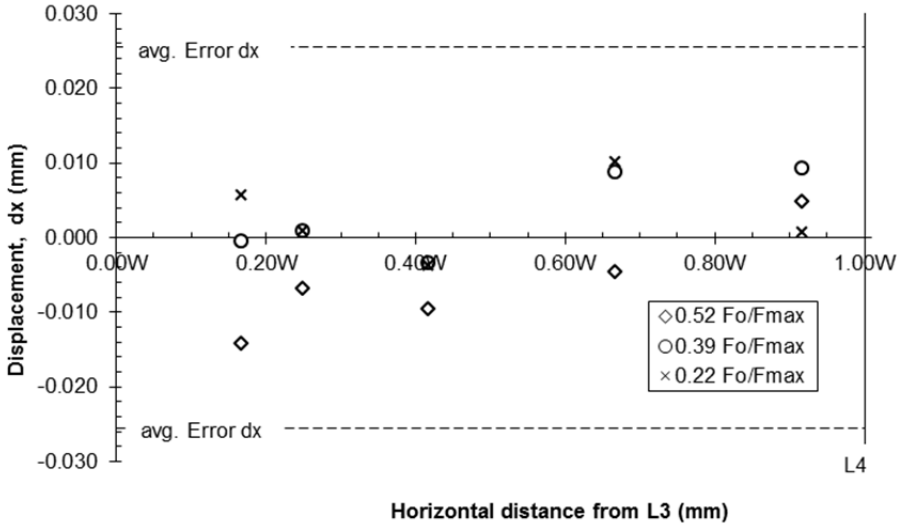


Figure A. 8: Test1: Horizontal displacement of soil markers between L3 and L4 at 2 mm from the interface.

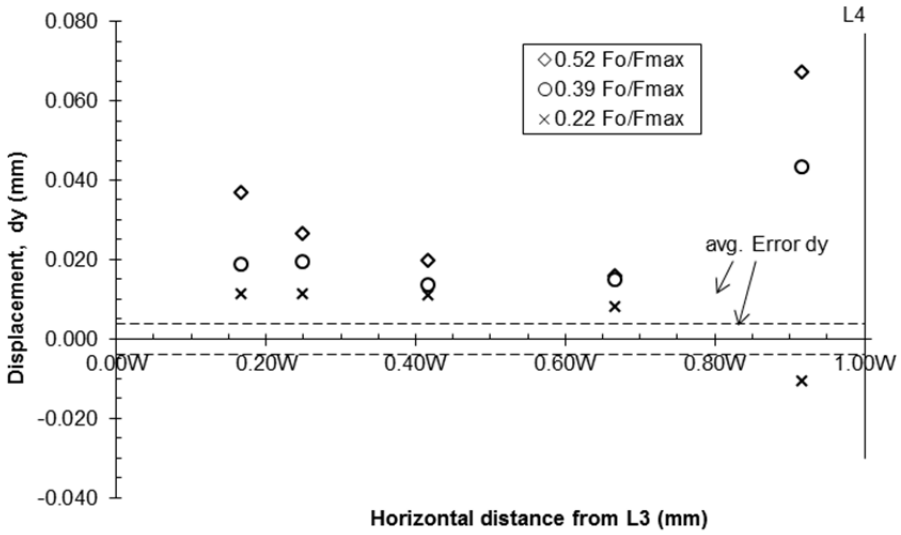


Figure A. 9: Test1: Vertical displacement of soil markers between L3 and L4 at 2 mm from the interface.

***Images from cam1 (side view of the test)***

The images from cam1 provide the side view of the test. In these images, the lines of markers parallel to the pullout direction are observed (Figure A. 10). The lines of soil markers in Figure A. 10 are to the left of the geogrid at 15, 33 and 48 mm from the interface.

The data of the horizontal and vertical displacements of the pullout box are shown in Figure A. 11 and Figure A. 12, respectively. The data of the horizontal and vertical displacements of the soil markers are shown from Figure A. 13 to Figure A. 18.

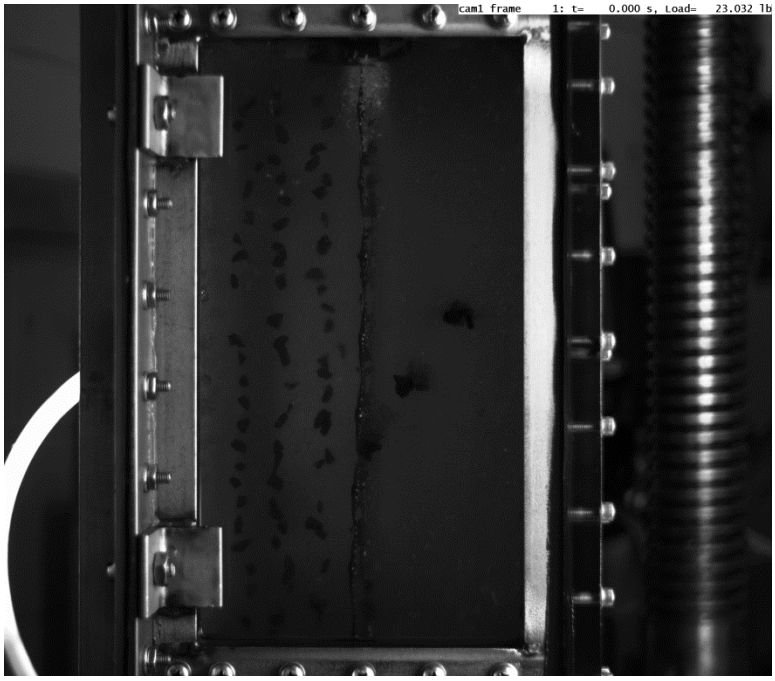


Figure A. 10: Test 1: Image of the side view of the box (cam1) and lines of soil markers placed parallel to the pullout direction.

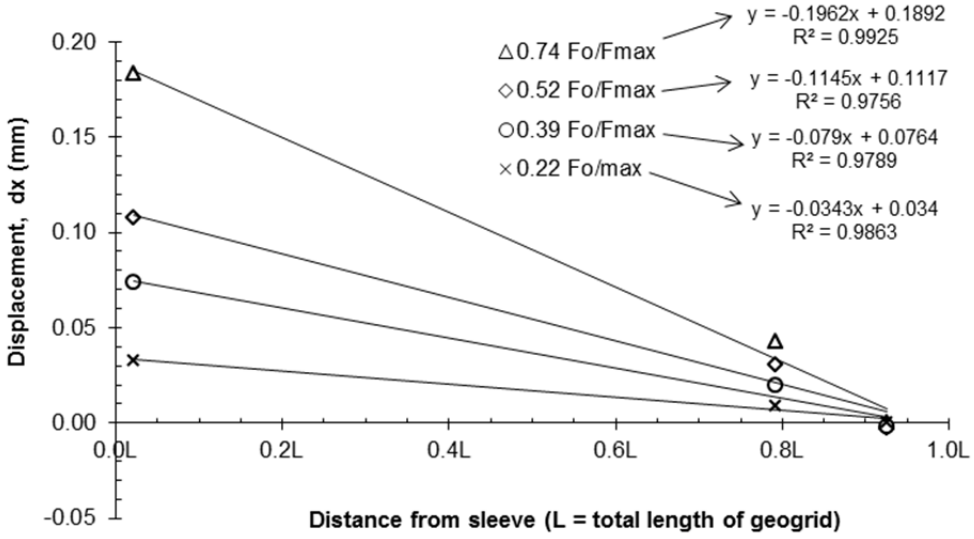


Figure A. 11: Test 1: Horizontal movement of the box calculated with the PIV software with images from cam1 (side view).

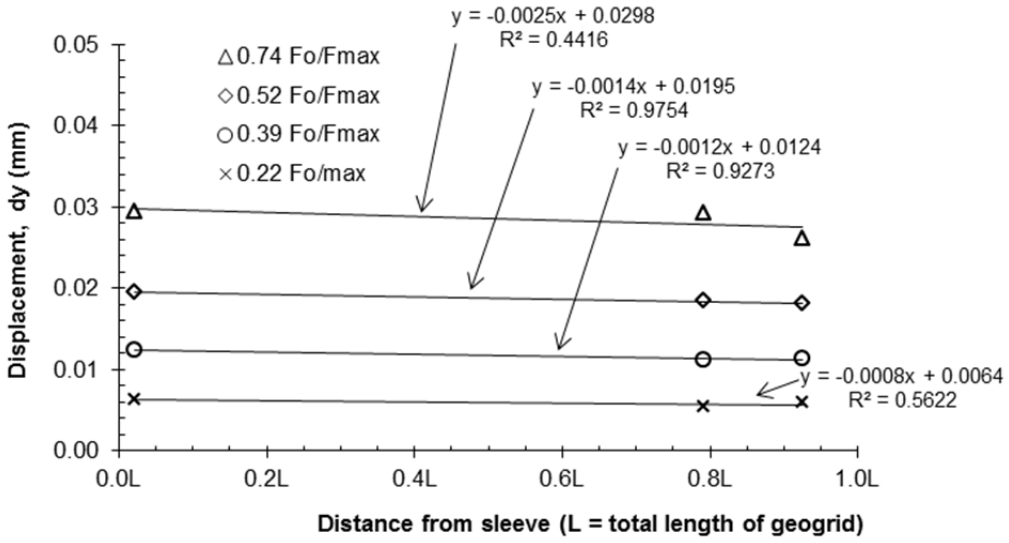


Figure A. 12: Test 1: Vertical movement of the box calculated with the PIV software with images from cam1 (side view).

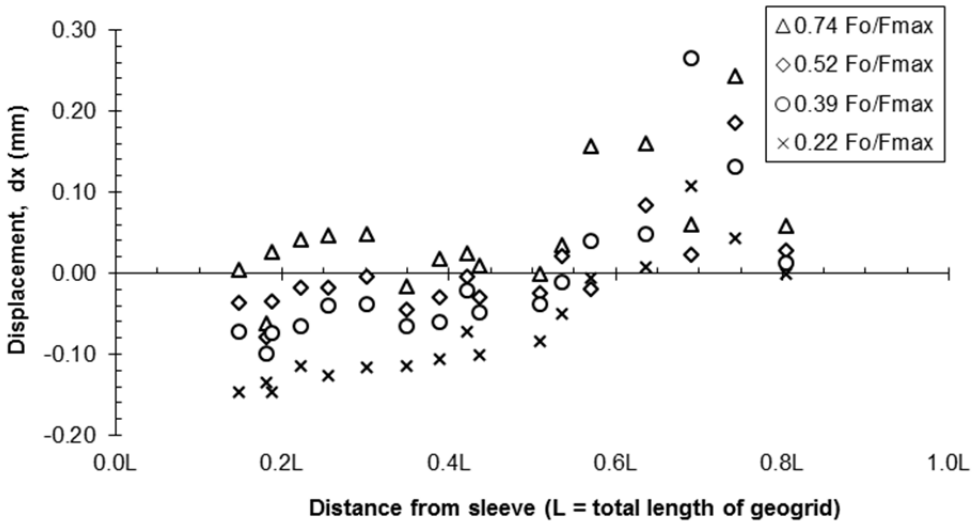


Figure A. 13: Test 1: Horizontal displacement of soil markers along the geogrid at 15 mm from the interface.

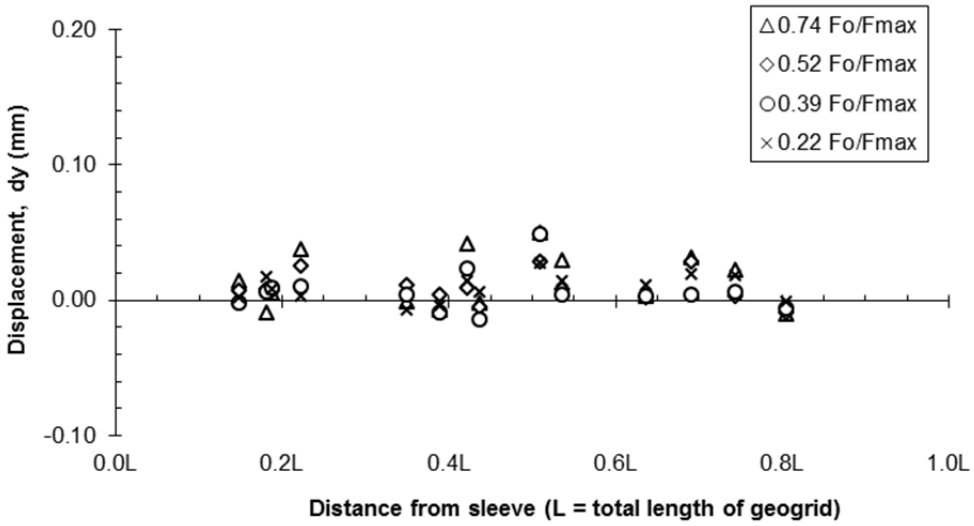


Figure A. 14: Test 1: Vertical displacement of soil markers along the geogrid at 15 mm from the interface.

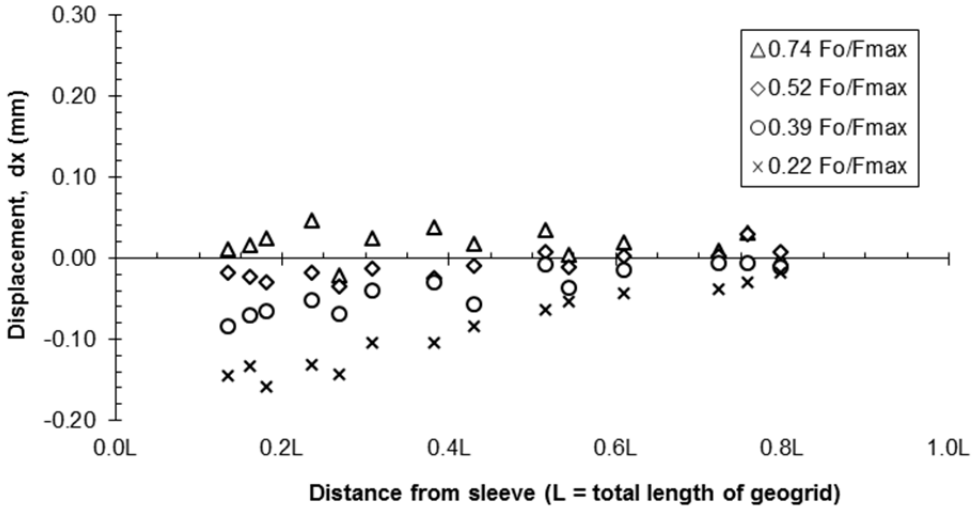


Figure A. 15: Test 1: Horizontal displacement of soil markers along the geogrid at 33 mm from the interface.

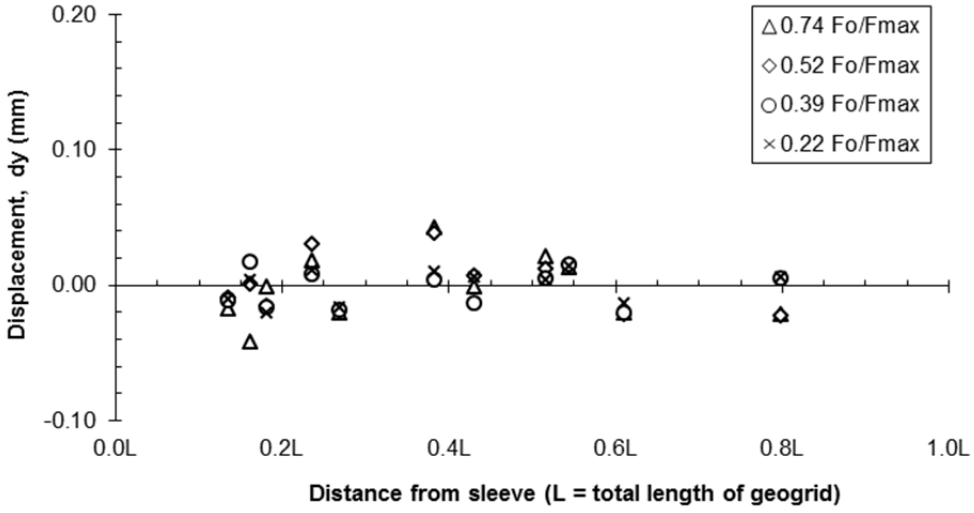


Figure A. 16: Test 1: Vertical displacement of soil markers along the geogrid at 33 mm from the interface.

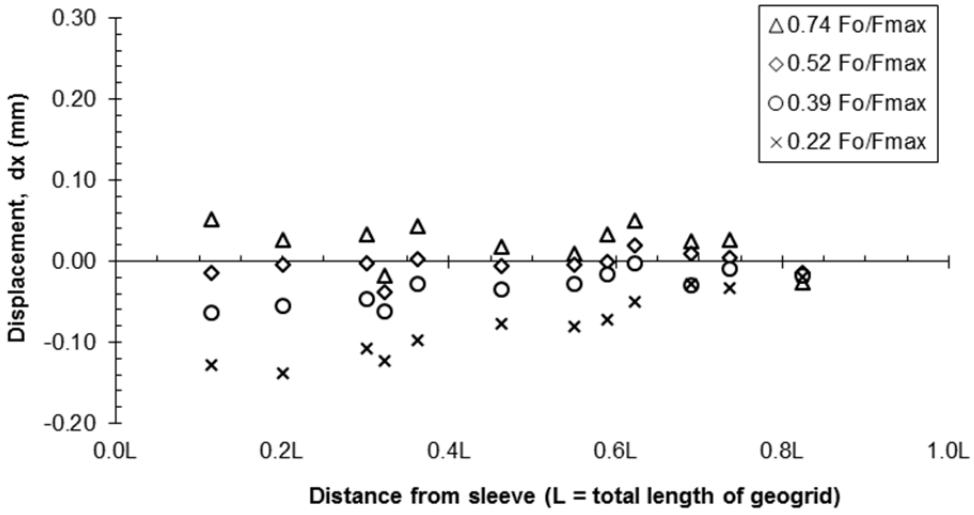


Figure A. 17: Test 1: Horizontal displacement of soil markers along the geogrid at 48 mm from the interface.

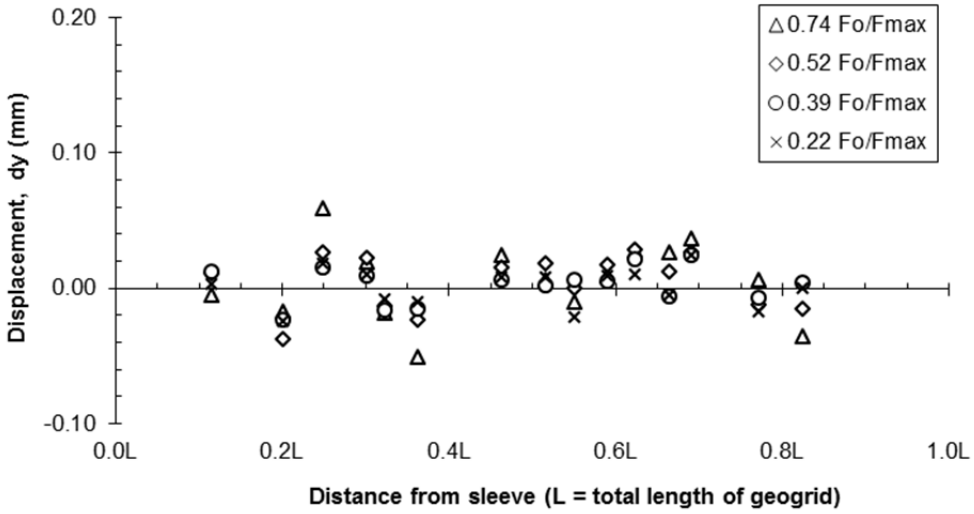


Figure A. 18: Test 1: Vertical displacement of soil markers along the geogrid at 48 mm from the interface.

**Test 2**

***Images from cam0 (plan view of the test)***

The images from cam0 provide the plan view of the test. In these images, the line of markers perpendicular to the pullout direction are observed (Figure A. 19). The top, middle and bottom lines of soil markers in Figure A. 19 are at 47 mm (1.85 in.), 25 mm (0.98 in.), and 10 mm (0.39 in.) from the interface, respectively.

The data of the horizontal and vertical displacements of the pullout box are shown in Figure A. 20 and Figure A. 21, respectively. The data of the horizontal and vertical displacements of the soil markers are shown from Figure A. 22 to Figure A. 27.

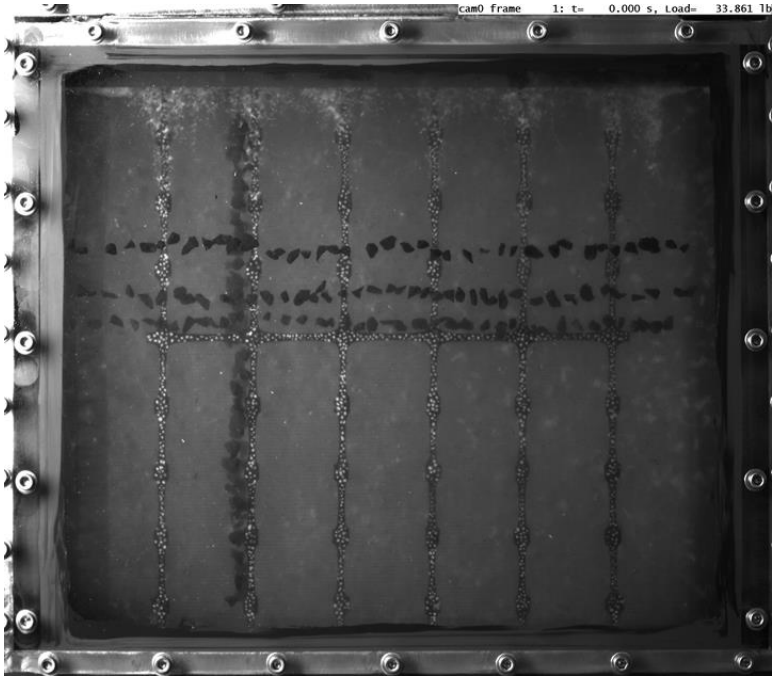


Figure A. 19: Test2: Image of the plan view of the box (cam0) and lines of soil markers placed perpendicular to the pullout direction.

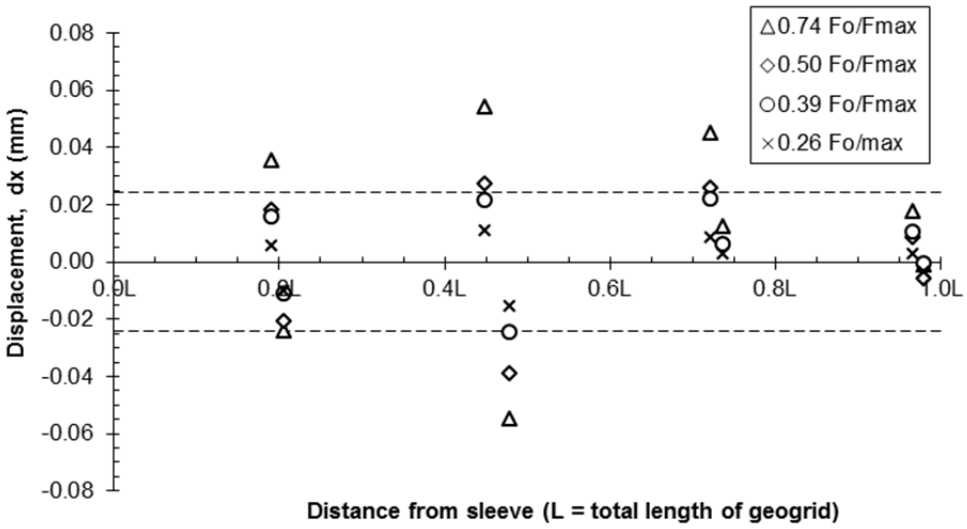


Figure A. 20: Test 2: Horizontal movement of the box calculated with the PIV software with images from cam0 (plan view).

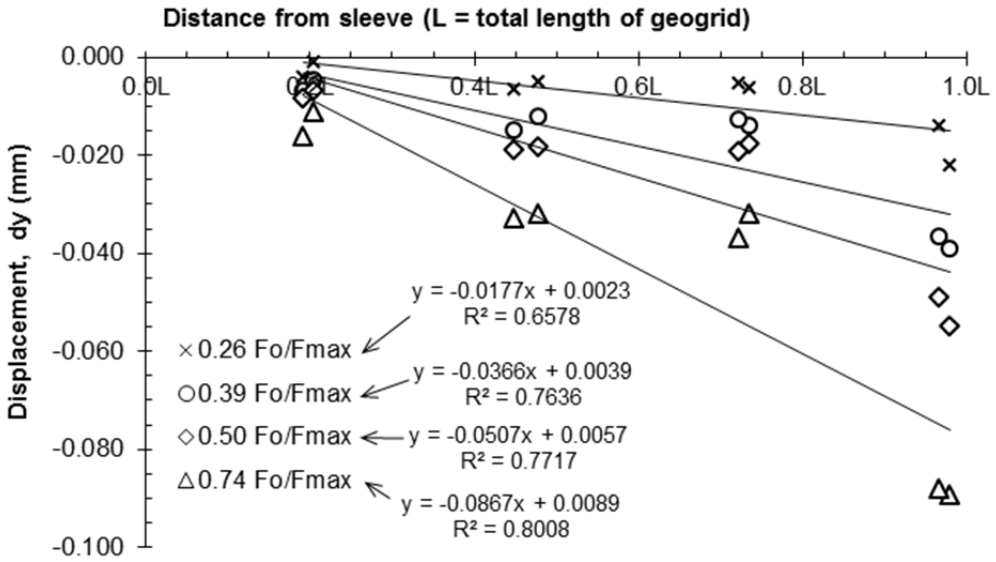


Figure A. 21: Test 2: Vertical movement of the box calculated with the PIV software with images from cam0 (plan view).

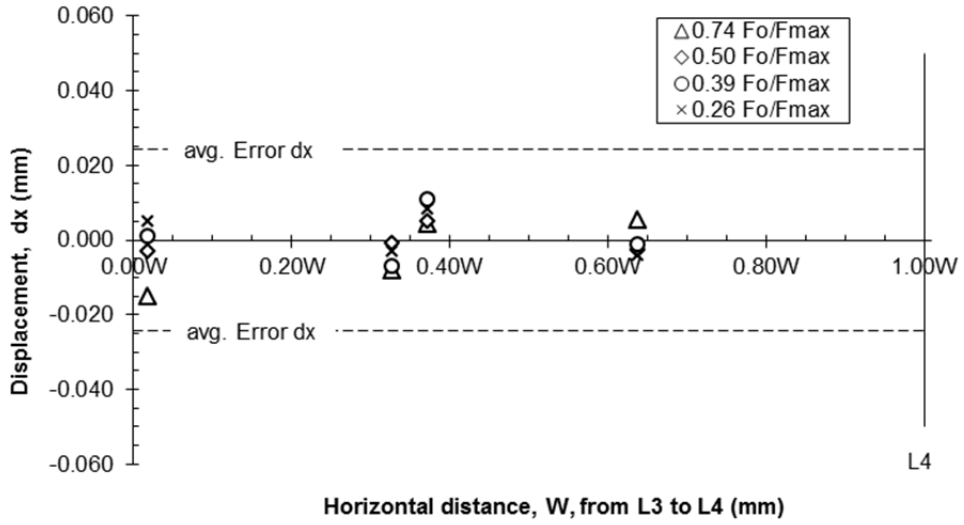


Figure A. 22: Test 2: Horizontal displacement of soil markers between L3 and L4 at 47 mm from the interface.

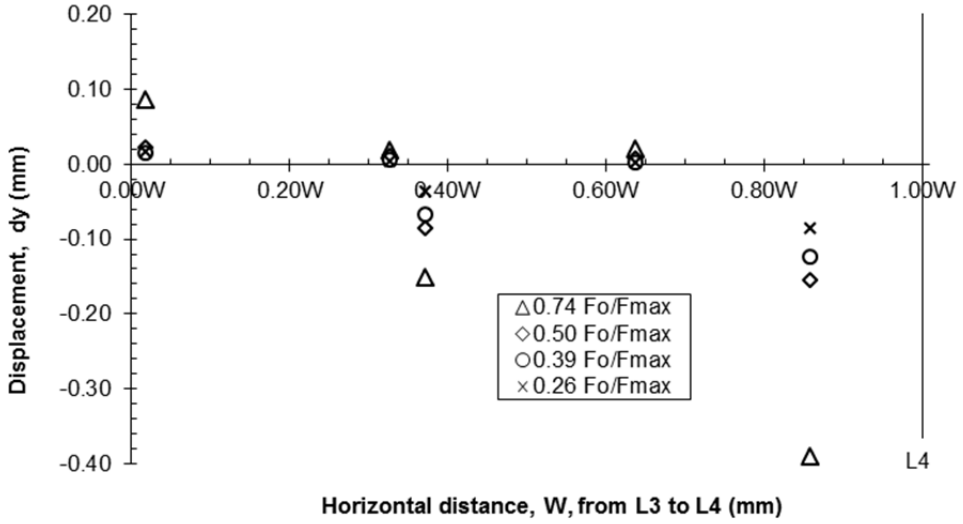


Figure A. 23: Test 2: Vertical displacement of soil markers between L3 and L4 at 47 mm from the interface.

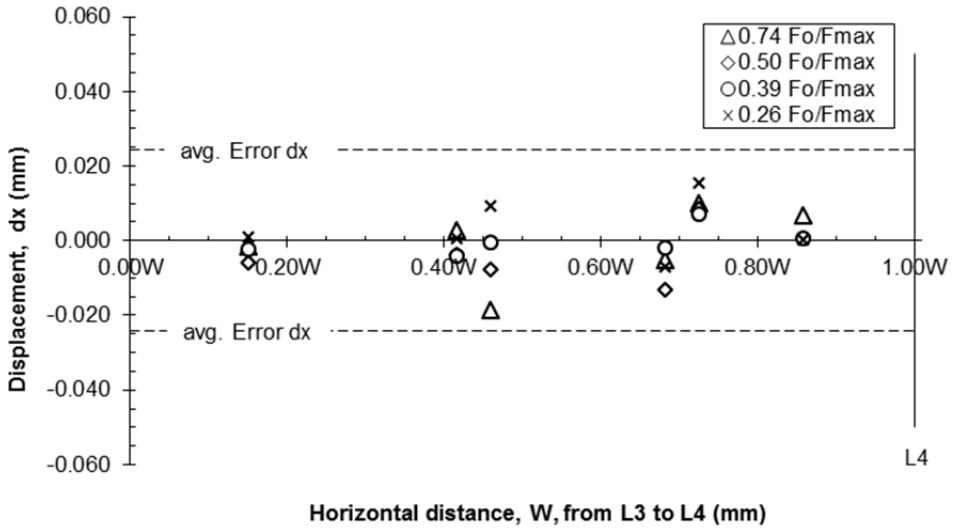


Figure A. 24: Test 2: Horizontal displacement of soil markers between L3 and L4 at 25 mm from the interface.

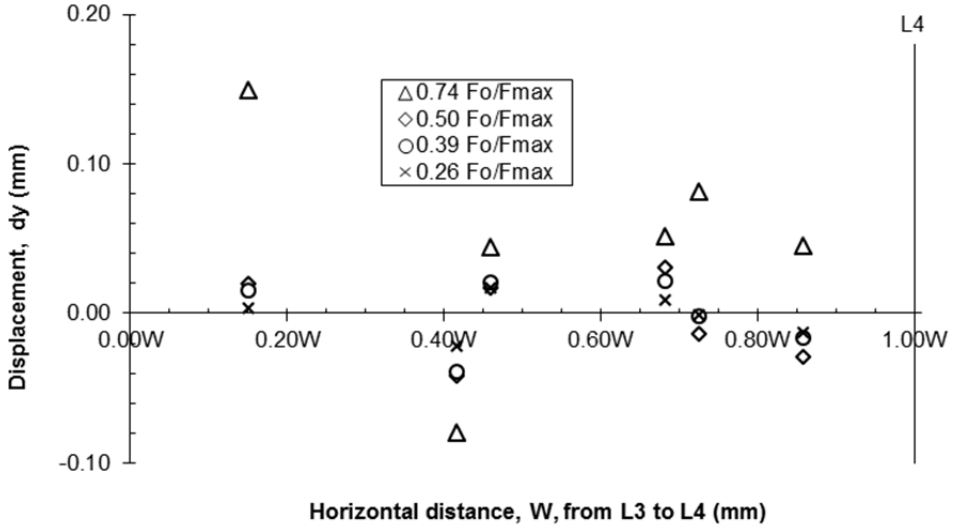


Figure A. 25: Test 2: Vertical displacement of soil markers between L3 and L4 at 25 mm from the interface.

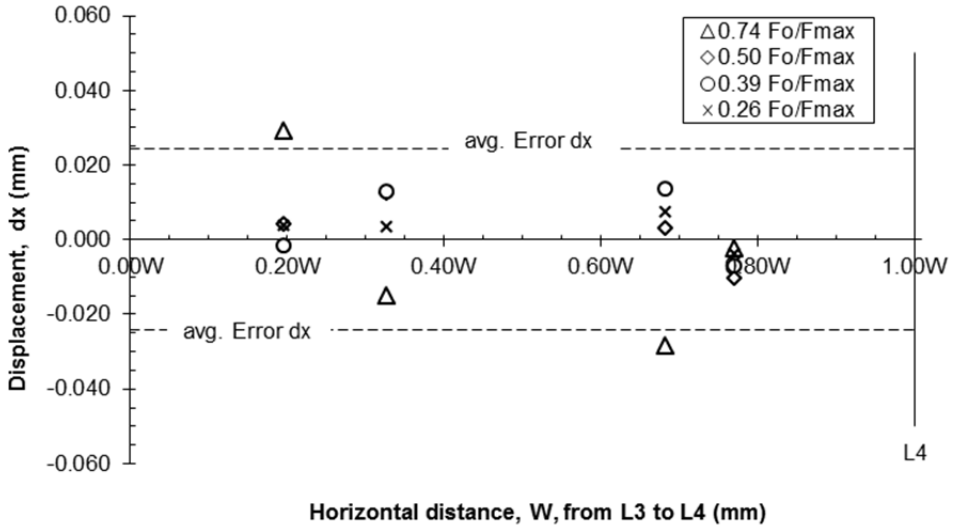


Figure A. 26: Test 2: Horizontal displacement of soil markers between L3 and L4 at 10 mm from the interface.

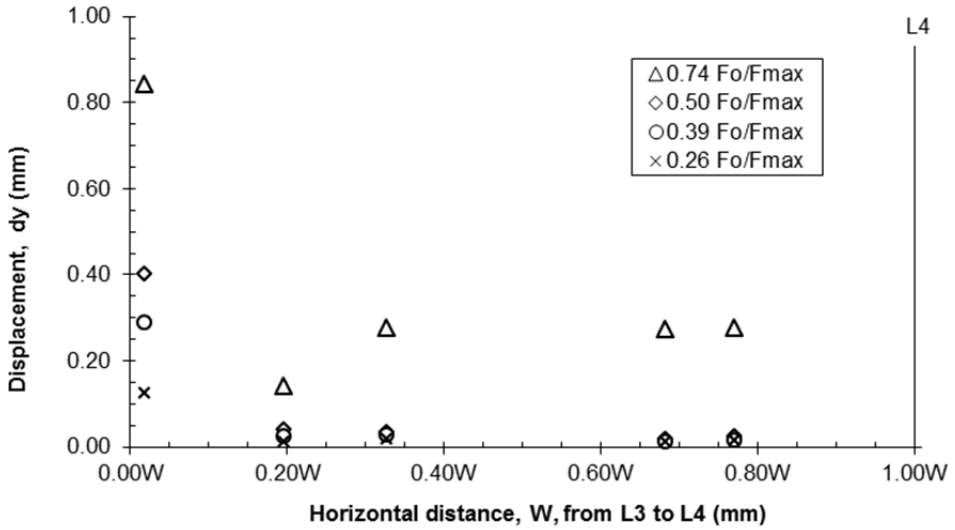


Figure A. 27: Test 2: Vertical displacement of soil markers between L3 and L4 at 10 mm from the interface.

***Images from cam1 (side view of the test)***

The images from cam1 provide the side view of the test. In these images, the lines of markers parallel to the pullout direction are observed (Figure A. 28). The lines of soil markers in Figure A. 28 are to the left of the geogrid at 7, 30 and 42 mm from the interface.

The data of the horizontal and vertical displacements of the pullout box are shown in Figure A. 29 and Figure A. 30, respectively. The data of the horizontal and vertical displacements of the soil markers are shown from Figure A. 31 to Figure A. 34. Data from the soil markers at 42 mm from the interface could not be obtained due to the lack of contrast between the soil markers and the illumination.

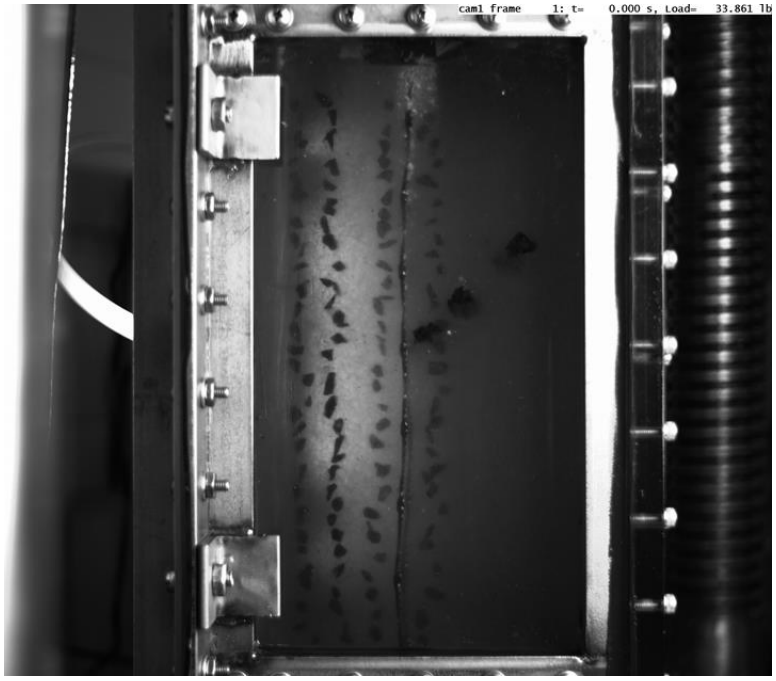


Figure A. 28: Test 2: Image of the side view of the box (cam1) and lines of soil markers placed parallel to the pullout direction.

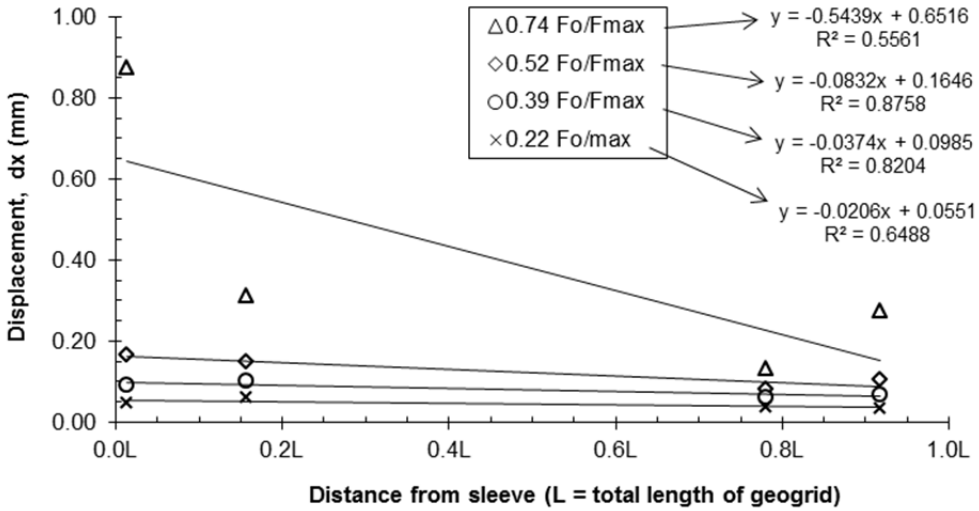


Figure A. 29: Test 2: Horizontal movement of the box calculated with the PIV software with images from cam1 (side view).

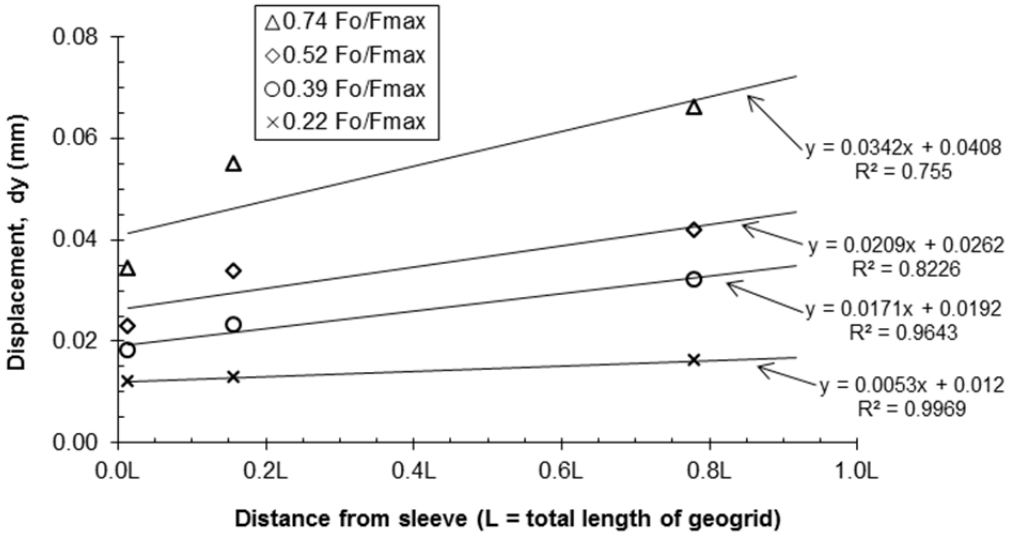


Figure A. 30: Test 2: Vertical movement of the box calculated with the PIV software with images from cam1 (side view).

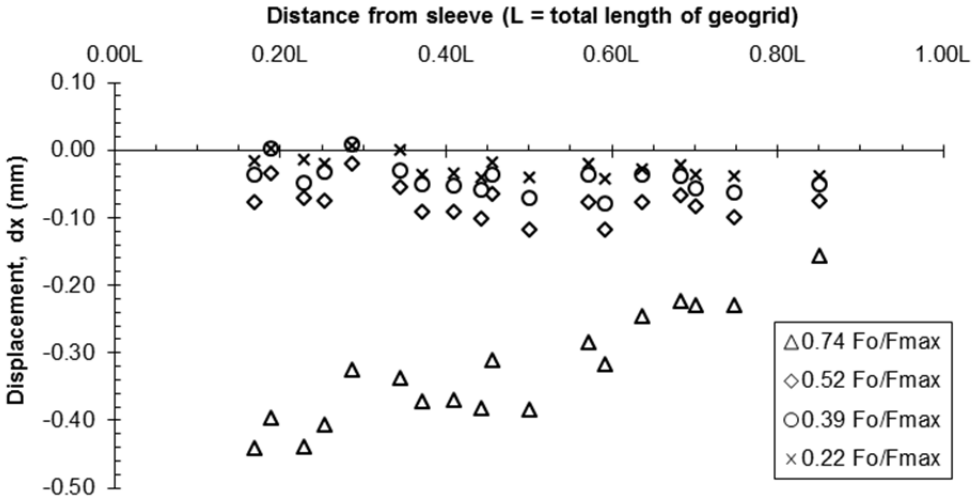


Figure A. 31: Test 2: Horizontal displacement of soil markers along the geogrid at 7 mm from the interface.

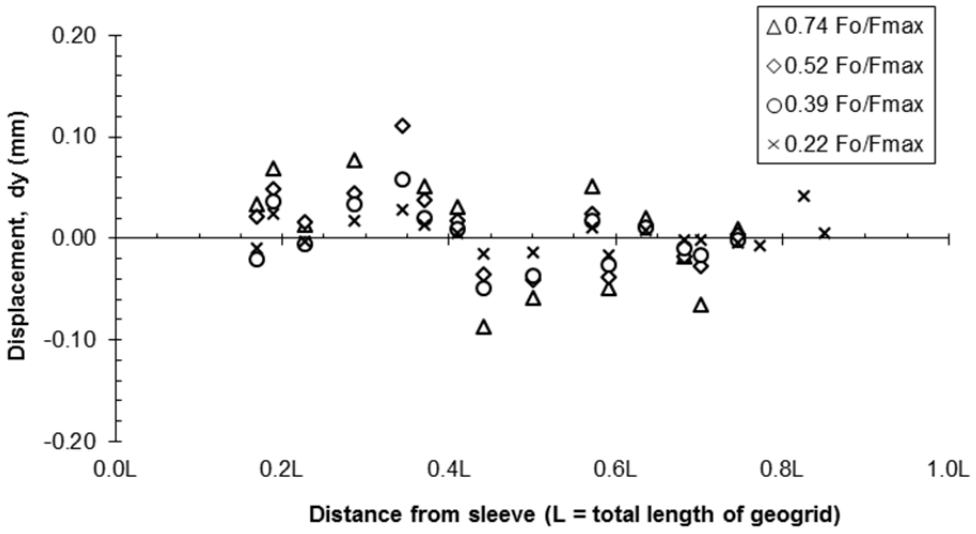


Figure A. 32: Test 2: Vertical displacement of soil markers along the geogrid at 7 mm from the interface.

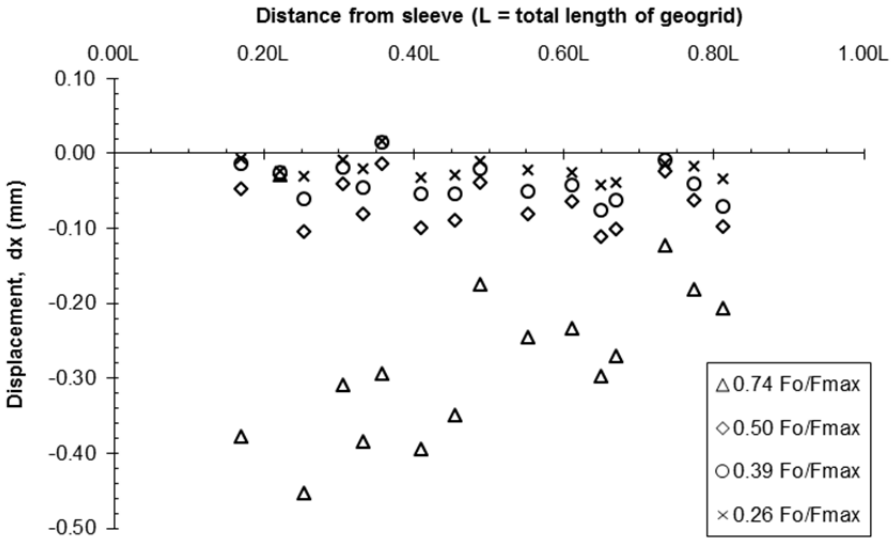


Figure A. 33: Test 2: Horizontal displacement of soil markers along the geogrid at 30 mm from the interface.

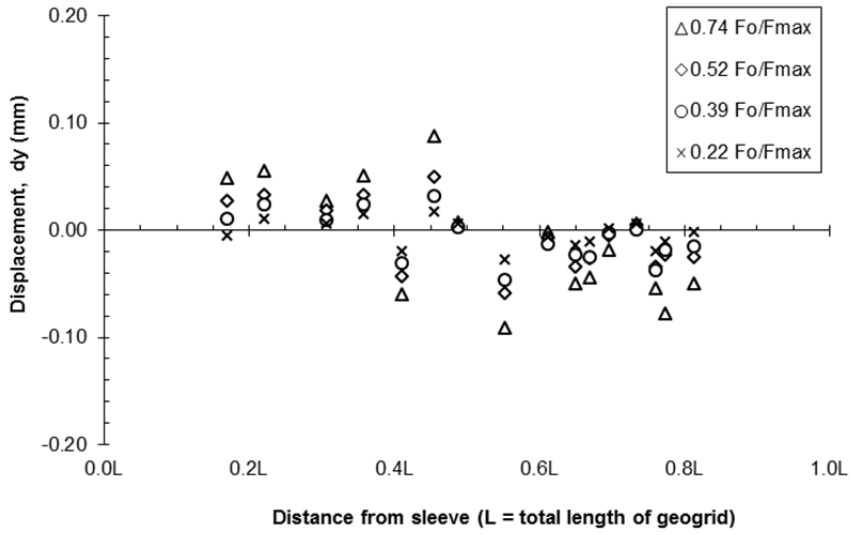


Figure A. 34: Test 2: Vertical displacement of soil markers along the geogrid at 30 mm from the interface.

**Test 3**

***Images from cam0 (plan view of the test)***

The images from cam0 provide the plan view of the test. In these images, the line of markers perpendicular to the pullout direction are observed (Figure A. 35). The top, middle and bottom lines of soil markers in Figure A. 35 are at 45 mm (1.77 in.), 25 mm (0.98 in.), and 8 mm (0.31 in.) from the interface, respectively.

The data of the horizontal and vertical displacements of the pullout box are shown in Figure A. 36 and Figure A. 37, respectively. The data of the horizontal and vertical displacements of the soil markers are shown from Figure A. 38 to Figure A. 43.

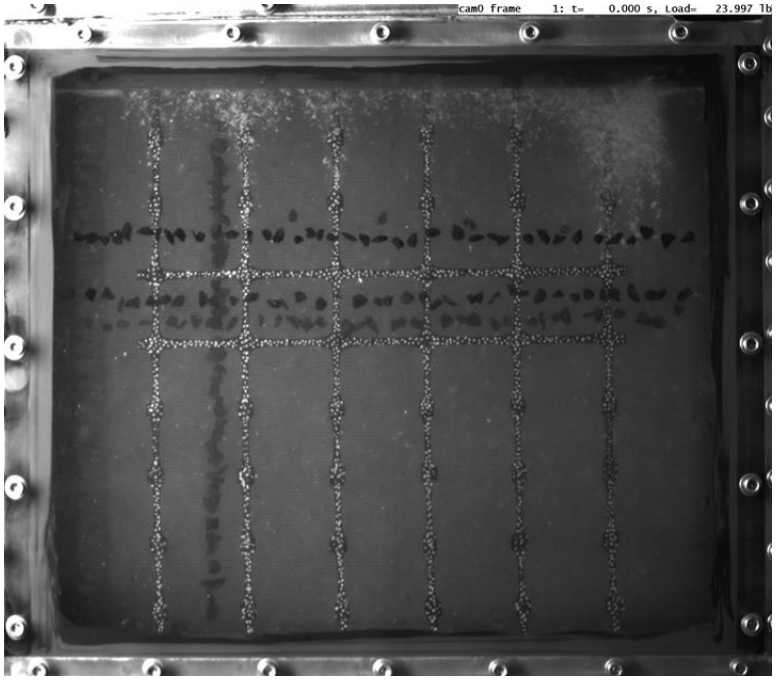


Figure A. 35: Test3: Image of the plan view of the box (cam0) and lines of soil markers placed perpendicular to the pullout direction.

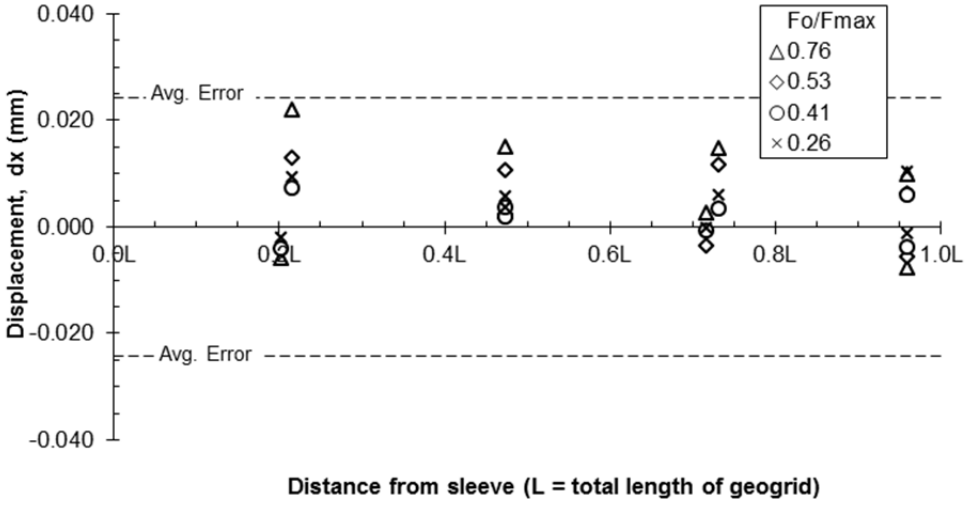


Figure A. 36: Test 3: Horizontal movement of the box calculated with the PIV software with images from cam0 (plan view).

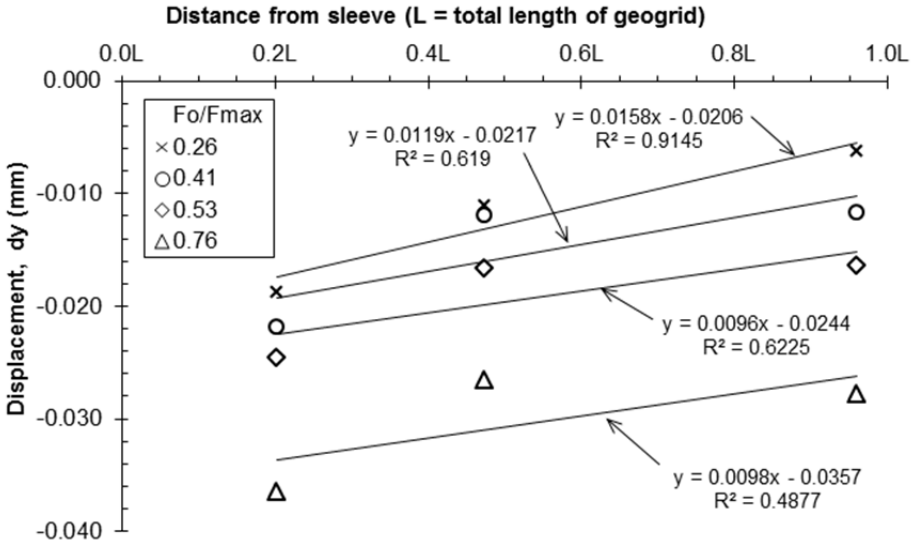


Figure A. 37: Test 3: Vertical movement of the box calculated with the PIV software with images from cam0 (plan view).

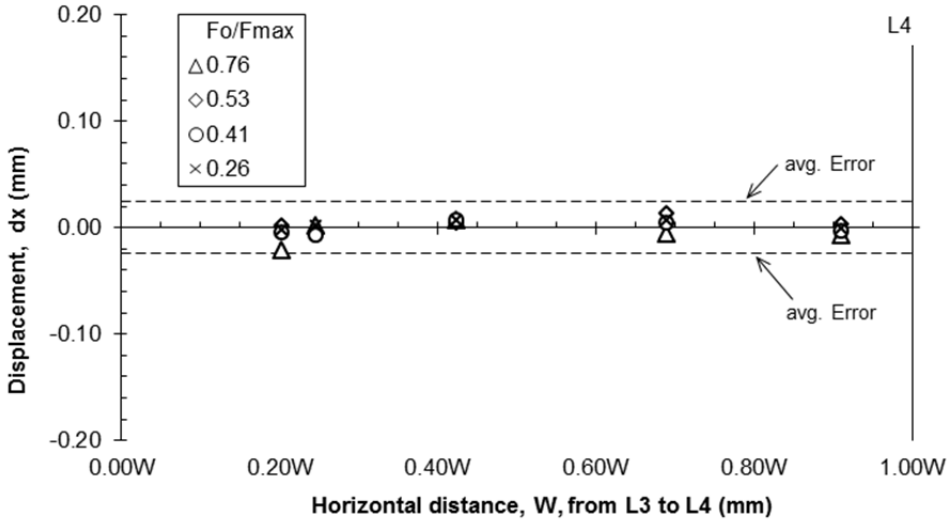


Figure A. 38: Test 3: Horizontal displacement of soil markers between L3 and L4 at 45 mm from the interface.

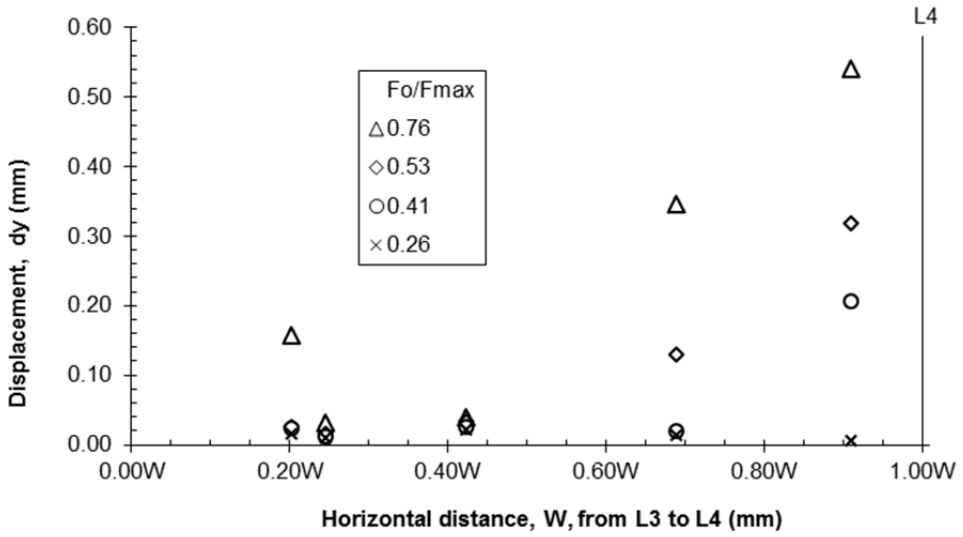


Figure A. 39: Test 3: Vertical displacement of soil markers between L3 and L4 at 45 mm from the interface.

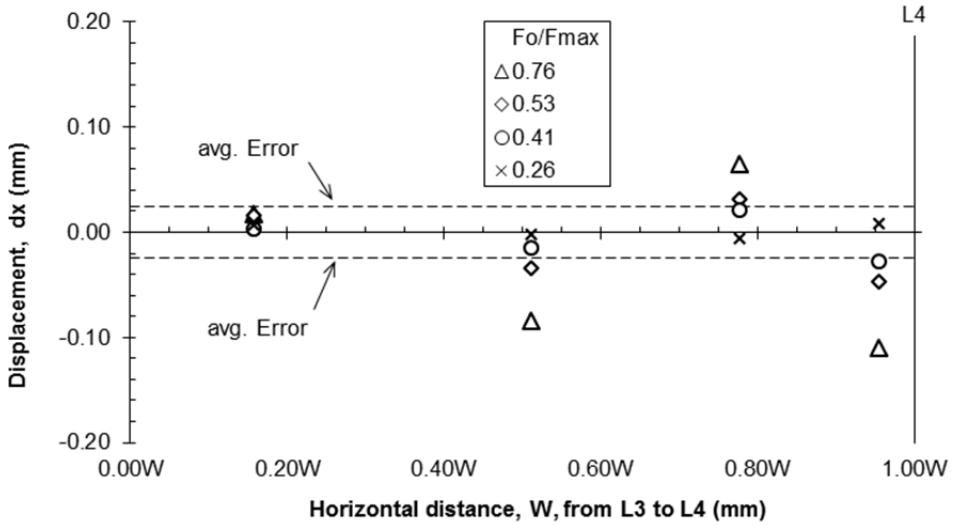


Figure A. 40: Test 3: Horizontal displacement of soil markers between L3 and L4 at 25 mm from the interface.

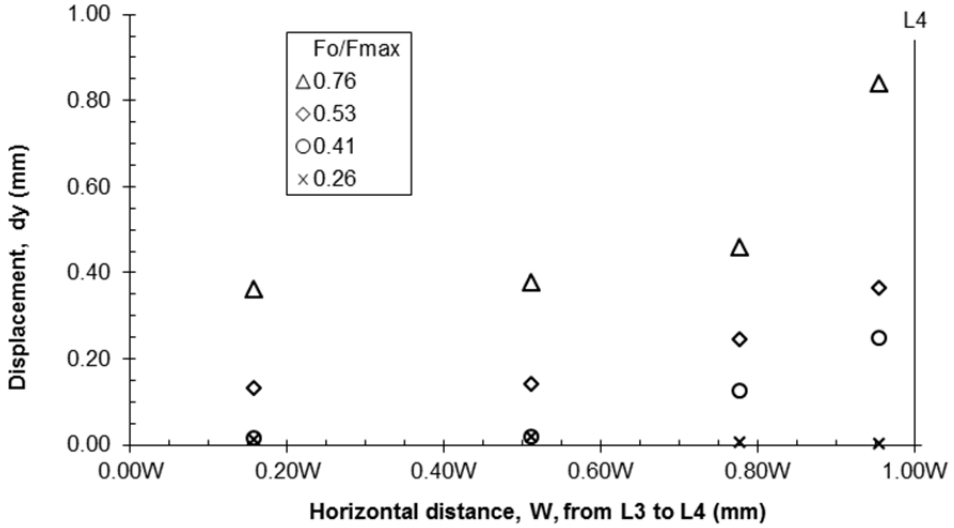


Figure A. 41: Test 3: Vertical displacement of soil markers between L3 and L4 at 25 mm from the interface.

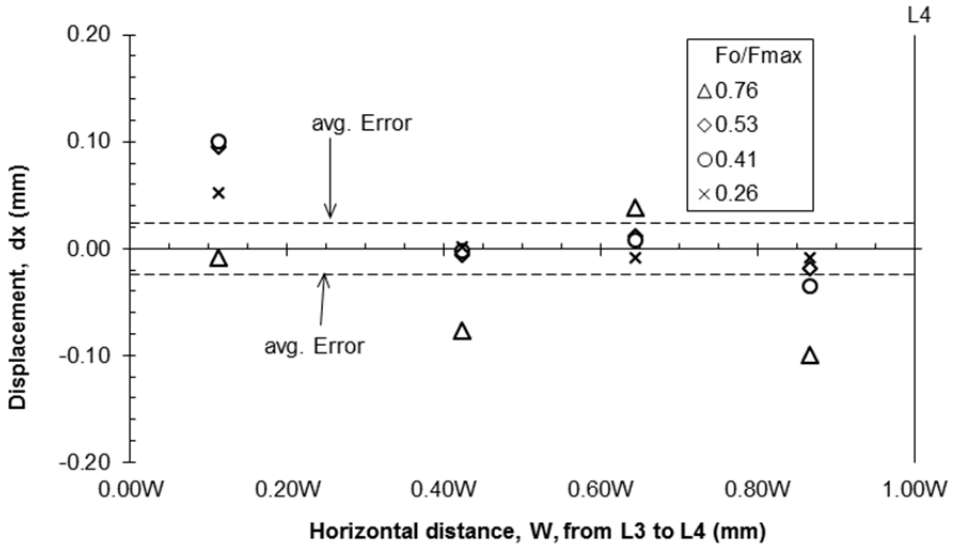


Figure A. 42: Test 3: Horizontal displacement of soil markers between L3 and L4 at 8 mm from the interface.

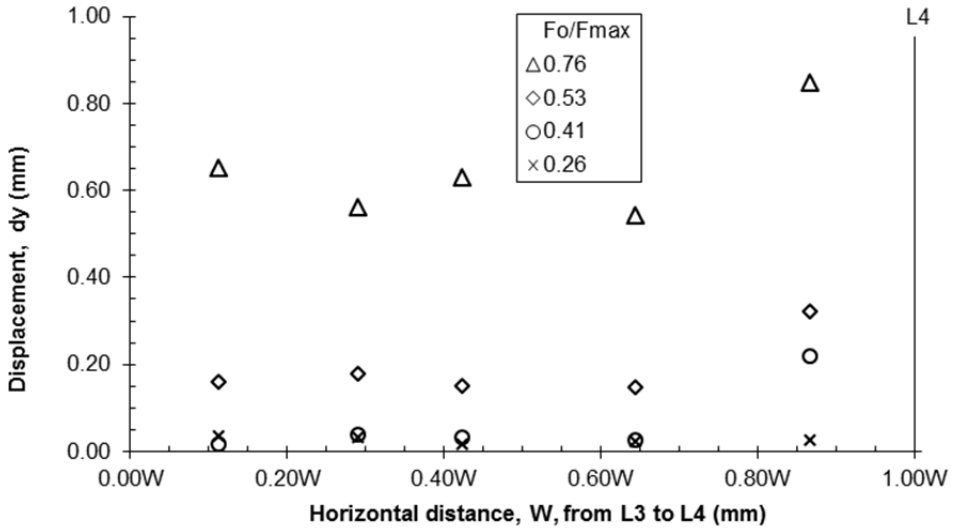


Figure A. 43: Test 3: Vertical displacement of soil markers between L3 and L4 at 8 mm from the interface.

***Images from cam1 (side view of the test)***

The images from cam1 provide the side view of the test. In these images, the lines of markers parallel to the pullout direction are observed (Figure A. 44). The lines of soil markers in Figure A. 44 are to the left of the geogrid at 8, 24 and 39 mm from the interface.

The data of the horizontal and vertical displacements of the pullout box are shown in Figure A. 45 and Figure A. 46, respectively. The data of the horizontal and vertical displacements of the soil markers are shown from Figure A. 47 to Figure A. 52.

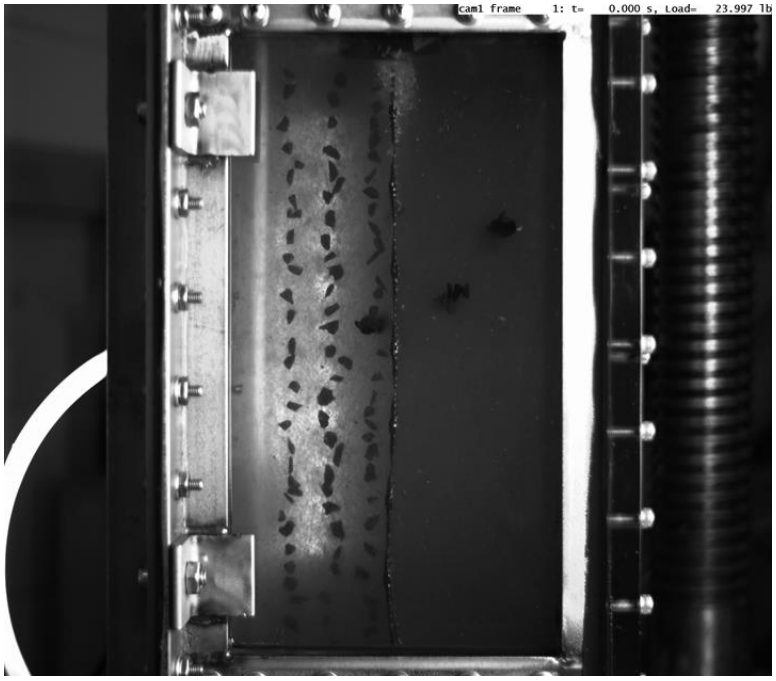


Figure A. 44: Test 3: Image of the side view of the box (cam1) and lines of soil markers placed parallel to the pullout direction.

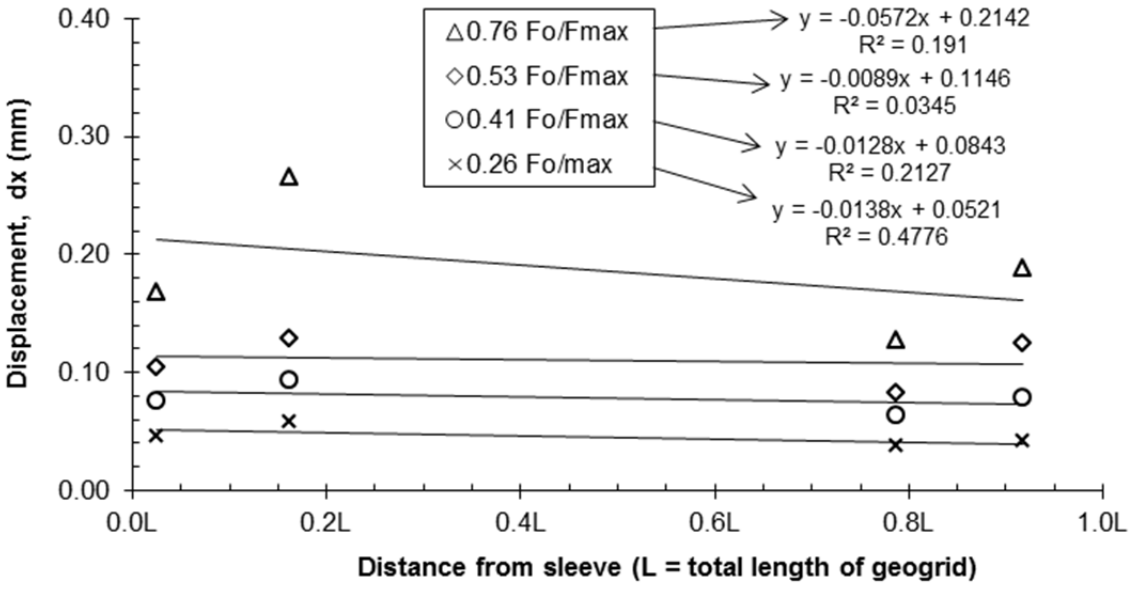


Figure A. 45: Test 3: Horizontal movement of the box calculated with the PIV software with images from cam1 (side view).

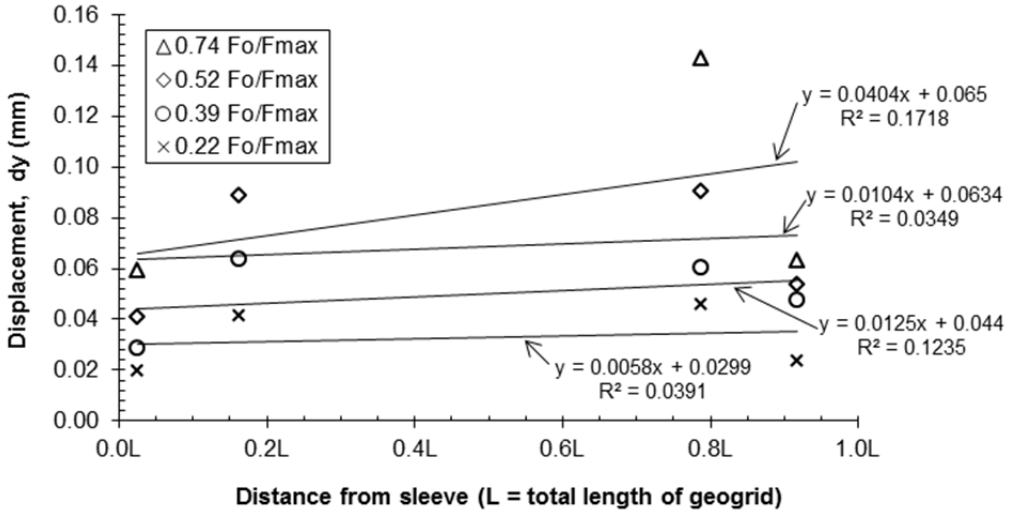


Figure A. 46: Test 3: Vertical movement of the box calculated with the PIV software with images from cam1 (side view).

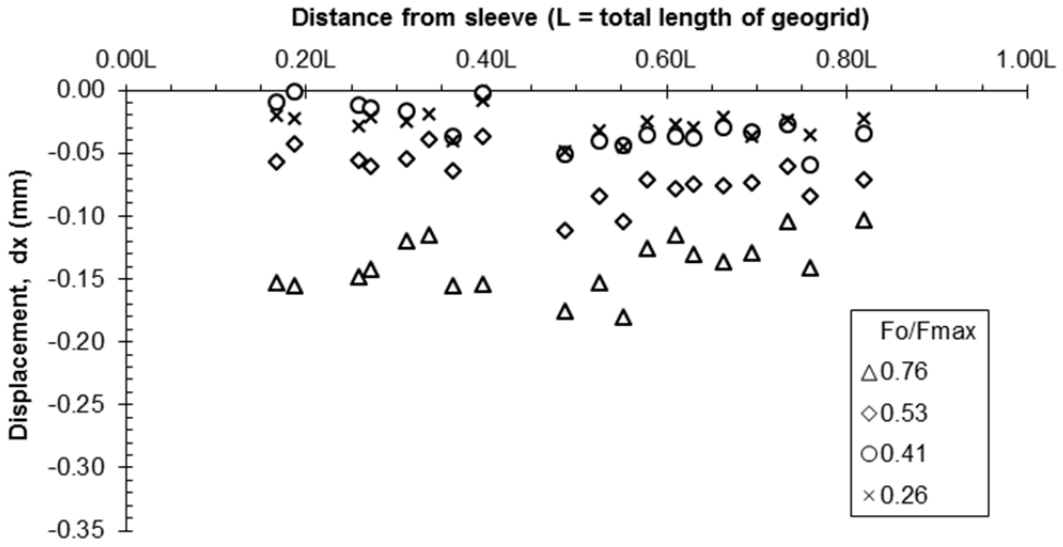


Figure A. 47: Test 3: Horizontal displacement of soil markers along the geogrid at 8 mm from the interface.

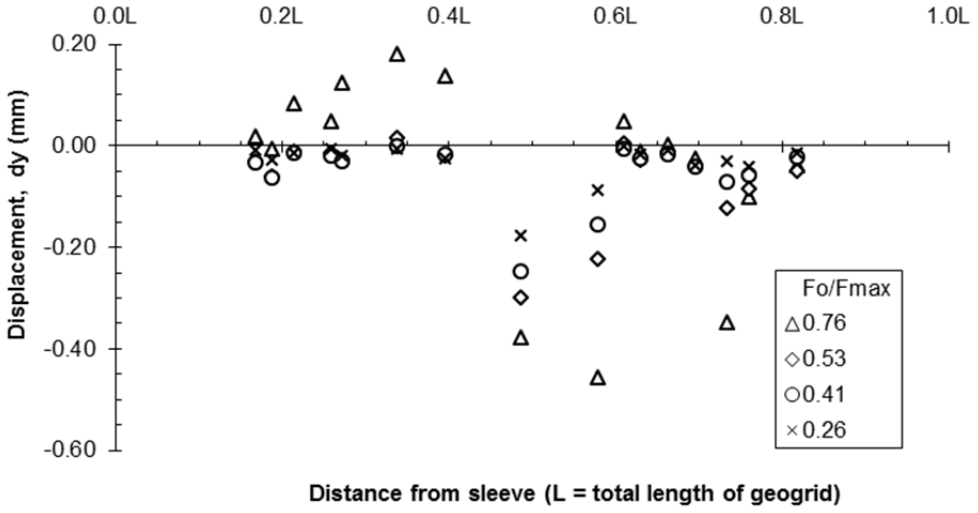


Figure A. 48: Test 3: Vertical displacement of soil markers along the geogrid at 8 mm from the interface.

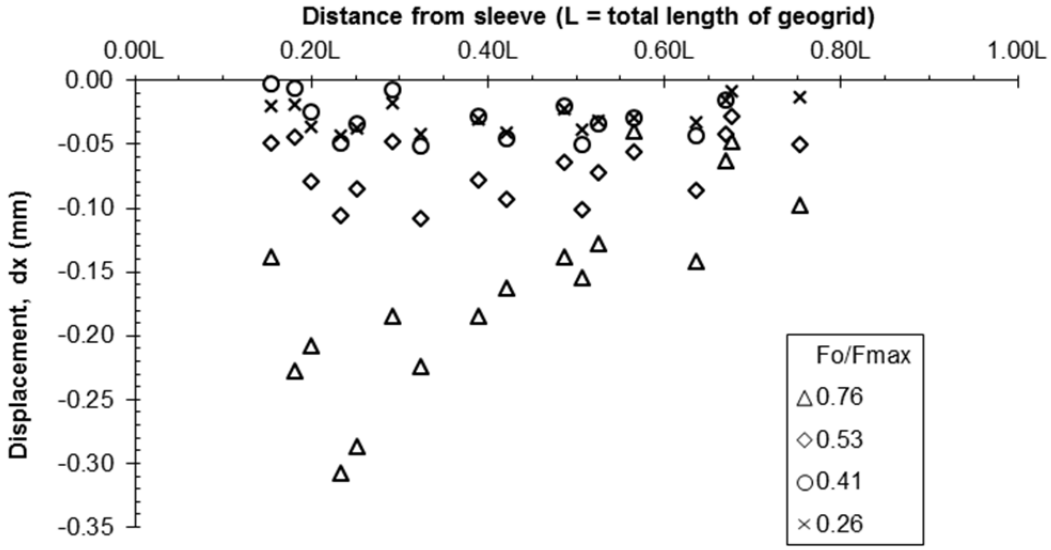


Figure A. 49: Test 3: Horizontal displacement of soil markers along the geogrid at 24 mm from the interface.

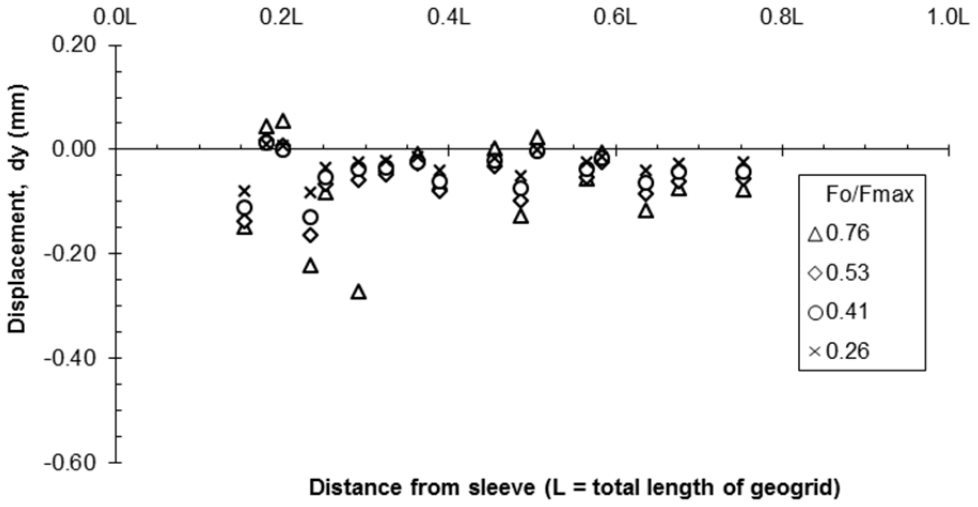


Figure A. 50: Test 3: Vertical displacement of soil markers along the geogrid at 24 mm from the interface.

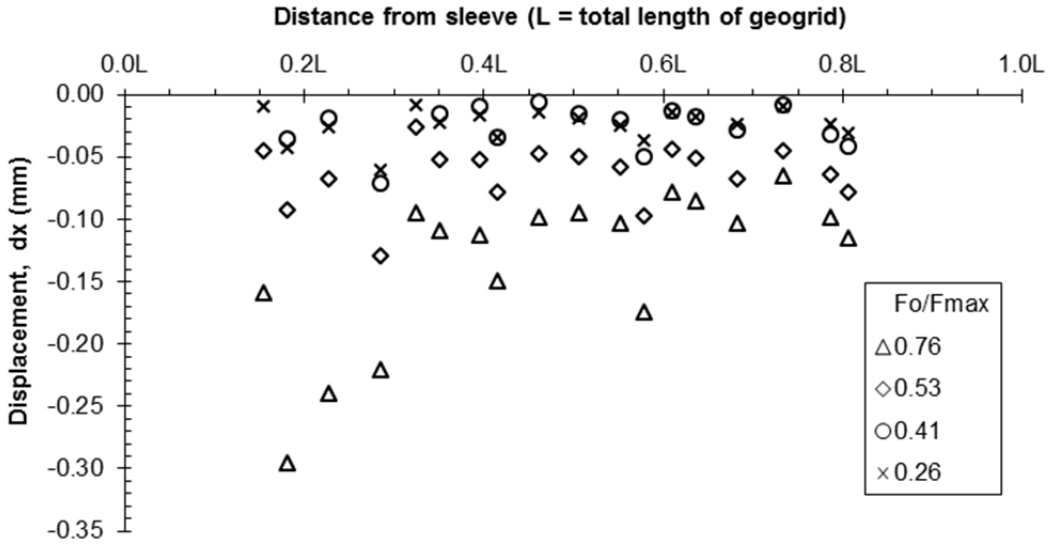


Figure A. 51: Test 3: Horizontal displacement of soil markers along the geogrid at 39 mm from the interface.

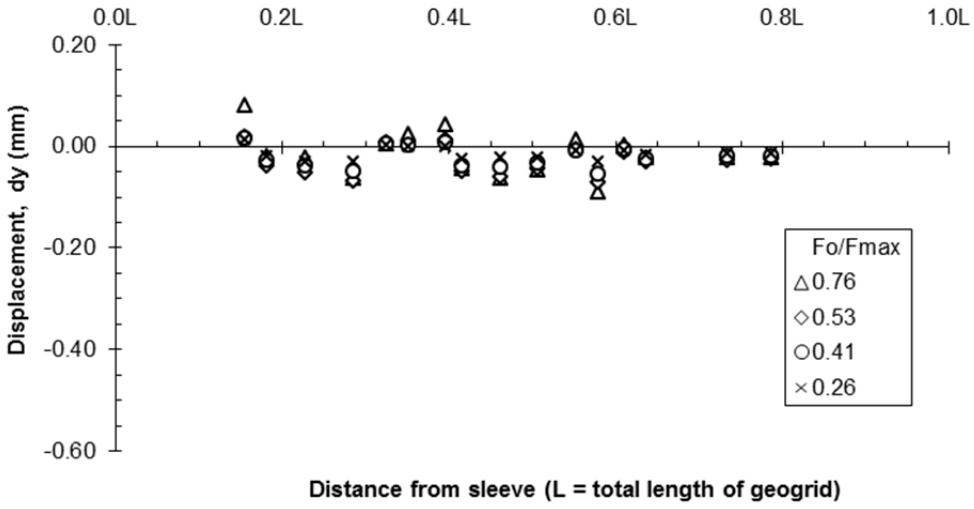


Figure A. 52: Test 3: Vertical displacement of soil markers along the geogrid at 39 mm from the interface.

**Test 4**

***Images from cam0 (plan view of the test)***

The images from cam0 provide the plan view of the test. In these images, the line of markers perpendicular to the pullout direction are observed (Figure A. 53). The top, middle and bottom lines of soil markers in Figure A. 53 are at 43 mm (1.69 in.), 25 mm (0.98 in.), and 11 mm (0.43 in.) from the interface, respectively.

The data of the horizontal and vertical displacements of the pullout box are shown in Figure A. 53 and Figure A. 54, respectively. The data of the horizontal and vertical displacements of the soil markers are shown from Figure A. 55 to Figure A. 61.

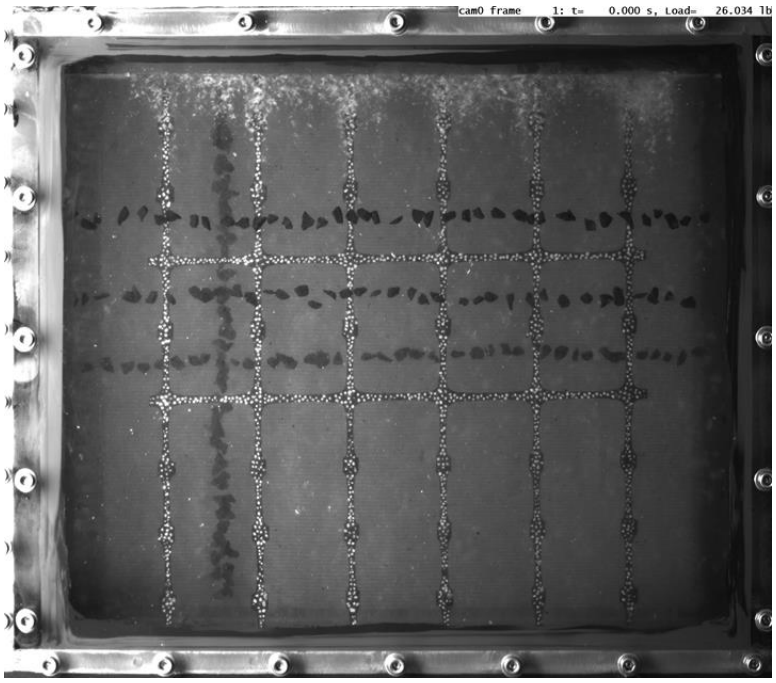


Figure A. 53: Test4: Image of the plan view of the box (cam0) and lines of soil markers placed perpendicular to the pullout direction.

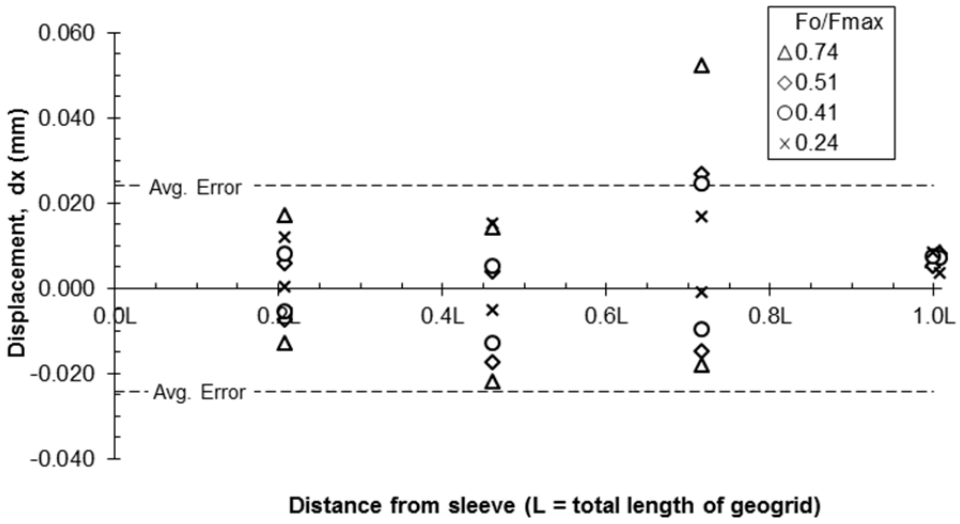


Figure A. 54: Test 4: Horizontal movement of the box calculated with the PIV software with images from cam0 (plan view).

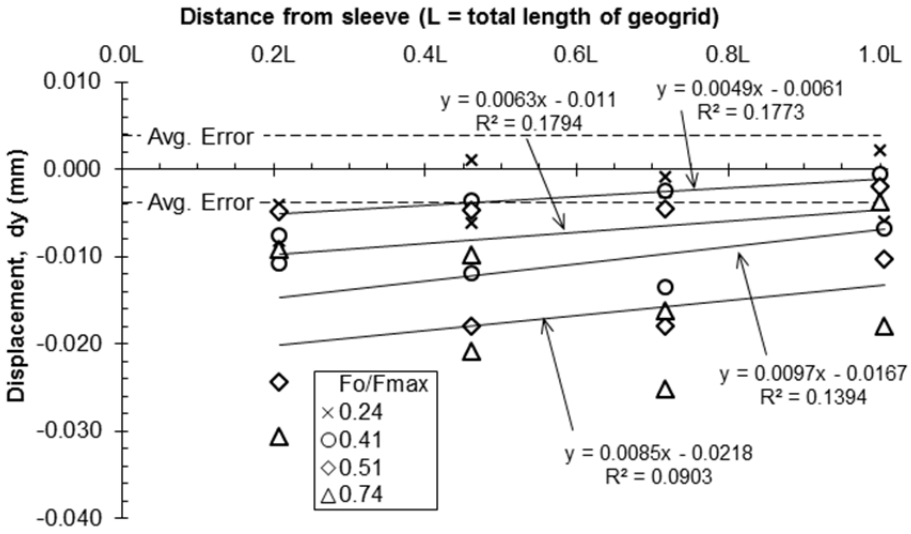


Figure A. 55: Test 4: Vertical movement of the box calculated with the PIV software with images from cam0 (plan view).

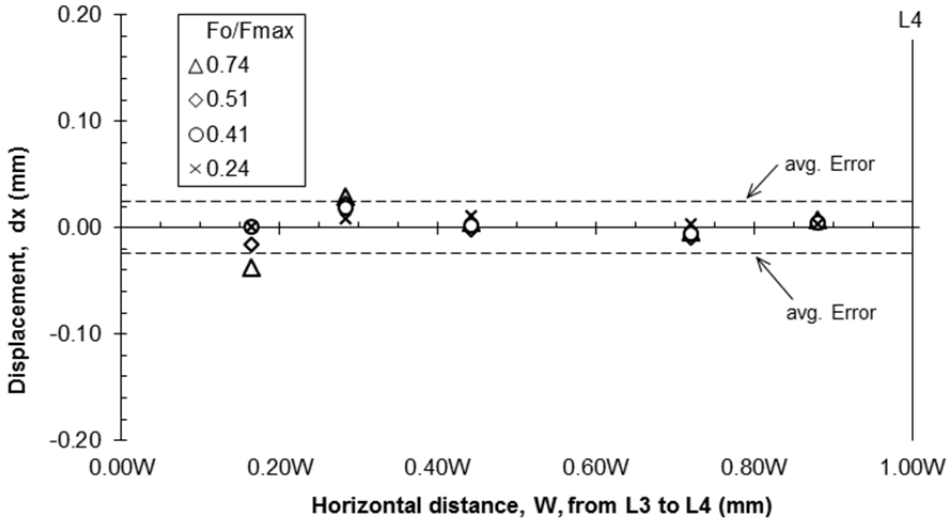


Figure A. 56: Test 4: Horizontal displacement of soil markers between L3 and L4 at 43 mm from the interface.

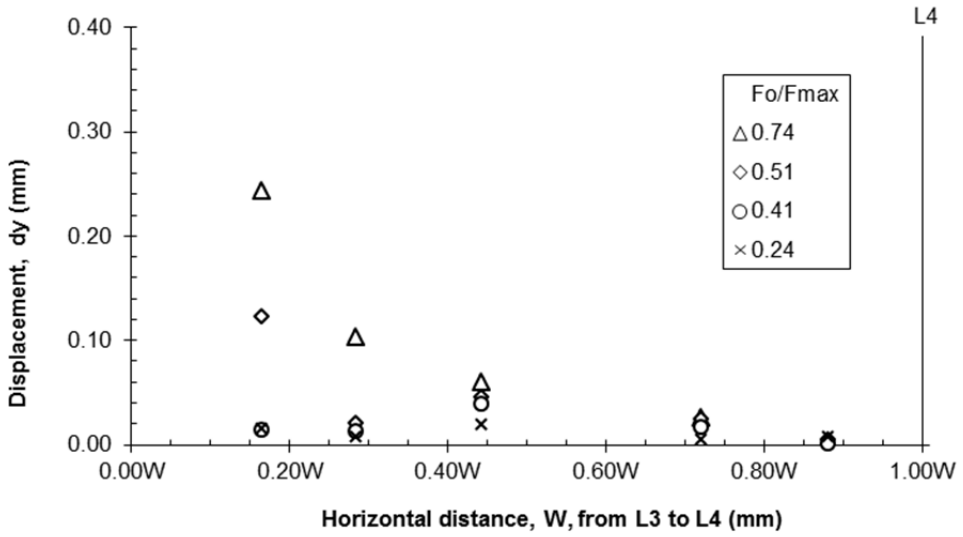


Figure A. 57: Test 4: Vertical displacement of soil markers between L3 and L4 at 43 mm from the interface.

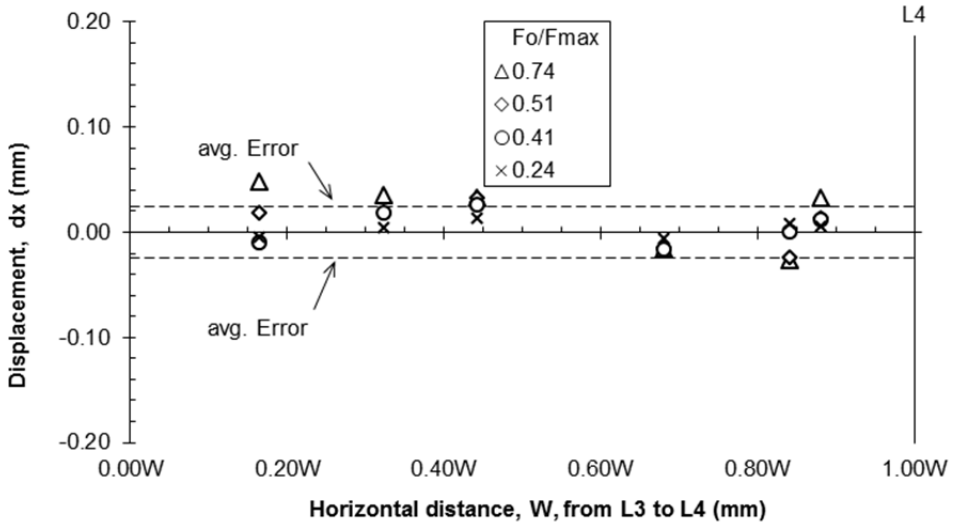


Figure A. 58: Test 4: Horizontal displacement of soil markers between L3 and L4 at 25 mm from the interface.

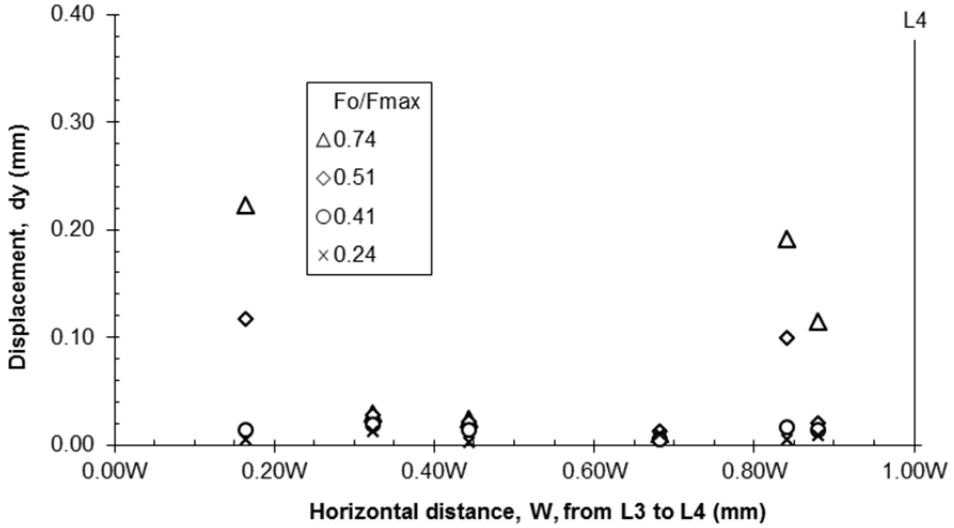


Figure A. 59: Test 4: Vertical displacement of soil markers between L3 and L4 at 25 mm from the interface.

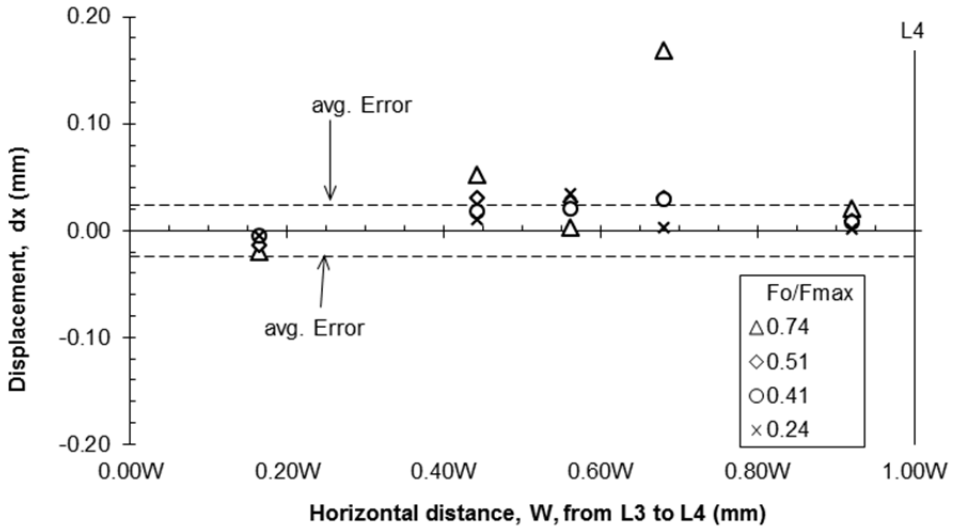


Figure A. 60: Test 4: Horizontal displacement of soil markers between L3 and L4 at 11 mm from the interface.

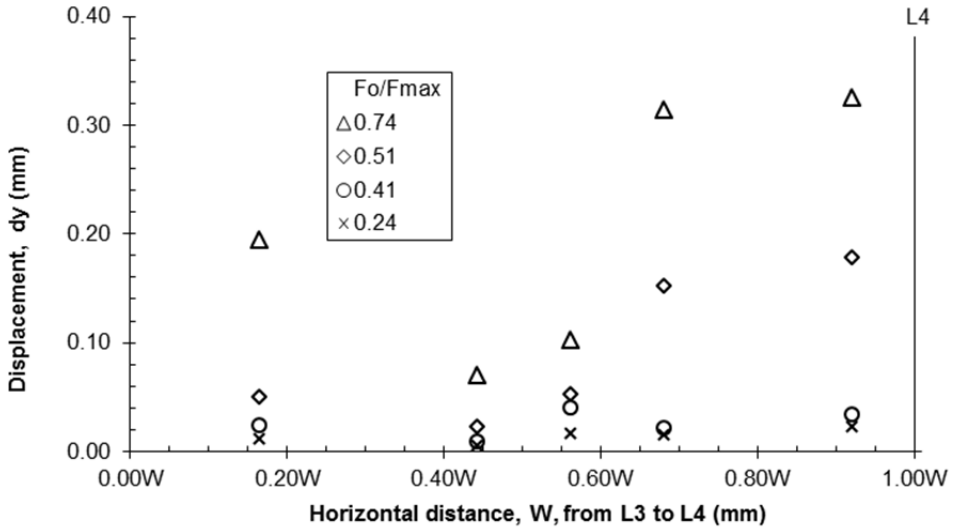


Figure A. 61: Test 4: Vertical displacement of soil markers between L3 and L4 at 11 mm from the interface.

***Images from cam1 (side view of the test)***

The images from cam1 provide the side view of the test. In these images, the lines of markers parallel to the pullout direction are observed (Figure A. 62). The lines of soil markers in Figure A. 62 are to the left of the geogrid at 7, 25 and 40 mm from the interface.

The data of the horizontal and vertical displacements of the pullout box are shown in Figure A. 63 and Figure A. 64, respectively. The data of the horizontal and vertical displacements of the soil markers are shown from Figure A. 65 to Figure A. 70.

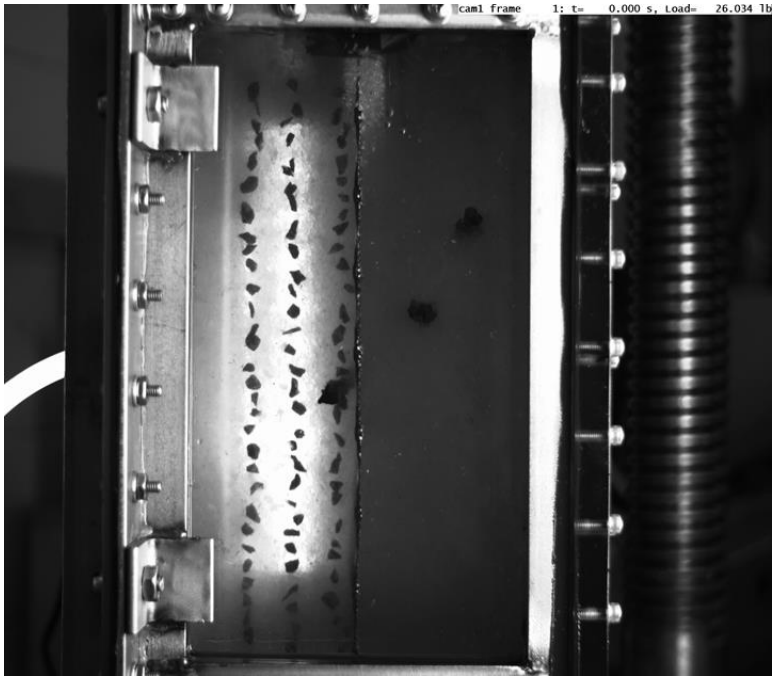


Figure A. 62: Test 4: Image of the side view of the box (cam1) and lines of soil markers placed parallel to the pullout direction.

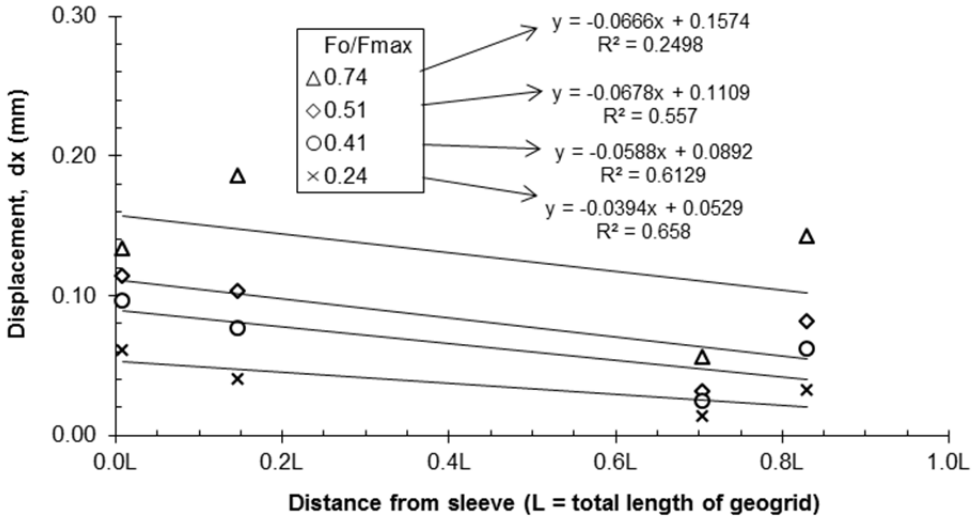


Figure A. 63: Test 4: Horizontal movement of the box calculated with the PIV software with images from cam1 (side view).

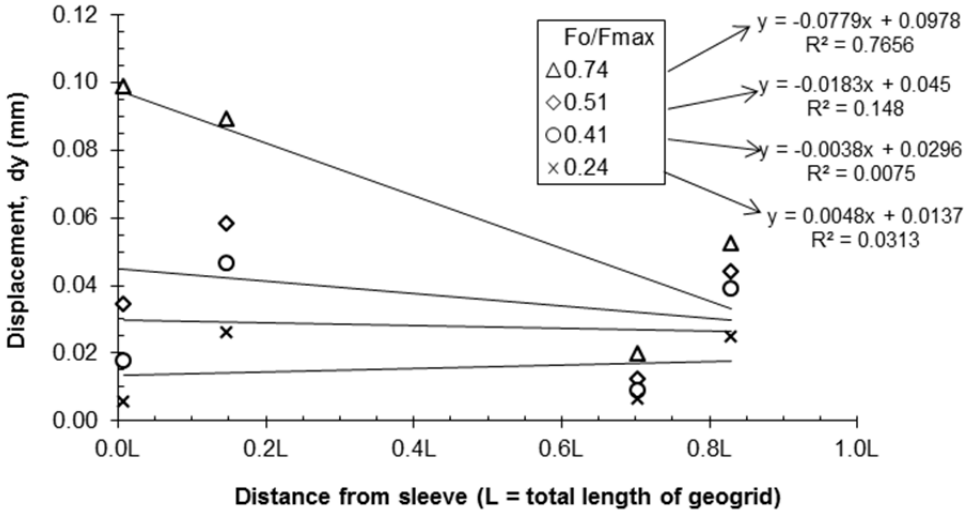


Figure A. 64: Test 4: Vertical movement of the box calculated with the PIV software with images from cam1 (side view).

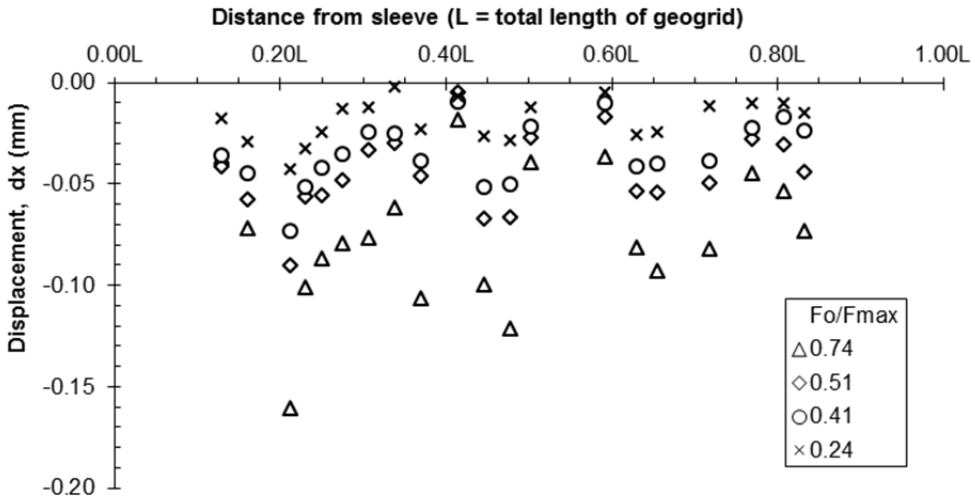


Figure A. 65: Test 4: Horizontal displacement of soil markers along the geogrid at a distance of 7 mm from the interface.

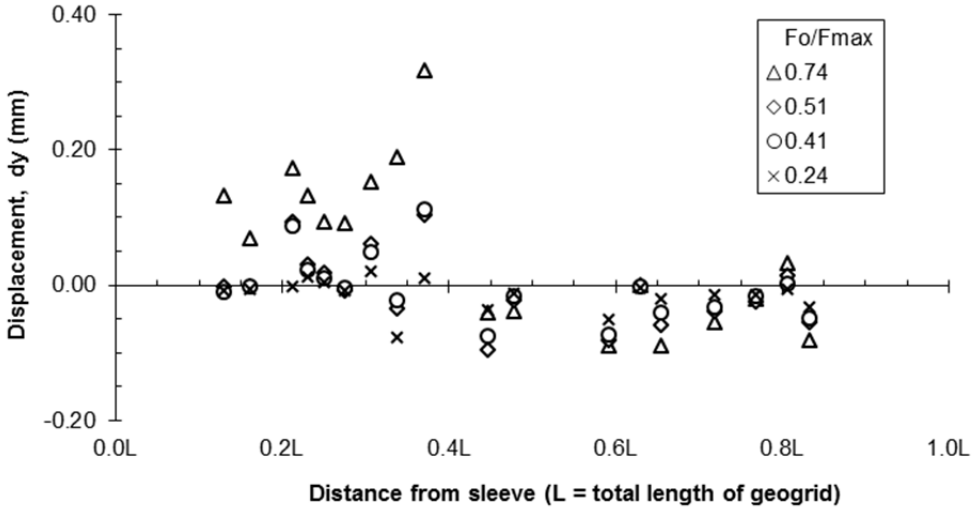


Figure A. 66: Test 4: Vertical displacement of soil markers along the geogrid at 7 mm from the interface.

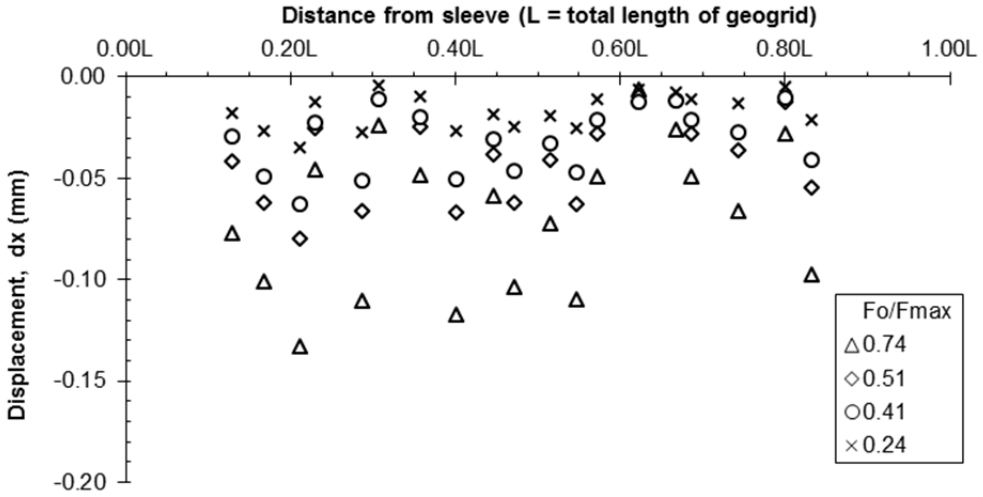


Figure A. 67: Test 4: Horizontal displacement of soil markers along the geogrid at 25 mm from the interface.

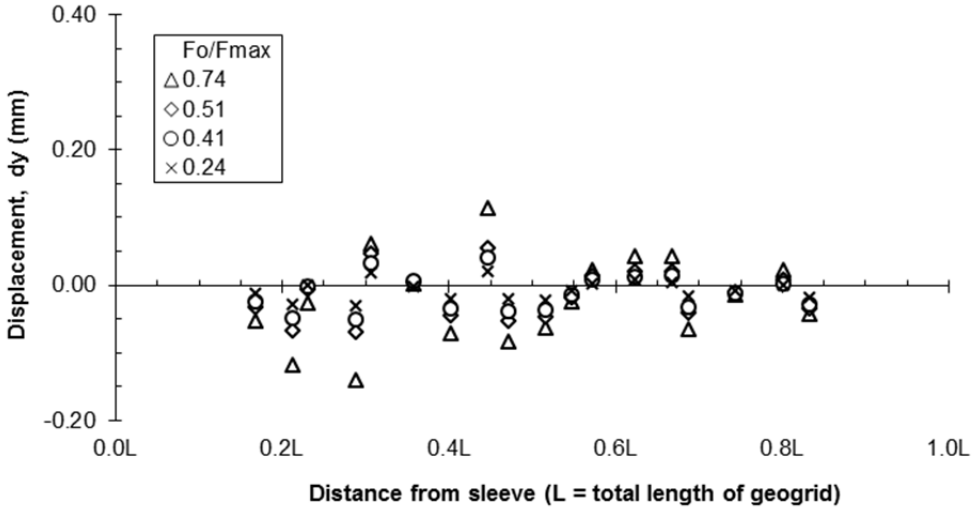


Figure A. 68: Test 4: Vertical displacement of soil markers along the geogrid 25 mm from the interface.

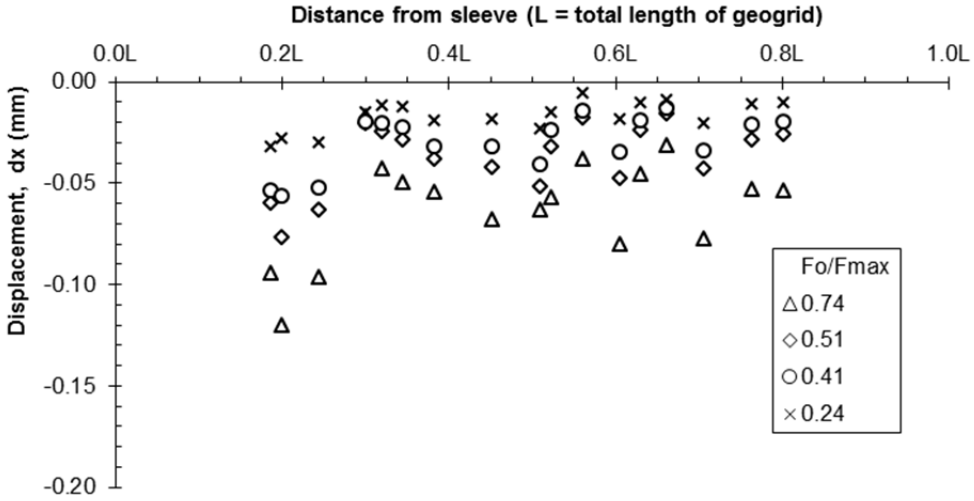


Figure A. 69: Test 4: Horizontal displacement of soil markers along the geogrid at 40 mm from the interface.

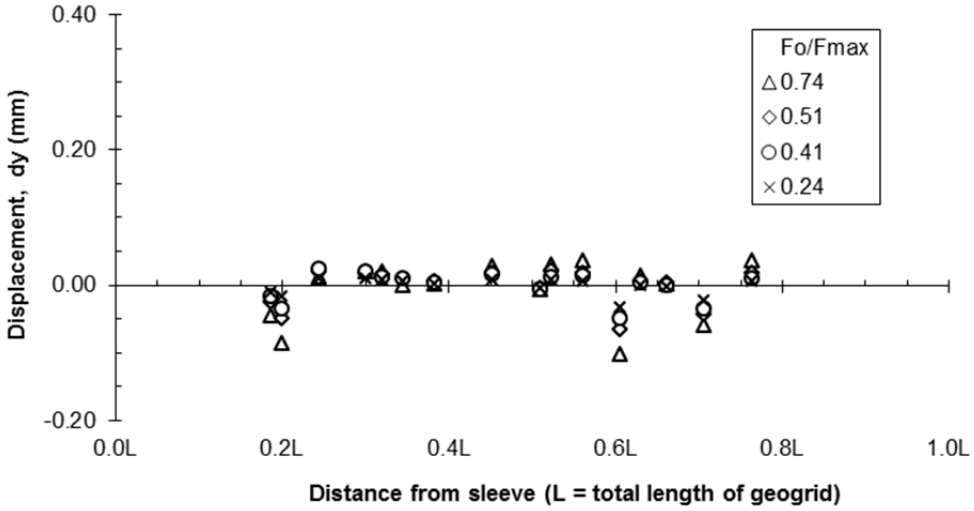


Figure A. 70: Test 4: Vertical displacement of soil markers along the geogrid at 40 mm from the interface.

**Test 5**

***Images from cam0 (plan view of the test)***

The images from cam0 provide the plan view of the test. In these images, the line of markers perpendicular to the pullout direction are observed (Figure A. 71). The top, middle and bottom lines of soil markers in Figure A. 71 are at 51 mm (2.01 in.), 31 mm (1.22 in.), and 7 mm (0.28 in.) from the interface, respectively.

The data of the horizontal and vertical displacements of the pullout box are shown in Figure A. 72 and Figure A. 73, respectively. The data of the horizontal and vertical displacements of the soil markers are shown from Figure A. 74 to Figure A. 79.

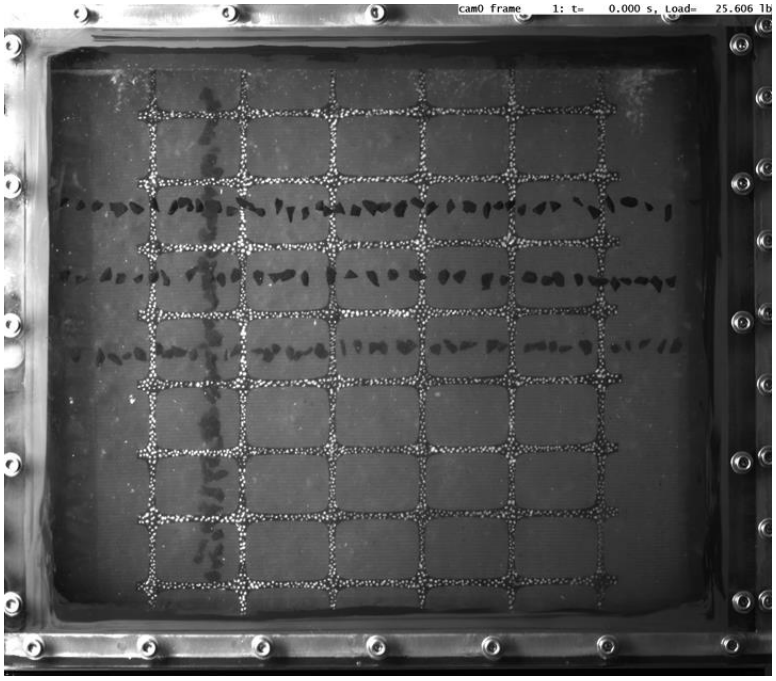


Figure A. 71: Test5: Image of the plan view of the box (cam0) and lines of soil markers placed perpendicular to the pullout direction.

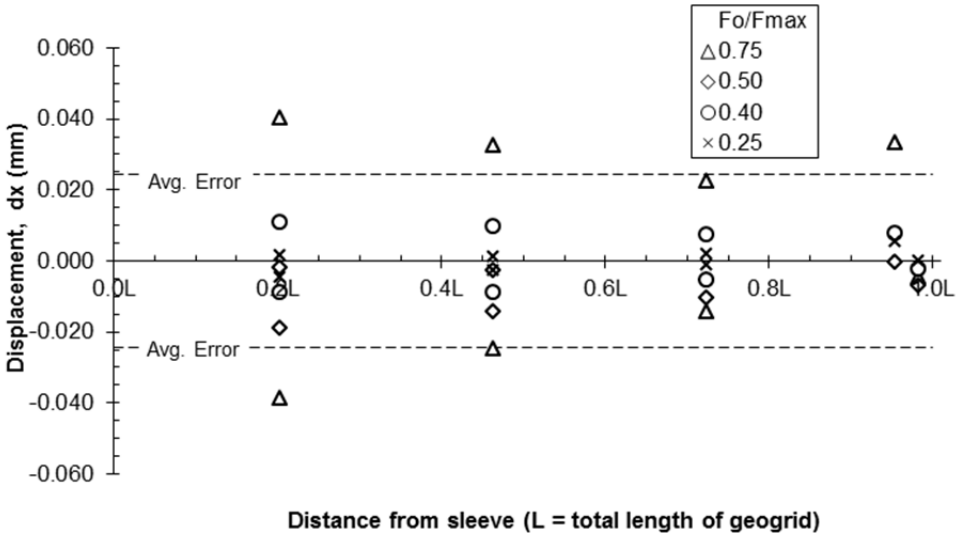


Figure A. 72: Test 5: Horizontal movement of the box calculated with the PIV software with images from cam0 (plan view).

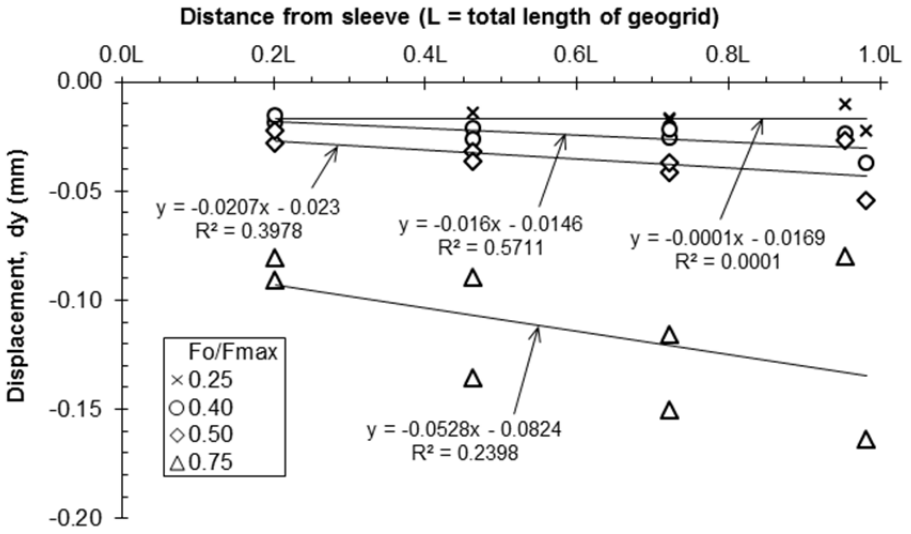


Figure A. 73: Test 5: Vertical movement of the box calculated with the PIV software with images from cam0 (plan view).

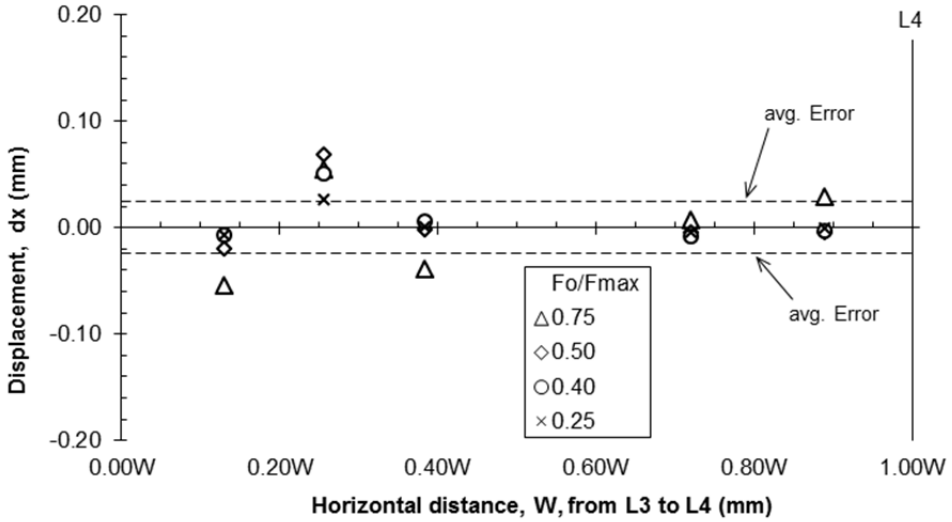


Figure A. 74: Test 5: Horizontal displacement of soil markers between L3 and L4 at 51 mm from the interface.

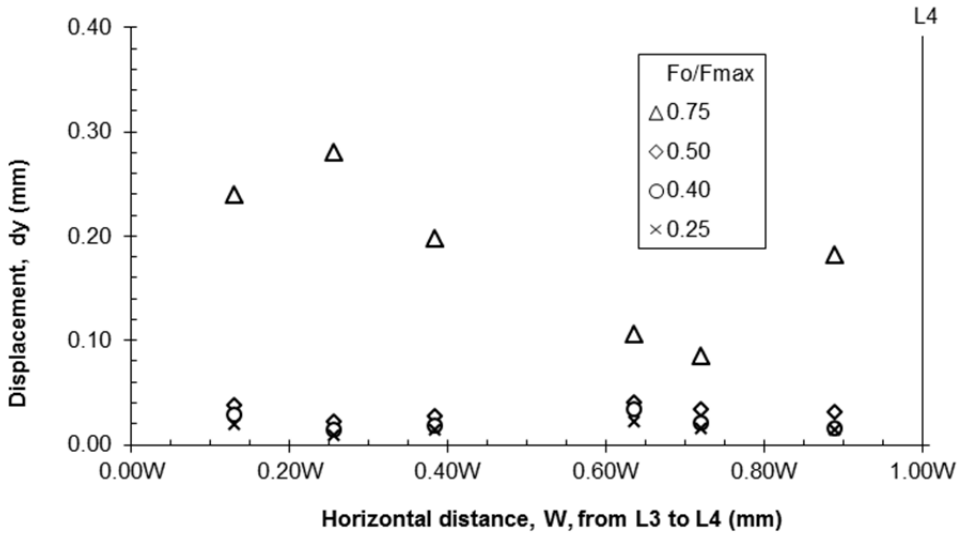


Figure A. 75: Test 5: Vertical displacement of soil markers between L3 and L4 at 51 mm from the interface.

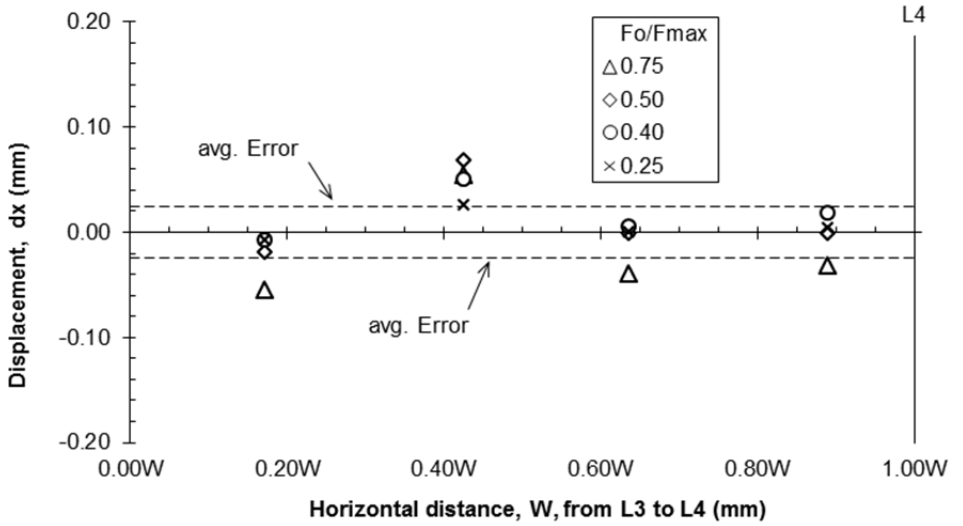


Figure A. 76: Test 5: Horizontal displacement of soil markers between L3 and L4 at 31 mm from the interface.

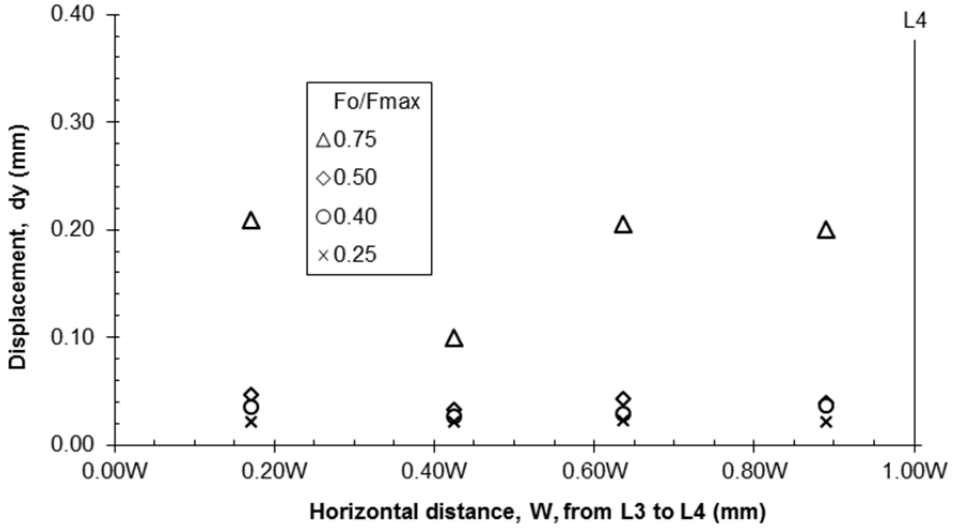


Figure A. 77: Test 5: Vertical displacement of soil markers between L3 and L4 at 31 mm from the interface.

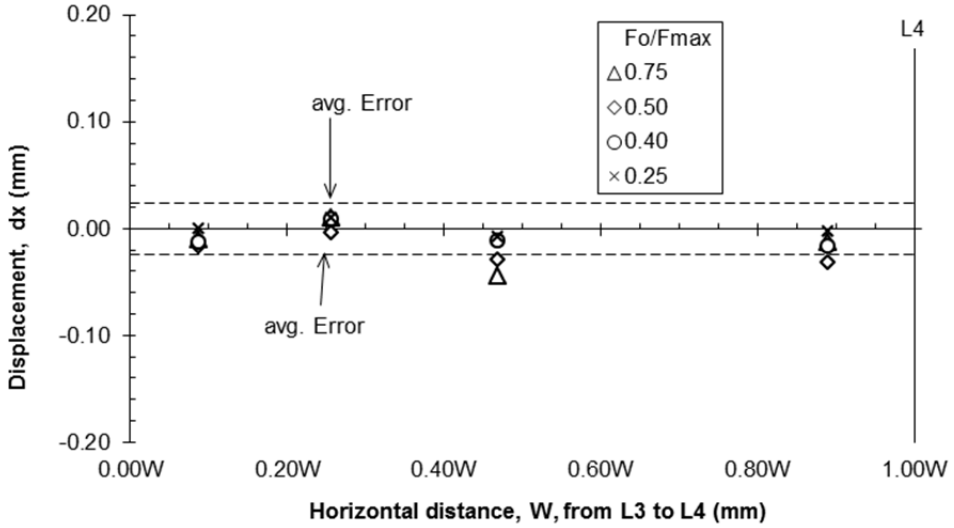


Figure A. 78: Test 5: Horizontal displacement of soil markers between L3 and L4 at 7 mm from the interface.

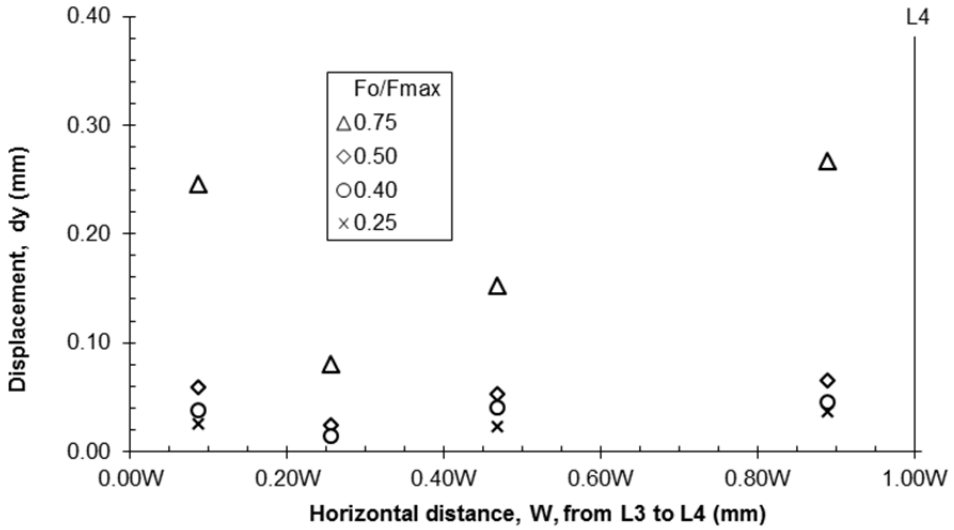


Figure A. 79: Test 5: Vertical displacement of soil markers between L3 and L4 at 7 mm from the interface.

***Images from cam1 (side view of the test)***

The images from cam1 provide the side view of the test. In these images, the lines of markers parallel to the pullout direction are observed (Figure A. 80). The lines of soil markers in Figure A. 80 are to the left of the geogrid at 8, 23 and 40 mm from the interface.

The data of the horizontal and vertical displacements of the pullout box are shown in Figure A. 81 and Figure A. 82, respectively. The data of the horizontal and vertical displacements of the soil markers are shown from Figure A. 83 to Figure A. 88.

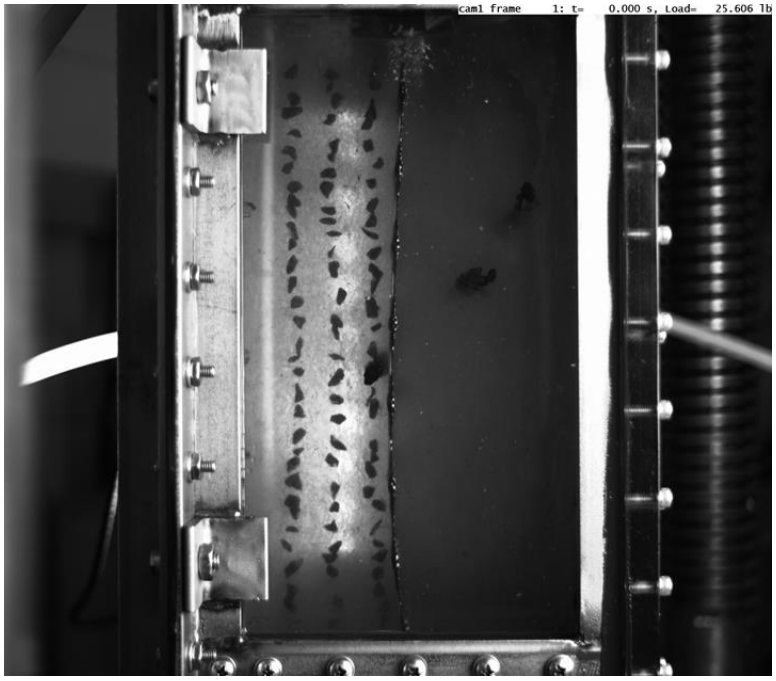


Figure A. 80: Test 5: Image of the side view of the box (cam1) and lines of soil markers placed parallel to the pullout direction.

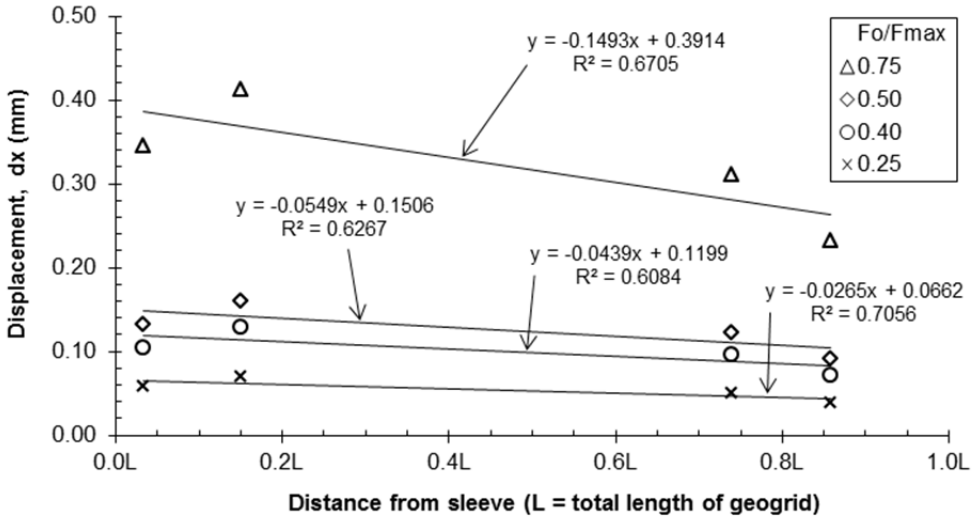


Figure A. 81: Test 5: Horizontal movement of the box calculated with the PIV software with images from cam1 (side view).

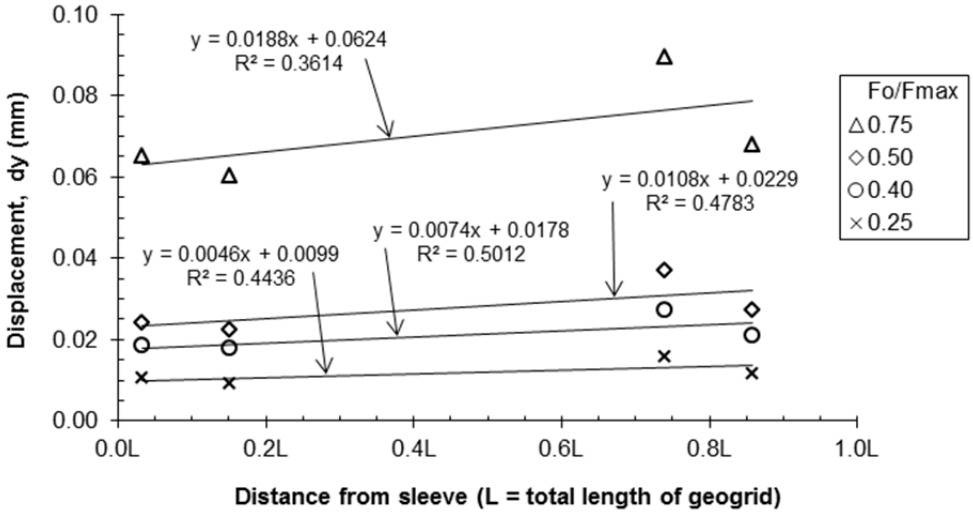


Figure A. 82: Test 5: Vertical movement of the box calculated with the PIV software with images from cam1 (side view).

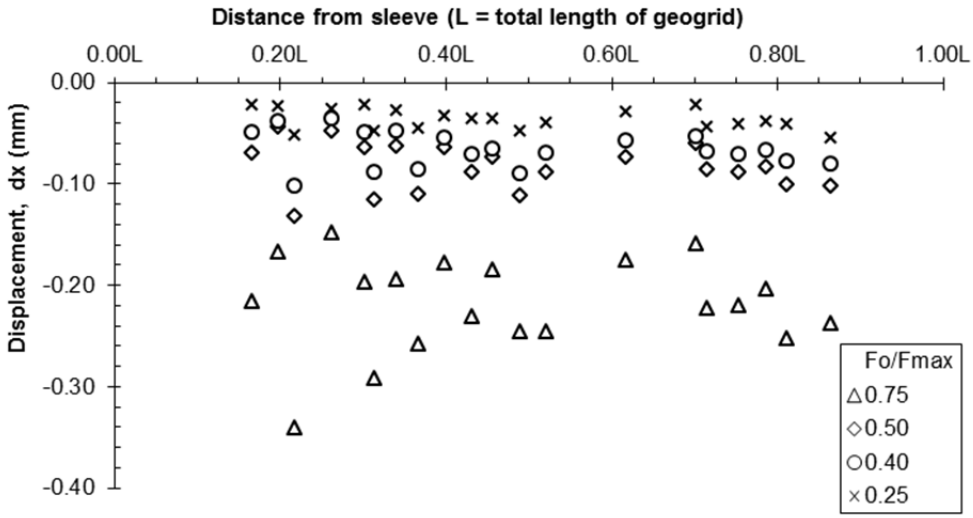


Figure A. 83: Test 5: Horizontal displacement of soil markers along the geogrid at 8 mm from the interface.

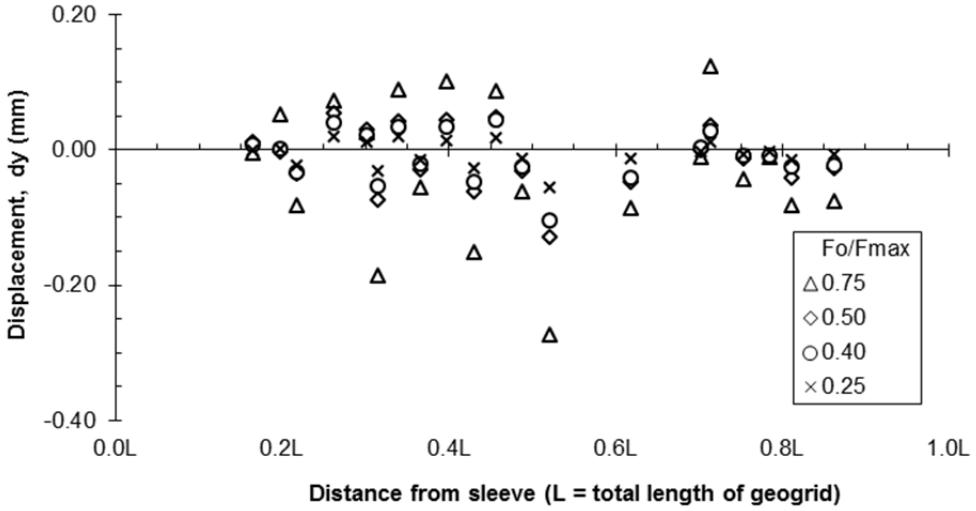


Figure A. 84: Test 5: Vertical displacement of soil markers along the geogrid at 8 mm from the interface.

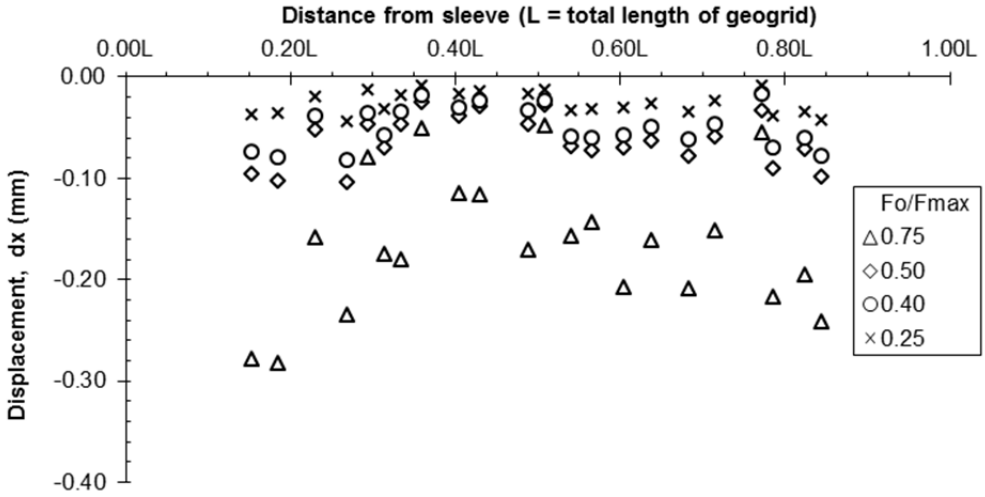


Figure A. 85: Test 5: Horizontal displacement of soil markers along the geogrid at 23 mm from the interface.

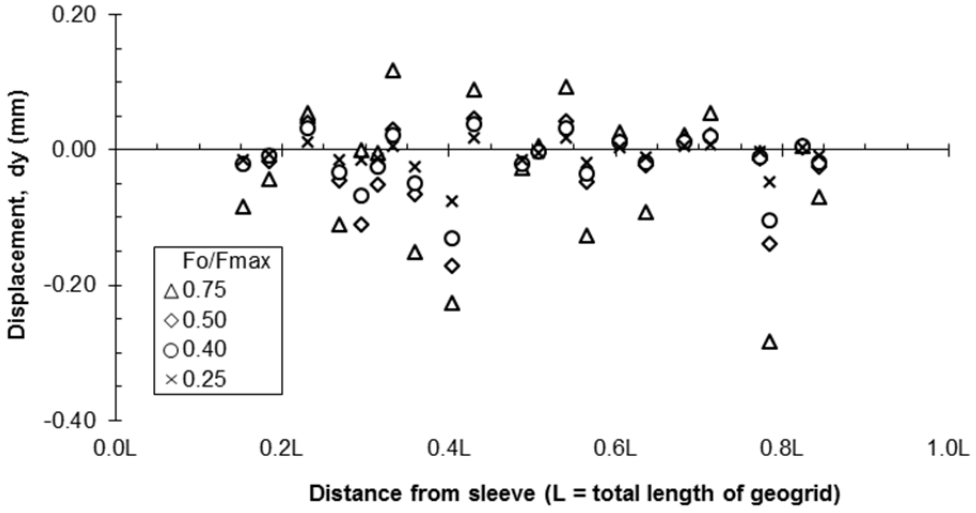


Figure A. 86: Test 5: Vertical displacement of soil markers along the geogrid at 23 mm from the interface.

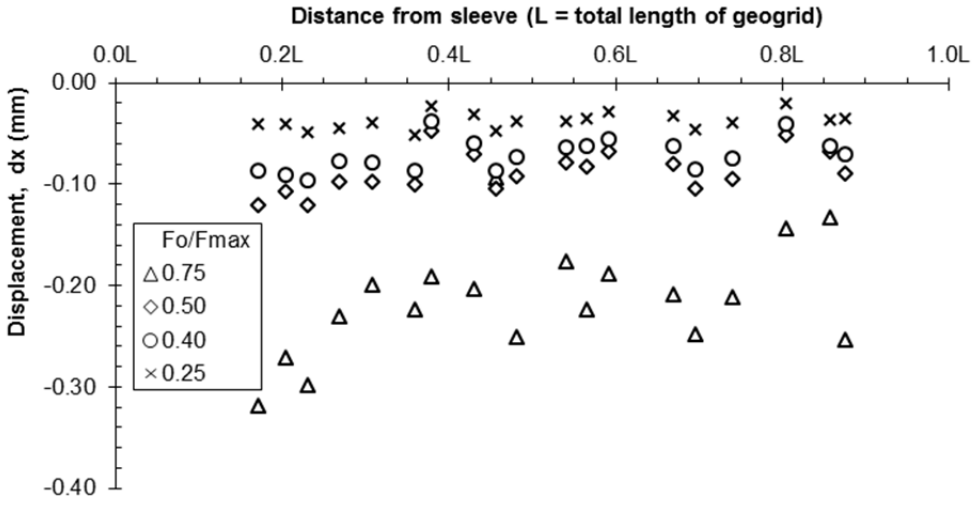


Figure A. 87: Test 5: Horizontal displacement of soil markers along the geogrid at 40 mm from the interface.

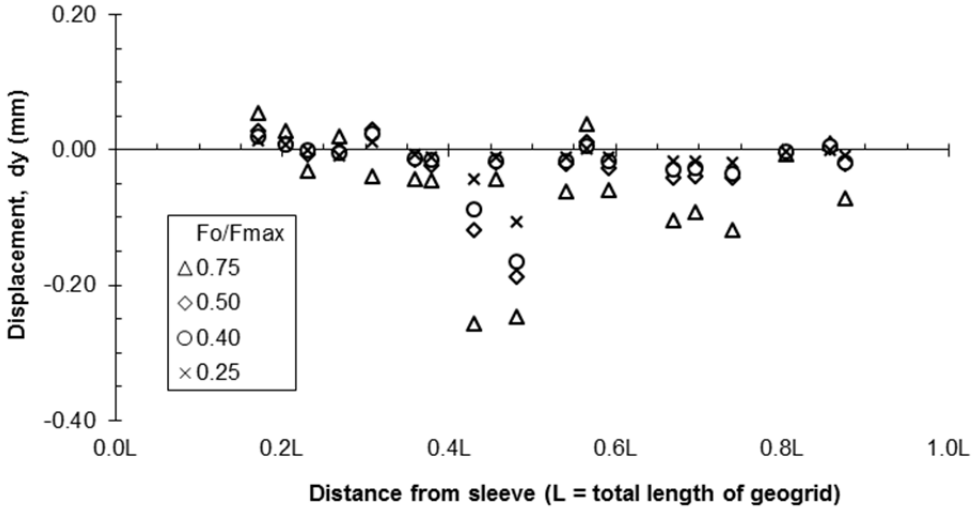


Figure A. 88: Test 5: Vertical displacement of soil markers along the geogrid at 40 mm from the interface.

# Appendix B: Data fitting process of displacement profiles obtained from Test 1 to 5

This appendix shows the values obtained for the parameters and the plots used for fitting the data of the displacement profiles obtained from the transparent pullout Tests 1 to 5.

## TEST 1

The values of the parameters used to fit Equation 3.1 to the displacement data of Test 1 are shown in Table B. 1 and Table B. 2. The plots used in this data fitting process are shown in Figure B. 1 and Figure B. 2.

| Fo/Fmax | $\alpha$ | $\beta$ | $\gamma$ |
|---|---|---|---|
| 0.22 | 0.2133 | 0.4769 | 0.3721 |
| 0.39 | 0.4498 | 1.1313 | 0.3695 |
| 0.52 | 0.5992 | 1.9348 | 0.4165 |
| 0.74 | 1.9981 | 3.7657 | 0.2438 |

Table B. 1: Test 1: Parameters found to fit data from longitudinal member L3.

| Fo/Fmax | $\alpha$ | $\beta$ | $\gamma$ |
|---|---|---|---|
| 0.22 | 0.1495 | 0.6420 | 0.3247 |
| 0.39 | 0.3764 | 1.3091 | 0.3254 |
| 0.52 | 0.4527 | 2.0930 | 0.3266 |
| 0.74 | 1.5197 | 3.7166 | 0.3165 |

Table B. 2: Test 1: Parameters found to fit data from longitudinal member L4.

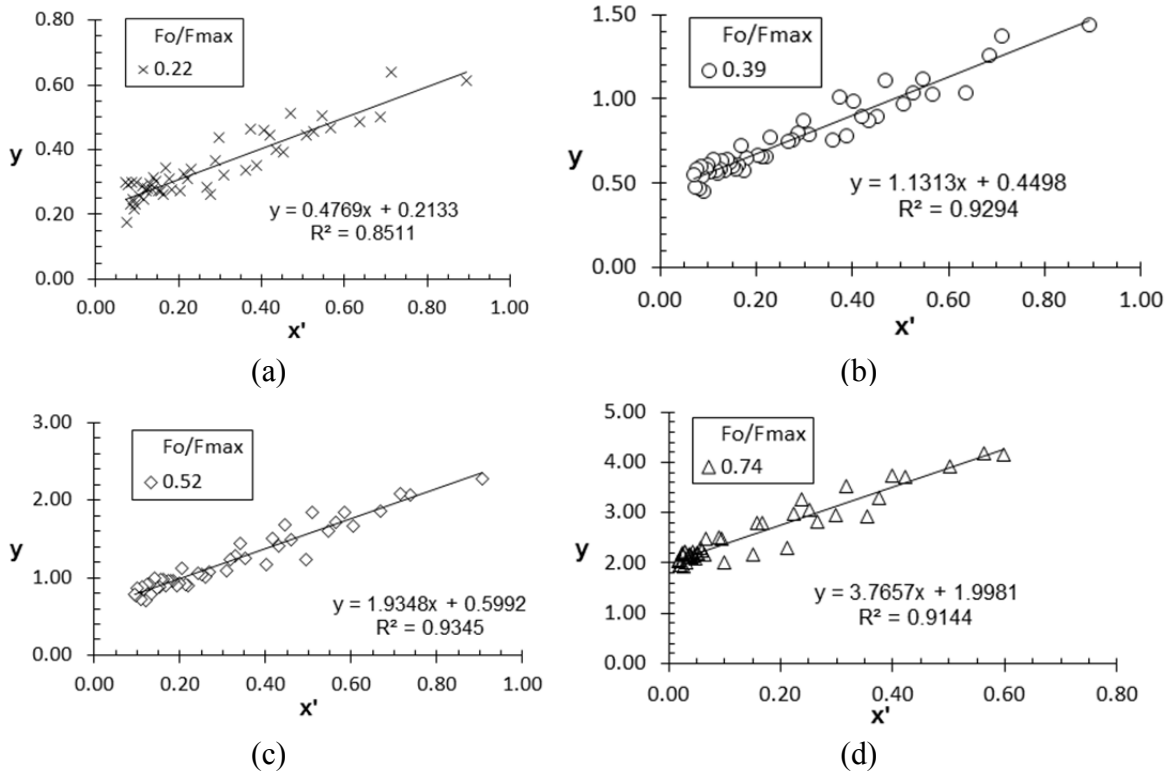


Figure B. 1: Test 1: Plots used to fit data from longitudinal member L3: (a) 0.22 Fo/Fmax. (b) 0.39 Fo/Fmax. (c) 0.52 Fo/Fmax. (d) 0.74 Fo/Fmax.

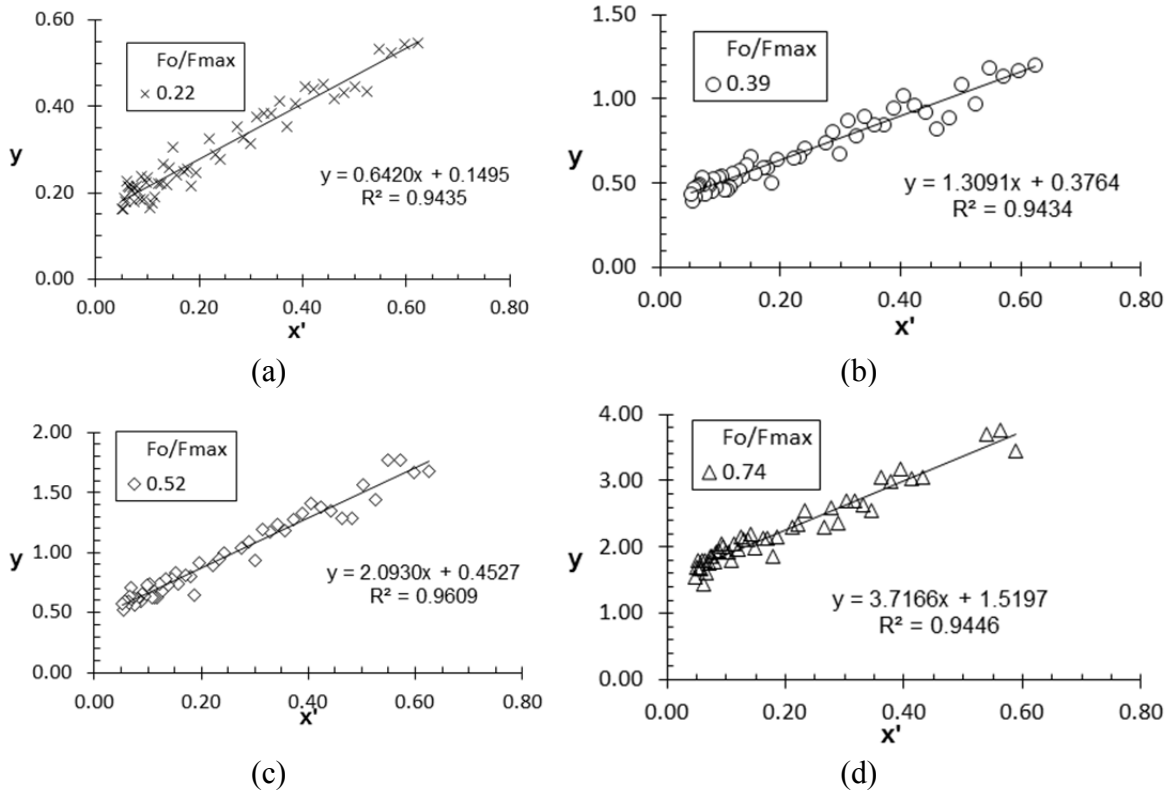


Figure B. 2: Test 1: Plots used to fit data from longitudinal member L4: (a) 0.22 Fo/Fmax. (b) 0.39 Fo/Fmax. (c) 0.52 Fo/Fmax. (d) 0.74 Fo/Fmax.

**TEST 2**

The values of the parameters used to fit Equation 3.1 to the displacement data of Test 2 are shown in Table B. 3 and Table B. 4. The plots used in this data fitting process are shown in Figure B. 3 and Figure B. 4.

| Fo/Fmax | α | β | γ |
|---|---|---|---|
| 0.26 | 0.0898 | 0.8831 | 0.2454 |
| 0.39 | 0.2276 | 1.4537 | 0.2558 |
| 0.50 | 0.3217 | 2.3409 | 0.2429 |
| 0.74 | 0.7961 | 4.1825 | 0.2326 |

Table B. 3: Test 2: Parameters found to fit data from longitudinal member L3.

| Fo/Fmax | α | β | γ |
|---|---|---|---|
| 0.26 | 0.0978 | 0.7992 | 0.2581 |
| 0.39 | 0.1749 | 1.5840 | 0.2476 |
| 0.50 | 0.4067 | 2.4904 | 0.2608 |
| 0.74 | 0.9099 | 4.3563 | 0.2608 |

Table B. 4: Test 2: Parameters found to fit data from longitudinal member L4.

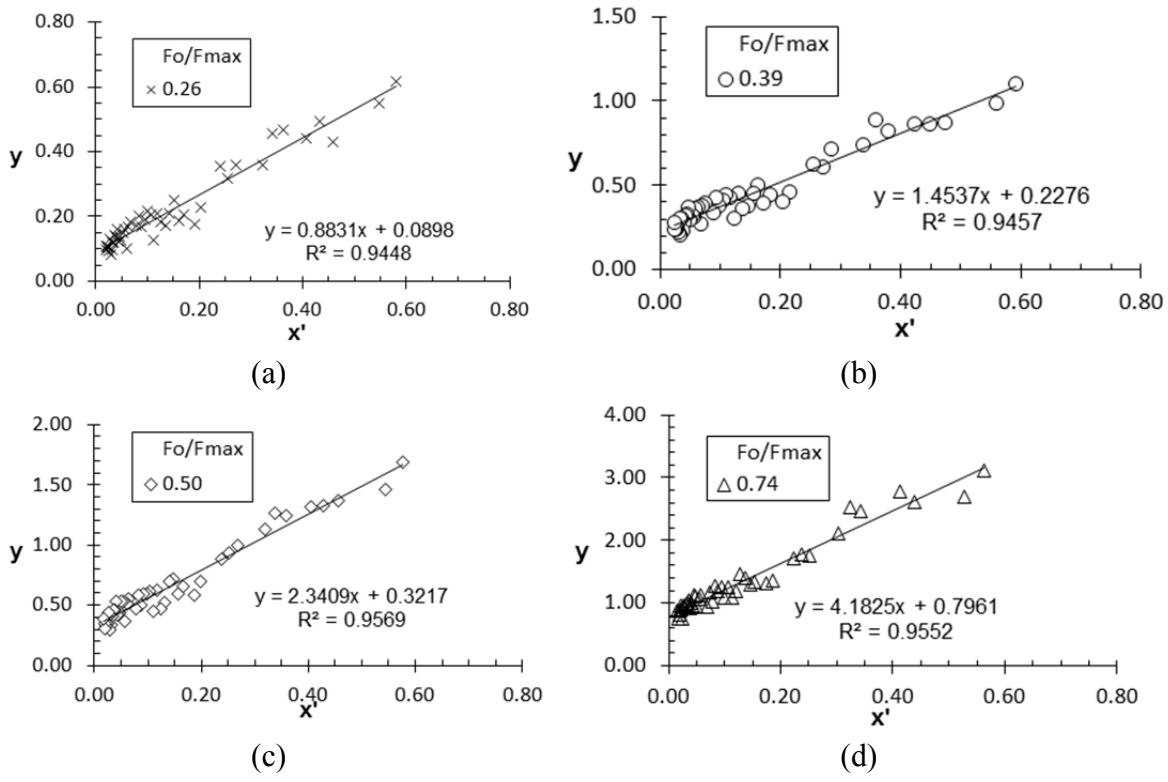


Figure B. 3: Test 2: Plots used to fit data from longitudinal member L3: (a) 0.26 Fo/Fmax. (b) 0.39 Fo/Fmax. (c) 0.50 Fo/Fmax. (d) 0.74 Fo/Fmax.

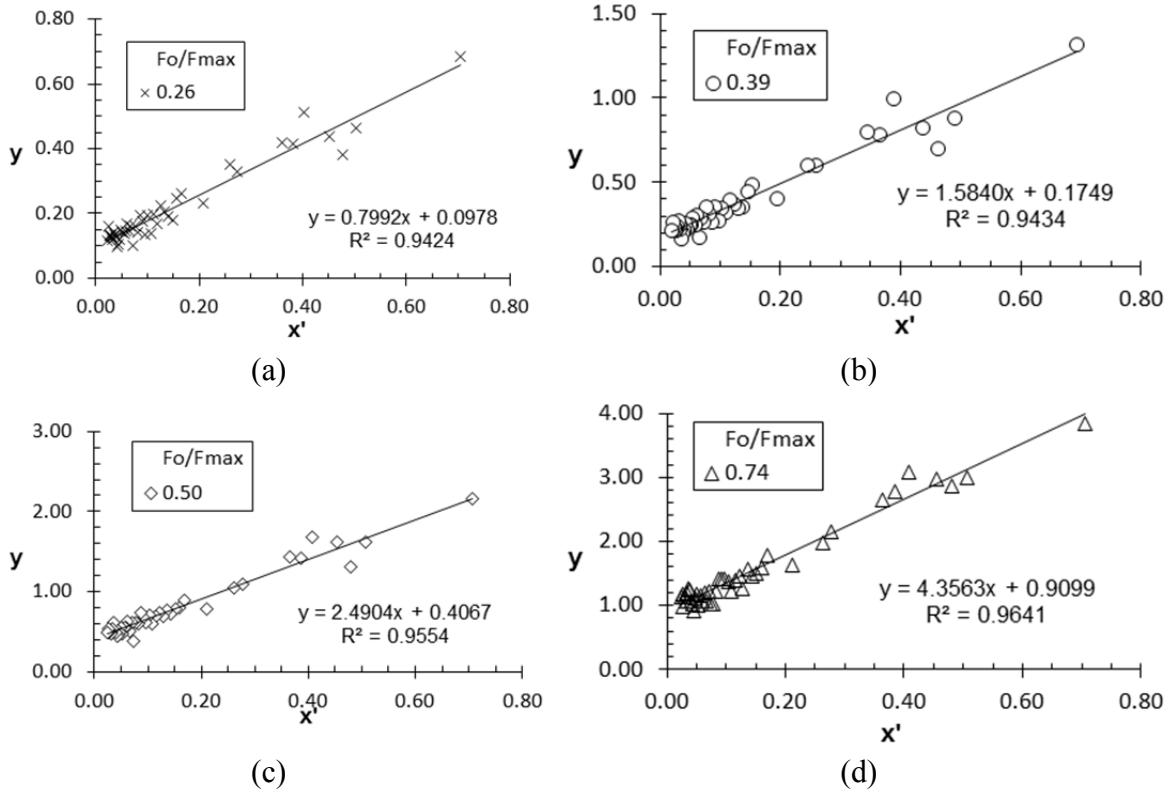


Figure B. 4: Test 2: Plots used to fit data from longitudinal member L4: (a) 0.26 Fo/Fmax. (b) 0.39 Fo/Fmax. (c) 0.50 Fo/Fmax. (d) 0.74 Fo/Fmax.

**TEST 3**

The values of the parameters used to fit Equation 3.1 to the displacement data of Test 3 are shown in Table B. 5 and Table B. 6. The plots used in this data fitting process are shown in Figure B. 5 and Figure B. 6.

| Fo/Fmax | α | β | γ |
|---|---|---|---|
| 0.26 | 0.0392 | 0.7943 | 0.2466 |
| 0.41 | 0.0967 | 1.5160 | 0.2385 |
| 0.53 | 0.2470 | 2.1044 | 0.2529 |
| 0.76 | 0.8933 | 3.8401 | 0.2452 |

Table B. 5: Test 3: Parameters found to fit data from longitudinal member L3.

| Fo/Fmax | α | β | γ |
|---|---|---|---|
| 0.26 | 0.0723 | 0.8795 | 0.2019 |
| 0.41 | 0.3104 | 1.6933 | 0.2078 |
| 0.53 | 0.4042 | 2.4109 | 0.1999 |
| 0.76 | 1.1205 | 3.8840 | 0.2054 |

Table B. 6: Test 3: Parameters found to fit data from longitudinal member L4.

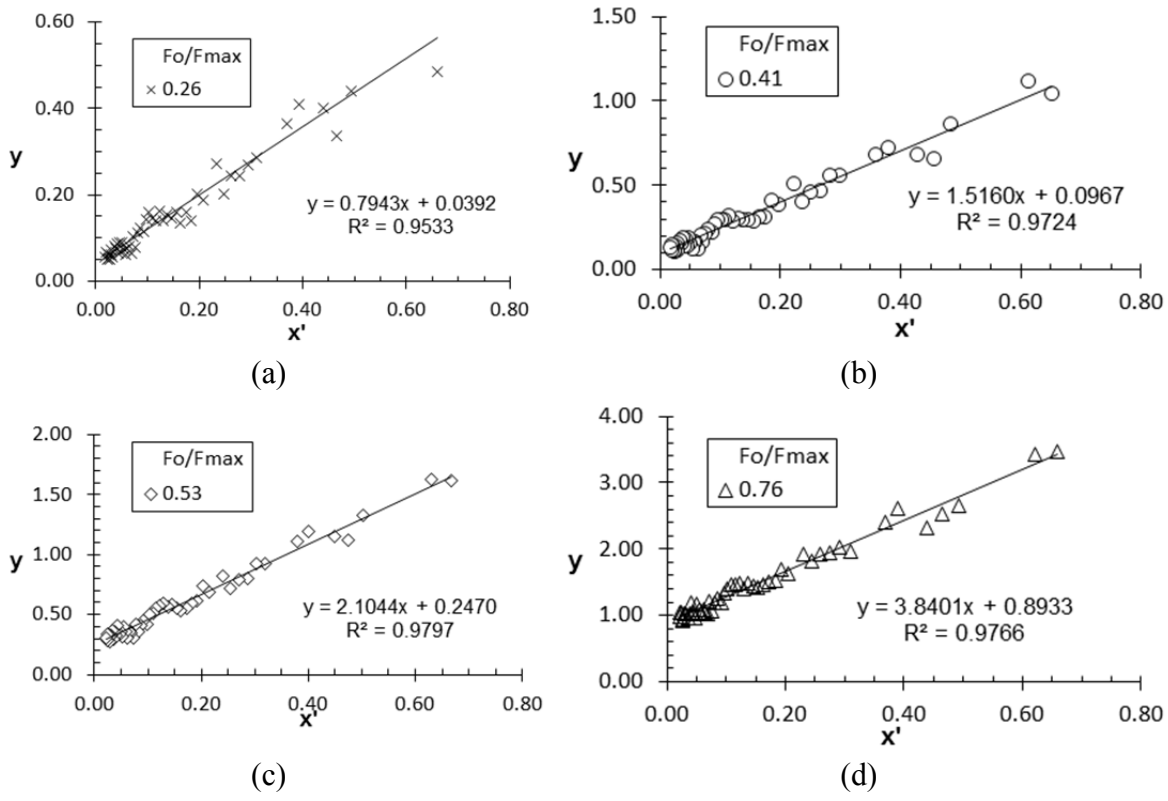


Figure B. 5: Test 3: Plots used to fit data from longitudinal member L3: (a) 0.26 Fo/Fmax. (b) 0.41 Fo/Fmax. (c) 0.53 Fo/Fmax. (d) 0.76 Fo/Fmax.

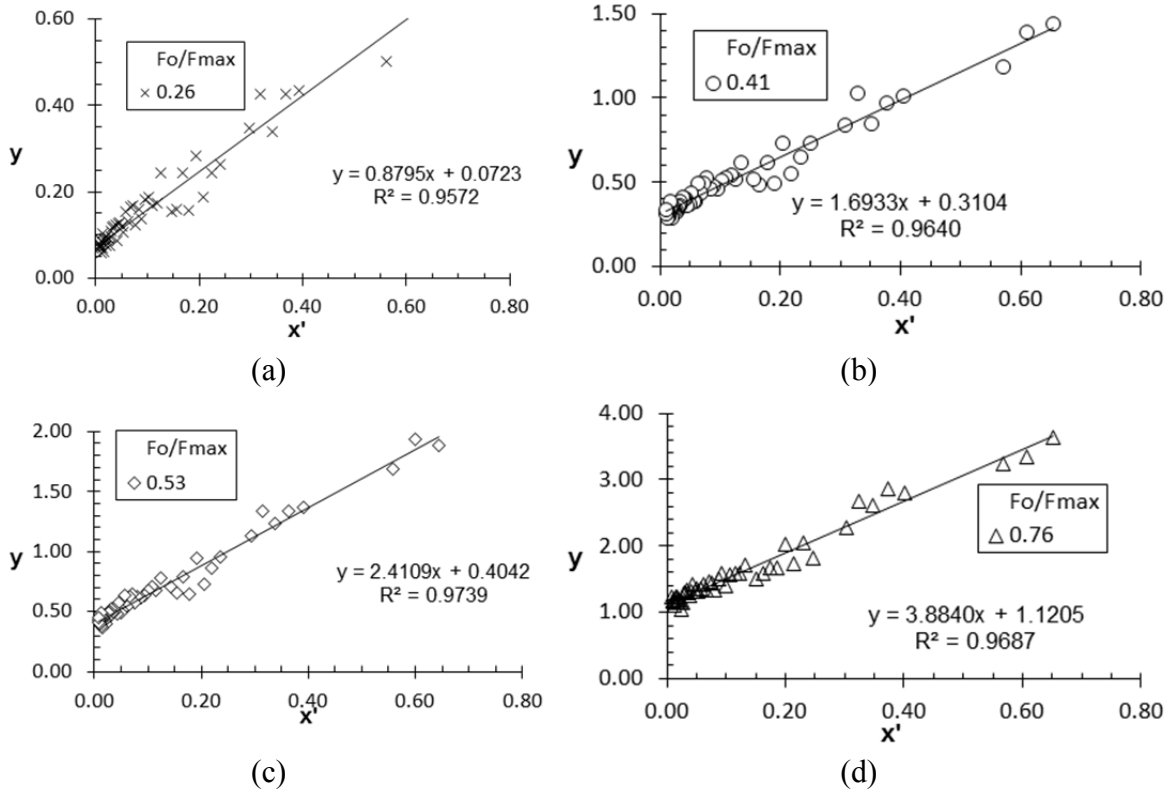


Figure B. 6: Test 3: Plots used to fit data from longitudinal member L4: (a) 0.26 Fo/Fmax. (b) 0.41 Fo/Fmax. (c) 0.53 Fo/Fmax. (d) 0.76 Fo/Fmax.

**TEST 4**

The values of the parameters used to fit Equation 3.1 to the displacement data of Test 4 are shown in Table B. 7 and Table B. 8. The plots used in this data fitting process are shown in Figure B. 7 and Figure B. 8.

| Fo/Fmax | α | β | γ |
|---|---|---|---|
| 0.24 | 0.0635 | 0.7730 | 0.2128 |
| 0.41 | 0.2138 | 1.6959 | 0.2171 |
| 0.51 | 0.4035 | 2.4693 | 0.2007 |
| 0.74 | 0.7917 | 3.4275 | 0.2106 |

Table B. 7: Test 4: Parameters found to fit data from longitudinal member L3.

| Fo/Fmax | α | β | γ |
|---|---|---|---|
| 0.24 | 0.0633 | 0.5517 | 0.3244 |
| 0.41 | 0.1475 | 1.2959 | 0.2426 |
| 0.51 | 0.3727 | 1.8984 | 0.2101 |
| 0.74 | 0.7103 | 3.2666 | 0.2072 |

Table B. 8: Test 4: Parameters found to fit data from longitudinal member L4.

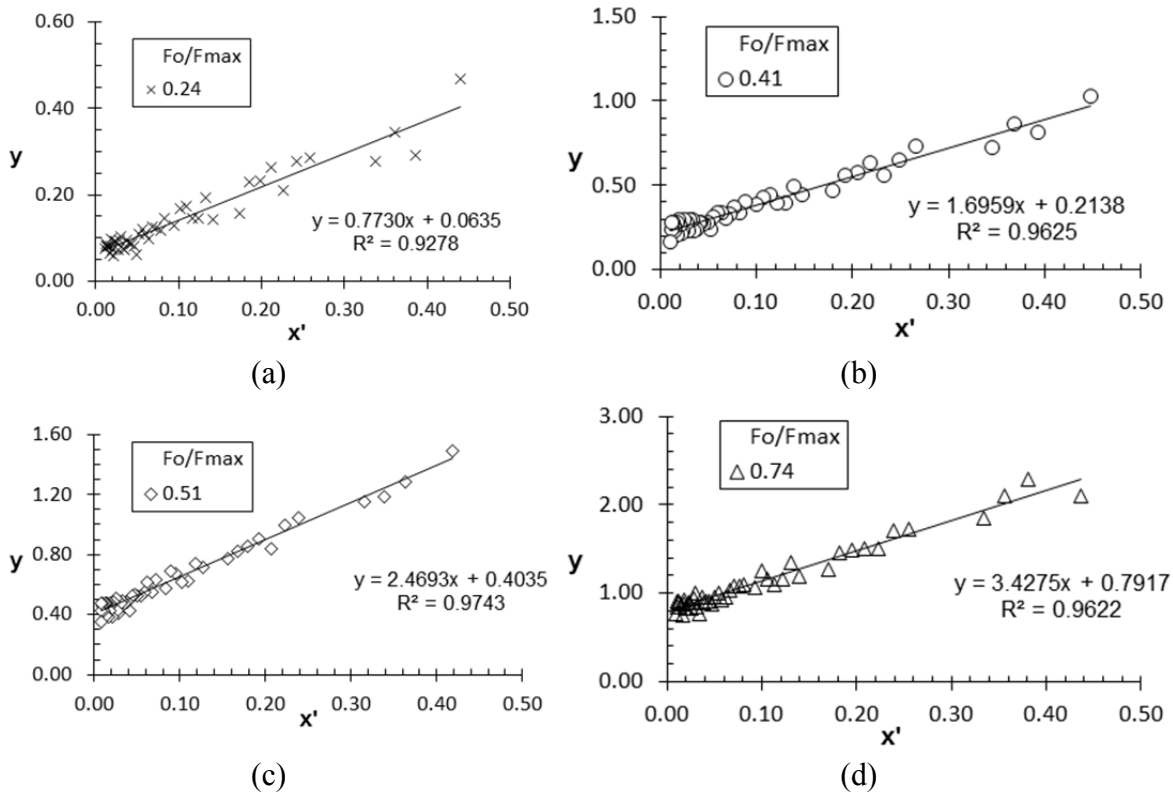


Figure B. 7: Test 4: Plots used to fit data from longitudinal member L3: (a) 0.24 Fo/Fmax. (b) 0.41 Fo/Fmax. (c) 0.51 Fo/Fmax. (d) 0.74 Fo/Fmax.

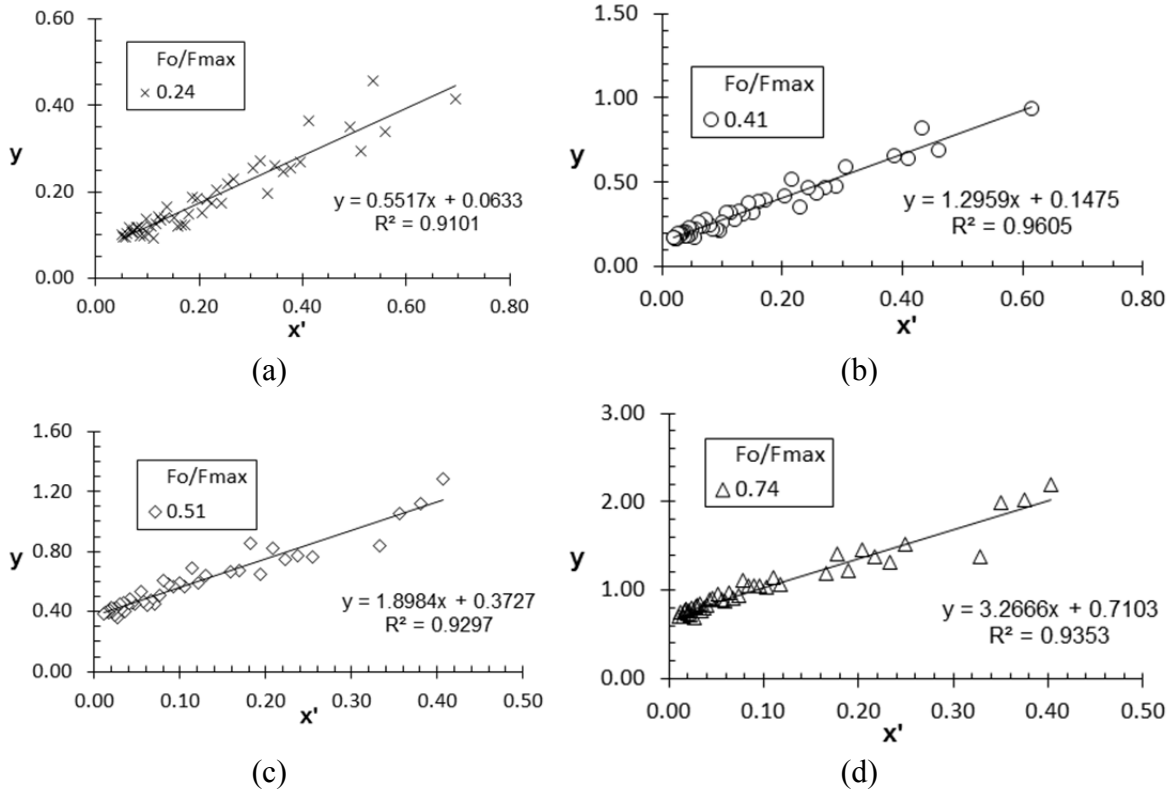


Figure B. 8: Test 4: Plots used to fit data from longitudinal member L4: (a) 0.24 Fo/Fmax. (b) 0.41 Fo/Fmax. (c) 0.51 Fo/Fmax. (d) 0.74 Fo/Fmax.

**TEST 5**

The values of the parameters used to fit Equation 3.1 to the displacement data of Test 5 are shown in Table B. 9 and Table B. 10. The plots used in this data fitting process are shown in Figure B. 9 and Figure B. 10.

| Fo/Fmax | α | β | γ |
|---|---|---|---|
| 0.25 | -0.0034 | 0.5429 | 0.2658 |
| 0.40 | -0.0033 | 1.2605 | 0.2886 |
| 0.50 | -0.0014 | 1.6802 | 0.2761 |
| 0.75 | 0.0384 | 3.0203 | 0.2698 |

Table B. 9: Test 5: Parameters found to fit data from longitudinal member L3.

| Fo/Fmax | α | β | γ |
|---|---|---|---|
| 0.25 | -0.0002 | 0.5318 | 0.2708 |
| 0.40 | -0.0035 | 1.1138 | 0.3028 |
| 0.50 | -0.0006 | 1.5465 | 0.2940 |
| 0.75 | 0.0643 | 2.8244 | 0.2822 |

Table B. 10: Test 5: Parameters found to fit data from longitudinal member L4.

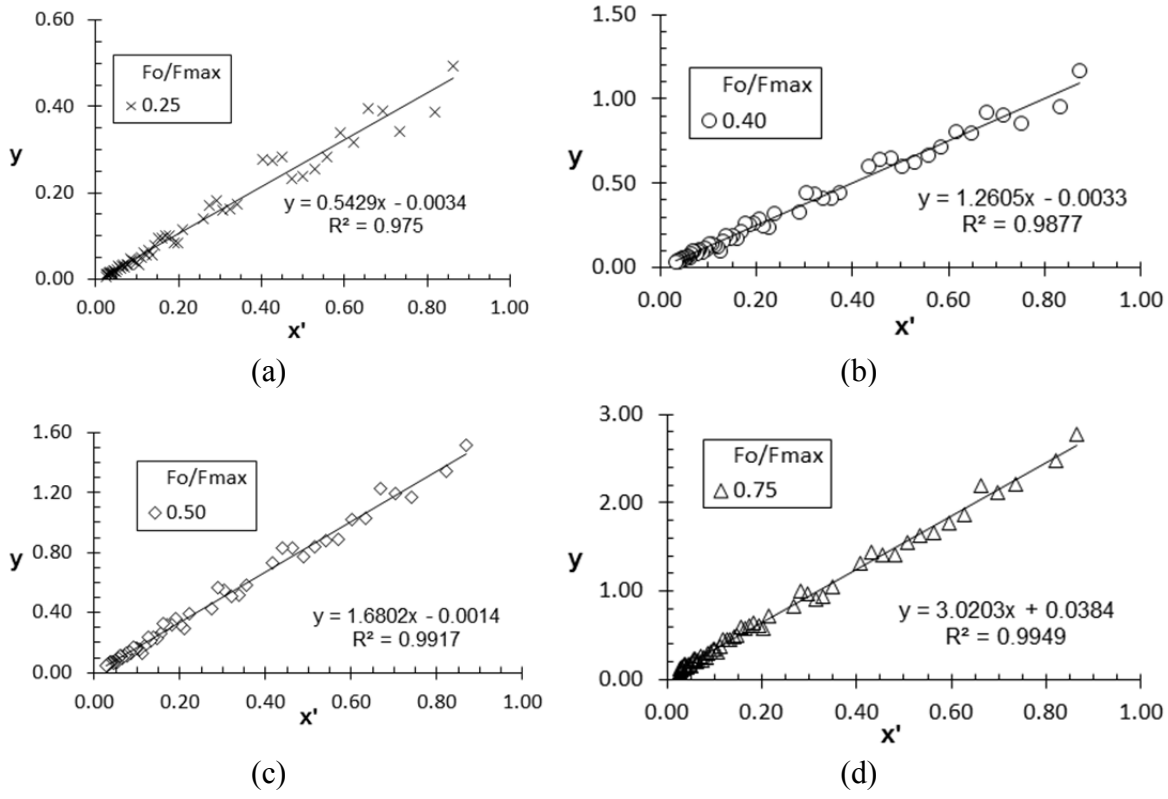


Figure B. 9: Test 5: Plots used to fit data from longitudinal member L3: (a) 0.25 Fo/Fmax. (b) 0.40 Fo/Fmax. (c) 0.50 Fo/Fmax. (d) 0.75 Fo/Fmax.

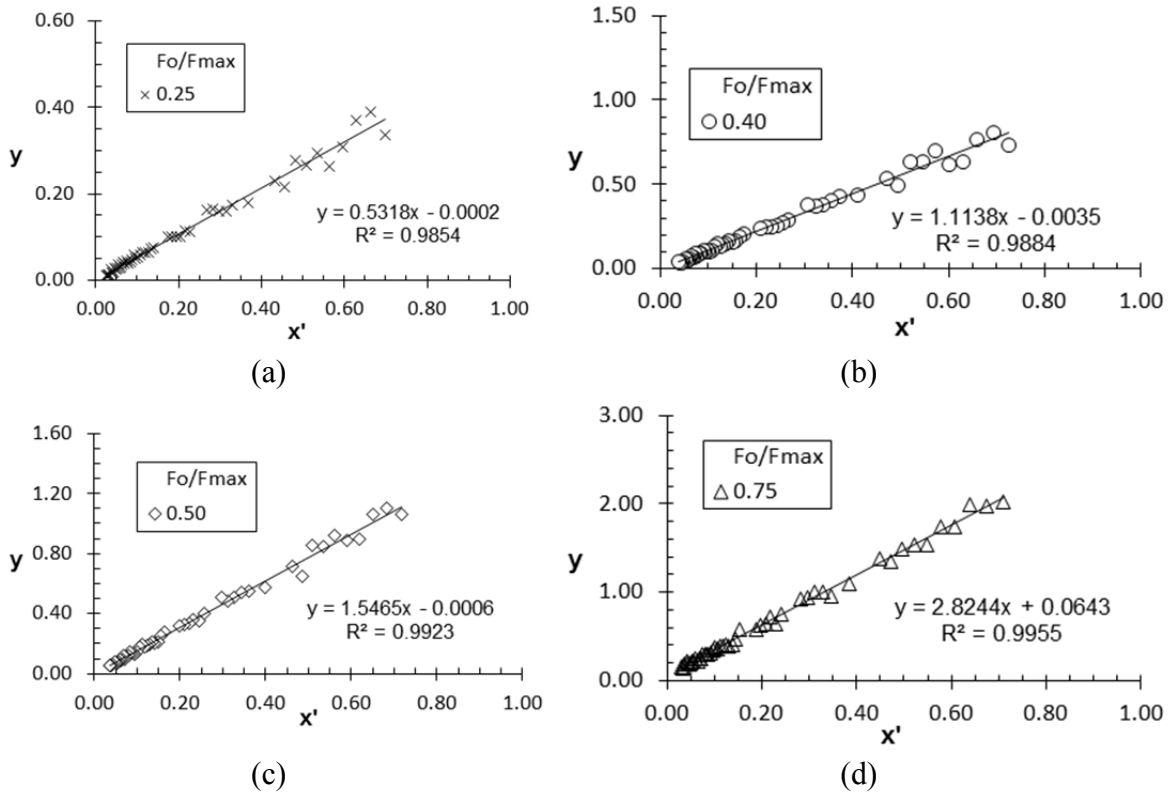


Figure B. 10: Test 5: Plots used to fit data from longitudinal member L4: (a) 0.25 Fo/Fmax. (b) 0.40 Fo/Fmax. (c) 0.50 Fo/Fmax. (d) 0.75 Fo/Fmax.

# References


Al-Qadi, I.L., Dessouky, S.H., Kwon J. and Tutumluer, E. (2008), "Geogrids in Flexible Pavements: Validated Mechanisms", Journal of the Transportation Research Board, No. 2045, pp. 102-109.

Alshibli, K.A., Roussel, L.E.,(2006), "Experimental investigation of slip-stick behaviour in granular materials", International Journal for Numerical and Analytical Methods In Geomechanics, v.30, pp.1391–1407.

Alfaro,M.C., Miura,N., Bergado, D.T. (1995), " Soil-Geogrid Reinforcement Interaction by Pullout and Direct Shear Tests, Geotechnical Testing Journal, v.18, n. 2, pp. 157-167.

ASTM D854 (2006). "Standard Test Methods for Specific Gravity of Soil Solids by Water Pycnometer", American Society for Testing and Materials, West Conshohocken, PA.

ASTM D3080 (2011). "Standard Test Method for Direct Shear Test of Soils Under Consolidated Drained Conditions", American Society for Testing and Materials, West Conshohocken, PA.

ASTM D4253 (2000). "Standard Test Methods for Maximum Index Density and Unit Weight of Soils Using a Vibratory Table", American Society for Testing and Materials, West Conshohocken, PA.

ASTM D4254 (2000). "Standard Test Methods for Minimum Index Density and Unit Weight of Soils and Calculation of Relative Density, American Society for Testing and Materials, West Conshohocken, PA.

ASTM D 4595 (2009). "Standard Test Method for Tensile Properties of Geotextiles by the Wide-Width Strip Method, West Conshohocken, PA.

ASTM D6637 (2009). "Standard Test Method for Determining Tensile Properties of Geogrids by the Single or Multi-rib Tensile Method", American Society for Testing and Materials, West Conshohocken, PA.

ASTM D6706 (2003). "Standard Test Method for Measuring Geosynthetic Pullout Resistance in Soil", American Society for Testing and Materials, West Conshohocken, PA.

Brown, S.F., Kwan, J., Thom, N.H. (2007)."Identifying the Key Parameters that Influence Geogrid Reinforcement of Railway Ballast". Geotextiles and Geomembranes, v.25, pp.326-335.

Brown, S.F., Thom, N.H., Kwan, J. and McDowell, G.R. (2008). "Improving the Performance of Railway Track Through Geogrid Reinforcement of Ballast", Proceedings of EuroGeo 4, Edinburgh, Scotland, 8p.

Chan F., Barksdale R.D. and Brown, S.F. (1989). “Aggregate Base Reinforcement of Surfaced Pavements”, Geotextiles and Geomembranes, v.8, pp. 165-189.

Chang, D.T., Sun, T.S., Hung, F.Y. (1995). “Pullout Mechanism of Geogrids Under Confinement by Sandy and Clayey Soils”, Transportation Research Record, v.1474, pp.64-72.

Cuelho, E.L. and Perkins, S.W. (2005). “Resilient Interface Shear Modulus from Short-Strip Cyclic Pullout Tests”, American Society of Civil Engineers (ASCE) GSP 140: Slopes and retaining structures under seismic and static conditions, Geo-frontiers, Austin, Texas.

Dantec Dynamics (2005). “2D PIV Reference Manual”, Tonsbakken, Denmark, p.58.

Duttine, A., Tatsuoka, F., Kongkitkul,W., Hirakawa, D., (2008) “Viscous Behaviour of Unbound Granular Materials in Direct Shear. Japanese Geotechnical Society, v. 48, n.3, pp.297-318.

Dyer, M.R. (1985). “Observations of the stress distribution in crushed glass with applications to soil reinforcement”, D.Phil. Thesis, University of Oxford, Oxford, UK.

Ezzein, F.M. and Bathurst, R. (2011a). “A Transparent Sand for Geotechnical Laboratory Modeling”, Geotechnical Testing Journal, v. 34, n. 6, pp. 1-12.

Ezzein, F.M. and Bathurst, R. (2011b). “Development of a Geosynthetic Pullout Test Apparatus with Transparent Granular Soil”, Proceedings 2011 Pan-American Canadian Geotechnical Society Geotechnical Conference, Toronto, Canada, 6p.

Farrag, K., Acar, Y.B., Juran, I. (1993). “Pull-out resistance of geogrid reinforcements”, Geotextiles and Geomembranes, v. 12, pp. 133-159.

Ferreira, J.A.Z. (2007). “Study of pavement reinforcement with pullout tests using equipment of small dimensions” (In Portuguese), M.S. Thesis, University of Sao Paulo at Sao Carlos, 114p.

Ferreira, J.A.Z, Bueno, B.S., and Zornberg, J.G. (2008). “Pavement Reinforcement Study using Small Dimension Pullout Equipment.” Proceedings of GeoAmericas 2008, Cancun, Mexico, pp.963-972.

Gill, D. R. and Lehane, B. M. (2001). “An Optical Technique for Investigating Soil Displacement Patterns,” Geotechnical Testing Journal, v. 24, n. 3, pp. 324–329.

Gupta, R. (2009). “A Study of Geosynthetic Reinforced Flexible Pavement System”, Ph.D. Dissertation, The University of Texas at Austin, 282p.

Han, J., Zhang, Y. and Parsons, R.L. (2011). “Quantifying the Influence of Geosynthetics on Performance of Reinforced Granular Bases in Laboratory”, Geotechnical Engineering Journal of the SEAGS & AGSSEA, v. 42, n.1.

Hertzberg, R.W., Vinci, R.P. and Hertzberg, J.L. (2012). "Deformation and Fracture Mechanics of Engineering Materials", Hoboken, Wiley, pp.128-180.

Iskander, M. and Liu, J. (2010). "Spatial Deformation Measurement Using Transparent Soil", Geotechnical Testing Journal, v. 33, n. 4, pp.1-8.

Jensen, K.D. (2004). "Flow Measurements", Proceedings of ENCIT 2004: 10th Brazilian Conference of Thermal Engineering and Sciences, Rio de Janeiro, Brazil, pp. 1-24.

Kakuda, F.M., Bueno, B.S., Teixeira, S.H.C. (2006). "Geogrid pullout tests using small scale equipment", Proceedings of the 8th International Conference on Geosynnthetics, Yokohama, Japan, pp.1443-1446.

Koerner, R.M. (2012). "Designing with Geosynthetics", v.1, Xlibris, pp.48.

Liu, J. and Iskander, M. (2004). "Adaptive Cross Correlation for Imaging Displacements in Soils", Journal of Computing in Civil Engineering, v.18, n. 1, pp.46-57.

McKelvey, D., Sivakumar, V., Bell, A. and Graham, J. (2004). "Modeling vibrated stone columns in soft clay", Proceedings of the Institution of Civil Engineers: Geotechnical Engineering 157, Issue GE3, pp. 137-149.

McDowell, G.R., Harireche, O., Konietzky, H., Brown, S.F., Thom, N.H. (2006). "Discrete Element Modeling of Geogrid-Reinforced Aggregates". Geotechnical Engineering, v.159, pp.35-48.

Moghaddas-Nejad, F. and Small, J.C. (2003). "Resilient and Permanent Characteristics of Reinforced Granular Materials by Repeated Load Triaxial Tests", ASTM Geotechnical Testing Journal, v. 26, n. 2, pp. 152-166.

Nakamura, T., Mitachi,T., Ikeura,I. (2003). "Estimating Method for the In-Soil Deformation Behavior of Geogrid Based on the Results of Direct Box Shear Test", Soil and Foundations, v.43, n.1. pp.47-57.

NCHRP (2004). "Guide for Mechanistic-Empirical Design of new and rehabilitated pavement structures", National Cooperative Highway Research Program (NCHRP) Project 1-37A, Washington, D.C.

Ochiai, H., Otani, J., Hayashic, S., Hirai, T. (1996). "The pullout resistance of geogrids in reinforced soil", Geotextiles and Geomembranes, v. 14, pp. 19-42.

Palmeira, E. M. (2004). "Bearing force mobilization in pullout tests on geogrids", Geotextiles and Geomembranes, v. 22, pp. 481-509.

Palmeira, E.M. (2009). "Soil-Geosynthetic Interaction: Modelling and Analysis", Geotextiles and Geomembranes, v.27, pp.368-390.

Palmeira, E.M. and Milligran, W.E. (1989). "Scale and Other Factors Affecting the Results of Pull-Out Tests of Grids Buried in Sand", Geotechnique, v.39, n.3, pp.511-524.

Perkins, S.W. (1999). “Mechanical Response of Geosynthetic-Reinforced Flexible Pavements”, Geosynthetics International, v. 6, n. 5, pp. 347-382.

Perkins, S.W. and Ismeik, M. (1997). “A Synthesis and Evaluation of Geosynthetic-Reinforced Base Layers in Flexible Pavements: Part I”, Geosynthetics International, v. 4, n. 6, pp. 549-604.

Perkins, S.W., Christopher, B.R., Cuelho, E.L., Eiksund, G.R., Hoff, I., Schwartz C.W., Svanø, G. and Want, A., (2004). “Development of design methods for geosynthetic reinforced flexile pavements”, FHWA-DTFH61-01-X-00068, Final report, 263p.

Raffel, M., Willert, C.E., Wereley, S.T. and Kompenhans, J. (2007). “Particle Image Velocimetry: A Practical Guide”, Dordrecht, Springer, 464p.

Ren, H. and Wu, S.T. (2012). “Introduction to Adaptive Lenses”, Hoboken, Wiley, 288p.

Saad, B., Mitri, H. and Poorooshasb, H. (2006). “3D FE analysis of flexible pavement with geosynthetic reinforcement”, Journal of Transportation Engineering, v.132, n.5, pp.402-415.

Sadek, S., Iskander, M. and Liu, J. (2002). “Geotechnical properties of transparent silica”, Canadian Geotechnical Journal, v. 39, n.1, pp.111–124.

Sadek, S., Iskander, M.G. and Liu, J. (2003). “Accuracy of Digital Image Correlation for Measuring Deformations in Transparent Media”, Journal of Computing in Civil Engineering, v. 17, n. 2, pp. 88-96.

Song, Z., Hu, Y., O’Loughlin, C., Randolph, M.F. (2009). “Loss in Anchor Embedment During Plate Anchor Keying in Clay”, Journal of Geotechnical and Geoenvironmental Engineering, v. 135, n.10, pp. 1475-1485.

Teixeira, S.H.C., Bueno, B.S., Zornberg, J.G. (2007). “Pullout resistance of individual longitudinal and transverse geogrid ribs”, Journal of Geotechnical and Geoenvironmental Engineering, v. 133, n. 1, pp. 37-50.

TxDOT DMS-6240 (2010). “Departmental Material Specification: Geogrid for base/embankment reinforcement”. Texas Department of Transportation (TxDOT), 3p.

Wakabayashi, T. (1950). “Photo-elastic Method for Determination of Stress in Powdered Mass,” Journal of the Physical Society of Japan, v. 5, n. 5, pp. 383–385.

White, D.J., Take, W.A. and Bolton, M.D. (2003). “Soil Deformation Measurement Using Particle Image Velocimetry (PIV) and Photogrammetry”, Geotechnique, v. 53, pp. 619-632.

Zhao, H. and Ge, L. (2010). “Camera Calibration Using Neural Networks”, Appendix in Moddeling with Transparent Soils by Magued Iskander, Springer, pp.299-312.

Zornberg, J.G., Ferreira, J.A.Z., Gupta, R.V., and Joshi, R.V. (2012). "Geosynthetic-Reinforced Unbound Base Courses: Quantification of the Reinforcement Benefits", Center for Transportation Research (CTR), Report No. FHWA/TX-10/5-4829-01-1, Austin, Texas, 170p.

Zornberg, J.G., Ferreira, J.A.Z., Roodi, G.H. (2013). "Geosynthetic-Reinforced Unbound Base Courses: Quantification of the Reinforcement Benefits", Center for Transportation Research (CTR), Report No. FHWA/TX-10/5-4829-02, Austin, Texas, 156p. [in press].